MODEL BASED IDENTIFICATION OF INTERNAL AND EXTERNAL DAMPING IN A CRACKED ROTOR

A Thesis Submitted in Partial Fulfilment of the Requirements

for the Degree of

DOCTOR OF PHILOSOPHY

by

DIPENDRA KUMAR ROY

DEPARTMENT OF MECHANICAL ENGINEERING

INDIAN INSTITUTE OF TECHNOLOGY GUWAHATI

GUWAHATI 781039, INDIA

MAY 2020

MODEL BASED IDENTIFICATION OF INTERNAL AND EXTERNAL DAMPING IN A CRACKED ROTOR

A Thesis Submitted in Partial Fulfilment of the Requirements

for the Degree of

DOCTOR OF PHILOSOPHY

by

DIPENDRA KUMAR ROY

(Roll No. 136103037)

DEPARTMENT OF MECHANICAL ENGINEERING

INDIAN INSTITUTE OF TECHNOLOGY GUWAHATI

GUWAHATI 781039, INDIA

MAY 2020

Department of Mechanical Engineering

Indian Institute of Technology Guwahati

Guwahati- 781 039, INDIA.

CERTIFICATE

It is certified that the work contained in this Thesis titled "**Model based Identification of Internal and External Damping in a Cracked Rotor**" submitted by **Mr. Dipendra Kumar Roy** (Roll no. 136103037) to the Indian Institute of Technology Guwahati for the award of the degree of Doctor of Philosophy has been carried out under my supervision in the Department of Mechanical Engineering, Indian Institute of Technology Guwahati. This work has not been submitted elsewhere for the award of any other degree or diploma.

MAY 2020

Dr. Rajiv Tiwari
Professor
Department of Mechanical Engineering
Indian Institute of Technology Guwahati
Guwahati- 781 039, INDIA.

Dedicated to the loving memory of my mentor, guide

and friend …….my 'family'

ACKNOWLEDGEMENTS

The journey towards the accomplishment of this thesis work has been ideal because of the presence of the people around me.

First, I would like to express my sincerest regards and gratitude to my supervisor, Prof. Rajiv Tiwari for his persistent guidance and suggestions during my PhD studentship and serving as my thesis supervisor. I thank him both for his encouragement and routine criticism, for the benefit of my thesis work. I wish to further correspond and learn from him in the coming days too. I also extend my deep sense of respect and thanks to my doctoral committee members, namely, Dr. S. K. Kakoty, Dr. A. Banerjee, and Dr. S. Talukdar for the valuable suggestions provided during my progress seminars. I thank the IIT Guwahati administration for whatever amenities I have utilised during my stay at the campus. I thank the past and present heads of Department of Mechanical Engineering, Dr. P. Mahanta, Dr. A. K. Dass and Dr. S. K. Dwivedy, for availing various departmental facilities.

My stay during IIT Guwahai was made pleasant by many friends and seniors of the research fraternity. Dr. D. J. Bordoloi of Vibration and Acoustics lab has been one such person was instrumental in helping me whenever it was required. I specially mention Dr. C. Sharavankumar, Dr. Sandeep Singh, Dr. Purushottam Gangsar, Dr. Shruti Janani Rapur. Specially thanks to the lab mates, Nilakshi Sarmah, Gyan Ranjan, Gargi Majumder and Prabhat Kumar for being helpful in research related discussions and in experimental work.

The pain taken by my wife Juganu Kumari and children Venumadhavi (Adya) to keep me free from the daily household routines so that I could focus on my thesis work and this cannot be expressed in words. I am obliged for all the sacrifices they made for this endeavour.

I pay my foremost respect to my parents, Shri Baikunth Deo Roy and Late Jagadmba Devi (comes in my dreams to bless me),banking on whose advice and well-wishes I have been able to successfully carry out my Ph.D. I will cherish the memories, I have spent with all of my friends here at Guwahati and elsewhere. I would like to thank to all my brothers (Ramesh Roy, Jitendra Roy and Nripendra Roy) and sisters (Vidya Devi, Indu Devi and Sunita Devi), from childhood providing me their possible support. I remember all others who helped to me directly or indirectly during my stay at Guwahati.

I would like to thank the Almighty God for having blessed me with all the happiness in life to keep me motivated towards the goal.

May 2020

Dipendra Kumar Roy

IIT Guwahati

ABSTRACT

In rotor systems both external and internal damping are present. External damping mainly occurs due to bearings and its force direction is fixed. Internal (rotating) damping is an important fault parameter in rotor system, which appears due to rubbing of free surfaces and material hysteresis during shaft rotation in dynamic conditions. Rubbing of free surfaces occurs at shaft and disc interface, and crack faces during opening and closure. Direction of internal damping force changes with shaft rotation and due to this, it is also called rotating damping. It is also one of the causes of instability in rotors, when the rotor system rotates above critical speeds. Experimental estimation of the internal damping is a challenging task as compared to the external damping in a cracked rotor system. Hence, the main aim of the present work is to distinctly estimate the internal and external damping in a cracked rotor-bearing system. For estimation proposes a model based identification procedure has been developed and tested through numerical simulation and experimental investigation.

In the process of development of identification procedure in the form of regression equation for the estimation of internal and external damping other important unknown system parameters, like the unbalance and loss of stiffness of shaft due to the crack, are also identified. This reduces the estimation error of main parameters to be estimated. For this purpose, initially a simple two degrees-of-freedom (DOFs) rotor model has been considered, which includes two translational co-ordinates only. In the rotor system, the crack model is based on the assumption of a switching crack, which gives excitation at multiple harmonics both in forward and backward whirl. Full spectrum responses are obtained through fast Fourier transform (FFT) of numerically generated displacement responses and are utilized in the developed identification procedure to

estimate rotor system parameters, which is found to be robust even in the presence of measurement noise in system responses and bias errors in system parameters. For the application of the developed identification procedure in the physical system, experimentally generated responses from a cracked rotor test rig are converted into frequency domain (both amplitude and phase) by regression based full spectrum and FFT based full spectrum. Residual bow in the shaft affects the 1X component of the frequency domain response, which is removed by utilizing slow run response of the rotor system. Estimates from experimental measurements are found to be consistent even at different rotor speeds.

To have more realistic cracked rotor system, in which the effect of the gyroscopic couple is also present due to an offset disc, a rotor model with four-DOFs has been considered. It includes two transverse translational and two rotational displacements for the estimation of internal damping. Analytical model of the rotor system has been developed in the present work, which is used in developing identification procedure for the estimation of internal and external damping along with other unknown parameters of the system. To overcome the practical difficulty of measuring rotational DOFs accurately, the dynamic condensation has been carried out in the identification algorithm. The identification algorithm is tested with a numerical simulation considering measurement noise in responses and bias error is system parameters. Then with experimental data from a rotor test rig, the application of the identification procedure is illustrated. It requires slow run removal to reduce effect of shaft bow and complete number of cycles of signals for the reduction of leakage errors. Moreover, ambiguity in phase while using FFT to get full spectrum is tackled by using multi-frequency reference signal. The estimates are found to be consistent at different rotor speeds as well as with previous 2-DOF rotor model.

Finally, the present work has been extended for cracked flexible-rotor flexible-bearing with multiple-disc rotor system using finite element modelling considering four-DOF per node. Herein, apart from internal damping, bearing stiffness and damping coefficients have also been estimated using the developed identification algorithm with the help of full spectrum. To check the robustness of the algorithm random noise is added to the time domain responses.

TABLE OF CONTENTS

LIST OF FIGURES

LIST OF TABLES

NOMENCLATURE

$\mathbf{A}$	Regression matrix
1X, 2X, 3X…	First harmonic, second harmonic, third harmonic, …
$\mathbf{b}$	Right-hand side vector of regression equation
c_E	External damping
$\mathbf{C_E}$	External damping matrix
CEF	Crack excitation function
c_H	Internal damping
CWT	Continuous wavelet transform
d	Diameter of shaft
e	Disc eccentricity
E	Young's modulus
EOM	Equation of motion
$\mathbf{f}$	Force vector
F	Force
FEM	Finite element method
FFT	Fast Fourier transform
$\mathbf{G}$	Gyroscopic matrix
g	Gravity constant
I	Diametral area moment of inertia
j	$\sqrt{-1}$

K	Stiffness matrix
K_0	Intact shaft stiffness
l	Length of shaft
m	Disc mass
M	Mass matrix
n	Integer number
NDE	Non-destructive evaluation
p_i	Participation factor of switching crack function
q	Displacement vector
r, s	Complex displacement with and without static deflection (in stationary frame)
R_i	Displacement at i^{th} harmonics
SCEF	Switching crack excitation function
t	Time
u	Shaft displacement from static equilibrium position
$\boldsymbol{u}$	Transverse translational vectors
VFD	Variable frequency drive
X	Vector of unknown parameters
x, y	Vertical and horizontal displacement of disc

Greek Letter

δ_w	Static deflection of shaft

ϕ	Phase of unbalance
$\boldsymbol{\varphi}$	Rotational displacement vectors
Δk_{ξ}	Additive crack stiffness
$\sigma(t)$	Switching crack excitation function (SCEF)
θ_i	Phase of multiple i^{th} harmonic
ψ_i	Phase of reference i^{th} harmonic Rotating axis system
ξ, η	Displacement in rotating frame
ζ	Complex displacement (in rotating frame)
π	Mathematical constant
ω	Rotor spin speed

Superscripts

o	Degree
D, d	Dynamic
T	Transpose of matrix

Subscripts

br	Bearing
C	With Crack
E	External damping
exp	Experimental
H	Internal damping

Im	Imaginary
m	Master DOFs
Re	Real
rot	Rotational
s	Slave DOFs
S	Shaft sub-model
st	Static deflection
th	Theoretical
unb	Unbalance
x, *y*	Stationary axis system
xd, *yd*	Direction of damping force
ξ, η	Rotating axis system

CHAPTER 1

Introduction and Literature Survey

1.1 Introduction

Rotating machinery is the backbone of the industrial world and its application can be found in diverse field of manufacturing, automobile, transport, power generation, household, and medical fields. There is increasing demand of high-power and high-speed in rotating machinery that are used in generators, turbines, compressors, pumps, and motors. In industrial perspective, a breakdown of the rotating machinery leads to huge monetary losses and even in a worst cases damage to the human being. Hence, for safe operation of the rotating equipment a maintenance strategy, such as fault detection and diagnosis is required to increase the life of machinery and human protection. An increased effective life of the machinery is accomplished through proactive and predictive maintenance based on conditioning monitoring. The rotor shaft is a critical part of the rotor machinery, which transmits the power. Hence, fault detection and diagnosis is needed for the shaft. Most common faults in the shaft are unbalances, cracks, bow, misalignment, rubs, looseness, etc., which come during persist dynamic conditions in the rotor system (Rao, 1996; Adams, 2009; Lees, 2016; Sinha, 2014).

Sometimes, rotors are subjected a self-excited vibration, which is one kind of instability due to the rotor internal damping among others. Such damping is also called rotating damping. This type of damping causes instability of rotating machinery above the rotor critical speed. Rotor internal damping force is present in the rotating frame. Often the root cause of failure of machinery may not be diagnosed properly, which causes other mechanisms to initiate a breakdown of machinery. Assessment of internal damping present in the system is not reliable and its estimation is very crucial for predicting instabilities. The root cause of approximately 80%

of failures in machinery is due to process variation, which are not observed in the design phase (Forsthoffer, 2011). Other destabilizing mechanism are oil whip, steam whirl, Morton's effect, asymmetric rotor, etc., which are diagnosed as the other main causes of self-excited vibration in rotor system (Adams, 2009).

In following sections, literature reviews are presented and organized in five parts as: a brief review on condition monitoring of rotating machinery, crack modelling, internal damping modelling, identification procedures using full spectrum signal processing, and experimental studies on rotor fault identification.

1.2 Healthmonitoring of rotating machinery

The instability phenomena in the rotor system arises due to different types of faults and rotor-bearing system properties. One of the common faults in rotating machinery is a crack in the shaft. The crack propagates owing to the high stress intensity factor at micro defect locations due to fatigue loading. While the crack appears in the shaft, initially it is undetected in its dynamic response behaviour. The crack may grow over time and gradually the shaft changes its stiffness. Moreover, due to opening and closure of crack surfaces rubbing take place and it introduces the internal damping. It introduces double complexities of combined effects of the crack as well as the associated internal damping. This can lead to instability and it may be the main cause of breakdown or failure.

Different methods that are utilized in industries for the crack detection, which are listed as

- Vibration based condition monitoring and diagnostics
- Based on lubrication and oil analysis
- Acoustic and ultrasound emission
- Infrared thermography

- Motor current signature analysis
- Other method such as visual inspection, scanning electron microscopy, atomic force microscopy, die penetration test and wear debris analysis

The crack identification methods have been studied by researchers, as per the review paper of Sabnavis et al. (2004), broadly by three methods, such as the model-based and signal-based methods; the modal testing method; and non-traditional methods.

Observation and diagnosis of faults, which are present in the machinery, based on signal methods is commonly performed through the vibrational signature of the machine. The vibration signatures are compared with fault and without fault conditions or any other reference of vibration signature of the machine. Whereas, in the model based method, it utilizes an analytical model of faults and fitting between model and experimental data is performed to estimate unknown fault parameters in fault models. The mathematical model of crack depends upon the behaviour of crack opening and closure with the shaft rotation. Methods exist for the crack identification based on genetic algorithm, neural network, fuzzy logic, along with signal-processing techniques such as fast Fourier transform, wavelets, Hilbert transform, etc. Doebling et al. (1996) proposed a review regarding the identification of damage and health monitoring for a wide range of multi-disciplinary structure. Herein, the most of them were illustrated for the damage identification based on the visual or localized methods. As per expectation of probable damage location in structures a visual inspection for the crack detection is done. However, for the case of rotor system, which in complex structure due to assembly of many components, it demands a global damage detection and identification method. This method can be utilized to find out the condition of machinery and its components through vibration characteristics.

The condition monitoring based on damage detection of the machinery is discussed to study various machine parameters continuously related to the mechanical condition of machinery. It assists in reviewing whether the machine is mechanically healthy or unhealthy, which could prevent from otherwise unexpected damages. Edwards et al. (1998) presented a review paper on conditioning monitoring of fault diagnosis techniques in rotating machinery, such as for the mass unbalance, crack, misalignment and bow shaft. They concluded that the model based fault diagnosis technique were necessary to be developed rapidly in order to meet the present demand of conditioning monitoring of the rotating machinery. Friswell (2007) reported a review on the inverse problem method that is utilized in the fault identification in rotor system.

In condition-based maintenance (CBM) strategy the machine breakdown is predicted through regular condition monitoring of machinery and based on this subsequently an optimum maintenance decision is carried out (Randall, 2011). Most of the methods studied are based on model updating techniques, which are categorised as the sensitivity method and the direct method. Sensitivity methods produce more options to choose the physically expressive fault parameters and preferably minimises a penalty function, which is a part of error in between observations and model predictions. On the other hand, direct methods reproduce the measure data by updating the whole mass or stiffness matrices of the dynamic systems.

The organized damage identification process expressed by Rytter (1993) divided in four stages (steps) as follows (i) Stage 1: Identification - Identifying the presence of damage in the structure, (ii) Stage 2: Localisation – Determination of the geometrical position of damage, (iii) Stage 3: Sizing - Quantification of the severity of the damage, and (iv) Stage 4: Prognosis - Prediction of the remaining useful life of structure.

The identifying Stage 4 from the above process mostly depends on quantification of fatigue life, structural design analysis and fracture mechanics theory, i.e. it is not addressed in the vibration or model based analysis. The process of Stages 1 to 3 are directly related to the modelling and testing in structure dynamic, and approaches to the inverse method based on model analysis.

A simple problem that is present in the system analysis is a modelling error, and without accurate parameters even the undamaged model will produce an error in the responses. For the minimization of modelling error the model updating method is required, such as the finite element based updating method, which is useful in illustration of the difference in responses between damage and undamaged models. Other problems that include the effect of environmental, non-stationarity, non-linearity and frequency range of operation. The condition with the frequency range is that in high-frequency range vibrations can locate the localized fault accurately, but require position sensor and actuator locations in very close to the position of the fault. Hence, the inverse method depends upon a model of the damage and the estimation performance is dependent of accuracy and reliability measured physical responses.

Hill and Baines (1988) illustrated the design of an expert system for the analysis of captured data based on computer algorithm to simulate the human expert. He concluded that the vibration monitoring of system based on expert system approach may be more helpful provided details of design of the system is known. Isermann (1994) suggested that for accurate fault diagnosis more than one method of fault diagnostics and identification (FDI) to be utilized. Condition monitoring is key feature in the production cost and maintenance of rotor system. Several of rotor faults initiate the self-excitation vibration owing to dynamic instability. Vibration are also generates owing to some externally applied loads, such as the crack, and bow shaft effect and mass unbalances.

Iwatsubo (1976) discussed the effect of different possible errors on the critical speeds, instability and unbalance responses of rotating machinery. It was pointed out that variation in bearing dynamic coefficients influence much more on the rotor instability than the others effects, such as the mass and stiffness of the system. He et al. (1990) studied a method for the identification of shaft rub. Principal components and autoregressive spectra technique (PCAT) was utilized in identifying the shaft rubbing based on the coloured noise intensity in a large machinery. Lee and Joh (1994) illustrated the direction frequency response functions (dFRFs) for the analysis of the support anisotropy and the shaft asymmetry. Childs and Jordan (1997) presented the rub analysis and improves the system stability owing to a clearance at the rub location. Isermann and Balle (1997) suggested standardization of terminology and also discussed historical development of model based fault detection. Model based fault detection technique was categorised as estimators, parity equations and parameter estimations. Ayoubi and Isermann (1997) studied automatic diagnosis of various faults and focused on neural network and fuzzy logic algorithm, and also summarised different fault classification and inference methods.

Varney and Green (2015) used a rotor-stator contact model considering anisotropic support stiffness, and studied cross-coupling stiffness and coulomb friction for the case of nonlinear phenomena. They found that the effect of gravity is negligible above threshold speed of rotor system. Subsequently, Varney and Green (2016) extended the work to observe contact force in a linear elastic contact model considering a rough surface in a rotor-stator rub model. In another work, Smyth et al. (2016) considered viscoelasticity in stator support and studied influence on dynamic responses of rotor-stator rub. Varney and Green (2016) used a rough surface contact model to study behavior of quasi-static contact force versus radial deflection of rotor, and investigated different contact force models for its comparison. Subsequently, Varney and Green (2017) worked on a non-contacting mechanical face seal. Seal equations of motion were simulated according to clearance of seal face to estimate contact pressure. Waveforms in frequency spectra were used for the same.

The detection based on vibration signal of the most common faults, such as the unbalance, crack, bow and misalignment are discussed in the next section.

1.2.1 Vibration based monitoring on rotating machinery

Vibration signatures of rotor defects are not as unique as to be distinctly identifiable, due to overlapping dynamics and statistical reasons. After the pioneering works of Hookes (1660), Bernoulli (1705), Bernoulli (1751), Euler (1774) and others, researchers were able to solve the problem of vibrations of a bar. Continuous beam theories appeared and established after the work of many later scientists, including Rayleigh and Timoshenko. However, due to complexities associated with the crack mechanism, theories on damaged beams and rotors are far from being established. Even after a volume of papers published on cracked structures in the last three decades, a consistent cracked beam theory is yet to be developed. Downham (1976) made a comprehensive study about vibration based analysis of recent advancement in fault diagnosis in rotating machinery by outlining various case studies of rotor faults, such as the gear and bearing wear and turbine blade failure. Thomas (1984) illustrated vibration monitoring technique for large (above 500 MW) turbo-generator using the frequency measurement and its type for the data analysis. Gottlich (1988) adopted the idea of offline performance map of vibration based condition monitoring to describe the performance efficiency of a rotating machine. The performance map is constructed relative to the actual maximum efficiency data and the design efficiency, whose combination with the measured vibration data enhances the running conditions of system. Smalley et al. (1996) illustrated a method for assessing the severity of fault using vibrational data and its related cost effectiveness using the net present value method. Some guidelines were formulated in comparison of maintenance and downtime cost against the possible cost after damage of machinery. Vibration based condition monitoring aided an immense performance of machinery fault diagnosis and is examined by Stewart (1976), Smith (1980) and Taylor (1995). Smith (1980) analyzed the faults qualitatively using vibration characteristic including the nonlinear effects. In the same way Stewart (1976) and Taylor (1995) included how the measured vibration data can be utilized for the fault diagnosis process.

Vibration signatures of a cracked rotor are not unique and the cost associated with failure due to cracks is high, hence the investigation of cracked rotors draws considerable attention from academia and industry alike. Using signal based methods researchers, such as Bently and Muszynska (1986a), Allen and Bohanick (1991), and Eisenmann (1998), reported the crack detection onto the shaft for the various cases. The root cause of shaft cracks for various cases are studied, such as due to the misalignment, fretting corrosion, and heavy side loads in generators, compressors, gears and nuclear coolant pumps. Based on the vibration method for the crack detection, Bently and Muszynska (1986a) presented a work in which spectrum amplitude at 1x gradually increases during rotation of shaft.

However, other researchers illustrated that 2x component is the good indicator of shaft cracks. The judgement by Werner (1993) was that spectral at 1x trend is a better indicator for crack in the shaft response, but at 2x it is mainly because of the local asymmetric stiffness of shaft owing to the crack. Also he gave the recommendation that the response at 2x spectral is too much sensitive owing to other factors, like misalignment, side loads, support system asymmetry, etc., to be a reliable behaviour of cracks onto the shaft. Various authors have also recommended in their studied the spectral at 2x response for the crack detection in the shaft, such as Saavedra and Cuitino (2002). They demonstrated the spectral at 2x behaviour in theoretical and experimental analysis of a cracked shaft. They observed based on the vibration at half of the critical speed of cracked rotor for horizontal shafts, and found that it is clearer in behaviour as the crack indicator. As per the study through fracture mechanics by Lazzeri et al. (1992), it is observed that in monitoring of operational diagnosis, the utilization of 2x spectral in a machineries to identify the cracks is better. Bently and Muszynska (1986b) illustrated 2x spectral based on comparison of start-up/coast-down of rotor, which is more useful than steady-state operation. Sanderson (1992) presented detection of crack based on the propagation of crack in a nuclear plant of 935 MW turbo-generator. Herein, the crack was detected when it reaches 25% of the shaft diameter and then machine was sent for maintenance. Muszynska et al. (1992) illustrated that the torsional vibrations are excited even through purely radial forces in a cracked shaft due the presence of unbalance and misalignment. Based on observation in the horizontal and vertical machines during monitoring of torsional vibrations they studied that the spectrum at 4x, 6x, 8x, etc. were found to the lowest torsional frequency, which was helpful in the detection of crack.

Gasch and Liao (1996) illustrated the detection of crack based on orbit shape method. Herein, the vibration of shaft in the spectrums are forward orbits of 1x, 2x and 3x frequencies and same also for backward frequencies. The monitoring on backward harmonics, particularly in transients case, can be used to detect presence of cracks. An experimental verification of the above method has been illustrated by Liao and Gasch (1992) based on a different depth levels of crack in a test rig. Plaut et al. (1994) studied the transient behaviour of a cracked shaft based on a constant acceleration or deceleration passed a critical speed. The review paper of Dimarogonas (1996) emphasizes the importance of analysis of cracks. Goldman and Muszynska (1999) presented the periodicity of major rotor malfunctions, most defects cause rotor vibration component at multiples (nX) or fractions {(n / m) X} of the shaft spin speed. Tiwari (2005) discussed improving estimation of the bearing dynamic parameters along with residual unbalance in a two-degree of freedom rotor-bearing system using a specific identification algorithm with the help of regression matrices. Zhao et al. (2012) used multivariate empirical mode decomposition (EMD) and full spectrum for the condition monitoring of centrifugal pumps. A brief summary of defects and their periodicity is presented in Table 1.1, based on the compilation of Goldman and Muszynska (1999), and Bachsmid et al. (2010).

Table 1.1 Periodicity of common rotor defects

S. N.	Defect	Frequency	Nature
1	Mass unbalance, rotor eccentricity	1X	generally an elliptical orbit
2	Bearing misalignment	1X, 2X, 3X	Axial and radial vibration components present
3	Bearing wear off	0.5X, 1X	
4	Shaft bow	1X	
5	Rotor stator rub	0.33X, 0.5X	bifurcation diagrams and Poincare maps helpful
6	Transverse crack	1X, 2X	2X components are the indicators
7	Axial rotor asymmetry	2X	native vibration due to intrinsic asymmetry
8	Flexible coupling misalignment	1X, 2X, 3X	1X predominant but other harmonics present
9	Rigid coupling misalignment	1X	
10	Loosening bearing bushes	2X	up to 6X may be present, out of phase with 1X

1.3 Internal damping in rotors

Many researchers have studied on the destabilizing mechanism of rotating damping in the rotor system in past years, but the research on the model-based identification are still going on. Usually, the main obstacle is the identification of source of the physical phenomena of instability at the operational speed. This is the reason of difficulty in the modelling and identification of the system parameters, such as the case of rotating internal damping and it is a real challenge. The researcher focused on the modelling of internal damping due to different reasons, such elastic hysteresis, internal viscous and rubbing between disc and shaft. Ehrich (1964) observed the whirling of the shaft in the presence of internal damping and found that an individual whirl mode is induced by different damping conditions. The instability occurs beyond a certain threshold speed and depends upon the ratio of the external to internal damping. Shaw and Shaw (1991) presented the stability analysis of the rotor shaft incorporating the internal damping in obtaining synchronous steady state solution. They also studied the unbalanced rotating shaft with internal damping at the non-linear resonance.

Osinski (2018) presented the role of damping, which is very important for the high spin speed dynamic machineries and technically can be possibility source of problems. He divided the vibration damping phenomena into following groups

1. *Internal damping*: This embraces all possible root of energy dissipation only from the internal structure of a vibrating element. The cause of internal damping is found related to all phenomena involving material under variation of stress and strain in an irreversible way. Process in the structure, such as the molecular diffusion within a crystal lattice and relative motion between the crystals inside the material. The level of internal damping depends upon construction of material including the stress magnitude. The internal

friction is also considered strongly affected by temperature, such as polycrystalline materials the present of friction is belonging to mode of heat treatment, plastic working and surface condition. Apart from this, the characteristic of internal friction effects can also lead as a bifurcation-type instability in rotating shaft.

2. *Structural damping*: This damping includes energy dissipation arising at contact surface and interaction layer of elements in permanent joints, parts of structures, etc. These elements decides the mutual layers by self and undergo micro-slip being the outcome of material elasticity deformability. This phenomena is governed by Coulomb's laws. The structural damping mainly influences mechanical system, such as machine and devices which are related to the sources of damping present in the system. Unlike internal friction, the structural damping strongly affects vibration frequency.

3. *Friction in sliding joints*: In joints are characterised with a distinct relative motion, such as in slide bearing, guide poles, etc. The character of the friction known to be different that is present in the dry friction without lubricant. It is a linear behaviour and produces a viscous resistance, when lubricant is added it becomes a non-linear behaviour. Both of these behaviours are attenuated the vibration of the moving body. The dry friction can also introduce a self-excitation vibration at high spin speed.

4. *Hydrodynamic and aerodynamic damping*: Damping because of resistive force developed in between moving element with the layer of liquid or gas, having relative motion, is known as the hydrodynamic and aerodynamic damping. This damping depends upon

viscous property of liquid or gas. The design of a machine is most important and the damping information can be observed by testing the property of the fluid separating solid elements. These information are applied in the sliding bearings, hydrostatic and aerostatic dampers.

1.3.1 Internal damping due to rubbing or friction

Friction forces develop between two mating surfaces of rotor parts during whirling, such as between a disc mounted on a shaft (Rao, 1996; Adams, 2009; Tiwari, 2017). It is caused due to differential extension and contraction of shaft and disc mating surfaces during whirling and due to this rubbing takes place. For example, the shaft elongates at the location of interface AA (Figure 1.1) and the friction force at disc interface opposes the shaft deformation, and these forces provide a hysteretic damping effect. Similar effect will be there at interface BB. This kind of damping can be modelled as force proportional to the time rate of shaft deformation instead of proportional to the time rate of shaft displacement.

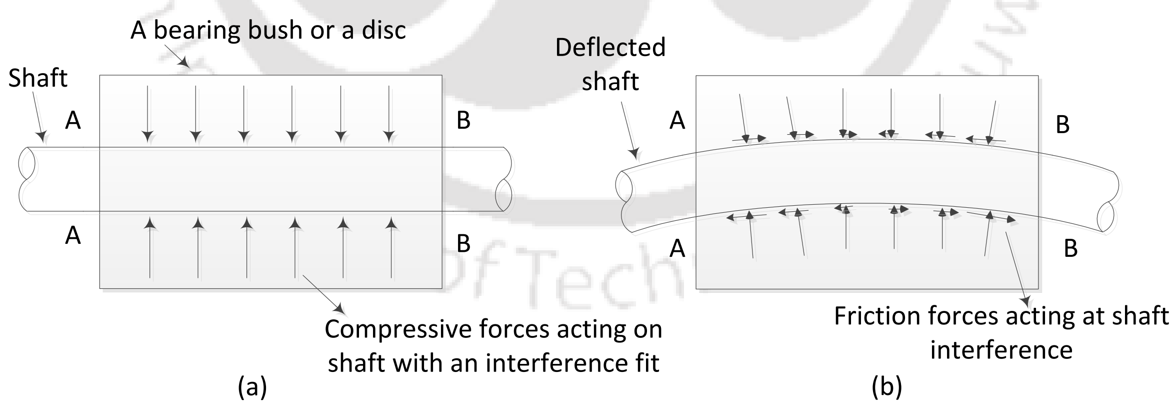

Figure 1.1 A shaft-disc systems with an interference fit (a) without shaft deformation and (b) with shaft deformation

Gunter (1967) developed equations of motion and presented a modal analysis on the stability of a single mass flexible rotor system due to influence of rotor internal friction. He estimated the stability threshold with the help of numerical simulation and compared that with experimental data. It was found that the stability achieved due to incorporation of flexibility and damping into the support bearing of the rotor system. Similar work was extended by Gunter and Trumpler (1969) for a single mass rotor system model with the incorporation of anisotropic supports and inclusion of the internal friction damping characteristics on the stability analysis for different rotor spin speeds up to and including of stability threshold. Bently and Muszynska (1985) discussed the stability of rotating machineries by two ways of internal friction mechanisms. The first, it is found that the effective damping level decreases due to internal friction in rotating elements of rotor system. This effective damping reduces duration of rotor sub synchronous and backward precessional vibrations, which is caused by other instability mechanisms, such as the rub or fluid flow dynamic forces, and promotes the unstable motion. Secondly, the internal friction is found to be the main root of rotor self-excitation displacement, which are due to various faults, such as incorrect shrink fits, loosening of shrink fits by mechanical fatigue, or by differential thermal growth.

Fischer and Strackeljan (2006) studied the viscous internal damping and dry friction damping at disc-shaft joints and its instability effects in the Jeffcott rotor model. The developed model illustrated the effect of instability based on the possibility of occurrences in real laboratory centrifuges and that was simulated by the models with 4 and 8 degrees of freedom. Lund (1990) worked on the influence of the stability in a rotor system and studied the friction in a joint, which was due to the rotor bent slope caused by discontinuity and it provided a micro-slip. Walton et al. (1990) studied the effect of internal friction at interference-fit joint of turbomachinery. They observed an unstable sub-synchronous vibration effect when the spin speed crosses the bending critical speed of the rotor system.

Recently, Sarmah and Tiwari (2019a) considered the internal and external damping in a cracked rotor model integrated with active magnetic bearing and studied the effect of the crack parameter and unbalance on rotor responses. The crack breathing model was developed based on breathing behaviour utilizing of Fourier series expansion. The development of mathematical analysis of the crack model was considered for a simple rotor with an offset disc. The proposed model using full spectrum approach and regression based method was utilized to estimate the rotor dynamic parameters. Again, Sarmah and Tiwari (2020) extended their previous work (2019a) using the model based identification of crack parameters. In this work crack model was assumed based on switching behaviour function (whereas earlier was based on breathing behaviour crack function) of to the rotor shaft. In addition, the shaft residual bow effect was also considered to the analysis.

Different types of internal damping can exist in the rotor system. Apart from the internal friction damping mentioned previously, the hysteretic damping also is another root cause of instability. In the next section literature review on the hysteretic damping is presented.

1.3.2 Hysteretic and other form of internal damping

Melanson and Zu (1998) performed a modal analysis based on Timoshenko beam theory by incorporating the internal damping, such as the internal viscous and the hysteretic damping in the rotating shaft. They studied the stability of the rotating shaft due to internal damping through numerical simulations. Genta (2004) studied the effect of hysteretic damping in the dynamics of rotors at the subcritical and supercritical speeds for the case of the forward and backward whirl modes. The dynamic behavior of the rotating shaft was obtained with random variations of the internal damping that causes dynamic instability of the system (Dimentberg, 2005; Vatta and Vigliani, 2008). Montagnier and Hochard (2007) did a comparative instability study between the viscous and hysteretic internal damping models using the Euler-Bernoulli beam theory in a rotor system. The model contains the internal viscous (or hysteretic damping), translational and rotating inertia and gyroscopic effect.

Chouksey et al. (2010) studied the effect of stationary and rotating damping on rotor behavior. The source of the rotating damping is considered due the material damping of shaft. Chouksey et al. (2012) used the modal analysis to estimate the internal damping and fluid-film forces on a rotor system supported on journal bearings. The result showed that the internal damping of shaft material reduced the stability threshold speed considerably. Bucciarelli (1982) analysed the phenomenon of dynamic instability effects due to internal damping above critical speeds of a shaft system. He observed that the whirling of spinning shaft along with occurrence of unbounded growth in axial displacement. Chandra and Sekhar (2016) studied the nonlinear internal and external damping based on Krylov–Bogoliubov method. The method was used to find solution of a nonlinear equation of motion based on an approximate method including of the continuous wavelet transform based approach for the identification of rotor system parameters, both numerically and experimentally. Vervisch et al. (2014) designed an experimental setup to verify a theoretical modeling of internal (rotating) damping and studied its effect on the stability of rotor system. The stability threshold speed is estimated and investigated the parameters that the threshold speed. The damping is considered proportional to the stiffness in this model. In a separate work, the authors (Vervisch, 2016 and Vervisch et al. 2016) presented experimental details to investigate rotating damping in a thin shaft of rotating machinery. A disc was attached at middle of a shaft and the damping was considered due to rubbing between disc and shaft.

Prediction of the stability threshold of the rotating machinery was performed and validated through measurements.

Many authors have worked on the finite element modelling of rotor-bearing system. Nelson and McVaugh (1976) presented a rotor-bearing model based on the finite element method to study the nature of whirl speeds and modes for the different damping and stiffness conditions. In this study, they considered the effect of rotary inertia, gyroscopic and axial load effect. Further the linear finite element model was extended by Zorzi and Nelson (1977) to obtain the detailed analysis of damped rotor stability of a rotor-bearing system in presence of internal viscous and hysteretic damping effects. Nelson (1980) extended the work using the Timoshenko beam theory including of the internal damping. Chen and Ku (1991) and Ku (1998) studied the instability due to hysteretic damping in the forward and backward whirling of a rotor-bearing system. Forrai (2000) presented the stability analysis in a symmetrical rotor-bearing systems based on the finite element method and incorporating the internal damping. The uniform circular shaft in the rotor system modelled using Rayleigh beam theory and additionally including of both internal viscous and hysteretic damping, rigid disc, and discrete isotropic damped bearings. In the mathematical model, the rotatory inertia and gyroscopic moment effects were also considered. It was observed that the whirling motion grew towards unstable form beyond the threshold spin speed and further found that it improved the stability condition by increasing bearing damping.

Sino et al. (2007) dealt with studies of dynamic instabilities in a rotating system due to internal damping based on finite element beam approach by considering of transversal shear effect. Lemahieu et al. (2012) proposed that the internal damping is one of the main root cause of instability in a rotor system. The methodology was constructed in two steps. Firstly, they developed a finite element model of the beam by considering the viscous and hysteretic damping.

This model was utilized to obtain the threshold spin speed for instability and shaft resonance frequencies. Further, they studied the unbalance responses for different damping conditions to compare the relation between damping properties and instability. In second step, the work was extended through an experimental approach to test the damping model. Ren et al. (2017) studied the internal damping effect of a rotating composite shaft at high spin speed. It is found that at a supercritical speed shaft it achieved unstable self-excited vibration under the action of material internal damping. Herein, using the relations of strain-displacement of composite material, the potential energy, the kinetic energy, and the dissipative energy due to internal damping of the rotor shaft are combined for formation of equations of motion. The internal damping dissipative energy was developed based on the Euler- Bernoulli beam theory of the rotor system also for composite shaft, which considers the dissipative characteristics of viscoelastic damping. Finally, they developed the equations of motion applying of Hamilton principle on these combining form of energies. After that they used of the Galerkin method to solve the equations of motion. Jha and Dasgupta (2019) presented an unbalanced flexible shaft with an eccentric disc mounted at the mid-span by considering of the internal damping. Herein, they attenuate the Sommerfeld effect by linearized active magnetic bearing (AMB).

Other than the internal damping, the study of crack model is also important for the identification of crack parameters, so in the next section discusses the details of crack models in literatures.

1.4 Crack model in rotor systems

It is known that cracks commonly cause loss of structural integrity in mechanical structures. A crack generally start at a small imperfection and propagates during the operation due to high stress concentration. As initiation and development of a crack will eventually lead to catastrophic failure adding to the downtime and liability costs to the operator, hence they are considered as the most expensive of all rotor faults. Though straight transverse cracks have the highest probability of occurrence, other crack shapes and orientations have been found in the field and reported in literature (Bachsmid et al., 2010). Also a variety of cracks, like the transverse, slant and helical cracks have been reported and documented some of the incidences since 1953.

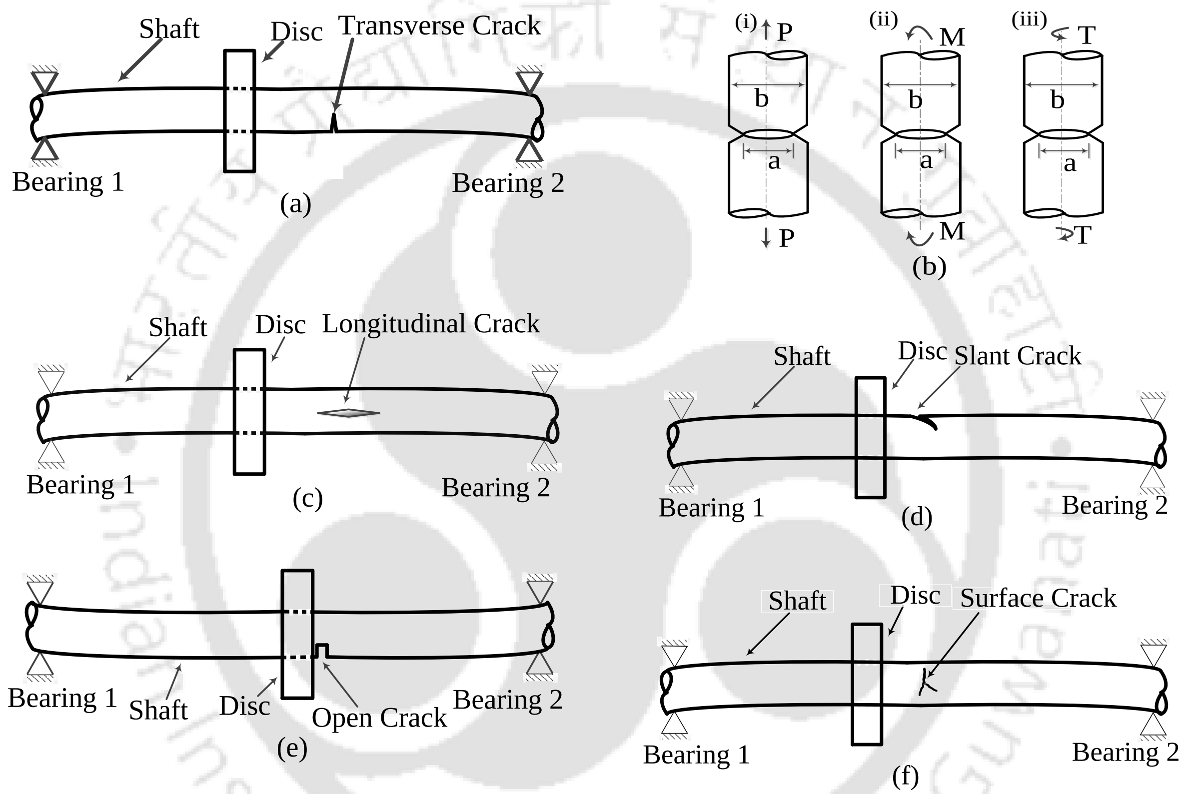

Figure 1.2 Various kinds of cracks (a) transverse crack (b) circumferential crack due to: (i) tensile load (ii) moment (iii) twisting moment (c) longitudinal crack (d) slant crack (e) open crack (f) surface crack

So the identification of crack is an important area, in which firstly the study of modelling of crack is mandatory according to the behavior of crack function in a form of opening and closure during dynamic condition of rotor with help of mathematical analysis. Various kinds of cracks are illustrated in Figure 1.2 (a-f), wherein represented by (a) transverse crack, (b) circumferential crack (due to (i) tensile load (ii) moment (iii) twisting moment), (c) longitudinal crack, (d) slant crack, (e) open crack and (f) surface crack. Cracks are classified as

Transverse Cracks: These cracks propagate in a plane perpendicular to the shaft axis and the most likely to be appear at sharp changes of diameter or of the geometry of the shaft (due to presence of holes, slots for keys, threads, etc.). Such cracks are initiated at a point of high stress concentration or material discontinuity and grow under fluctuating (bending) loads (Bachschmid et al., 2010).

Circumferential cracks: These cracks appear and grow perpendicular to the rotor axis. Circumferential cracks formation in a shaft subjected to cyclic torsion.

Longitudinal Cracks: These types of cracks appear and grow parallel to the rotor axis. Longitudinal cracks mostly develop due to anisotropic material property and grow under monotonic loads.

Slant Cracks: These types of cracks appear at an angle to the rotor axis due to the nature of loading and material property at the critical location. They are also known as helicoidal cracks, it develops when crack is caused by sudden brittle fracture (Lin and Chu, 2010).

Surface Cracks: These cracks are open on the surface. They are easily detectable by techniques such as the dye-penetrant or visual inspection (Bachschmid et al., 2010).

Open or Gaping Cracks: These cracks remain open all the times thus mimics a notch. A cracked rotor with an open crack behaves as an asymmetric shaft due to presence of the transverse edge crack (Al-Shudeifat, 2013). In the surface crack, the crack is open in all directions of the surface but in open or gaping crack, the crack is open in single transverse direction.

Breathing Cracks: This is a modeling idealization, to study the dynamics of a transverse crack on a rotor. It opens when the affected part of the material is subjected to tensile stress and closes when stress is reversed. Opening and closure may be gradual or switching. Flexibility of the rotor element containing the crack increases when the crack opens and the vice versa (Sekhar,2004a).

Switching Cracks: It is a subset of the breathing crack group, when a crack opening and closure is sudden instead of gradual then it is called as the switching crack.

The stiffness of the shaft depends upon typical breathing state of the crack, the shaft rotation governing the transition from the open to closure states of the crack or vive a versa. The full shaft stiffness can be considered when the crack is in fully closed condition. Further, when the crack comes into fully open condition then the stiffness reduces to a maximum value. In the identification of crack, a mathematical model of crack is important for the rotor system, which depends on many factors according to the type of crack. Main factors in the crack modeling are the stiffness, damping and its nonlinearity. According to the literature survey the stiffness and its non-linearity have been considered in the crack model. Some of researchers considered other factors, such as the thermal effect (Bachsmid et al., 2004) and the damping in crack modeling (Wauer, 1990). Many researchers presented crack model, based on reduction in stiffness at the crack section onto the rotor shaft. A review paper presented by Papadopoulos (2008) on a crack modeling was based on the strain energy release rate (SERR) approach.

Thomson (1943) and Kirmsher (1944) presented cracked shaft model based on a notch onto the shaft, which reduces the shaft cross-section. The effect of notch is included in the analysis based on reduction in cross section and illustrated the effect of notch location and its size on change in natural frequency of the rotor system. During the evolution of fracture mechanics in 1950s, Irwin (1957) and subsequently Rice (1968), Wells (1973) and Dimarogonas (1983) related the local flexibility of a fatigue crack to the crack stress intensity factor (SIF). Based on this theory, procedures were developed to obtain SIF from the local bending stiffness and vice versa. Formulae for the SIF as a function of the crack depth were provided in handbooks by several authors including by Tada (1985). Adams et al. (1978) modelled the crack as a linear spring.

Mayes and Davies (1976) illustrated the transverse crack effect on a rotating shaft during dynamic condition. A model of the crack was developed based on virtual work principle and the conservation of energy to investigate the crack phenomena. The SIF, which provides the stress distribution around the transverse crack a prior condition for the existence of crack. Similarly, the knowledge of bending moment around the transverse crack are also a pre-requisite. It can be understood from the theory given by authors that the crack response may be considered zero when the unbalance lies in the same phase of crack or the crack response can have two different synchronous responses, when the unbalance is in 180^0 phase with the crack. Experimentally, the crack is found to be most influencing between -45^0 to 135^0 phase of unbalance and crack. The shaft is observed to have intact behavior outside these limits. The 2x response represents the crack behaviour in the rotor, which gets a maximum amplitude when the unbalance and the crack are in phase.

Nelson and Nataraj (1986) presented a breathing crack model for the shaft based on finite element model. The model is expressed as switching function, which is represented as Fourier series to mimic an actual crack opening and closure phenomena. Herein, the function value for open crack state is one and the zero when the crack state is closed in the dynamic condition of machinery. This gives multiple harmonics both in forward and backward whirls.

Jun et al. (1992) worked on comparative study of two crack models, such as breathing crack as well as switching crack. It is found that breathing crack referred to partial opening and closure of crack due to the existence of cross coupled stiffness during rotation of the rotor shaft which is small relation with the direct stiffness. Herein, due to only direct stiffness in the switching crack model mathematically it is simple, less computational effort and also physically sensible to mimic the opening and closure behaviour of a crack.

Chondros and Dimarogonas (1998) illustrated the dynamics of cracked rotor system with single-edge or double-edge open cracks using fracture mechanics approach. The crack is modeled based on the hinge model, which divides the structure into two parts that are pinned at the crack location and the crack is simulated by the rotational and torsional springs. Experimental results from aluminum beams with fatigue cracks were found close to the predicted values from the continuous cracked beam and a lumped cracked beam vibration analyses.

Gasch (1993, 2008) studied the dynamic and stability analyses of a simple hinge model of Laval rotor. Developed equations of motion are linearized based on assumption of weight dominance and it was found that it was valid in the unstable speed ranges. Herein, the approach illustrated only one fault parameter, which is called as the additive stiffness owing to crack. It is found that in the crack modelling, the static deflection is also included in the vibrational displacement owing to consideration of weight dominance, while simplifying the crack opening and closure phenomenon. The switching crack excitation function in the form of square wave is taken to show the behavior of crack. Using Floquet analysis the stability of the cracked system was study. The author suggested the spectral analysis monitoring for increasing amplitude of 1x, 2x and 3x frequency components for the identification of crack.

Friswell and Penny (2002) studied various crack models classifying as the local stiffness reduction, discrete spring models, complex finite element crack models and bilinear breathing crack model. Identification of the crack depth and its location utilizing inverse methods was done. The crack modeling as a reduction in stiffness was obtained by Christides and Barr (1984) using continuous system approach for a cracked beam. Lee and Chung (2001) extended the same work on the crack flexibility matrix utilizing the fracture mechanics approach. Herein, based on percentage difference in the natural frequency for a cracked beam, was observed utilizing of various methods. The methodology demonstrated the structural health monitoring using the low frequency vibration of simple models of crack, like the stability based on beam elements. Moreover, a breathing crack behaviour utilizing bilinear stiffness model to estimate the crack location was studied.

Darpe et al. (2004) analyzed the coupled bending, longitudinal and torsional vibration of a cracked rotor considering Timoshenko beam model with all six degrees-of-freedom (DOFs). Based on the strain energy method, the additional stiffness matrix due to crack was formulated and the concept of crack closure line (CCL) to correlate the crack flexibility variation with the amount of crack opening was introduced. Green and Casey (2005) and Varney and Green (2012) studied crack detection in an overhung rotor system for the global and local effective asymmetry crack models. In responses, second harmonic was observed with the analysis and experimental results. Darpe (2007) described the dynamic behavior of rotor with a slant crack by finite element model. The flexibility matrix due to slant crack was derived by taking into account the influence of slant crack orientation. It was observed that the slant crack stiffness matrix consisting of additional cross-coupled stiffness terms, unlike in the transverse cracks. Those cross-coupled stiffness terms possess larger value for the slant crack leading to a stronger cross-coupling in bending-torsional-longitudinal vibrations. An accurate modeling of a crack requires an exact representation of the breathing mechanism. Bachschmid et al. (2008) developed breathing mechanism approach to accurately calculating crack characteristics from the cracked rotor system. Herein, the approach is based on a linear stress/strain distribution. The crack location was chosen to estimate the accurate prediction of the breathing crack. The finite element method utilized for the estimation and the prediction was based on three-dimensional nonlinear analysis. They illustrated that the linear model and the nonlinear finite element model for finding the breathing mechanism of the crack was in very close agreement.

Shravankumar and Tiwari (2013) studied a Laval rotor with the transverse crack and disc unbalance, and identified different rotor system parameters, such as the viscous damping, disc eccentricity along with the stiffness and crack excitation force in the switching crack model, using a regression matrix approach. Singh and Tiwari (2016) extended the identification of crack using a Jeffcott rotor incorporating active magnetic bearing (AMB) with and without considering the gyroscopic effect, respectively. The AMB was used to suppress the vibration and the controller current of AMB along with the displacement of disc in the form of full spectrum data were used to identify the crack. Singh and Tiwari (2017) further extended the work based on the FEM modeling including gyroscopic effect incorporating with AMB onto the rotor system.

Varney and Green (2013) investigated the crack location and its depth in a fatigue crack model, which was constructed for an overhung rotor system to diagnose a mechanical face seal in dynamic condition. Again, Varney and Green (2017) worked on a cracked rotor and investigated instability of a rotor with spin speed for deeper cracks. Liu and Jiang (2017) studied the lateral, axial and torsional vibration signals from the slant cracked rotor model of a steam turbine. Singh and Srinivas (2018) worked on the crack estimation including its location using of change in natural frequency prediction through approach of transfer matrix. The crack location matrix was illustrated in the form of stress intensity factors. The local flexibility of a crack in rotor shaft with its location variation were illustrated in the form of changes in natural frequencies of the system. Developed a generalized transfer matrix and validated from the finite element modelling. The analytical results were numerically compared with ANSYS. Hossain (2018) studied thebreathing of fatigue crack in the form of opening and closure behaviour during once per revolution rotational the shaft. The second area moment method was used estimation of in reduction of bending stiffness in the crack rotor and related to the breathing of fatigue crack at the location of crack. Further, the developed upgraded model is used to obtain the second area moment of inertia of crack cross-section at any axial location of crack along the shaft length under the effect of unbalance force. The updated developed unbalance model numerically validated with 3D FEM. Peng and He (2019) studied the stability analysis by utilizing of root locus method and observe the whirling motion at different axial locations of a rotor in presence of breathing crack. They discussed the estimation the eigenvalue problem in breathing cracked rotor in form of infinite complex mode solution based on the multiple scales method.

AL-Shudeifat et al. (2019) worked on the combined effect of faults, such as a crack with unbalance force vector orientation, for a cracked rotor disc systems. They investigated the locations of the critical whirl amplitudes through numerically simulations and experimentally during starting up operations. They developed equations of motion of the cracked system and formulated the finite element time-varying stiffness matrix. They utilized that for different unbalance angles with respect to the crack opening and that got significantly change in some zones of speeds value during critical speed traverse. Wang et al. (2019) used an anisotropic rotor-bearing system in presence of transverse crack to estimate the instability characteristic parameters, which was dependent on the breathing of crack and bearing characteristics. Herein, they developed the governing equations for the rotor system including of breathing crack model and bearing with eight-coefficient model by using the finite element method. They estimated the eigenvalues of the periodically time-variant system using the Hill's method to study the stability of the system. Ahmed et al. (2019) studied the effect on vibration behaviour of rotor in presence of open transverse crack based on hybrid *h-p* version of the finite element method and estimated the time-varying stiffness of crack element. Modelling the rotor based on the Euler-Bernoulli beam and the shape functions were used through Hermit cubic function coupled with the Legendre polynomials of Rodrigues. They developed the global matrices of the equations of motion of the cracked rotor through the Lagrange equations.

Apart from a single crack, there is an existence of multiple cracks in a rotor system, which were studied by various researchers. Singh and Tiwari (2010) presented a multi-crack identification methodology analyzing transverse response functions. Timoshenko beam theory was utilized for modeling the beam with multiple cracks based on finite element methods. Herein, flexibility matrices of two cracks based on the fracture mechanics approach was modeled. An algorithm was formulated for identifying the location of cracks utilizing frequency domain system equations of motion by applying an external force excitation in vertical direction. In order to identify the actual locations and sizes, an optimization algorithm was designed. Khorrami (2016) studied the behaviour of the rotor system utilizing of two transverse cracks by considering of breathing phenomena. Subsequently, Khorrami et al. (2017) used two transverse cracks in a rotor shaft in the form of breathing function to study the dynamic behaviour of the system.

According to the literature, it is clear that the most common modelling of the crack is based on the fracture mechanics approach consisting with the flexibility matrix. This approach has the advantage of describing the form of flexibility matrix easily, the coefficients of that can be theoretically estimated through the SIT. Herein, several methods for models are utilized, such as, the spring models, local stiffness reduction, FEM models, continuous cracked beam models, bilinear switching functions, equivalent loads and the reduction of second moment of area. The most of models of cracks are based on the flexibility, which increases due to occurrence of the crack. The effects of coupling owing to the crack have also been studied. Accurate breathing phenomenon of the crack is difficult to model for studying its realistic behaviour on the dynamics of the rotor system. The crack breathing mechanism possess nonlinear behaviour, where partial opening and closure of cracked faces occurs during tension and compression, respectively. To simplify the model of crack and to make it linear the switching crack model is used by various researchers where sudden opening and closure of crack face occurs, which suffice the square waveform for the crack. In the next section, a review on the identification of crack in the rotor system ispresented.

1.5 Crack identification in rotor system

Unbalance, misalignment and crack are the most common faults present in rotating machinery. From several decades, there has been numerous study on the analysis and identification of these for fault diagnosis and condition monitoring purposes. Researchers worked rigorously on the analytical, numerical and experimental studies on rotors (Sabnavis et al., 2004, Dimarogonas, 1996, Friswell and Penny, 2002). There are various techniques for the identification crack, viz. the signal based, model and modal based methods (Basseville, 2001; Mevel et al., 1999). The non-destructive evaluation (NDE) techniques are classified in two broad categories, i.e. the global and the local methods. Local methods (e.g., thermography, X-ray, ultrasonic, magnetic, liquid penetration, visual inspection and eddy current) require the information corresponding to the location of the potential damage and cannot provide information regarding the rotor health. So, there is a need of damage inspection techniques that can help to obtain the global information related to the structure. In global methods the physical location of damage is not related to the identification and measurement of the health of the system. The global methods are basically classified in three categories, i.e. the modal/model based, signal based, and advance machine learning methodologies (Basseville, 2001; Mevel et al., 1999). In the present context mainly the model based identification approaches will be reviewed.

1.5.1 Model based approaches

The identification of crack based on mathematical model is very popular technique for estimation of crack parameters. These techniques mathematically model the faults along with the system itself and forces associated with it. Usually fault parameters and forces are unknown and to have estimates of them these equations are fit to experimental data from similar physical system. Through these unknown fault parameters are estimated, which gives fault condition and its severity. Often these methodologies are tested in numerical simulation environment before application of experimental data (Shravankumar and Tiwari, 2013; Singh and Tiwari, 2016, 2017 and 2018). Further, the updated model can be utilized to predict to the experimental behaviour.

By now, it is well established that the crack in a structure introduces local flexibility, which causes a change in dynamics of the structure. This makes possible the formulation of an inverse problem based on changes in modal parameters and the free and forced responses of the structure. In dealing with cracked rotors (as opposed to structures in general) a more accurate model is needed which should consider: the coupling between different motions such as the bending, longitudinal, and torsional vibrations, the splitting of natural frequencies due to the presence of a crack, the nonlinearity in stiffness due to the breathing, and the friction between cracked surfaces.

Moreover, when a crack is present in the dynamic structure due to fatigue loading, it is well known that it gives a local flexibility in the structure. This makes possible for an inverse problem formulation based on changes in modal parameters of the structure with the free and forced responses. Also, nonlinearities arise in the stiffness due to breathing behaviour of the crack and change in natural frequency owing to crack present in the system. These behaviour are the resources for identification of crack that is analysed by researchers. Furthermore, when crack is fully closed the stiffness of shaft is maximum, during rotation its local stiffness is minimum when the crack is opened and in other positions the crack is partially open. Herein, the phenomena of opening and closure of a rotor crack is crucial in comparison of other structural cracks, and its modelling plays an important role in its identification.

Dimentberg (1961) worked on the rotational motion of asymmetric shaft. Addition of two vectors are used in the rotational motion, first term was same as the angular speed of the shaft and second term was twice of angular speed. The angular motion was found in an elliptical orbit phenomenon through relative responses of two vectors. For this reason the shaft experienced two limiting stiffness twice in one revolution. The shaft would rest at a higher position when the stiffness was more and vice a versa (according to the two vectors). Hence, the resultant of this oscillation was the 2× component of spectrum in the frequency domain. He reported the loss of stiffness owing to presence of crack, which was perpendicular direction to the crack front.

Dimarogonas and Papodopoulos (1983) developed a method to identify open crack from the response of rotating shaft. Herein, they illustrated unstable region in responses, which were because of various reasons, such as a surface crack on a rotating shaft and the coupling of lateral and longitudinal vibrations. This coupling was the only reason due to the presence of crack and hence useful for the crack identification. Gounaris and Dimarogonas (1988) utilized a cracked prismatic beam for structural analysis through finite element method. In the crack modelling, the crack flexibility matrix was used using fracture mechanics principles. The crack stiffness matrix was obtained by inverting the flexibility matrix.

For small cracks, the coefficients in crack flexibility matrices are smaller than that in the stiffness matrices. As a result of this, the solutions obtained from such matrices are not dependable because of numerical uncertainties during the solution generation (i.e., inversion of the matrix). To solve this problem, Gounaris and Dimarogonas (1988) proposed a stiffness matrix for the cracked rotor element on the basis of shape functions and transfer matrices. In numerical results, they showed the presence of discontinuity in the slope of beam at the crack location.

Liang et al. (1992), Capecchi and Vestroni (1999) and Hasan (1995) worked on identification of crack and other structural parameters by utilising the local flexibility in the rotating machineries. Sehkar and his group (1994, 1997 and 1999) also used the local flexibility approach in identifying the transverse, slant and multiple cracks, respectively, based on the finite element analysis (FEA).

From behaviour of cracked structures and rotors, the information of crack presence in the structure based on vibration was illustrated by many authors and it has been discussed earlier, but its location and depth is also of the important aspect in the identification of crack. Pandey et al. (1991) worked on the damage size and its location based of the finite element analysis according to changes of eigenparameters. The changes in diverse eigenparameters, such as the natural frequency and mode shapes, was used for this purpose. The changes in mode shapes was examined for locating damages in the structure. Herein, change in the eigenparameters are related with change in the size of damage. Gasch (1993) analysed a linear crack model with the introduction of perturbation method with direct stiffness terms. They provided a method to estimate the size of the cracks by utilizing 1st, 2nd and 3rd harmonics in response of the system that increases with direct proportion to the crack size.

Dharmaraju et al. (2004) provided an approach based on updating of model for the identification of crack in a rotor system. They applied model reduction scheme in the system of equations to reduce the excessive number of measurement locations. They used an error function in terms of estimated flexibility coefficients to determine the depth of crack using the least-squares technique. The robustness of the identification algorithm was also checked against moderate level of noise. Sekhar (2004a, 2004b) proposed a model of crack based on equivalent forces to estimate its location and depth on the shaft. The fault identification was carried out using harmonics of the frequency spectrum response. He found out that the crack depth estimation improves with increase in the number of measurement locations. In other paper, Sekhar (2004c) proposed a continuous wavelet transform (CWT) method to obtain the sub-harmonics from a run-down time domain vibration response from the locations of journal in the cracked rotor systems supported on fluid film bearings. They also analysed the dissipation of energy through journal fluid-film for different spin speeds of the system. The detection of cracks was found to be better with the utilization of sub-critical response peaks in the CWT than time domain signals, even for the crack of lower depths.

Some of the researchers have also focused on the coupling between orthogonal flexibilities that indicates the presence of cracks in the rotor system. Darpe et al. (2004) carried out the identification of cracks from the coupling effect introduced in the crack flexibility matrix. The frequency domain response of the cracked rotor system showed 1st, 2nd and 3rd harmonics in the lateral vibration, 1st and 2nd harmonics in the longitudinal spectrum and 4th harmonics in the torsional spectrum. This indicates the coupling phenomenon arising in the flexibility matrix. Also, the torsional excitation was given at a frequency nearer to the natural frequency of bending. The combination of torsional and bending frequencies showed generation of difference and sum of frequencies nearer to bending natural frequencies.

El Arem and Maitournam (2008) studied dynamics of cracked beam by using a FEM model and analysed stability and its performance. The 3-D (3-Dimensional) FEM computations for unilateral crack faces was utilized to deduce variation in the crack stiffness. The element of the shaft was assumed to be rectangular strips for the analysis. Also, comparison of different crack models was done using FEM approach. Niu and Yang (2018) established a fast-slow coupling model of the rotor vibration according to dynamic theory and included the crack growth based on fracture mechanics. Herein, they proposed the iterative procedure for evaluation of the coupling model sequentially and studied the degradation behaviour of fatigue crack onto the rotor due to the coupling effect. Also studied degradation failure mode of the cracked rotor and the rapid crack growth failure and the unstable vibration.

Different methodology involved in the identification of cracks are reported in the present section. The 2nd harmonics present in the frequency domain signal indicates the presence of crack in the rotor system. Also, on the basis of change in modal parameters and mode shapes the identification of cracks are carried out. Due to complexity in the identification of the cracks, the increase in the trend of 1st, 2nd and 3rd harmonics of the vibration response is considered. Inverse problem approach and 3D models are also utilized for identification of crack depth, location and stiffness.

A real system and its model varies according to DOFs considered in the analysis. But based on continuous system theory, physical system can have infinite DOFs. Hence, the model can be proposed to be large DOFs. However, a large-DOF model of the system need more capacity of storage data and computational power. Because of this a model reduction technique (or condensation technique) is useful to reduce DOFs necessary to develop the analysis. After reduction of DOFs the time and cost of computational reduces drastically. Therefore, the number of equations to be solved reduces as per the reduction of DOFs. Also in identification of crack parameters through model based methods due to limited measurement availability, the mathematical model has to be reduced accordingly. Also in practical case measuring rotational DOFs accurately is very difficult. For the reduction method, it is the most important to handle such situation. Thus in next section, the literature survey on the condensation techniques are reviewed.

1.5.2 Condensation techniques

The condensation algorithm are used to eliminate some DOFs, called slave DOFs, from the original equations of motion, which consists of the combination of slave DOFs and master DOFs. Master DOFs represent the retained DOFs and these are the transverse translational displacement

DOFs, which are possible to measure experimentally. The condensation method was first proposed by Guyan (1965) and Irons (1965) in case of undamped system. Guyan (1965) reduction method is mostly preferred due to lower computational difficulties (Genta, 2007). The reduction method is applied in the original vectors and matrices **q**, **f**, **M** and **K,** which represent the displacement vector, force vector, mass matrix and stiffness matrix, respectively. These matrices and vectors are partitioned in the form of sub-vectors and sub-matrices corresponding to master DOFs (retained) and slave (eliminate or reduced) DOFs. On considering above aspect equations of motion becomes

$$\begin{bmatrix} \mathbf{M}_{mm} & \mathbf{M}_{ms} \\ \mathbf{M}_{sm} & \mathbf{M}_{ss} \end{bmatrix} \begin{Bmatrix} \ddot{\mathbf{q}}_m \\ \ddot{\mathbf{q}}_s \end{Bmatrix} + \begin{bmatrix} \mathbf{K}_{mm} & \mathbf{K}_{ms} \\ \mathbf{K}_{sm} & \mathbf{K}_{ss} \end{bmatrix} \begin{Bmatrix} \mathbf{q}_m \\ \mathbf{q}_s \end{Bmatrix} = \begin{Bmatrix} \mathbf{f}_m \\ \mathbf{0} \end{Bmatrix} \tag{1.1}$$

where subscripts*m* and *s* denotes the master and slave DOFs, respectively. On ignoring the inertia the following transformation can be obtained (Henshell and Ong, 1974)

$$\begin{Bmatrix} \mathbf{q}_m \\ \mathbf{q}_s \end{Bmatrix} = \begin{bmatrix} \mathbf{I} \\ -\mathbf{K}_{ss}^{-1}\mathbf{K}_{sm} \end{bmatrix} \{\mathbf{q}_m\} = \mathbf{T}_s \mathbf{q}_m \tag{1.2}$$

Further, the above Guyan reduction algorithm cannot estimate the correct eigen solutions because of ignoring the effect of mass and it is not rationally consistent when estimating the reduced matrices in the system (Jeong et al., 2012). The error obtained is typically small (Genta, 2007) at low frequencies only or at zero frequency. Therefore, the Guyan reduction scheme is also called the static reduction. When excitation frequency increases, in this situation, the inertia term which is neglected in the static reduction process plays a vital role in the process of reduction. Here, comes the dynamic reduction scheme for higher frequency system, where inertia terms influence in the reduction scheme. Henshell and Ong (1974) reported an iterative technique for the selection of master or slave DOFs in the static reduction on the basis of comparing the magnitude between the elastic and inertia force terms, automatically. The procedure has the ability to remove one DOF in each iteration.

Leung (1978) illustrated an alternative dynamic reduction procedure for more accurate results but in contrary to this, the dynamic reduction developed by Paz (1984) was considered as better alternative to the static reduction method in which the reduction is exact for a particular frequency, which may be chosen arbitrarily. In the dynamic analysis of rotor, there is an advantage to choose the frequency of reduction independently, since the scheme may be utilized at the frequency of external forcing, which gives rise to a multiple/factor of the spin frequency of rotor. The reduction transformation at a frequency ω_0, is expressed as (Singh and Tiwari, 2018)

$$\begin{Bmatrix} \mathbf{q}_\mathrm{m} \\ \mathbf{q}_\mathrm{s} \end{Bmatrix} = \begin{bmatrix} \mathbf{I} \\ -\left[\mathbf{K}_\mathrm{ss} - \omega_0^2 \mathbf{M}_\mathrm{ss}\right]^{-1} \left[\mathbf{K}_\mathrm{sm} - \omega_0^2 \mathbf{M}_\mathrm{sm}\right] \end{bmatrix} \mathbf{q}_\mathrm{m} = \mathbf{T}_\mathrm{d} \mathbf{q}_\mathrm{m} \tag{1.3}$$

O’Callahan (1989) and Gordis (1992) modified the static reduction technique by the use of the improved reduced systems (IRS) scheme in the transformation of slave DOFs, where approximation up to the first order of a binomial series expansion is done. Suarez (1992) presented an iterative procedure for the reduction of matrices based on the developed equation of motion of a system. Friswell et al. (1995, 1998) developed an iterative IRS (IIRS) procedure in order to obtain more accurate reduction. The IIRS method updates a transformation matrix between the master and slave DOFs in a repetitive way with the help of iteration procedures. Also, Xia and Lin (2004) presented an iterative order reduction (IOR) technique to improve the computational efficiency in applying condensation in a system of equations. On the basis of the requirements in the numerical analysis and experimental model updating, condensation schemes were developed, for example a hybrid condensation (or high frequency) scheme for elimination of transverse rotational degrees of freedom in identification of beam crack parameters (Dharmaraju et al., 2005).

The model reduction technique finds wide applications in the field of numerical modelling, and systems and control. With the advancement in the developments in the model reduction technique in one field does not influence the other field quickly, rather most of the developments are independent. Besselink et al. (2013) reviewed model reduction schemes in the above three fields and compared the popular methods of modelling, system and control fields against a common benchmark for the accuracy and the ease of implementation in detail. For the verification of the methodology experimentally, the numerical modelling aids maximum benefit to the practitioner.

The model improvement and updating can be done through experimental verification. The experiment works in the field of rotor cracks are less frequent than the faults, like misalignment and unbalance in the rotors. The most difficult work in the experimentation of the rotor cracks is the generation of crack in the laboratory. A review work on experimental evaluation on rotor cracks is discussed in the next section.

1.6 Experimental studies on rotor cracks

Fatigue cracks results in catastrophic failure of the structures as well as machinery. Crack detection is difficult in early stage of formation and it grows rapidly causing the structure to fail before any counter measure can be taken. A rotating system having large static deflection due to the added weights is the most vulnerable candidate to the formation of fatigue cracks. Therefore, it is challenging to detect and estimate the damage caused due to the cracks and its condition monitoring. A lot of research work has been done in model based numerical simulation to study the effect of cracks, but very few works are done in the experimental study of the fatigue cracks.

Also, most of the experimental works found in the literatures are focused on the study of the cracks developed on the rotor shaft with electro-discharge machining (EDM) or hacksaw, which hardly shows breathing or switching behaviour of the fatigue cracks. In the recent years, the researchers have carried out experimental work on the fatigue crack developed through three-point bending test on the shaft.

Gudmundson (1983) worked on the cross-sectional crack in cantilever beam with rectangular cross-section beam as for modelling and experimental analysis studies. He considered two different techniques, first one based on static stress intensity factors estimated the flexibility matrix and other using finite element equations. He proposed a saw-cut edge-cracked on to a beam of cantilever, which was considered in the experimental analysis and simulated a crack in a preloaded beam, based on varying crack lengths and 0.4 mm width.

The behaviour of vibration of a more complex system that involve of multi-bearing, multi-shaft including transverse crack, which is more relevance to real machines, has also has found less attention by researchers. For such systems, Mayes and Davies (1984) studied the effects of a transverse crack experimentally in a spin test rig. It is found that crack reduces the second moment of inertia at crack shaft section. Damping forces are included in the analysis due to dynamic bending moment, which causes the crack opening. A test rig was prepared with the arrangement of two solidly coupled rotors and four supported journal bearings, in which each bearing supporter was flexible. The rotor shaft section was reduced up to 25 mm diameter for the setup with centre alignment of notch. The crack depth of 6.5 mm was estimated during propagation from the notch, while the spin speed of the shaft was 2000 rpm. The crack was generated at the centre of the reduced portion in the form of transverse slot by spark erosion process. The potential drop methodology was utilized to monitor the depth of the crack. To obtain the dynamic stresses developed in the shaft strain gauges were placed in the opposite direction of the crack. The opening and closure of the crack followed a pattern of $(1 + \cos\omega t)$ (ω is the spin speed of the system, t is time) with 1× stiffness variation. They concluded that the calculation involved in the rates of crack growth requires the consideration of dynamic bending moment, if the depth of the crack is greater than 1/3 of the diameter of shaft.

Darpe et al. (2003) carried out experimental study to investigate the coupled vibration responses generated with the application of periodic axial excitation to the system. The coupling of bending and longitudinal vibrations were observed with the introduction of axial excitation frequencies. They also observed that the bending natural frequencies can be generated through the axial excitation frequencies or differences and sum of the combination frequencies. The findings obtained in the work were suggested to be utilized for the detection of the cracks with axial excitations in the slow run condition.

The experimental work related to the nonlinear dynamic behaviour of the rotor systems with cracks have been discussed in few literatures. Zhou et al. (2005) developed a fatigue crack in the shaft having a right angled notch using three-point bending test. They tested four specimens, one with open slot, two with fatigue cracks and one with no crack. The orbit plots were drawn that showed two-circle topological shape due to presence of the crack. They also correlated the speed range and the depth of cracks. The 2x frequency component was found to be the leading one. With the increase in the crack depth, the amplitudes corresponding to the 2x and 3x components also increased. The vibration amplitude due the disc eccentricity was found to increase or decrease depending on the orientation of the crack and the unbalance vector. The crack features were visible even in the presence of faults, such as the rub impact, oil-film and noise. In case of deep cracks, higher order frequency components were leading and the dominance of 1x component was visible only near the critical speeds.

Pennacchi et al. (2006) used the transverse fatigue crack model approach to identify the crack of industrial rotor machines. The model of rotor crack was considered as linear by utilizing ~~of~~ Fourier series of harmonic components. They estimated crack element is based on bending moment on to the nodes of FEM in the mathematical analysis. The crack based on three cases were studied: (i) an open crack introduced by electro-erosion, (ii) a fatigue crack created from the notch having depth of 14% of the shaft diameter, and (iii) a fatigue crack with a depth of 47% of the shaft diameter. Multiple harmonic responses were observed at the scale of 1^{st}, 2^{nd} and 3^{rd} times of spin speed on the frequency axis. The 1^{st}times of spin speed at the frequency axis were observed in the displacement due the shaft bow and unbalance effects. For the case of slot in the absent the breathing, 2^{nd} harmonic (at the scale of two times of spin speed on frequency axis) was observed due to stiffness asymmetry. This was used in identification of the moment and crack parameters. For fatigue cracks, the crack position and its depth was identified based on the 2^{nd} harmonic. Whereas, 1^{st} and 3^{rd} harmonic components were observed only for 47% of the crack depth. The bow effect, which add to the measured vibration responses, firstly the unbalances parameters are estimated and then, it is subtracted from data of the dynamic behaviour, which are measured from the system.

Advanced signal processing of experimental data has been utilized in crack identification. Sinha (2007) utilized higher-order spectra (HOS) tools, such as the bi-spectrum and the tri-spectrum, in measured responses to identify the crack and misalignment faults in a rotating machinery. Herein, HOS tools were introduced to identify the non-linear behaviour due to the effect of coupling in the response of harmonic components. They reported that HOS tools was crucial for the recognition of crack and misalignment fault characteristics in responses. In addition, they presented the breathing effect of crack in which crack was made based on welding of two shaft pieces. The depth of crack was half of the shaft diameter. When rotor spin speed increases near to half of the critical speed, the change in orbit behaviour was found along with the phase and amplitude changes at the 2× component. However, the amount of misalignment introduced was 0.5 mm in between two bearing pedestals. The appearance of the peaks in responses were in the bi-spectrum, it was observed that four peaks for the crack and five peaks for misalignment fault were found. A similar result was observed in the tri-spectrum, which can classify the crack and misalignment faults.

Karthikeyan and Tiwari (2010) developed an identification algorithm based on forced vibration. They investigated experimentally the detection, location and sizing of a structural flaw in a beam. An experimental setup was developed with the presence of an open flaw in a circular beam, which was supported by ball bearings at both ends. A sine-sweep excitation force was given to the test beam and corresponding force and the responses were measured. The modelling of system was developed by considering Timoshenko beam theory and the open flaw was modelled by the 4×4 flexibility matrix. The element flexibility matrix with flaw was developed based on addition of flexibility matrices of the intact shaft and the crack. They presented two algorithm, first was for the crack location and other was for the flaw size. Herein, the fundamental natural frequency was utilised to estimate the crack location iteratively by initialising the flaw depth ratio. The natural frequency variation was obtained through FE modelling with respect to assumed flaw locations. Based on iterative procedure the flaw depth ratio and the flaw location were obtained up to desired accuracy. These algorithms were utilized in experimental responses and numerical simulation responses correction to get updated theoretical model. Estimated flaw parameters were found to be in agreement with the experimental data.

Cai (2011) observed the vibration based crack detection in rotor shafts. He studied three types of transverse crack models, firstly the fatigue crack, then welded crack and last was the wire-cut crack. Based on the experimental results he concluded that the fatigue initiated crack through the three-point bending represented accurately true breathing behaviour of the crack. The bending stiffness variation as a function of rotational angle was observed and found that the switching crack model did not describe the periodic stiffness of a transverse crack, precisely.

Singh and Tiwari (2014) presented an experimental study of cracked rotor based on algorithms, which was developed for detecting the slope discontinuity. The transverse deflections were measured utilizing of a laser vibrometer at regular axial location. External excitation forces were provided with sine-sweep function in between 1 Hz to 60 Hz. They obtained the Frequency Response Functions (FRFs) and used in the identification algorithm. They also derived the crack probability functions for the localization of the crack that showed the probability of crack's presence along the shaft length. Shravankumar and Tiwari (2014) carried out an experimental estimation of breathing crack forces. They introduced a breathing crack experimentally in a healthy shaft through three-point bending test in laboratory. The full-spectrum tool was utilized to obtain the force and the displacement coefficients. An identification algorithm was developed to estimate the unbalance, crack parameter and viscous damping.

Prasad and Sekhar (2018) studied the vibration based fatigue life to avoid catastrophic failure of rotating shaft based on fluctuation of stress continuously. They proposed the fatigue lives of rotating shaft in experimental test setup based on the three specimen of shaft with different notch configurations. They measured the vibrational signals of test rig for the three specimens and compared with fatigue lives using two approaches. Firstly is the time domain approach (based on Rainflow cycle counting) and the other is the frequency domain approach (based on power spectral density moments). The fatigue life in frequency domain approach was estimated with utilization of narrow-band approximation and Dirlik's empirical solution. In the conclusion, the correlation between Dirlik'srainflow range probability density function in fatigue life estimation and experimental life was found to be good. Again, in (Prasad and Sekhar, 2019) worked on the fatigue crack shaft of rotor machinery. Using of spectral kurtosis (SK) and fast kurtogram in the diagnostic for earlier detection of fatigue cracks of the shaft based on utilization of vibration data. These methods were to be used based on the literature available and that was used in the bearing and gear fault by other researcher. They proposed the experimental analysis based on utilization of three specimen of shaft with same configuration with V-Notch and developed the artificial fatigue crack as per ASTM E468-11 standard. Herein, the continuous application of stochastic loads has been applied on the shaft through electrodynamic shaker along with unbalance force that was produces under normal operational conditions. The vibrational data at different location of the rotor using of various types of sensors were acquired (such as laser vibrometer, miniature accelerometers and wireless telemetry strain gauge) till fatigue crack develops in the specimen. In the analysis, the results are illustrated based on combination SK and fast kurtogram of fatigue crack through signal process.

Shravankumar and Tiwari (2019) estimated the transverse fatigue crack parameter along with other system parameters such as viscous damping and unbalance (disc eccentricity and its phase angle) experimentally. For this a mathematical identification algorithm has been developed based of crack model rotor system. The measured time domain vibrational data from the experimental rig was utilized in the identification model. A V-notched on the shaft was initially made, then an artificial fatigue crack on it was generated in transverse direction based on three-point bending method. In the experimental studies they described the spectral analysis of multiple harmonics in the forward and backward whirl components, which was used in identification of rotor and crack parameters. Similarly, Sarmah and Tiwari (2019b) illustrated the behaviour of transverse fatigue crack response experimentally integrated with AMB, the model of crack was artificially initiated in a shaft based on the three-point bending test at V-notch of the shaft.

In the present section, experimental works done on the fatigue cracks by several researchers are presented. The research works of Pennacchi et al. (2006), Shravankumar and Tiwari (2014, 2019) and Prasad and Sekhar (2018, 2019) provided the information regarding the behaviour of the artificial fatigue crack generated through three-point bending test in the laboratory setupand used a V-notch on the shaft. The notch helps in generation of fatigue crack at a chosen location of the shaft during at three-point bending test. They studied the experimental measurement and described the spectral analysis of multiple harmonic in forward and backward whirl components, which was used in the parameters identification. Prasad and Sekhar(2018) used spectral kurtosis (SK) and fast kurtogram in the diagnostic for earlier detection of fatigue cracks. Also they used the application of stochastic loads applied on the shaft through electrodynamic shaker along with unbalance force that was produced by normal operational conditions. Karthikeyan and Tiwari (2010) experimentally investigated the detection of crack with location and sizing of a structural flaw in a beam setup with the presence of an open flaw in a circular beam.

The next section summarizes the shortcomings in the literatures reviewed of in present section.

1.7 Shortcomings of the present literature

The existing literatures mainly focused on the effect of various faults on rotating machinery. Most of the fault detection and diagnosis methods were aimed for the maintenance and prognosis of machinery. The mathematical model based methods were used for quantifying fault parameters and have more profound and advantageous for the predicting of machinery behavior at different operating conditions. The following are the shortcomings observed in the above discussed literatures.

1. Most of the researchers analyzed the effect of internal damping on the stability of the rotor system. There is hardly any literature where the model based identification of internal damping is found. The previous literature focuses on material hysteresis and dry friction damping at rotor-shaft joints and internal viscous damping.

2. Many researchers have worked on the identification of crack additive stiffness along with residual unbalance and external damping. Full spectrum is utilized to estimate the coefficients of the crack force, which is in multiple harmonics and that excites the rotor in the clockwise and anti-clockwise directions.

3. A variety of crack models in the literature have been used, e.g. the open crack, switching crack and gradually breathing crack. Crack opening-closure behaviour makes the rotor system non-linear, however, using the weight dominance the equations of motion of rotor systems can be linearized.

4. The combined effect of internal damping and transverse crack including external damping and residual unbalance is required to be studied. Analysis and observations of the stability behaviour of internal damping and crack models are required.

5. The experimental analysis of a cracked rotor system with an offset disc is also required. It is important to analyze the effect of gyroscopic couple on the rotor system with internal damping.

6. The detailed description of the utilization of measurement data with complete and incomplete cycle in identification is not provided. The effect of leakage in incomplete cycle in measured signals need to be studied.

7. Torque measurements are useful and additional techniques are required for the detection and monitoring of coupling misalignment.

8. The vibration monitoring during start-up, shut-down or steady state operation to detect cracks and coupling misalignment especially for machines, such as aircraft engines, can be extended by considering more complex cases of torsional-bending coupling.

9. The multi-fault identification in simple rotor-bearing- coupling systems based on forced response measurements can be extended to versatile and practical numerical modelling method, such as the FEM, for multi-fault parameter identification, and to test the method in a laboratory test rig is a real challenge.

10. Quantification of multiple fault parameters in flexible turbo-generator systems with incomplete rundown vibration data are performed. The challenge would be to test the method in a laboratory test rig and to verify in a real machine where even the foundation flexibility has to be modelled and to be identified.

11. Further test investigations on shaft bow under higher operating speeds are essential for engineering applications and are still on the way. It is extremely important since most industrial turbine machines operate with shaft warp. Methods of accurately predicting machine responses in different residual shaft bow values need to be studied.

12. The case involving internal damping along with different types of misalignment in the rotor system is required to be studied.

1.8 Objectives of the present work

The main focus of the present survey is on faults in rotors and associated modelling, analysis and experimental investigations. However, due to very less work on experimental investigation related to the internal damping effect on rotors, which has practical importance. Since it is the main objective of the dissertation, and the same limited literatures have been reported. The present work deals with a mathematical model-based estimation of internal and external damping in a cracked rotor-bearing system. The crack is considered to follow switching behaviour during the opening and closure of faces of the crack. The rubbing of crack faces while opening and closure results in additional internal damping. The estimation of internal damping and additive stiffness of cracked shaft along with system parameters and unbalances is carried out in the present work. The objectives of the present work are summarized as follows,

1. To develop mathematical model of 2-DOF simple rotor system consisting of external and internal damping, unbalance and crack force. The transverse crack, which is modeled as linearized switching crack, is based on existing literature. To develop identification algorithm based on developed equation of motion (EOM) for estimating fault parameters, such as the external and internal damping, disc eccentricity and its phase, and additive stiffness of crack. The generated full spectrum response of the developed mathematical model will be used as an input to test the proposed identification algorithm for estimating fault parameters. To check the robustness of the developed algorithm against different levels of measurement noise in responses and bias errors in system parameters.

2. To experimentally study and validate the developed identification algorithm of 2-DOF rotor system.

3. To develop mathematical model of 4-DOF rotor system considering gyroscopic effect, external and internal damping, unbalance and crack force. To eliminate rotational DOF, which arises due to tilting of an offset disc, dynamic condensation will be used. To develop and test numerically the model based identification algorithm for estimating rotor fault parameters.

4. To experimentally study and validate the developed identification algorithm of 4-DOF rotor system.

5. To develop general EOMs of rotor-bearing system through finite element method (FEM) considering internal and external damping, crack force, unbalance and gyroscopic effect. To develop and numerically test the general identification algorithm for the estimation of bearing parameters, internal and external damping, unbalance and additive crack stiffness parameter.

1.9 The organization of the present work

The organization of various chapters in the present thesis are as.

Chapter 1: Introduction and Literature Survey

This chapter comprises an overview and the motivation of the current work. It derives the objectives of the present work based on extensive literature survey and identifying gaps in the literature in the chosen research field.

Chapter 2: Identification of internal and external damping in a simple cracked rotor system

A simple 2-DOF rotor system with a switching crack has been modelled considering internal and external damping in it. Rotor responses in full spectrum are obtained from derived equations of motion (EOMs). Later EOMs are utilized to develop a model-based identification algorithm to estimate distinctly internal and external damping of the cracked rotor system along with crack additive stiffness and unbalance. Subsequently, a numerical testing of the identification algorithm is performed with noise in responses and bias error in the model parameters. This chapter laid the foundation of proposed identification algorithm for estimating internal and external damping distinctly.

Chapter 3: The experimental identification of internal and external damping in a simple cracked rotor system

To apply the developed methodology in a real test data, a simple cracked rotor test rig was developed in Advanced Dynamics Laboratory at IIT Guwahati. Description of test rig development, instrumentation, measurement and signal processing have been given in this chapter. The experimental time-domain data was collected from the experimental-setup and utilized in the model-based identification algorithm developed in Chapter 2. Estimated parameters are used in EOMs to get responses from updated rotor model and the same is compared with test rig responses for validating the estimated parameters.

Chapter 4: Model-based identification of internal and external damping of a cracked rotor system with gyroscopic effects

Complexity of rotor system with an offset disc increases in the presence of gyroscopic effects. Now apart from translational DOFs, rotational DOFs also appear in EOMs. Difficulty comes in developing identification algorithm since now rotational DOFs also need to be measured along with translational DOFs, which is difficult to measure accurately. To overcome this difficulty dynamic condensation is applied to eliminate rotational DOFs from EOMs before developing identification methodology. Numerical testing of identification methodology is performed with noise in responses and bias error is system parameters.

Chapter 5: The experimental identification of internal and external damping in a cracked rotor system with gyroscopic effects

Identification methodology developed after elimination of rotational DOFs using condensation scheme is applied for the experimental estimation of internal and external damping. Measured transverse translational DOFs at offset disc locations from the cracked rotor system are used for the estimation. Comparison is made of estimated parameters that with in Chapter 3.

Chapter 6: Finite element model based identification of internal and external damping of a cracked rotor-bearing system

The proposed identification methodology is generalized for a more realistic flexible-shaft flexible-bearing rotor system with the help of finite element modelling technique. Herein, apart from internal and external damping, unbalances in discs, crack additive stiffness and bearing parameters are also estimated. Numerical testing of the identification methodology has been done on a two-disc cracked rotor supported on two flexible end bearings.

Chapter 7: Conclusions and Future Scopes from the Present Work

This chapter provides an overall conclusions and contribution of the present research work. Also, it gives future direction derived from the limitations of the present work.

CHAPTER 2

Identification of internal and external damping in a simple cracked rotor system

A simple 2-DOF rotor system with a switching crack has been modelled considering internal and external damping in it. Rotor responses in full spectrum are obtained from derived equations of motion (EOMs). Later, EOMs are utilized to develop a model-based identification algorithm to estimate distinctly internal and external damping of the cracked rotor system along with crack additive stiffness and unbalance. Subsequently, a numerical testing of the identification algorithm is performed with noise in responses and bias error in the model parameters. This chapter lays the foundation of proposed identification algorithm for estimating internal and external damping distinctly

2.1 Introduction

A fatigue crack is asymmetric in general and that leads to excitation forces and subsequently responses in both forward and backward whirl. To have characterization of such crack model it is essential that estimation procedure should incorporate full spectrum to have physically meaningful crack parameters.

A model based identification algorithm has been developed in the present chapter to estimate internal and external damping in a rotor with a transverse fatigue crack. The crack is considered near to the disc location and studied translational displacements of 2 Degrees of freedom (DOF) rotor system in this chapter. The modeling of crack is derived based on crack local flexibility with assumption of switching behavior in the rotating frame of reference. The internal damping is considered based on the rubbing between two free faces of the crack during shaft rotation. This type of damping also comes into the system due to rubbing between disc and shaft as well as due material hysteresis. All these damping effects are considered in combined form in the present rotor system.

The modeling of opening and closure behavior of a crack as a crack switching function is considered according to the work of Gasch (2008). This function represents switching phenomenon. Hence, it is utilized to represent the cracked shaft with its value zero for crack closure to one for crack opening. For the shaft stiffness variation due to crack, this switching function is utilized with multiplication of additive crack stiffness. Equations of motion (EOMs) is developed in the rotating frame of reference and then it is converted into the stationary frame of reference.

Forces act on the rotor system due to the crack and the unbalance while rotor rotates. The system vibrates due to these combined forces and excite it at multiple harmonics of the rotor spin frequency. Due to these forces, the rotor whirls in the same direction of spin (i.e. the forward whirl) and in reverse direction of spin (i.e., the backward whirl) at multiple harmonics.

2.2 System model and mathematical formulations

Present section describes development of governing equations of a cracked rotor system incorporating the internal and external damping, and subsequently responses are obtained numerically.

In the present work, a simple rotor model configuration is considered with a disc at mid-span of shaft in presence of transverse crack as shown in Figure 2.1. End bearings are assumed to be rigid in the simple rotor model, however, in actual practice no bearing is rigid, while modelling the present case, the bearing in mind was rolling element bearings. These bearings do deform and give the stiffness during rolling element deformation and the damping in the form of squeeze-film action between outer races and housing as well as friction at rolling surfaces. In the present model an equivalent stiffness of shaft and bearing is considered. And similarly, the equivalent external (stationary) damping comes from the bearing/housing interface due to squeeze-film action and friction at rolling surfaces. Accordingly, the rigid bearing assumption is not considered in the present work. External damping and internal (rotating) damping are considered in the rotor model, and the viscous damping model is assumed for both types of damping. Traditionally, internal damping due to material damping and rubbing due to disc and shaft interfaces have been modelled as viscous rotating damping (Dimentberg, 1961; Tondl, 1965). The concept involves basically finding an equivalent viscous damping of Coulomb's damping based on equating energy dissipation per cycle of these two damping models (Thomson, 2018), and obtaining an equivalent viscous damping factor. The damping in rolling element bearings is generally very small and that is why often it is referred to as anti-friction bearings. Usually, the squeeze-film damper effect in rolling element bearing is obtained by providing clearance between outer race and housing, and by providing fluid-film in between the clearance (Chouksey et al., 2012). In the present case, additionally internal (rotating) damping comes due to the crack face rubbing of the fatigue crack in the rotor shaft during the opening and closure of the crack. Therefore, the present method will find an equivalent rotating damping due to all these effects as well as the stationary damping, distinctly. This helps in keeping the system model linear but still representing the system reasonably well.

Various system parameters are as follows: the equivalent stiffness of the shaft-support is k_0, the decrease in the shaft stiffness due to the crack is Δk_{ξ}, which is in the crack front direction, the disc mass is m and the eccentricity and unbalance phase of the disc are e and ϕ, respectively. Displacements of the disc are x and y in two orthogonal transverse directions. In the present analysis, the crack model has been considered as switching crack that has sudden opening and closure behavior, during the rotation of the system.

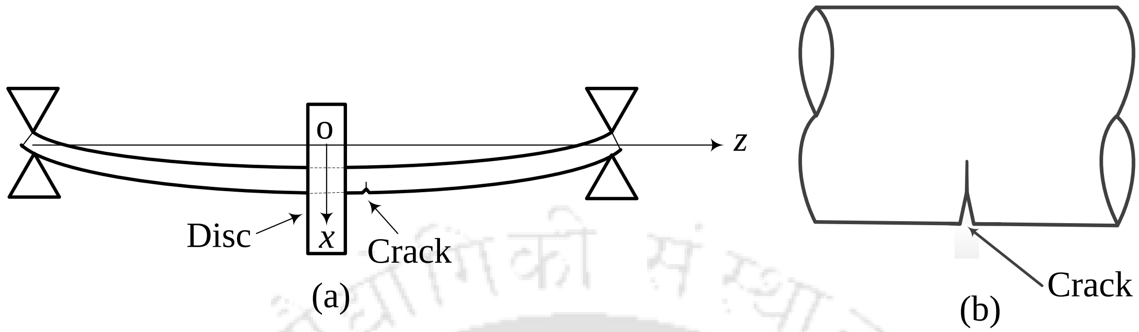

Figure 2.1 (a) A simple rotor in the presence of a transverse switching crack (b) enlarged view of crack

2.2.1 Development of equations of motion of the rotor system

Rotor system flexibility increases due to a switching crack on the shaft and it changes the system natural frequency (Mayes and Davies, 1984; Gasch, 2008). Stationary coordinate axes are x and y in the vertical and horizontal directions, respectively; and their origin is at the mid-span on the bearing center line. Disc displacements in corresponding directions are (x, y). The self-weight of the disc (i.e., mg) is considered and it is in x-direction. Rotating axes are ξ and η. The crack front is taken in the direction of ξ axis. At initial time, t = 0, both x and ξ are assumed to be aligned. Disc displacements in rotating axis directions (ξ, η) are as shown in Figure 2.2. Herein, ω is the spin speed of shaft and t is the time. From the geometry (as shown in Figure 2.2), O is the bearing axis location; C and G are geometric center (i.e., center of rotation) and center of gravity of the disc, respectively. Herein, e denotes disc eccentricity, which is a distance between C and G, and ϕ is phase angle between unbalance force and crack front direction (i.e., ξ axis direction). In this work, forces due to internal damping (c_H), external damping (c_E) and gravity are considered as shown in Figure 2.3 (Jun et al., 1992). In Figure 2.3, u_x, u_y and δ_w denote the dynamic displacement in the vertical and horizontal directions, and static deflection, respectively. EOMs of the cracked rotor when expressed in the ξ and η directions, respectively, are (Tiwari, 2017; Mayes and Davies, 1984; Jun et al. 1992) given as

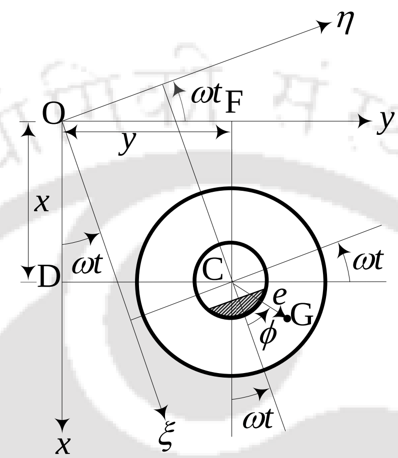

Figure 2.2 The disc motion with respect to the fixed and rotating frame of references

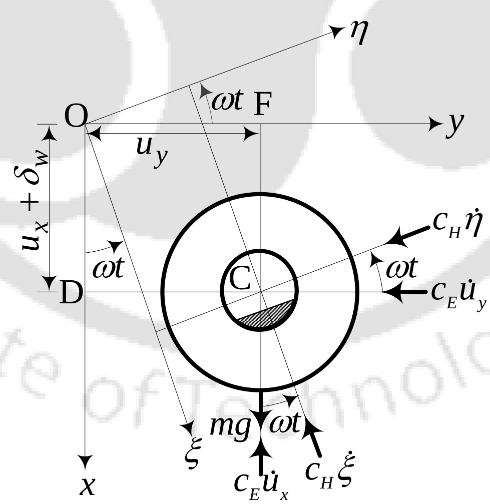

Figure 2.3 The rotor with self-weight, internal and external damping forces and displacements

($x = u_x + \delta_w$ and $y = u_y$)

$$m\left(\ddot{\xi}-2\omega\dot{\eta}-\omega^{2}\xi\right)+c_{E}\left(\dot{\xi}-\omega\eta\right)+c_{H}\dot{\xi}+\left(k_{0}-\Delta k_{\xi}(t)\right)\xi=mg\cos\omega t+me\omega^{2}\cos\phi \tag{2.1}$$

and

$$m\left(\ddot{\eta}+2\omega\dot{\xi}-\omega^{2}\eta\right)+c_{E}\left(\dot{\eta}+\omega\xi\right)+c_{H}\dot{\eta}+k_{0}\eta=-mg\sin\omega t+me\omega^{2}\sin\phi \tag{2.2}$$

In Equation (2.1), $\Delta k_{\xi}(t)$ represents the crack additive stiffness, which is time-dependent and provides an effective change in shaft stiffness during rotation of the rotor shaft. The details of crack modeling are presented in next section.

2.2.2 Modeling of the crack

The present section describes the mathematical modeling of transverse additive crack stiffness, which is time-dependent. It is based on the opening and closure of crack phenomenon with the period of 2π rad. It is controlled by various factors, and the most prominent being the crack depth. The crack opening and closure are usually modeled by an appropriate crack excitation function (CEF). The shaft losses its stiffness when crack portion is fully opened, so the crack excitation function has a value of '1' for this portion. Similarly, for the case of closed condition, the shaft has no loss of stiffness, for this crack excitation function has a value of '0'. Mayes and Davies (1984) proposed a breathing crack model, which ishaving gradually opening and closure behavior, and its crack excitation function is given as

$$\sigma\left(t\right)=\frac{1}{2}\left(1+\cos\omega t\right) \tag{2.3}$$

Herein,$\sigma(t)$ is crack excitation function. Gasch (1993) updated the Mayes' crack model as a switching crack excitation function (SCEF), which is an early stage of propagation of crack as a sudden open and closure behavior. The SCEF, based on a bilinear square wave approximation (Fig. 2.4), is given as

$$\sigma(t) = \frac{1}{2} + \frac{2}{\pi}\left(\cos\omega t - \frac{1}{3}\cos 3\omega t + \frac{1}{5}\cos 5\omega t - \frac{1}{7}\cos 7\omega t + \cdots\right) \tag{2.4}$$

The updated function $\sigma(t)$ denotes the switching crack excitation function (SCEF) and it is considered in the present work. It is close to zero, when the crack is closed or when shaft towards crack front is in the compression. It is near one, when the crack is open or when shaft towards crack front is in the tension of the shaft. Hence, the SCEF is characterized by a rectangular wave (switching) function as shown in Figure 2.4. Equation (2.4) shows Fourier series expansion of the SCEF.

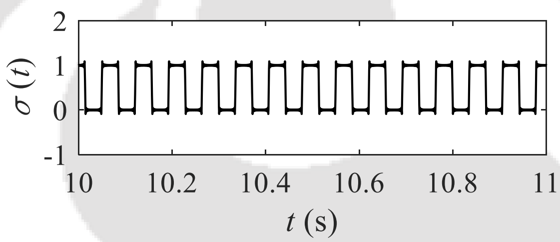

Figure 2.4 A typical switching crack function variation with time at rotor spin speed of 88 rad/s

The additive stiffness in the crack direction with SCEF is given as

$$\Delta k_{\xi}(t) = \sigma(t)\Delta k_{\xi} \tag{2.5}$$

On substituting Equation (2.5)into Equation (2.1) and combining with Equation (2.2)by defining $\zeta = \xi + \mathrm{j}\eta$ with $\mathrm{j} = \sqrt{-1}$, it gives

$$m\left(\ddot{\zeta} + 2\mathrm{j}\omega\dot{\zeta} - \omega^2\zeta\right) + c_E\left(\dot{\zeta} + \mathrm{j}\omega\zeta\right) + c_H\dot{\zeta} + k_0\zeta - \sigma(t)\Delta k_{\xi}\xi = mge^{-\mathrm{j}\omega t} + me\omega^2 e^{\mathrm{j}\phi} \tag{2.6}$$

where, ζ is complex displacement in rotating coordinate system. The system model EOM in the stationary coordinate system can be represented as

$$m\ddot{r} + \left(c_E + c_H\right)\dot{r} + \left(k_0 - \mathrm{j}\omega c_H\right)r - \sigma(t)\Delta k_{\xi}\left(x\cos\omega t + y\sin\omega t\right)e^{\mathrm{j}\omega t} = mg + me\omega^2 e^{\mathrm{j}(\omega t+\phi)} \tag{2.7}$$

With

$$\xi = x\cos\omega t + y\sin\omega t \text{ and } \eta = -x\sin\omega t + y\cos\omega t$$

where $r = x + \mathrm{j}y$ is the complex displacement in the stationary coordinate system with $\zeta = re^{-\mathrm{j}\omega t}$.

Now Equation(2.7) is split into the real and imaginary parts, as

$$\begin{aligned} m\ddot{x} + \left(c_E + c_H\right)\dot{x} + k_0 x + \omega c_H y = mg + me\omega^2\cos\left(\omega t + \phi\right) + \\ \sigma\left(t\right)\Delta k_\xi\left(x\cos\omega t + y\sin\omega t\right)\cos\omega t \end{aligned} \tag{2.8}$$

and

$$\begin{aligned} m\ddot{y} + \left(c_E + c_H\right)\dot{y} + k_0 y - \omega c_H x = me\omega^2\sin\left(\omega t + \phi\right) + \\ \sigma\left(t\right)\Delta k_\xi\left(x\cos\omega t + y\sin\omega t\right)\sin\omega t \end{aligned} \tag{2.9}$$

Which are simplified as

$$\begin{aligned} m\ddot{x} + \left(c_E + c_H\right)\dot{x} + k_0 x + \omega c_H y = mg + me\omega^2\cos\left(\omega t + \phi\right) + \\ \tfrac{1}{2}\sigma\left(t\right)\Delta k_\xi\left\{x\left(1 + \cos 2\omega t\right) + y\sin 2\omega t\right\} \end{aligned} \tag{2.10}$$

and

$$m\ddot{y} + \left(c_E + c_H\right)\dot{y} + k_0 y - \omega c_H x = me\omega^2\sin\left(\omega t + \phi\right) + \tfrac{1}{2}\sigma\left(t\right)\Delta k_\xi\left\{x\sin 2\omega t + y\left(1 - \cos 2\omega t\right)\right\} \tag{2.11}$$

Now defining

$$x(t) = u_x(t) + \delta_w \text{ and } y(t) = u_y(t) \tag{2.12}$$

so that

$$\dot{x}(t) = \dot{u}_x(t);\ \ddot{x}(t) = \ddot{u}_x(t);\ \dot{y}(t) = \dot{u}_y(t);\ \ddot{y}(t) = \ddot{u}_y(t) \tag{2.13}$$

Where u_x and u_y are displacement components of shaft center from static equilibrium of the intact shaft, and it is assumed that static deflection δ_w is much larger than u_x and u_y. On substituting Equations(2.12) and (2.13)into Equations (2.10) and (2.11), we get

$$m\ddot{u}_x + \left(c_E + c_H\right)\dot{u}_x + k_0\left(u_x + \delta_w\right) + \omega c_H u_y = \tfrac{1}{2}\sigma\left(t\right)\Delta k_\xi\left\{\left(u_x + \delta_w\right)\left(1 + \cos 2\omega t\right) + u_y \sin 2\omega t\right\} + mg + me\omega^2\cos\left(\omega t + \phi\right) \tag{2.14}$$

and

$$m\ddot{u}_y + \left(c_E + c_H\right)\dot{u}_y + k_0 u_y - \omega c_H\left(u_x + \delta_w\right) = \tfrac{1}{2}\sigma\left(t\right)\Delta k_\xi\left\{\left(u_x + \delta_w\right)\sin 2\omega t + u_y\left(1 - \cos 2\omega t\right)\right\} + me\omega^2\sin\left(\omega t + \phi\right) \tag{2.15}$$

The weight dominance effect generally is considered for heavy rotors. In such case, the vibrational response is much smaller than the static deflection of the rotor due to its self-weight (Gasch, 2008). Considering, weight dominance effect for the present analysis, terms u_x and u_y in the right side of Equations (2.14) and (2.15) are considered negligible. Hence, equations are simplified to

$$m\ddot{u}_x + \left(c_E + c_H\right)\dot{u}_x + k_0 u_x + \omega c_H u_y = \frac{1}{2}\sigma\left(t\right)\frac{\Delta k_\xi mg\left(1 + \cos 2\omega t\right)}{k_0} + me\omega^2\cos\left(\omega t + \phi\right) \tag{2.16}$$

and

$$m\ddot{u}_y + \left(c_E + c_H\right)\dot{u}_y + k_0 u_y - \omega c_H u_x = \frac{mg}{k_0}\left\{\frac{1}{2}\sigma(t)\Delta k_\xi \sin 2\omega t + \omega c_H\right\} + me\omega^2\sin\left(\omega t + \phi\right) \tag{2.17}$$

with

$$k_0\delta_w = mg$$

On defining $s = u_x + \mathrm{j}u_y$ and combining above equations, we get

$$m\ddot{s}+\left(c_E+c_H\right)\dot{s}+\left(k_0-\mathrm{j}\omega c_H\right)s=\frac{mg\Delta k_\xi}{2k_0}\sigma\left(t\right)\left(1+e^{2\mathrm{j}\omega t}\right)+me\omega^2e^{\mathrm{j}(\omega t+\phi)}+\mathrm{j}\omega c_H\frac{mg}{k_0} \tag{2.18}$$

First term on right side of Equation (2.18) is expressed in summation series of multiple harmonics through Equation (2.4), as

$$\frac{1}{2}\sigma\left(t\right)\frac{mg\Delta k_\xi}{k_0}\left(1+e^{2\mathrm{j}\omega t}\right)=\frac{mg\Delta k_\xi}{k_0}\left(0.25+0.319e^{\mathrm{j}\omega t}+0.25e^{2\mathrm{j}\omega t}+0.106e^{3\mathrm{j}\omega t}-0.021e^{5\mathrm{j}\omega t}+0.009e^{7\mathrm{j}\omega t}+0.106e^{-\mathrm{j}\omega t}-0.021e^{-3\mathrm{j}\omega t}+0.009e^{-5\mathrm{j}\omega t}\right) \tag{2.19}$$

Equation (2.19) in notational form is expressed as

$$\frac{mg\Delta k_\xi}{2k_0}\sigma\left(t\right)\left(1+e^{2\mathrm{j}\omega t}\right)=\frac{mg\Delta k_\xi}{k_0}\sum_{i=-\infty}^{\infty}p_ie^{i\mathrm{j}\omega t} \tag{2.20}$$

Herein, p_i represents the participation factor in the crack force given by Equation (2.20), which is a short form of Equation (2.19). The response due to crack force has been described in the next section.

2.2.3 Response due to crack

Equation (2.20) is substituted into Equation (2.18) to get

$$m\ddot{s}+\left(c_E+c_H\right)\dot{s}+\left(k_0-\mathrm{j}\omega c_H\right)s=\frac{mg\Delta k_\xi}{k_0}\sum_{i=-\infty}^{\infty}p_ie^{i\mathrm{j}\omega t}+me\omega^2e^{\mathrm{j}(\omega t+\phi)}+\mathrm{j}\frac{\omega c_H mg}{k_0} \tag{2.21}$$

Particular integrals of Equation (2.21) have been used to obtain a closed form solution, as

$$s\left(t\right)=\sum_{i=-\infty}^{+\infty}\frac{p_i\Delta k_\xi\left(mg/k_0\right)}{m\left(i\mathrm{j}\omega\right)^2+c_E\left(i\mathrm{j}\omega\right)+c_H\left(i\mathrm{j}\omega-\mathrm{j}\omega\right)+k_0}e^{i\mathrm{j}\omega t}+\frac{me\omega^2e^{\mathrm{j}\phi}}{-m\omega^2+c_E\left(\mathrm{j}\omega\right)+k_0}e^{\mathrm{j}\omega t}+\frac{j\omega c_H\left(mg/k_0\right)}{c_H\left(-\mathrm{j}\omega\right)+k_0} \tag{2.22}$$

Equation (2.22) can be used to find the time-varying displacement responses for the cracked rotor system. For the present numerical study, the value of i has been taken as 1, 2, 3, 5, 7, -1, -3, and -5 since amplitudes of higher harmonics are comparatively smaller than the lower ones. But more terms can be taken depending upon the response behavior. The velocity and acceleration responses may also be found by an appropriate order of differentiation of the above equation with respect to time. Also, using a numerical integration method (e.g., in the state space form) these responses can be found. The closed-form analytical method and Runge-Kutta direct integration method have been used in the present work to have an assessment of the more general time integration method, which is generally used for complex rotor systems (for example in Chapters 4 and 6).

The presence of switching crack gives rise to both forward and backward whirls, and to segregate these, full spectrums have been obtained by two methods: first, the regression-based and another using FFT. For the former case least-squares fit is used to solve forward and backward whirl amplitude and phase. In latter method, since FFT based method is popular for experimental data processing due to its faster working than the regression based method. But one drawback is in utilizing this method is that the phase error introduced due to leakage error. To have assessment of phase compensation methodology developed in the present study, the regression-based methodology is also used. In next two sections, these will be explained.

2.2.4 Generation of full spectrum responses

In the identification procedure, a solution of $s_i(t)$ for a particular harmonic of crack force excitation is considered as $R_i(\omega)e^{ij\omega t}$. Conventional FFT shows only the positive frequency (half-spectrum). In rotors, the whirling take place in the same and opposite sense as compared to rotor spin speed. So to depict the so called forward and backward whirls in spectrum, the negative frequency is also shown. Such plots are called full spectrum or directional FFT. In full spectrum two orthogonal displacements are combined as $s_i(t)$ or $r(t) = x(t) + \mathrm{j}\, y(t)$. It is found that multiple harmonics exist in a transverse crack rotor system, not only in forward whirl direction but in backward whirl direction also. Since the present equation of motion (EOM) (i.e., Equation (2.21)) is linear, the superposition principle will be applied, to sum up the assumed individual harmonic solutions. This particular form can be vividly seen from the closed-form response of Equation (2.22), and further, it can be considered as

$$s(t) = \sum R_i e^{\mathrm{ij}\omega t} \text{ , for } i\text{=0, 1, 3, 5, 7, -1, -3, -5} \tag{2.23}$$

Equation (2.23) converts EOM to frequency domain, as coefficients of exponential terms of Equation (2.22) are separated according to each harmonics, as

$$R_0 = \frac{p_0 \Delta k_\xi \left(mg / k_0 \right) + j\omega c_H \left(mg / k_0 \right)}{c_H \left(-\mathrm{j}\omega \right) + k_0} \tag{2.24}$$

$$R_1 = \frac{p_1 \Delta k_\xi \left(mg / k_0 \right) + me\omega^2 e^{\mathrm{j}\phi}}{\left(m\left(-\omega^2 \right) + c_E \left(\mathrm{j}\omega \right) + k_0 \right)} \tag{2.25}$$

$$R_i = \frac{p_i \Delta k_\xi \left(mg / k_0 \right)}{\left(m\left(-i^2\omega^2 \right) + c_E \left(i\mathrm{j}\omega \right) + c_H\, j\omega\left(i-1 \right) + k_0 \right)} \text{ , for } i = 2, 3, 5, 7, -1, -3, -5 \tag{2.26}$$

Equation (2.23) will be used for different harmonics in estimation of unknown complex displacements. These displacements will be further used in frequency domain equation, i.e. Equations (2.24), (2.25) and (2.26), for estimation of unknown system parameters. Equation (2.23) gives following regression equation

$$\mathbf{A}_{1_{n\times 9}} \mathbf{x}_{1_{9\times 1}} = \mathbf{b}_{1_{n\times 1}} \tag{2.27}$$

with

$$
\mathbf{A}_{1_{n\times 9}} = \begin{bmatrix} 1 & e^{\mathrm{j}\omega t_1} & e^{\mathrm{j}2\omega t_1} & e^{\mathrm{j}3\omega t_1} & e^{\mathrm{j}5\omega t_1} & e^{\mathrm{j}7\omega t_1} & e^{-\mathrm{j}\omega t_1} & e^{-\mathrm{j}3\omega t_1} & e^{-\mathrm{j}5\omega t_1} \\ 1 & e^{\mathrm{j}\omega t_2} & e^{\mathrm{j}2\omega t_2} & e^{\mathrm{j}3\omega t_2} & e^{\mathrm{j}5\omega t_2} & e^{\mathrm{j}7\omega t_2} & e^{-\mathrm{j}\omega t_2} & e^{-\mathrm{j}3\omega t_2} & e^{-\mathrm{j}5\omega t_2} \\ 1 & e^{\mathrm{j}\omega t_3} & e^{\mathrm{j}2\omega t_3} & e^{\mathrm{j}3\omega t_3} & e^{\mathrm{j}5\omega t_3} & e^{\mathrm{j}7\omega t_3} & e^{-\mathrm{j}\omega t_3} & e^{-\mathrm{j}3\omega t_3} & e^{-\mathrm{j}5\omega t_3} \\ . & . & . & . & . & . & . & . & . \\ . & . & . & . & . & . & . & . & . \\ 1 & e^{\mathrm{j}\omega t_n} & e^{\mathrm{j}2\omega t_n} & e^{\mathrm{j}3\omega t_n} & e^{\mathrm{j}5\omega t_n} & e^{\mathrm{j}7\omega t_n} & e^{-\mathrm{j}\omega t_n} & e^{-\mathrm{j}3\omega t_n} & e^{-\mathrm{j}5\omega t_n} \end{bmatrix}
$$

$$
\mathbf{x}_{\mathbf{1}_{9\times 1}} = \begin{Bmatrix} R_0(\omega) \\ R_1(\omega) \\ R_2(\omega) \\ R_3(\omega) \\ R_5(\omega) \\ R_7(\omega) \\ R_{-1}(\omega) \\ R_{-3}(\omega) \\ R_{-5}(\omega) \end{Bmatrix} \text{and}\, \mathbf{b}_{1_{n\times 1}} = \begin{Bmatrix} s(t_1) \\ s(t_2) \\ s(t_3) \\ . \\ . \\ s(t_n) \end{Bmatrix} \tag{2.28}
$$

For estimation of unknown vector $\mathbf{x}_1$from Equation (2.27), displacement responses will be used as input that is obtained from a closed-form solution, i.e. Equation (2.22), or by direct time integration method (or in case of the experimental setup, it can be measured directly as in Chapters 3 and 5). Now, for computation of the unknown vector, Equation (2.27) may be expressed as

$$
\mathbf{x}_{1_{9\times 1}} = \left(\mathbf{A}_1^{\mathrm{T}}\mathbf{A}_1\right)^{-1}\mathbf{A}_1^{\mathrm{T}}\mathbf{b}_1 \tag{2.29}
$$

The estimates $\mathbf{x}_1$, thus can be found from Equation (2.29), are in the complex form and they represent complex displacements at various harmonics (both in the forward and backward directions). The above estimation requires large data to be handled in time domain so the FFT based full spectrum has been applied. But it gives a phase shift and that need to be corrected that is described in next section.

2.2.5 FFT based full spectrum estimation and phase correction

FFT is a practical tool to estimate full-spectrum, which was discussed earlier by Equation (2.29) to obtain through the regression equation also. The former method is faster than the latter method. Because various harmonics have negative and positive frequencies, as shown in Equations (2.22) and (2.23), the full-spectrum plot obtained from FFT may be numerically similar to that with Equation (2.22). It is observed that in both the FFT based and regression-based full spectra, the amplitudes of harmonics remain the same, whereas the phases are dissimilar. It is required to pass the time domain data from the response to FFT algorithm, initiating at the same time instants with respect to a reference signal as well as a complete cycle of the signal, (i.e., instants such that $\omega t=2\pi n$ with n is an integer). The former condition is required for consistency of phase among various signals captured at different times while transforming to frequency domain through FFT, and the latter is required to avoid leakage error (the leakage error may change the amplitude also). It is very difficult to capture signal in the aforementioned methods for all practical purposes. An adequate phase compensation can be provided for removing the uncertainty in phase difference, which is due to picking at random instant of time domain signal to match the rotor system configuration with the help of a reference signal. In FFT, the reference for phase is cosine function. That means on taking FFT of a cosine function it gives its phase equal to zero. So if a harmonic signal is not captured as cosine signal it will have some phase. That means on capturing the same harmonic signal at different time it will give different phase in FFT. Same is valid for multi-harmonic signal. To avoid this error a multi-harmonic reference signal is used to have fixed reference for the phase of all signals measured at different times. In this work, with the help of a reference signal, the phase compensation has been provided. The full-spectrum carries multiple harmonics at various frequencies as represented in the flow chart in Figure 2.5, where $|R_i|$

magnitude and θ_i is phase of i^{th} harmonic of the displacement, and i is an integer (positive as well as negative). The multiple harmonic complex reference signal is used for all signal analyses, the harmonics that mentioned in the flow chart $s_c(t)$ is only required for the reference signal. The time domain quadrature reference signal is converted to frequency domain using FFT process.

Here, $|S_i|$ is magnitude and ψ_i is phase of complex reference signal for i^{th} harmonic after application of the FFT. Deducting ψ_i from the phase of i^{th} harmonic of displacement, i.e. θ_i compensates for phase shift in full-spectrum displacement obtained from the FFT. The displacement harmonic duly compensated for the phase shift takes following form as (Singh and Tiwari, 2017)

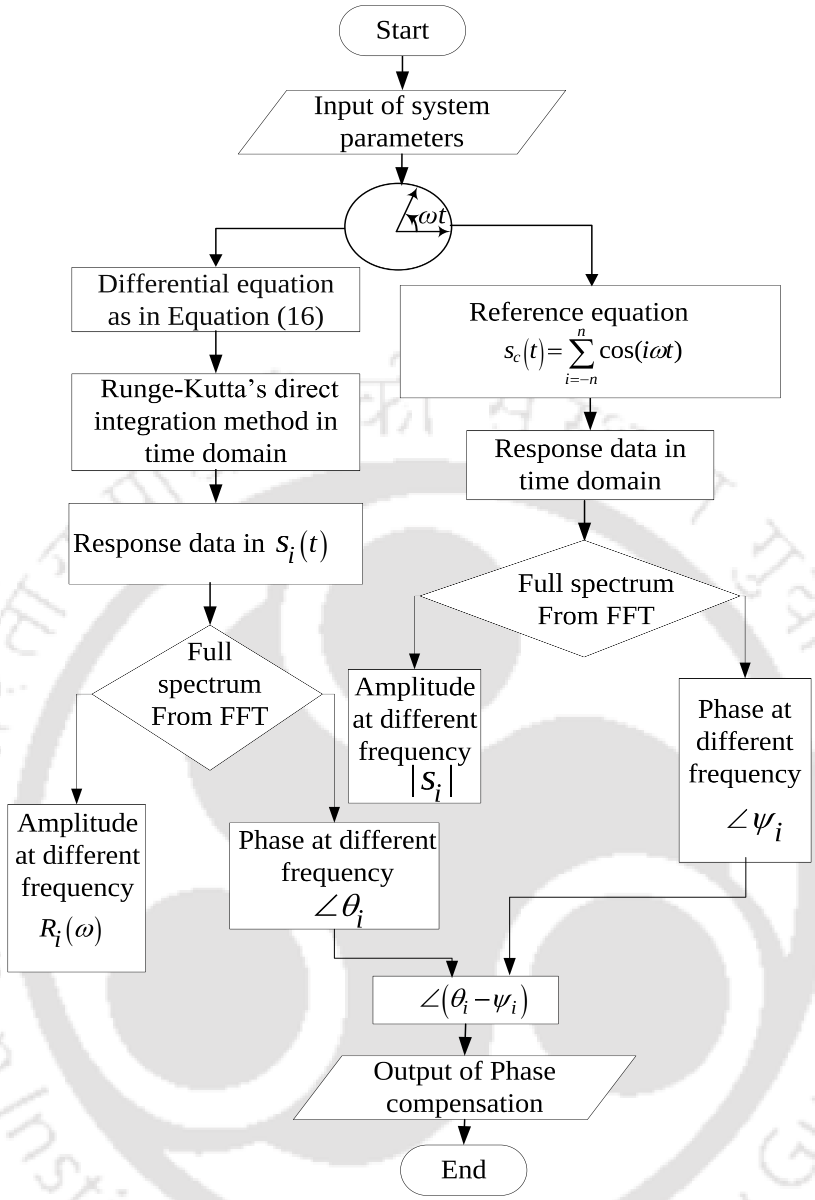

Figure 2.5 Phase compensation processing flow chart

$$R_{ci} = |R_i(\omega)| \angle(\theta_i - \psi_i) \tag{2.30}$$

Where $R_{ci}(\omega) = R_{ciRe} + jR_{ciIm}$ is the corrected full-spectrum complex displacement. Subscript c will not be used further to represent the phase corrected signal in the present analysis. Initially, the identification of system parameters is performed by above mentioned two methods, viz. the regression-based and the FFT-based, and are compared for correctness and accuracy.

2.3 Identification of internal damping and other rotor parameters

The developed governing equations of rotor system are changed to a regression form to identify the individual damping (internal and external), the crack parameter and the unbalance (amplitude and phase). For the second phase of identification, Equations (2.24), (2.25) and (2.26) have been divided into real and imaginary parts through $R_i(\omega) = R_{iRe} + \mathrm{j}R_{iIm}$. Real terms consisting of different harmonics are given as

$$-c_E R_{i\,\mathrm{Im}}(i\omega) - c_H \omega R_{i\,\mathrm{Im}}\left(i-1\right) - \left(me_{\mathrm{Re}}\omega^2\right)_{i=1} - mg\left(\Delta k_\xi / k_0\right) p_i = R_{i\,\mathrm{Re}}\left(i^2 m\omega^2 - k_0\right) \quad (2.31)$$

and imaginary terms consisting of different harmonics are given as

$$c_E R_{i\,\mathrm{Re}}(i\omega) + c_H \omega R_{i\,\mathrm{Im}}\left(i-1\right) - c_H \omega\left(mg / k_0\right)_{i=0} - \left(me_{\mathrm{Im}}\omega^2\right)_{i=1} = R_{\mathrm{iIm}}\left(i^2 m\omega^2 - k_0\right) \quad (2.32)$$

Equations (2.31) and (2.32) are arranged in regression matrix form for identification of c_E, c_H, e_{Re}, e_{Im} and Δk_ξ at different harmonic frequencies, which is written in the form as

$$\mathbf{A}_2\mathbf{x}_2 = \mathbf{b}_2 \quad (2.33)$$

With

$$\mathbf{A}_2 = \begin{bmatrix} 0 & R_{0\,\mathrm{Im}}\omega & 0 & 0 & -\left(mg/k_0\right)p_0 \\ -R_{1\mathrm{Im}}\omega & 0 & -m\omega^2 & 0 & -\left(mg/k_0\right)p_1 \\ -2R_{2\,\mathrm{Im}}\omega & -R_{2\,\mathrm{Im}}\omega & 0 & 0 & -\left(mg/k_0\right)p_2 \\ -3R_{3\mathrm{Im}}\omega & -2R_{3\mathrm{Im}}\omega & 0 & 0 & -\left(mg/k_0\right)p_3 \\ -5R_{5\mathrm{Im}}\omega & -4R_{5\mathrm{Im}}\omega & 0 & 0 & -\left(mg/k_0\right)p_5 \\ -7R_{7\,\mathrm{Im}}\omega & -6R_{7\,\mathrm{Im}}\omega & 0 & 0 & -\left(mg/k_0\right)p_7 \\ R_{-1\mathrm{Im}}\omega & 2R_{-1\mathrm{Im}}\omega & 0 & 0 & -\left(mg/k_0\right)p_{-1} \\ 3R_{-3\mathrm{Im}}\omega & 4R_{-3\mathrm{Im}}\omega & 0 & 0 & -\left(mg/k_0\right)p_{-3} \\ 5R_{-5\mathrm{Im}}\omega & 6R_{-5\mathrm{Im}}\omega & 0 & 0 & -\left(mg/k_0\right)p_{-5} \\ 0 & -\left(R_{0\mathrm{Re}}+mg/k_0\right)\omega & 0 & 0 & 0 \\ R_{1\mathrm{Re}}\omega & 0 & 0 & -m\omega^2 & 0 \\ 2R_{2\mathrm{Re}}\omega & R_{2\mathrm{Re}}\omega & 0 & 0 & 0 \\ 3R_{3\mathrm{Re}}\omega & 2R_{3\mathrm{Re}}\omega & 0 & 0 & 0 \\ 5R_{5\mathrm{Re}}\omega & 4R_{5\mathrm{Re}}\omega & 0 & 0 & 0 \\ 7R_{7\mathrm{Re}}\omega & 6R_{7\mathrm{Re}}\omega & 0 & 0 & 0 \\ -R_{-1\mathrm{Re}}\omega & -2R_{-1\mathrm{Re}}\omega & 0 & 0 & 0 \\ -3R_{-3\mathrm{Re}}\omega & -4R_{-3\mathrm{Re}}\omega & 0 & 0 & 0 \\ -5R_{-5\mathrm{Re}}\omega & -6R_{-5\mathrm{Re}}\omega & 0 & 0 & 0 \end{bmatrix};$$

$$\mathbf{x}_2=\begin{Bmatrix} c_E \\ c_H \\ e_{\mathrm{Re}} \\ e_{\mathrm{Im}} \\ \Delta k_\xi \end{Bmatrix} \text{ and } \mathbf{b}_2=\begin{Bmatrix} \left(-k_0\right)R_{0\mathrm{Re}} \\ \left(m\omega^2-k_0\right)R_{1\mathrm{Re}} \\ \left(4m\omega^2-k_0\right)R_{2\mathrm{Re}} \\ \left(9m\omega^2-k_0\right)R_{3\mathrm{Re}} \\ \left(25m\omega^2-k_0\right)R_{5\mathrm{Re}} \\ \left(49m\omega^2-k_0\right)R_{7\mathrm{Re}} \\ \left(m\omega^2-k_0\right)R_{-1\mathrm{Re}} \\ \left(9m\omega^2-k_0\right)R_{-3\mathrm{Re}} \\ \left(25m\omega^2-k_0\right)R_{-5\mathrm{Re}} \\ \left(-k_0\right)R_{0\mathrm{Im}} \\ \left(m\omega^2-k_0\right)R_{1\mathrm{Im}} \\ \left(4m\omega^2-k_0\right)R_{2\mathrm{Im}} \\ \left(9m\omega^2-k_0\right)R_{3\mathrm{Im}} \\ \left(25m\omega^2-k_0\right)R_{5\mathrm{Im}} \\ \left(49m\omega^2-k_0\right)R_{7\mathrm{Im}} \\ \left(m\omega^2-k_0\right)R_{-1\mathrm{Im}} \\ \left(9m\omega^2-k_0\right)R_{-3\mathrm{Im}} \\ \left(25m\omega^2-k_0\right)R_{-5\mathrm{Im}} \end{Bmatrix}$$

For estimation of$\mathbf{x}_2$, Equation (2.33) converted into a least-squares fit in the following form

$$\mathbf{x}_2=\left(\mathbf{A}_2^{\mathrm{T}}\mathbf{A}_2\right)^{-1}\mathbf{A}_2^{\mathrm{T}}\mathbf{b}_2 \tag{2.34}$$

Identification of $\mathbf{x}_2$ with the combined effect of spin speed ω_1, ω_2, ...,ω_n, (with the assumption that parameters are speed-independent) may be written as

$$\begin{bmatrix} \mathbf{A}_{2(\omega_1)} \\ \mathbf{A}_{2(\omega_2)} \\ \vdots \\ \mathbf{A}_{2(\omega_n)} \end{bmatrix} \mathbf{x}_2 = \begin{Bmatrix} \mathbf{b}_{2(\omega_1)} \\ \mathbf{b}_{2(\omega_2)} \\ \vdots \\ \mathbf{b}_{2(\omega_n)} \end{Bmatrix} \tag{2.35}$$

First by choosing values of $\mathbf{x}_2$ in the numerical model in Equation (2.21) responses are generated. The generated responses are further used for estimating parameters using least-square regression technique (i.e., Equations (2.34) and (2.35)), which is illustrated by the numerical simulation in the following section. It is usual practice to test the developed identification algorithm first through numerical simulation since we have control over all system parameters and noise level to be added. Once it is tested then it is applied to experimental data and often we do not have system parameter estimation independently by some other method so it is difficult to verify them.

2.4 Numerical simulation

A numerical simulation in MATLAB™ environment has been done considering EOMs for the present rotor model given in Equation (2.18). The simulation runs for a number of complete cycles (n) is considered for $2\pi n/\omega$ s as mentioned in Section 4 and time domain signals are shown for a very short interval of time for better clarity. The numerical simulation of the developed cracked simple rotor model by two methods have been performed, viz. closed form solution of Equation (2.22) and Runge-Kutta based numerical integration.

2.4.1 Time domain and full spectrum response

For a numerical simulation model, initial rotor system parameters are assumed, which are summarized in Table 2.1. These parameters have been used in simulation to find the time domain and full-spectrum responses. Time domain signals have been generated for the value of ωt, which has to be taken as integer multiples of 2π (considering time duration as 2π s). The consideration of complete cycles for generation of responses is necessary to avoid leakage error during FFT. Fundamental critical speed of the rotor system for the proposed system is 616.44 rad/s. Choice of the spin speed, for generation of responses both in time and frequency domain is based on the critical speed of rotor system. For present simulation the complete cycles, ωt, have been taken as 166 πrad and 616 πrad, where ω is equal to 88 rad/s (one-seventh of the critical speed) and 308 rad/s (half of the critical speed), respectively. The additive stiffness has been taken for numerical simulation on the basis of literatures (Mayes and Devies (1984) used 15 % and Singh and Tiwari (2015, 2017) used 39 %, experimental investigation of additive stiffness are 35 to 40 % by Shravankumar (2014)).

Table 2.1 Assumed initial parameter of rotor model for numerical solution

Parameters	Value	Units
Mass of disc, m	2	kg
Intact shaft stiffness, k_0	7.6×10^5	N/m
Additive crack stiffness, Δk_ξ	2.5×10^5	N/m
External damping, c_E	100	Ns/m
Internal damping, c_H	20	Ns/m
Phase of unbalance, ϕ	30	deg
Shaft deflection, δ_w	2.58×10^{-5}	m
Disc eccentricity, e	5×10^{-6}	m

The generated time domain signals have been used for obtaining full spectrum responses to show multiple harmonics both in the forward and backward whirling conditions. For the full spectrum analysis, firstly, regression based through closed-form response solution and,secondly, FFT based through Runge-Kutta method response solution has been used to estimate amplitudes (R_i) and corresponding phases (θ_i). Two above mentioned methods are used to analyze full spectrum to check the effectiveness of one method over another. The full spectrum amplitudes and phases have been further used for identifying system parameters for the present cracked rotor model.

Time domain responses have been generated using Equation (2.21) of the proposed rotor model. Numerically generated time domain responses for spin speed of 88 rad/s are shown in Figure 2.6. Displacements in the vertical and horizontal directions of the cracked rotor are shown in Figure 2.6 (a, b). Figure 2.6(c) shows the orbit plot, which describes the whirling path of the shaft center. From the orbit plot, it can be seen that the path of rotor forms more than one loop, which gives an indication of a crack in the rotor system, as the crack force contains multiple harmonics. The reference signal in vertical direction is shown in Figure 2.6(d).

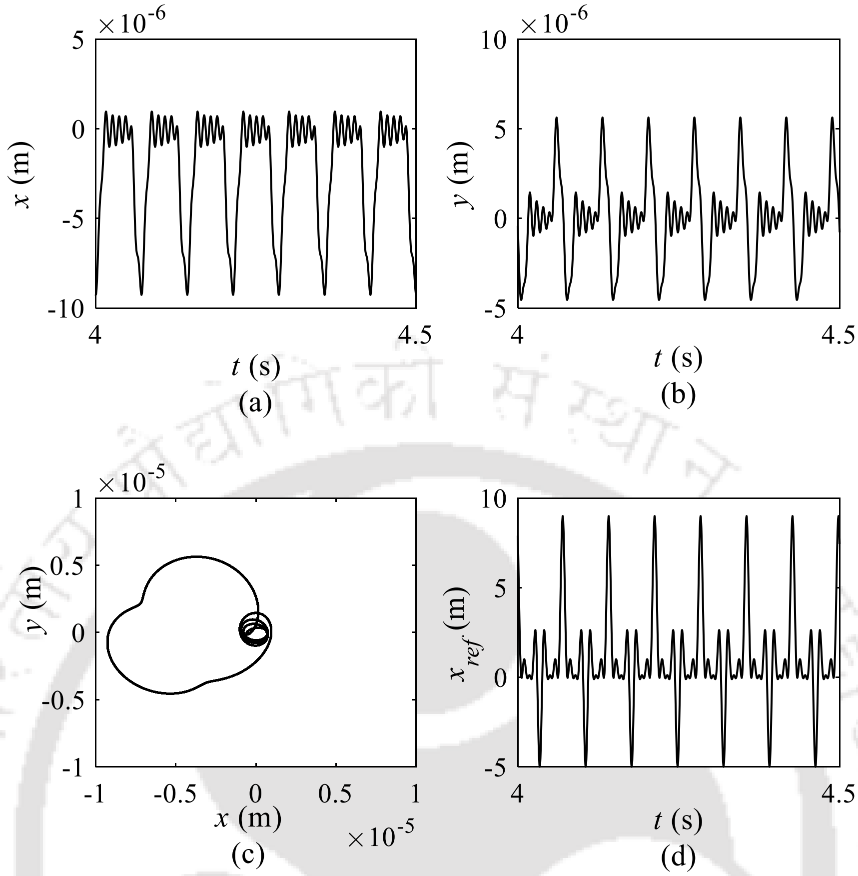

Figure2.6 Time domain response generated at spin speed of 88 rad/s: (a) vertical displacement, *x*, versus time, (b) horizontal displacement, *y*, versus time, (c) orbit plot (*x* versus *y*) and (d) vertical direction signal for reference, x_{ref}, versus time

The vertical direction reference signal at motor shaft is chosen in the analysis, which contains all real terms of complex signal in the reference equation, i.e. cosine terms as mentioned in the flow chart (Figure 2.5). Similarly, for a spin speed of 308 rad/s, the vibrational responses are found to be of the order of 10^{-5} m, except for the reference signal and are shown in Figure 2.7(a-d).

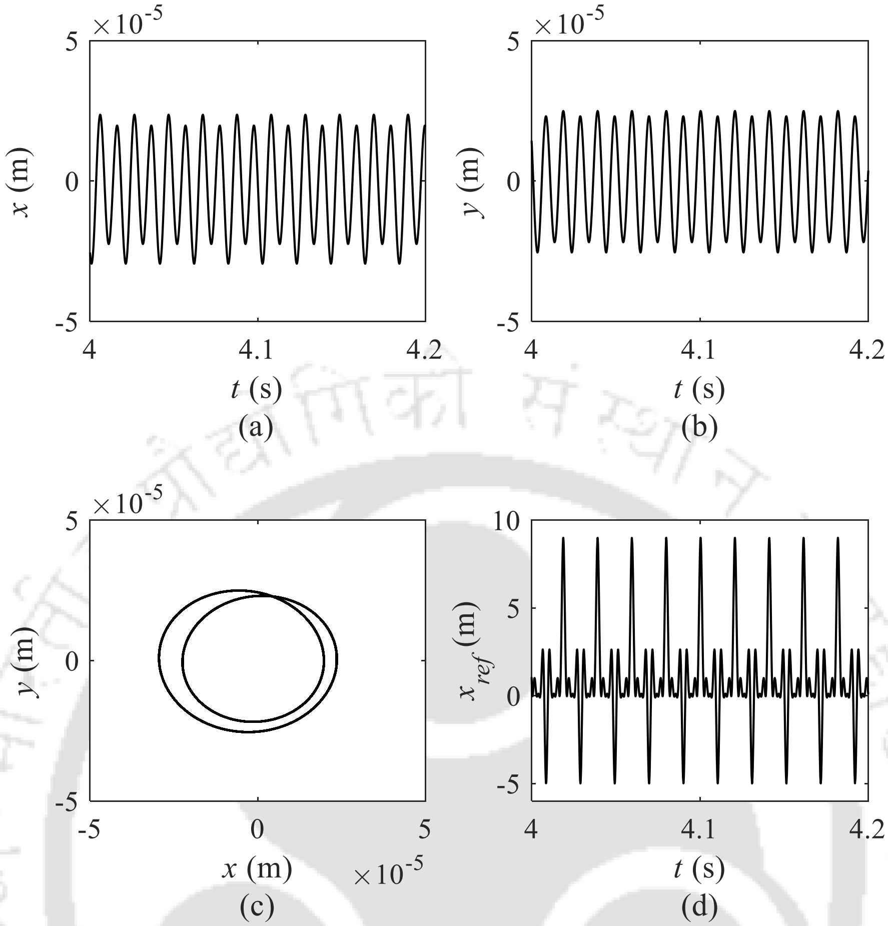

Figure 2.7 Time domain response generated at spin speed of 308 rad/s: (a) vertical displacement, *x*, versus time, (b) horizontal displacement, *y*, versus time, (c) orbit plot (*x* versus *y*) and (d) vertical reference displacement, x_{ref}, versus time

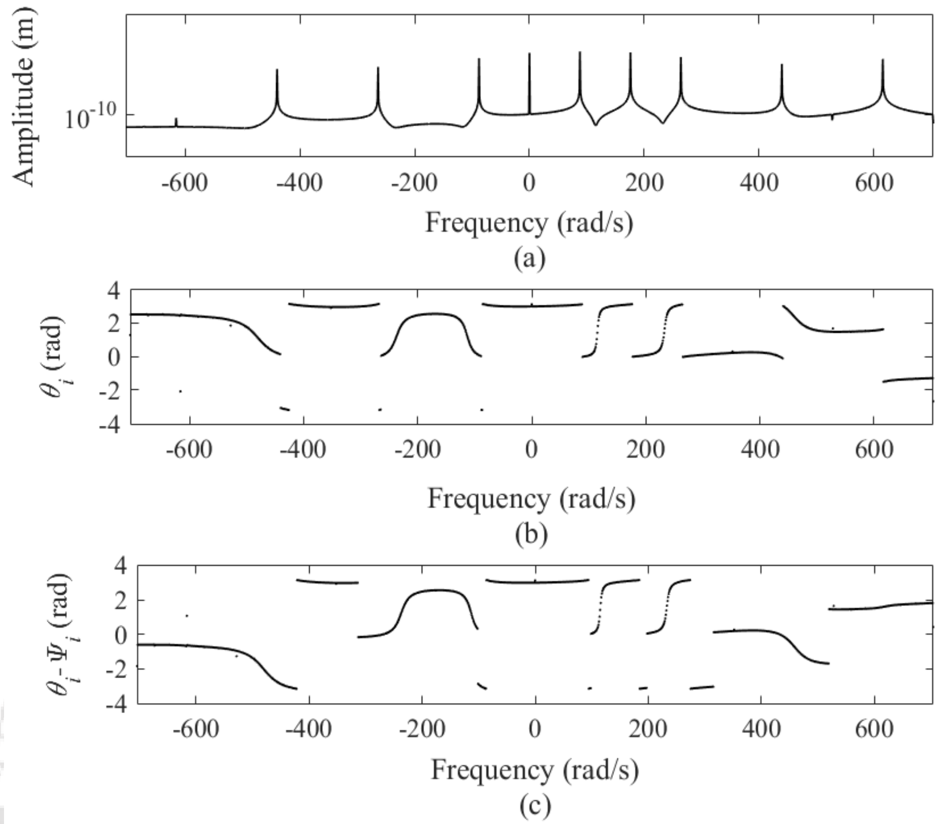

Figure 2.8 Full spectrum of displacement at 88 rad/s (a) amplitude and (b) phase without compensation (c) phase with compensation

Full spectrum amplitude and phase without compensation are shown for 88 rad/s and 308 rad/s in Figure 2.8(a-b) and Figure 2.9(a-b), respectively. Similarly, for same spin speeds the full spectrum phase with compensation are shown in Figure 2.8(c) and Figure 2.9(c), respectively.

Regression based full-spectrum amplitude and phase from closed form responses through Equation (2.22)and FFT based full spectrum amplitude and phase through Equation (2.29) for spin speed of 88 rad/s are shown in Tables 2.2 and 2.3, respectively. The maximum absolute percentage variation of amplitude with the regression based as compared to FFT based on Runge-Kutta method is found to be 0.1351 as provided in Table 2.2. Percentage variation in amplitude is found to be very smaller compared to that of phase. The discussion of the phase variation with compensation and without compensation is done in next section.

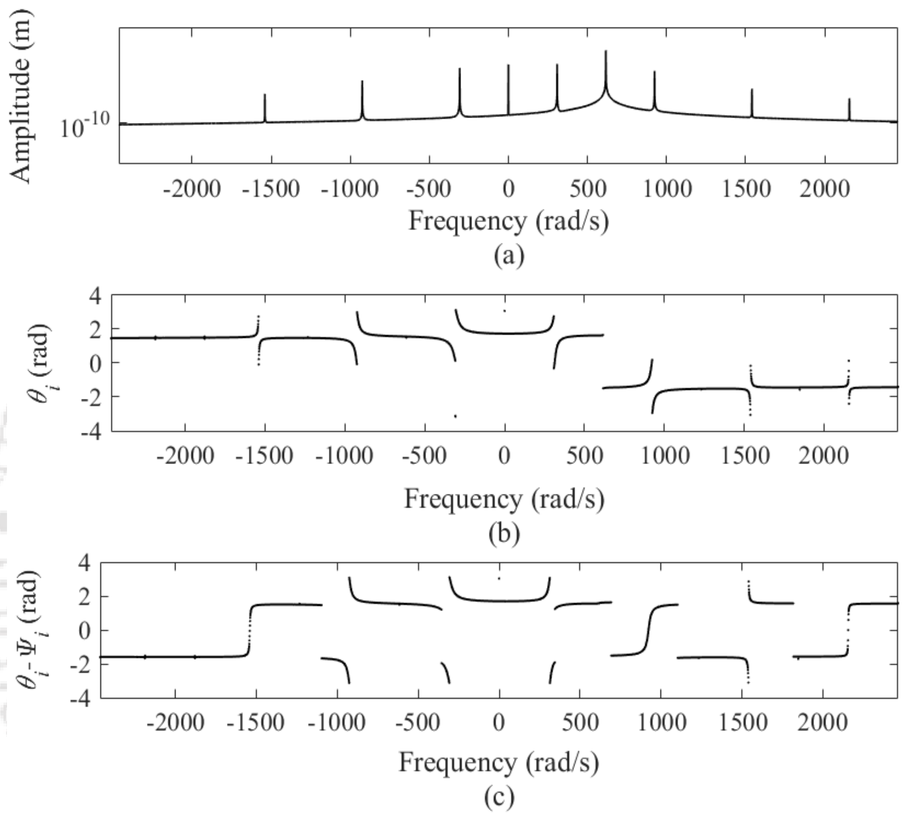

Figure 2.9 Full spectrum of displacement at 308 rad/s (a) amplitude and (b) phase without compensation (c) phase with compensation

Table 2.2 Amplitudes at different harmonics of full spectrum at 88 rad/s

Frequency	Regression based full spectrum amplitude (10^{-6} m)	FFT based full spectrum amplitude (10^{-6} m)	Percentage variation
0	2.1238	2.1239	-0.0047
ω	2.6695	2.6696	-0.0032
2ω	2.3105	2.3105	0.0012
$3\ \omega$	1.1021	1.1019	0.0128
$5\ \omega$	0.3639	0.3639	0.0084
7ω	0.8129	0.8118	0.1351
$-\ \omega$	0.9196	0.9196	-0.0051
$-3\ \omega$	0.2203	0.2203	0.0163
$-5\ \omega$	0.1557	0.1556	0.0240

2.4.2 Phase compensation of full spectrum

The phase of full spectrum corresponding to spin speed of 88 rad/s, as detailed in Table 2.3, has the maximum absolute percentage variation without phase compensation θ_i and with phase compensation (θ_i - ψ_i) (refer Section 2.4.1) of 23.42 and 0.40, respectively. The phase of reference signal, ψ_i,in full spectrum has been subtracted from the phase in full-spectrum, θ_i, of responses, as shown in Figure 2.8(c),which is obtained by using FFT of Runge-Kutta method based responses as provided in Table 2.3. The phase of reference signal at spin speed of 88 rad/s and 308 rad/s through the regression-based full spectrum is found to be very small and of the order of 10^{-16} rad as given in Table 2.4. Thus, variation of the reference signal phase through regression based method is very small and, hence, the compensation of phase is not required.

Table 2.3 Phase angles at different harmonics of full spectrum at spin speed of 88 rad/s

Frequency	Regression based full spectrum phase (θ_i) (rad) (A)	FFT based full spectrum phase (θ_i) without compensation (rad) (B)	Percentage variation $\frac{(A-B)}{A}$ %	FFT based full spectrum phase (θ_i) with compensation (rad) (C)	Percentage variation $\frac{(A-C)}{A}$ %
0	3.1157	3.1157	0.0002	3.1157	0.0002
ω	3.1102	3.1145	-0.1354	3.1102	0.0002
2ω	3.1138	3.1222	-0.2706	3.1138	0.0003
3ω	3.0934	3.1060	-0.4083	3.0933	0.0007
5ω	-0.1360	-0.1148	15.6104	-0.1359	0.1087
7ω	1.5858	1.6217	-2.2632	1.5922	-0.4012
$-\omega$	-3.1250	-3.1292	-0.1354	-3.1250	-0.0005
-3ω	0.0538	0.0412	23.4165	0.0538	-0.0931
-5ω	-2.9962	-3.0174	-0.7053	-2.9963	-0.0014

Moreover, the magnitude of phase based on regression and without compensation are found to be similar with the magnitude of phase by FFT based on Runge-Kutta method and with phase compensation.

Table 2.4 Comparison of reference angles of full spectrum at different harmonics by regression based method

Frequency	Spin speed at 88 rad/s		Spin speed at 308 rad/s	
	Regression based full spectrum reference angle (ψ_i) (10^{-16} rad)	FFT based full spectrum reference angle (ψ_i) (rad)	Regression based full spectrum reference angle (ψ_i) (10^{-16} rad)	FFT based full spectrum reference angle (ψ_i) (rad)
0	0.0927	0.6425×10^{-16}	0.0703	-9.5252×10^{-16}
ω	-0.4349	0.0084	-0.0008	0.0295
2ω	-0.0717	0.0169	0.8909	0.0591
$3\ \omega$	0.7589	0.0253	-0.4017	0.0886
$5\ \omega$	-0.1702	0.0422	-0.2921	0.1476
7ω	-0.4078	0.0590	-0.1932	0.2067
$-\ \omega$	-0.2637	-0.0084	-0.4477	-0.0295
$-3\ \omega$	0.7298	-0.0253	0.4048	-0.0886
$-5\ \omega$	-0.0491	-0.0422	-0.2886	-0.1476

2.4.3 Identification of parameters

The identification of parameters of the present rotor system starts with development of an inverse problem. The obtained amplitude and phase (with and without compensation based on FFT) have been incorporated in estimation method as given in Equation (2.34) to find these parameters, viz. c_E, c_H, e, ϕ and Δk_ξ as shown in Table 2.5. Identification of parameters has been done for a single speed as well as combined speeds as in Equation (2.34) and Equation(2.35), respectively. The fundamental natural frequency rotor system with an intact shaft is calculated as 616.44 rad/s. Parameter estimation has been done initially with a single speed at a time for two spin speeds of 88 rad/s and 308 rad/s. Whereas for the parameter estimation with multiple speeds, the speed ranges of 50 to 199 rad/s, and 200 to 350 rad/s with the increment of 1 rad/s is taken, which are below the critical speed of rotor. Identified parameters with phase compensation for both single and combined speeds are found to get closer values with respective assumed parameters as shown in Table 2.5. Similarly, without phase compensation it shows some speed dependent variation with the assumed ones. The maximum variation is found for lower speeds (for single speed at 88 rad/s and combined speeds from 50 to 199 rad/s) as compared to higher speeds (for single speed at 308 rad/s and as well as combined speeds from 200 to 350 rad/s) without phase compensation. Precisely, for lower single and combined speeds, especially the c_E and ϕ parameters without phase compensation and 0% noise gives an enormous variation with the assumed value. Rest of parameters. such as c_H, e, and Δk_ξ, nearly gets closer value. Instead, with phase compensation, variations of identified parameters are found to be smaller with 0% noise. To mimic real responses, noise of 1%, 2%, or 5% have been added to the numerical generated responses from the cracked rotor system model to test the robustness of the identification algorithm during the parameter estimation. Numerically generated random noise have been added to complex displacement (after phase compensation) of full spectrum and variations of estimated parameters are presented in Table 2.5. The variation is highly prominent in phase, i.e. ϕ, and eccentricity, e, with the addition of 5% noise, rest of estimated parameters are less deviates with noisy signals.

Table 2.5 Assumed and estimated rotor parameters through numerical simulation

Input speed in rad/s	Comparison		Parameters				
			c_H(Nms^{-1})	c_E (Nms^{-1})	e (10^{-}6 m)	ϕ (deg)	Δk_{22} (10^{5}N/m)
	A.V.	noise	20	100	5	30	2.5
Single speed 88	A	0%	20.4858	66.4484	4.6954	24.24	2.4991
	B	0%	20.0040	100.0023	5.0004	30.01	2.4999
		1%	20.1046	99.9956	5.5698	26.60	2.5057
		2%	20.2054	99.9882	6.1553	23.83	2.5115
		5%	20.5084	99.9618	7.9721	18.03	2.5287
Single speed 308	A	0%	20.0297	99.4815	4.8185	28.68	2.4922
	B	0%	20.0383	99.9672	5.0010	30.02	2.4998
		1%	20.1398	100.1509	5.0423	29.65	2.5078
		2%	20.2414	100.3341	5.0838	29.29	2.5158
		5%	20.5468	100.8803	5.2095	28.24	2.5398
Combined speed from 50 to 199 with increment +1	A	0%	20.3778	78.3644	4.7695	26.50	2.4976
	B	0%	20.0046	100.0048	5.0002	30.00	2.5000
		1%	20.1113	100.0662	5.1410	29.01	2.5037
		2%	20.2181	100.1271	5.2832	28.07	5.2832
		5%	20.5392	100.3067	5.7177	25.53	2.5187
Combined speed from 200 to 350 with increment +1	A	0%	20.1012	99.6069	4.8251	28.36	2.4966
	B	0%	20.0266	100.0368	5.0016	30.01	2.5001
		1%	20.1351	100.1114	5.0386	29.67	2.5054
		2%	20.2436	100.1856	5.0757	29.34	2.5108
		5%	20.5699	100.4064	5.1882	28.38	2.5269

A.V.: Assumed value; A: Without phase compensation; B: With phase compensation

Average percentage variation,for both single as well as combined speeds,in identified parameter are c_H is 2.71 %, c_E is 0.3027%, e is 20.43%, ϕ is -16.508% and Δk_{ξ} is 1.14% with 5% noise addition in responses. Therefore, it can be concluded that the proposed identification algorithm is robust against the measurement noise.

2.5 Conclusions

The estimation of internal damping has direct link with detection of the crack. The increase in the internal damping is an indicator of possible crack initiation. Even when cracks start developing inside the shaft surface that will reflect in the internal damping estimation as rubbing of crack surfaces will show in the form of increase in internal damping. Additionally, herein accurate internal damping estimation in laboratory environment will help in more accurate prediction of instable responses in an actual crack rotor system and possible prediction of it in the form of external damping to be provided by dampers, for example squeeze-film damper. The identification of internal damping due to a combination of rubbing of crack surfaces and hysteretic, and other rotor system parameters in a simple rotor model having a single transverse crack, has been performed in the present work. EOMs for the rotor system is developed mathematically. In addition to internal damping, estimation of other considered system parameters, i.e. the viscous external damping, eccentricity, and loss of stiffness has been performed. To estimate the internal damping and other system parameters, an identification algorithm is developed on the basis of the regression matrix method. Responses are generated through closed-form and numerical integration, which then transformed to full spectrum through regression-based and FFT based methods. In FFT based method, the phase ambiguity is found and for the phase compensation, multi-frequency reference signals are used. Also, it is illustrated that the time instance of picking of signal and capturing a complete cycle of the signal with the help of a reference signal aids a lot to avoid phase and leakage error. A comparison is made with two full spectrum generation methods for the identification of various system parameters and is found to be excellent with phase compensation. The measurement noise in responses, i.e. 1%, 2% or 5% has been added, sequentially, to test the identification algorithm robustness and it is found to be performing well against noise at both single and various ranges of multiple rotor speeds.

The experimental analysis of the present cracked simple rotor model is illustrated in the next chapter. A fatigue crack was developed onto shaft based on a three-point bending test for the experimental work. It consists of the estimation of the model parameter, based on the measured responses from an experimental rig.

CHAPTER 3

Experimental identification of internal and external damping in a simple cracked rotor system

To apply the developed methodology discussed in Chapter 2 in a real test data, a simple cracked rotor test rig was developed in Advanced Dynamics Laboratory at IIT Guwahati. Description of test rig development, instrumentation, measurement and signal processing have been given in this chapter. The experimental time-domain data was collected from the experimental setup and utilized in the model-based identification algorithm developed in Chapter 2. Estimated parameters are used in EOMs to get responses from updated rotor model and the same is compared with test rig responses for validating the estimated parameters.

3.1 Introduction

A model based experimental identification of internal damping in a cracked rotor system has been presented. The model based identification is taken from previous chapter and it experimentally investigated in present chapter. The internal damping and other critical unknown system parameters, like the external damping, additive crack stiffness, and disc unbalances have been estimated. For purpose of experimentation, an artificial fatigue crack was created in a shaft. The crack was positioned close to the disc. The amplitude and phase information of measured displacement signals have been extracted from full spectrum analysis with associated phase corrections. For the model based identification algorithm and equations of motion (EOM) of the rotor is used in experimental parameter estimation. The identification algorithm uses experimental full spectrum amplitudes and phases to estimate fault parameters of the rotor system.

3.2 Experimental setup of a fatigue crack

An artificial fatigue crack was created at the tip portion of a v-notch in a mild steel shaft. Firstly, a v-notch (which acts as stress raiser) was fabricated on the shaft bya milling machine at Central Workshop, IIT Guwahati. Then a fatigue transverse crack was initiated at the tip of v-notch through the INSTRON machine of Strength of Material Laboratory at IIT Guwahati based on standard *three-point bending fixture*.

The present test setup consists with a CNC spindle AC motor, shaft with artificial fatigue crack supported with two end (ball) bearings, a disc at mid-span of shaft and a flexible coupling interconnecting shaft with motor. A variable frequency drive (VFD) is used as a regulator to control the speed of motor as per requirement of shaft spin speed. Observation of transverse vibrational displacements of the shaft were carried out near to the disc location through two eddy current displacement probes, which were orientated in both horizontal and vertical directions. The third probe was positioned at motor shaft between coupling and motor for observation of reference signal in vertical direction. Time domain responses were acquired through these probes simultaneously with the help of a standard *data acquisition system* for individual spin speeds. Details of experimental setup is presented in next section.

3.2.1 Experimental design and analysis

The test rig design was planned to perform an experimental study based on the identification algorithm discussed in previous chapter to estimate critical parameters in a cracked rotor system. The parts of the experimental setup are summarized in Table 3.1 and illustrated in Figure 3.1. According to schematic in Figure 3.1, an experimental test rig was set up in the Vibration and Acoustics Laboratory at IIT Guwahati as shown in Figure 3.2. Fault analysis was done with the help of the rotor test rig, which consists of a shaft containing a transverse fatigue crack. Other elements of the test rig were the ball bearings, disc, shaft, coupling, motor and variable frequency drive (VFD). Figure 3.3 shows a slot on the motor shaft, which was used as a phase marker through a proximity probe. On the motor shaft, two different depth slots were available at 180^0 apart and the reference signal was measured corresponding to one of them in the present analysis.

Table3.1 Name of parts in the assembled experimental rotor setup

Part no.	Part name	Part no.	Part name
(1)	Bed	(6)	Eddy current probe
(2)	Rotor base plate	(7)	Probe holder
(3)	Motor	(8)	Disc
(4)	Bearing block	(9)	Flexible coupling
(5)	Ball bearing	(10)	Fatigue cracked shaft

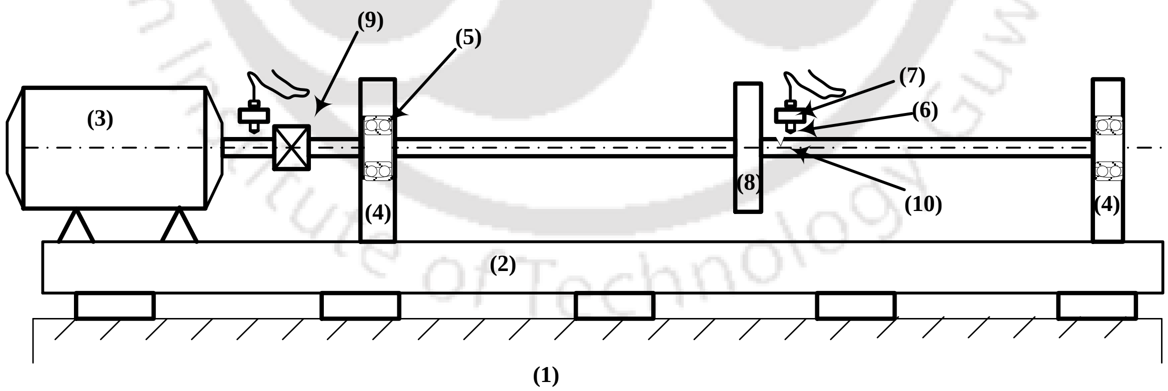

Figure3.1 Schematicof a cracked shaft experimental setup

Figures 3.4 and 3.6 show the position of crack onto shaft near to disc and a close view of fatigue crack at notch on the shaft, respectively. Fatigue crack on the shaft was generated through INSTRON machine as shown in Figure 3.5, in Strength of Material Laboratory at IIT Guwahati based on three-point bending test configuration as given in Table 3.2. A notch was generated to facilitate the generation of fatigue crack at the notch tip.

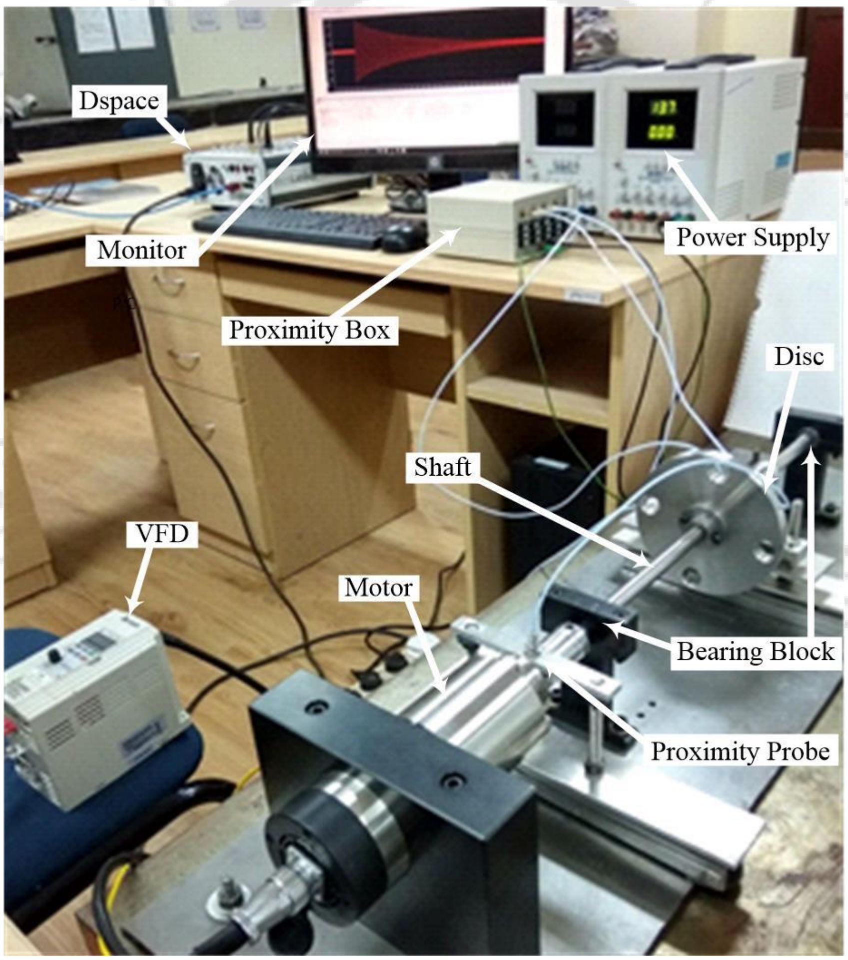

Figure3.2 Assembly of the cracked shaft experimental setup

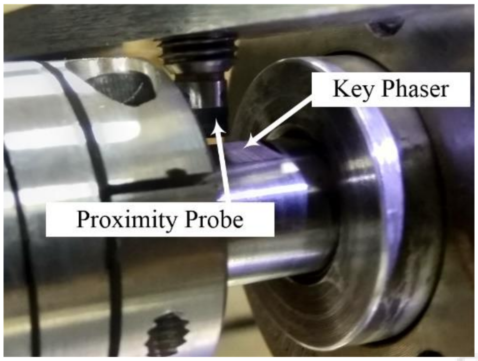

Figure3.3 Motor shaft with a slot and the sensor location for the reference signal

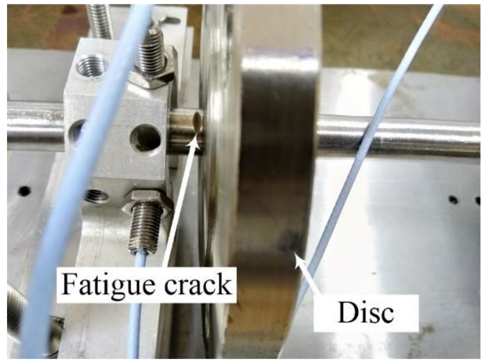

Figure 3.4 The shaft with a fatigue crack

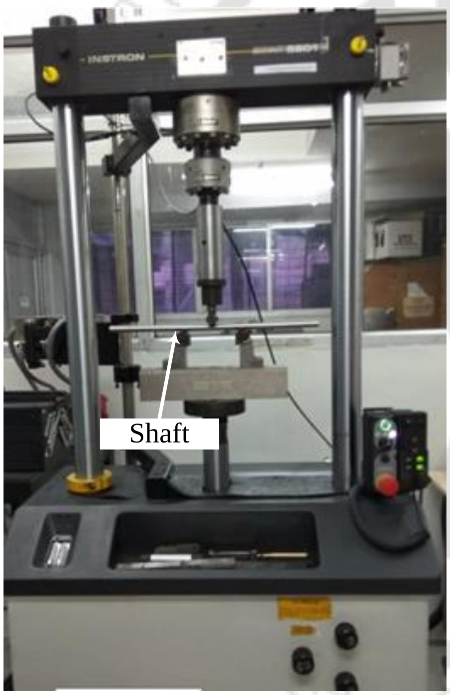

Figure3.5 Initiation of crack in three-point bending test in Instron machine

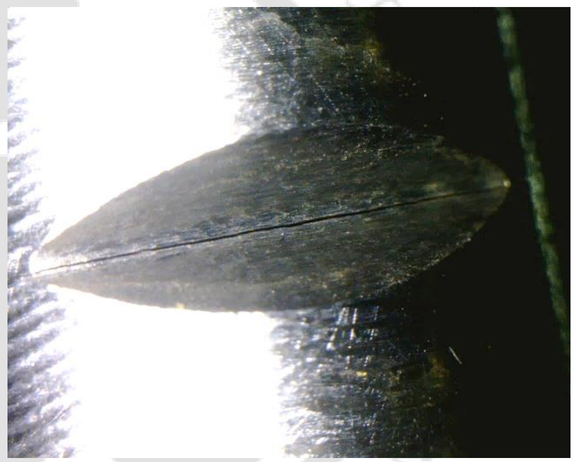

Figure 3.6 Close view of the fatigue crack at tip of a notch on the shaft

The notch was made to decrease efforts in generation of fatigue crack and to provide the desired path for propagation of the crack. Change in stiffness due to a particular depth of crack is modeled in the form of additive stiffness. However, exact fatigue crack depth was not known. Measurement unit consists of proximity sensors (non-contact type), DC power source units, data acquisition system and oscilloscope.

Table 3.2 Fatigue loading three-point bending test configuration

Test method	Three-point bending test
Operating frequency	10 Hz
Stress ratio	0.3 at 25^0 c
Compression	6 kN to 1.8kN
Support span	140 mm

3.2.2 Experimental observations

Two eddy-current proximity sensors placed in two orthogonal directions near the disc measured vibrational displacements of shaft. Sensitivity of the sensor was 7.478 Volt/mm. A third sensor was used for phase reference and was placed at motor shaft.

Impact tests were performed on stationary cracked shaft at different orientations to obtain corresponding natural frequencies. Maximum natural frequency of 60 Hz (377 rad/s) was obtained corresponding to shaft orientation when crack was in upward direction, where crack faces are expected to be in closed condition due to disc weight, as shown in Figure 3.7. Also, natural frequencies by placing the crack in vertical downward (fully open crack) and in horizontal (partially open crack) directions were found to be 58 Hz (364.4 rad/s) and 59 Hz (370.7 rad/s), respectively. For time domain plots in Figures 3.7 (a, c and e), the impact was given so that mainly the first natural frequency is excited. However, in Figures 3.7 (b, d and f) noise at higher frequencies can be seen. But, amplitudes of these noises are very small to be visible in time domain data of Figures 3.7 (a, c and e).

Motor speed was varied through a speed regulator. In measurements, slow roll spin speed was used at 3 Hz (Maalouf, 2007) and at this speed the rotor was running freely at uniform angular speed. A reference signal was used to acquire displacement signals in multiple of complete cycles of shaft rotation, $\omega t = 2\pi n$, where n is the number of complete cycles. This is to ensure minimum leakage errors during FFT. It was obtained with the help of peaks observed in a reference signal due to phase marker on motor shaft, as shown in Figure 3.8(a) at 3 Hz rotor speed for 3 complete cycles. Responses can be seen for 3 complete cycles as shown in Figure 3.8(a-c) both for displacements and the reference signal. Figure 3.8(a) shows the reference signal in x-direction, Figure 3.8(b) is displacement in x-direction (i.e. vertical direction) and displacement in y-direction (i.e. horizontal direction), is shown in Figure 3.8(c). Similarly, for higher speeds, Figures 3.9-3.11 show responses corresponding to spin speeds of 17 Hz, 20 Hz and 22 Hz, respectively. In Figures 3.8(b and c) (and also in Figures 3.9-3.11), it can be seen that around peak values the effect of crack opening and closure is visible in the form of deviation in signals (signals became thick in some parts). In remaining period, noise effect is not seen due to higher level of initial bow. Even it can be seen that the horizontal and vertical direction signals have such variation with some phase shift due to relative orientation of proximity probes during measurement. Figure 3.8(a) is a reference signal and noise effect can be seen at lower part of the signal. Crack effect may not come in the reference signal since it is near motor shaft, and in between motor shaft and cracked shaft there is a flexible coupling. Now, the FFT based full spectrum estimation through experimental data is discussed in following section.

Table 3.3 Parameters of rotor test rig

Parameters	Value	Unit
Mass of disc, m	1.87	kg
Length of shaft, l	455×10^{-3}	m
Diameter of shaft, d	15×10^{-3}	m
Young's modulus, E	2.10×10^{11}	N/m^2
Diametric area moment of inertia, ($I=\pi d^4/64$)	2.48×10^{-9}	m^4
Stiffness of intact shaft(k_0=48EI/l^3)	2.66×10^{5}	N/m
Theoretical natural frequency of intact shaft (ω_{nf}=($k_0/m)^{1/2}$)	377.10	rad/s
Experimental natural frequency of intact shaft (ω_{nf})	376.99	rad/s
Stiffness of intact shaft ($k_0 = m\omega_{nf}^2$)	2.66×10^{5}	N/m
Static deflection (δ_w= mg/k_0)	6.90×10^{-5}	m

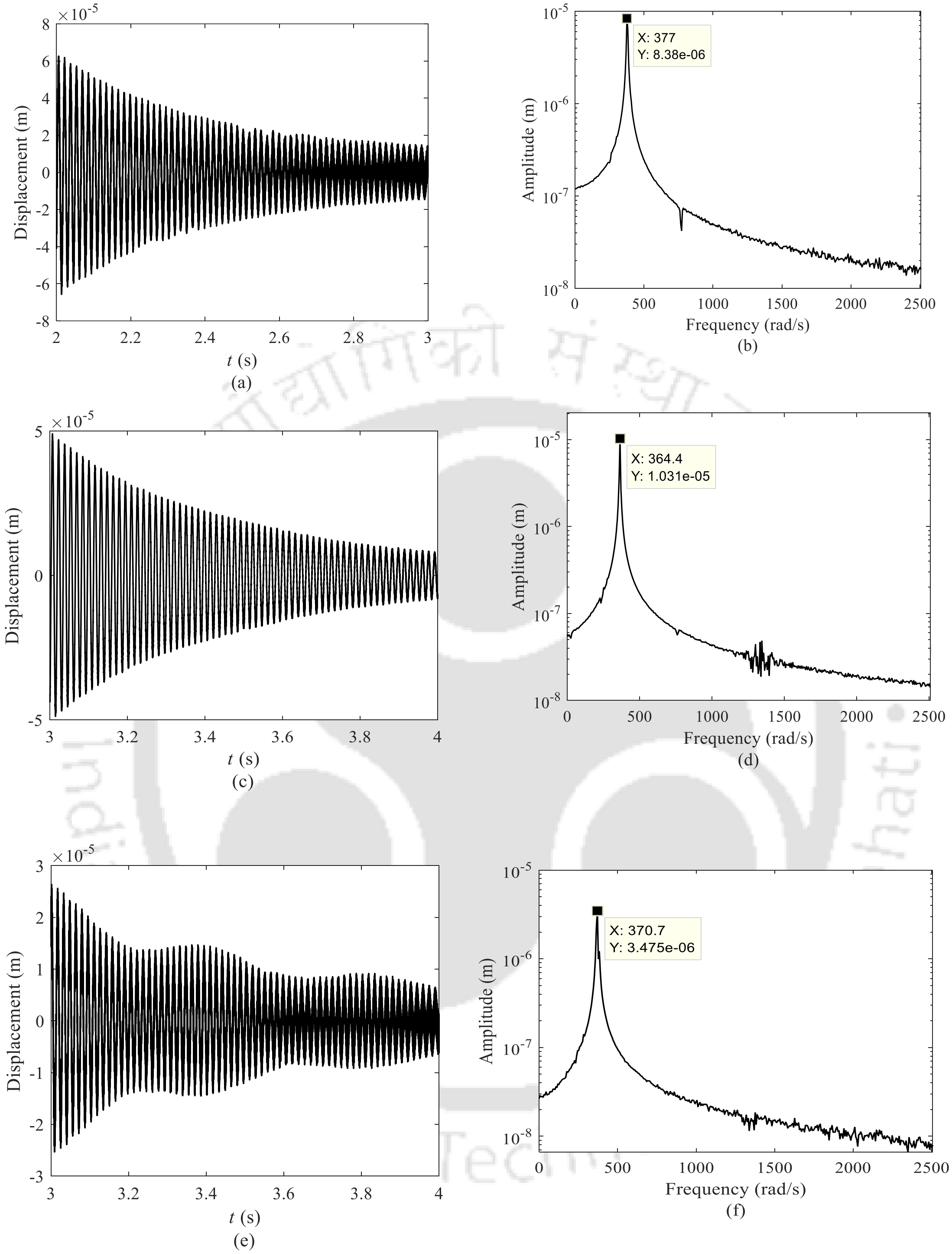

Figure 3.7 Response of shaft due to impulsive force (a) time domain response when crack in upward direction (b) frequency domain response when crack in upward direction (c) time domain response when crack in downward direction (d) frequency domain response when crack in downward direction (e) time domain response when crack in horizontal direction (f) frequency domain response when crack in horizontal direction

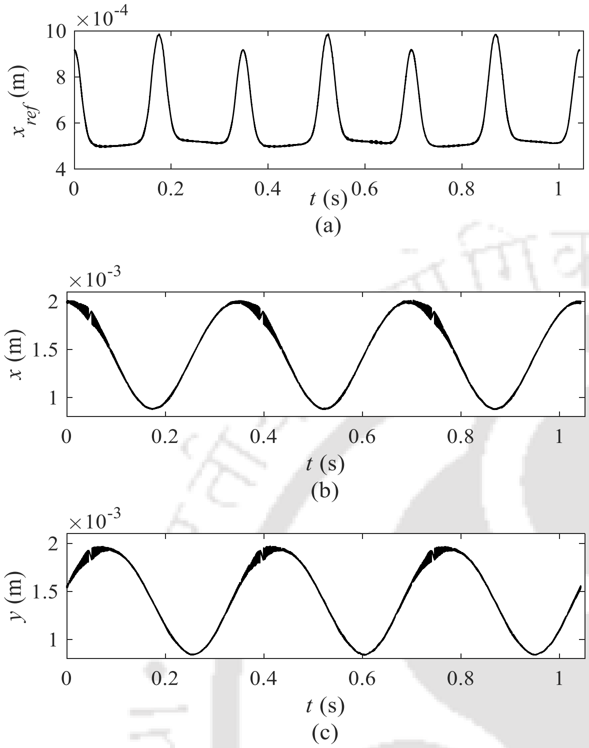

Figure 3.8 Time domain response for slow roll at 3 Hz for 3 complete cycles(a) reference displacement, (b) vertical displacement and (c) horizontal displacement

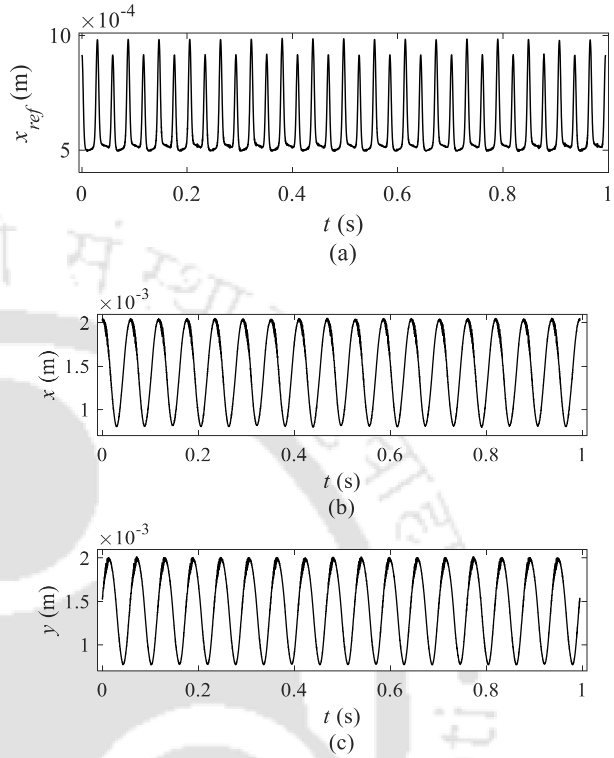

Figure 3.9 Time domain response for higher spin speed at 17 Hz for 17 complete cycles (a) reference displacement, (b) vertical displacement and (c) horizontal displacement

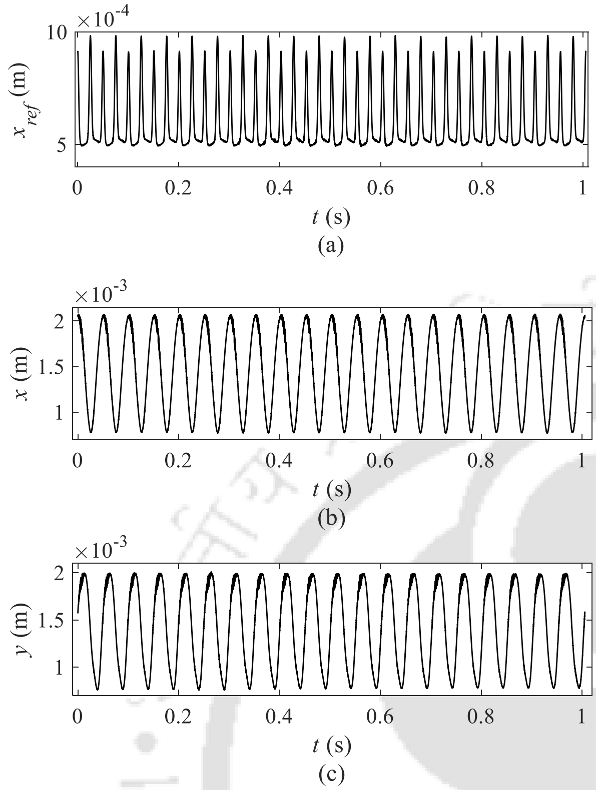

Figure 3.10 Time domain response for higher spin speed at 20 Hz for 20 complete cycles (a) reference displacement, (b) vertical displacement and (c) horizontal displacement

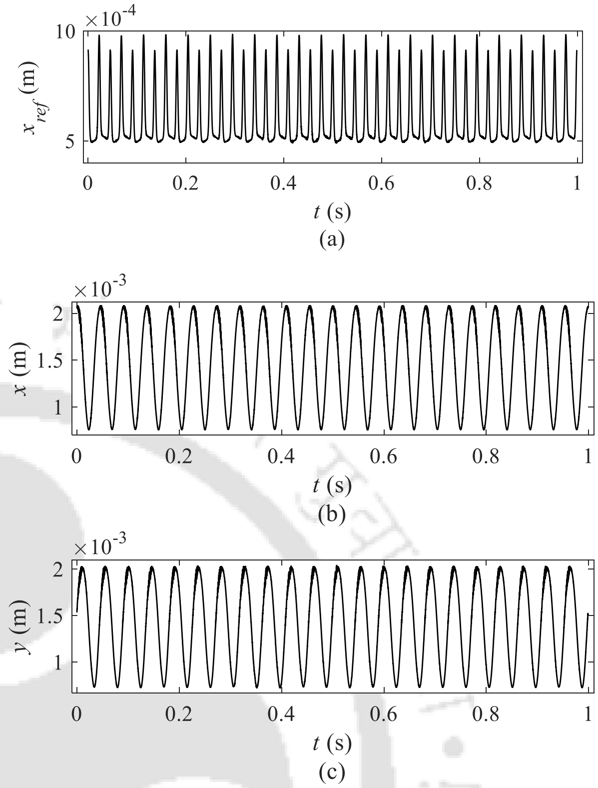

Figure3.11 Time domain response for higher spin speed at 22 Hz for 22 complete cycles (a) reference displacement (b) vertical displacement and (c) horizontal displacement

3.3 FFT based full spectrum analysis

FFT based full spectrum is a practical tool to estimate amplitude and phase of the forward as well as backward whirls from two orthogonal displacements in time domain. Time domain responses are obtained from experimental setup for the slow roll and higher spin speeds as discussed earlier. These data have been converted to frequency domain as illustrated in Figure 3.12 for slow roll condition. Figure 3.12(a) is referred to full spectrum amplitude of displacement and Figure 3.12(b) is full spectrum amplitude of reference signal. Figure 3.12(c) is full spectrum phase of displacement and Figure 3.12(d) is full spectrum phase of reference signal. Similarly, for higher spin speeds of 17 Hz, 20 Hz and 22 Hz, full spectra are shown in Figure 3.13, Figure 3.14, and Figure 3.15, respectively. In the present model for the case of intact shaft the response spectrum at negative frequencies would be mirror image of positive frequencies. Due to presence of crack experimental investigations (Figure 3.12 to 3.15) have been found that both forward and backward whirl take place in rotor response. Depending upon the crack shape and size the amplitudes of forward and backward whirls will be different. To mimic the similar behavior in the available literature (Gasch, 2008), the present crack model has been proposed and it is used in the present work. This model gives non-symmetric response spectrum with respect to zero frequency line.

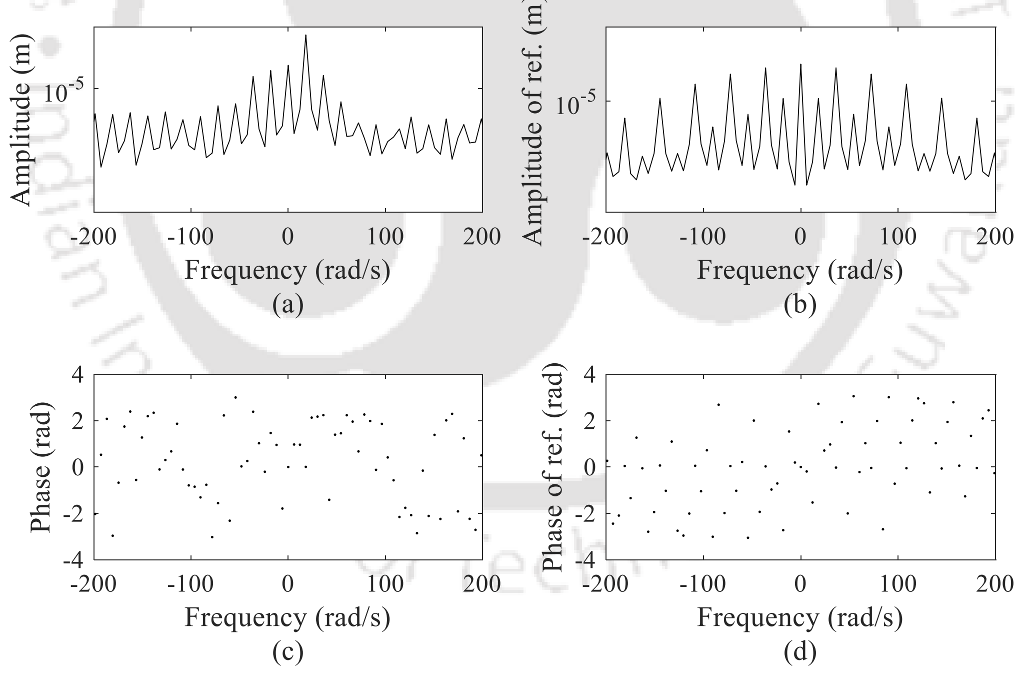

Figure 3.12 Full spectrum of measured responses for slow roll at 3 Hz (a) amplitude of displacement, (b) amplitude of reference signal, (c) phase of displacement and (d) phase of reference signal

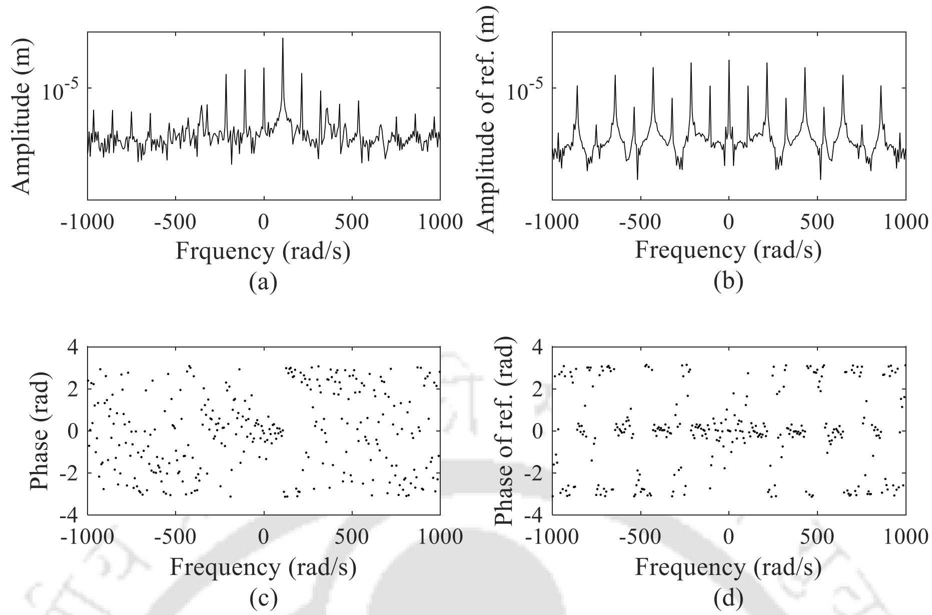

Figure 3.13 Full spectrum of measured responses for higher spin speed at 17 Hz for 17 complete cycles (a) amplitude of displacement, (b) amplitude of reference signal, (c) phase of displacement and (d) phase of reference signal

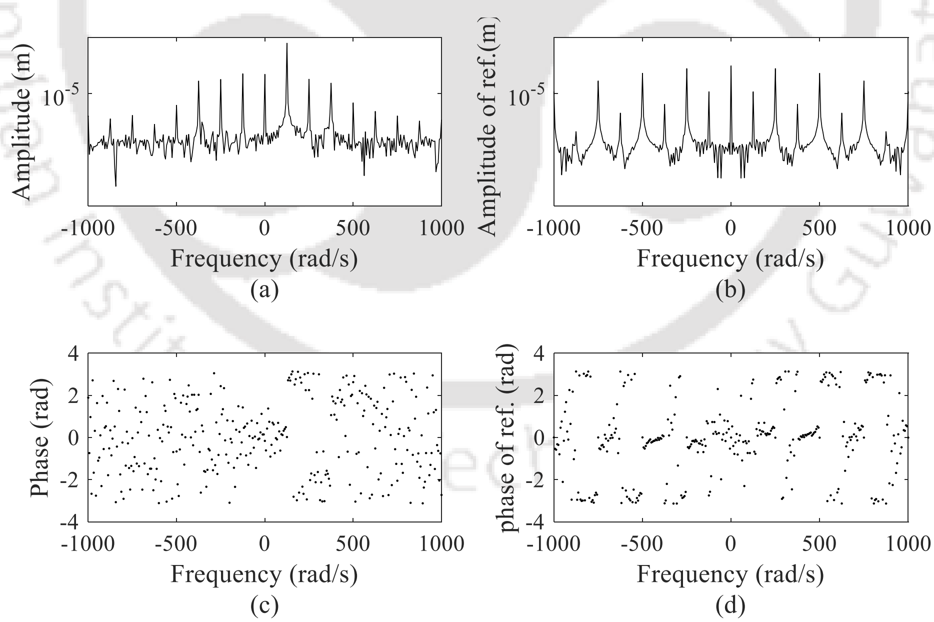

Figure 3.14 Full spectrum of measured responses forhigher spin speed at 20 Hz for 20 complete cycles (a) amplitude of displacement, (b) amplitude of reference signal, (c) phase of displacement and (d) phase of reference signal

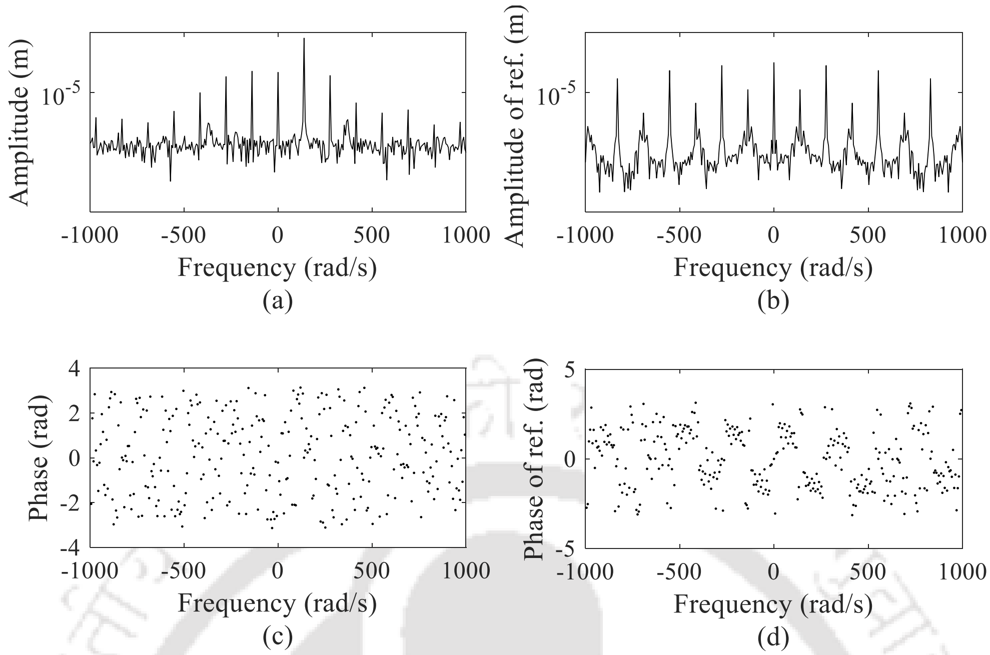

Figure 3.15 Full spectrum of measured responses for higher spin speed at 22 Hz for 22 complete cycles (a) amplitude of displacement, (b) amplitude of reference signal, (c) phase of displacement and (d) phase of reference signal

3.3.1 Comparisons in FFT with and without crack

A test was conducted for a different shaft without crack. Full spectrum of the same is shown in Figure 3.16. It shows main 1x component due to unbalance. It clearly indicates absence of higher harmonics as found in cracked shaft, as shown in Figure 3.13 for 17 Hz spin speed. Higher harmonics are present due to crack opening and closure during rotation of the shaft.

Since in present case, the crack was developed using a fatigue test, the control over crack depth is not there. In fact, actual depth is unknown until we cut the shaft and see the progress of the fatigue crack.

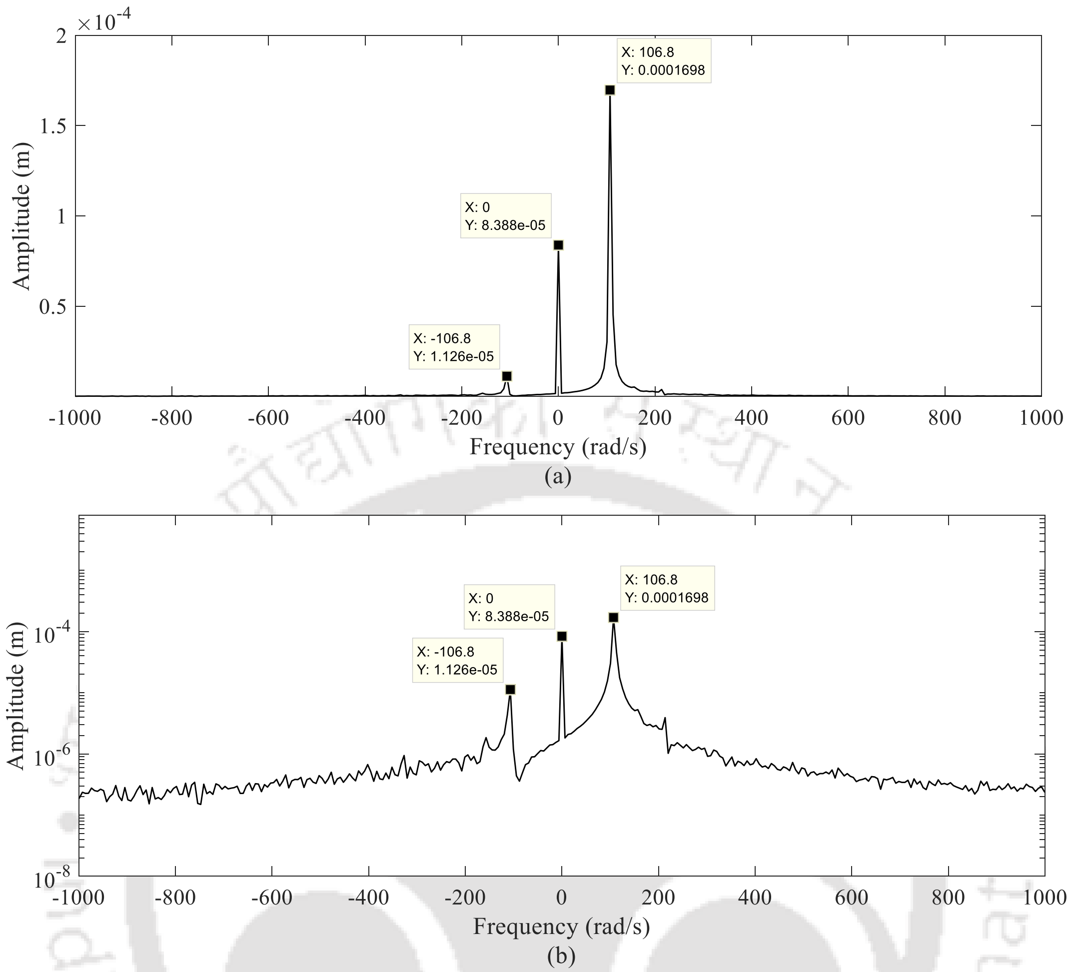

Figure 3.16 Full spectrum amplitudes of healthy rotor at 17 Hz using (a) a linear scale (b) a semi-log scale (in power on 10 scale)

3.3.2 Comparisons of FFT based and Regression-based method

In present section, estimation of full spectrum by regression-based method and FFT based method are compared. Full spectrum contains both amplitudes and its phase at different frequencies of complex displacements ($R_i(\omega) = R_{i\mathrm{Re}} + \mathrm{j}R_{i\mathrm{Im}}$). Phase angles of reference signal at different harmonics of full spectrum for slow roll (3 Hz) are provided for both methods in Table 3.4.

Table3.4 Displacement amplitudes and its phase angles, and reference signal phase angles at different harmonics of full spectrum for the slow run of rotor (3 Hz)

Frequency	Displacement amplitude		Displacement phase angle		Reference signal phase angle	
	Regression based full spectrum (10^{-5} m)	FFT based full spectrum (10^{-5} m)	Regression based full spectrum (10^{-2} rad)	FFT based full spectrum (10^{-2} rad)	Regression based full spectrum (rad)	FFT based full spectrum (rad)
0	205.42	205.42	0.77	0.77	0.00	0.00
ω	55.29	55.29	0.42	0.52	2.72	2.72
2 ω	2.70	2.70	223.21	223.55	-0.03	-0.02
3 ω	0.38	0.37	144.50	145.34	3.05	3.05
5 ω	0.07	0.07	-11.91	-12.22	3.00	3.01
7 ω	0.12	0.12	-207.94	-207.76	2.702	2.75
- ω	3.89	3.89	146.87	146.72	-2.72	-2.73
-3ω	0.32	0.32	300.02	299.89	-3.05	-3.05
-5ω	0.12	0.12	-131.50	-131.04	-3.00	-3.01

Amplitudes of reference signal are having no relevance in parameter estimation, however, phase angles will be useful for phase correction of displacements and will be described in next section. Full spectrum displacement amplitudes at different harmonics for higher spin speeds of 17 Hz, 20 Hz and 22 Hz are illustrated in Table 3.5. Similarly, the displacement and reference signal phases for higher spin speeds are shown in Table 3.6 and Table 3.7, respectively.

From these tables, displacement amplitudes and its phase angles, and reference signal phase angles at different harmonics by FFT based method are found close to the regression based method. Thus, it can be inferred that the variations are found to be negligible by two independent methods. This verifies usage of full spectrum correctly.

Table 3.5 Full spectrum displacement amplitudes at different harmonics for higher rotor spin speeds

Frequency	Spin speed at 17 Hz		Spin speed at 20 Hz		Spin speed at 22 Hz	
	Regression based (10^{-5} m)	FFT based (10^{-5} m)	Regression based (10^{-5} m)	FFT based (10^{-5} m)	Regression based (10^{-5} m)	FFT based (10^{-5} m)
0	204.59	204.59	204.24	204.24	203.89	203.91
ω	60.59	60.59	62.74	62.74	64.95	64.96
2 ω	3.30	3.31	3.28	3.28	3.62	3.62
3 ω	0.78	0.78	2.38	2.38	0.44	0.44
5 ω	0.34	0.34	0.23	0.23	0.25	0.25
7 ω	0.09	0.09	0.10	0.11	0.10	0.10
- ω	4.47	4.47	5.15	5.15	5.06	5.06
-3 ω	0.25	0.25	2.84	2.84	0.97	0.97
-5 ω	0.05	0.05	0.08	0.08	0.09	0.09

Table 3.6 Full spectrum displacement phase angles at different harmonics for higher rotor spin speeds

Frequency	Spin speed at 17 Hz		Spin speed at 20 Hz		Spin speed at 22Hz	
	Regression based (rad)	FFT based (rad)	Regression based (rad)	FFT based (rad)	Regression based (rad)	FFT based (rad)
0	0.77	0.77	0.77	0.77	0.77	0.77
ω	0.02	0.02	0.02	0.02	-0.00	0.01
2 ω	2.30	2.31	2.23	2.25	2.21	2.22

3 ω	1.81	1.83	1.04	1.06	1.56	1.59
5 ω	-0.50	-0.48	-0.54	-0.52	-0.44	-0.41
7 ω	-1.68	-1.65	-1.95	-1.91	-1.91	-1.87
- ω	1.43	1.42	1.43	1.42	1.44	1.44
-3ω	-2.03	-2.03	2.04	2.03	2.49	2.47
-5ω	-1.53	-1.54	-0.97	-0.98	-1.29	-1.31

Table 3.7 Full spectrum reference signal phase angles at different harmonics for higher rotor spin speeds

Frequency	Spin speed at 17 Hz		Spin speed at 20 Hz		Spin speed at 22 Hz	
	Regression based (rad)	FFT based (rad)	Regression based (rad)	FFT based (rad)	Regression based (rad)	FFT based (rad)
0	0.00	0.00	0.00	0.00	0.00	0.00
ω	2.73	2.74	2.74	2.75	2.75	2.76
2 ω	-0.03	-0.02	-0.01	-0.01	-0.01	-0.01
3 ω	3.10	3.11	3.10	3.12	3.13	-3.13
5 ω	3.09	3.11	3.12	-3.13	-3.10	-3.07
7 ω	3.01	3.05	3.10	-3.13	-2.87	-2.86
- ω	-2.73	-2.74	-2.74	-2.74	-2.75	-2.76
-3 ω	-3.10	-3.11	-3.10	-3.12	-3.13	3.13
-5 ω	-3.09	-3.11	-3.12	3.13	3.10	3.07

Shaft bow effect is nullified, in subsequent sections, from displacement amplitudes and a comparison of orbit plots is also presented. Finally, estimation of rotor system parameters is presented.

3.3.3 Phase compensation in full spectrum

Phase compensation in full spectrum is an important step so that measurements at different times can be synchronized with respect to a common phase reference on to shaft. In test rotor, all phases have to be measured with respect to a common physical mark on the shaft (for present case slots were considered on the motor shaft) and corresponding signal is used as a reference signal for all phase measurements. Since cracked shaft response contains multiple harmonics so a multi-harmonic phase reference signal is envisaged corresponding to measured reference signal (Singh and Tiwari, 2016). Measured displacement phases corresponding to various harmonics are obtained with respect to multi-harmonic phase reference signal for all sets of measured displacement data. So, phase of displacement for each harmonic is subtracted with phase of corresponding harmonic of reference signal to get a correct phase of displacements even when it has been captured at different times.

Table 3.8 Full spectrum phase compensation at different harmonics for higher rotor spin speeds

Frequency	Slow run at 3 Hz	Spin speed at 17 Hz	Spin speed at 20 Hz	Spin speed at 22 Hz
0	0.77	0.77	0.77	0.77
ω	-2.72	-2.72	-2.73	-2.76
2 ω	2.26	2.33	2.26	2.22
3 ω	-1.59	-1.29	-2.06	4.72
5 ω	-3.13	-3.60	2.61	2.66
7 ω	-4.82	-4.71	1.22	0.99
- ω	4.19	4.16	4.18	4.20
-3 ω	6.05	1.08	5.15	-0.66
-5 ω	1.69	1.57	-4.12	-4.38

Displacement phase after subtraction from reference phase is known as phase compensation and such phases are shown in Table 3.8, and are used for the identification of system fault parameters.

3.4 Removing the effect of shaft bow

Removal of bow effect from full spectrum is important for correct identification of rotor fault parameters and it is removed by using a slow roll measurement of displacement (Maalouf, 2007 and Shravankumar et al., 2015). For this purpose, complex displacement (i.e. in vector form) of full spectrum at slow roll for 1X harmonic is removed from complex displacement of full spectrum at higher rotor spin speeds. Similarly, for the sensor gap the complex displacement of full spectrum at slow roll for 0X harmonic (or mean of responses in x and y directions) is removed from the complex displacement of full spectrum at higher rotor spin speeds in both vertical and horizontal directions. However, the rest of harmonics of full spectrum remains the same and is expressed as

$$\underset{\text{Without bow and sensor gap}}{s_1(\mathbf{t})} = \underset{\text{Experimental data with bow and sensor gap}}{\mathbf{s}(\mathbf{t})} - \underbrace{\left(\left(\mathbf{R}_0+\mathbf{R}_1 e^{j\omega t}\right)_{\textbf{higher spin speed}}\right)}_{\text{Without phase compensation}} + \underbrace{\left(\left(\mathbf{R}_{0p}\right)_{\textbf{higher spin speed}} - \left(\mathbf{R}_{0p}\right)_{\textbf{slow roll}}\right)}_{\text{Removing sensor gap from equilibrium position after phase compensation}} + \underbrace{\left(\left(\mathbf{R}_{1p}\right)_{\textbf{higher spin speed}} - \left(\mathbf{R}_{1p}\right)_{\textbf{slow roll}}\right)}_{\text{Removing bow after phase compensation}} e^{j\omega t} \tag{3.1}$$

Equation (3.1) is used for finding out full spectrum at higher spin speeds after removal of bow effect. In Equation (3.1) $\mathbf{R}_{0p}$, $\mathbf{R}_0$, $\mathbf{R}_{1p}$ and $\mathbf{R}_1$ represents the vector form of complex displacement. Herein, subscript ‘0’ and ‘1’ represents the complex displacement at 0X and 1X respectively and subscript p represents with phase compensation, which is discussed in section 3.3.3. Amplitudes and phases of corrected full spectrum along with remaining harmonic also with phase compensation are used mainly for identification of rotor fault parameters, like internal damping, external damping, unbalance and additive crack stiffness. Comparisons of responses with and without bow and sensor gap with the help of Equation (3.1) are presented in next subsection.

3.4.1 Comparison of displacements with and without bow and sensor gap

Now the bow and sensor gap effect needs to be removed from measured signals for effective estimation of system fault parameters. The procedure described in beginning of Section 3.4 is used to remove bow and sensor gap effect. For rotor spin speeds at 17 Hz, 20 Hz and 22 Hz, displacements have been illustrated in Figures 3.17 through 3.19, respectively, without the effect of bow and sensor gap. Noise effects can be clearly seen in Figures 3.12-3.15 (full spectrum), in which no processing was performed on raw data. In Figures 3.17 through 3.19, sinusoidal form of signal effect is smaller due to removal of predominant bow effect by signal processing at first harmonic and the axial position is changed due to removal of the sensor gap effect. It can be seen that in these figures, displacements are reduced as compared to that shown in corresponding Figure 3.9(b, c), Figure 3.10(b, c) and Figure 3.11(b, c) with bow and sensor gap effect. Hence, during generation of fatigue crack in the shaft significant bow developed and now it is expected that estimates of fault parameters would be more reliable.

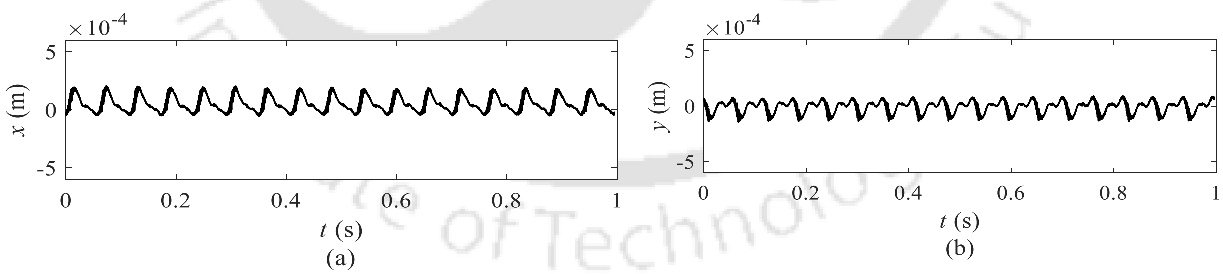

Figure 3.17 Response obtained at 17 Hz rotor spin speed for 17 complete cycles without bow and without sensor gap in (a) vertical direction (b) horizontal direction

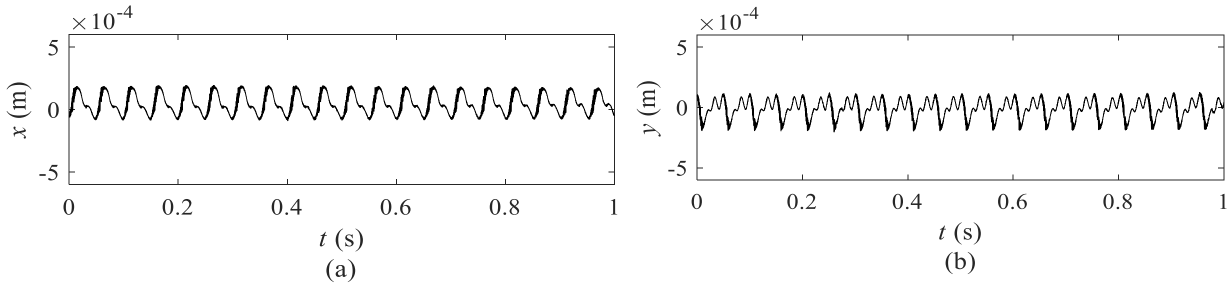

Figure3.18 Response obtained at 20 Hz rotor spin speed for 20 complete cycles without bow and without sensor gap in (a) vertical direction (b) horizontal direction

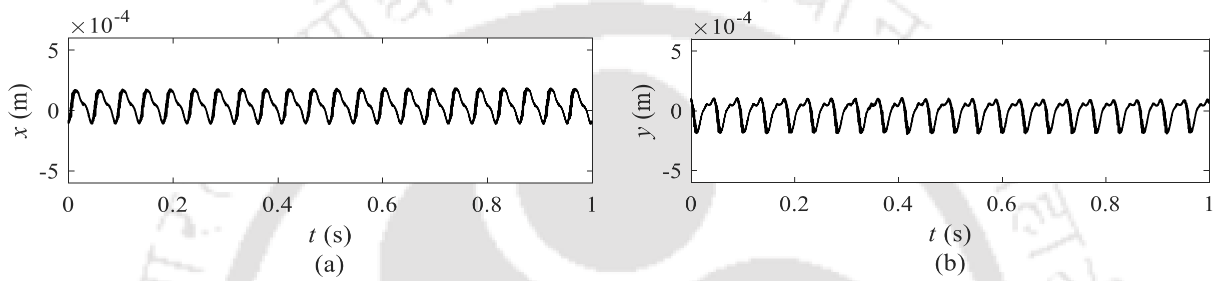

Figure3.19 Response obtained at 22 Hz rotor spin speed for 22 complete cycles without bow and without sensor gap in (a) vertical direction (b) horizontal direction

Rotor orbits with and without bow and sensor gap can be seen in Figure 3.20 through Figure 3.22 for rotor spin speed at 17 Hz, 20 Hz and 22 Hz, respectively. In Figures 3.20 through 3.22, orbit plots without removal of bow and sensor gap effect, the noise effect can be seen along with crack effect in some part of the orbit. Orbit plots with bow for corresponding spin speeds are shown in Figure 3.20(a), Figure 3.21(a) and Figure 3.22(a) directly using experimental data. Orbit plots without bow and sensor gap for corresponding spin speeds after phase compensation (i.e., using Equation (3.1)) are shown in Figure 3.20(b), Figure 3.21(b) and Figure 3.22(b). To have a direct comparison, the abscissa and ordinate ranges are kept consistent for both with bow and sensor gap, and without bow and sensor gap, and are 10^{-3} and 10^{-4}, respectively. A considerable reduction in size of orbit shapes are observed without bow and sensor gap as compared with bow and sensor gap. In addition, for different speeds without bow not much difference in size of orbit is observed due to variation of speed at low frequency range in presence of crack. Nevertheless, these orbits are definitely not circular indicating several harmonics present in it and possibly both forward and backward whirls due to crack opening and closure.

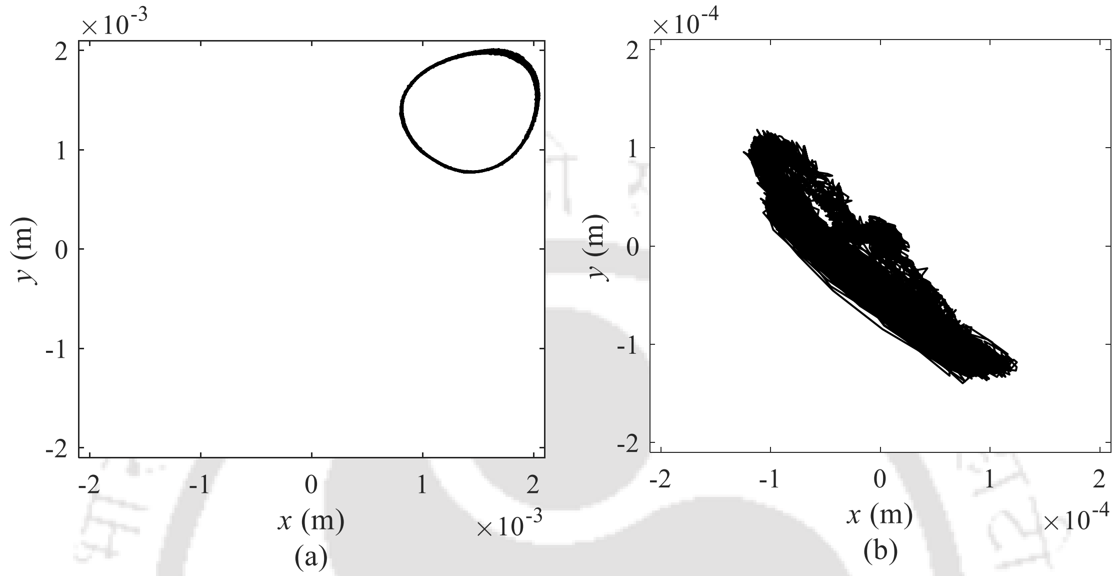

Figure 3.20 Orbit plot for rotor spin speed at 17 Hz (a) with bow and sensor gap (b) without bow and without sensor gap

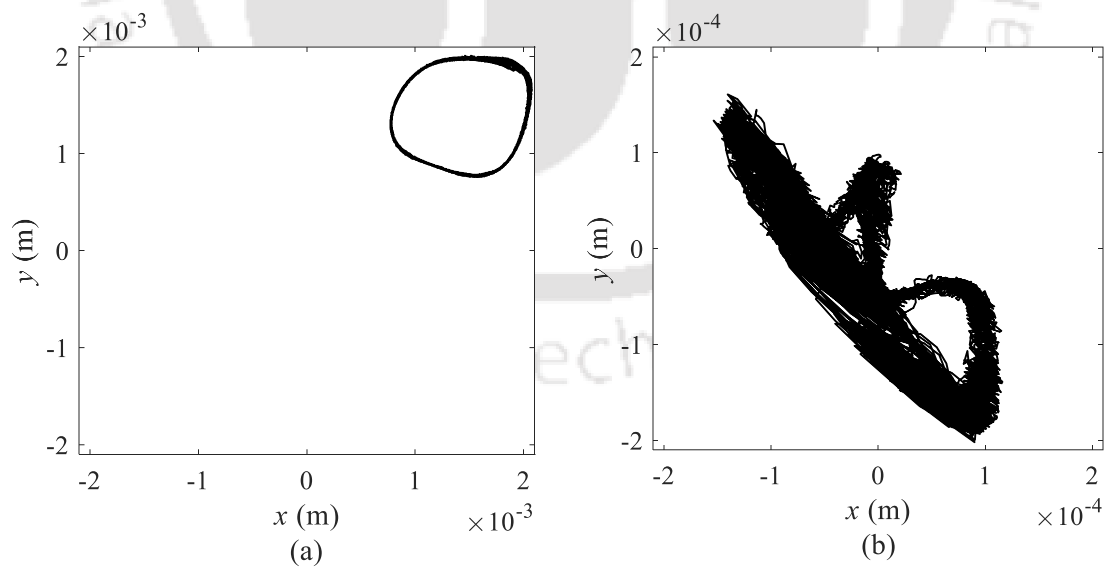

Figure 3.21 Orbit plot (x versus y) for higher spin speed at 20Hz (a) with bow and sensor gap (b) without bow and without sensor gap

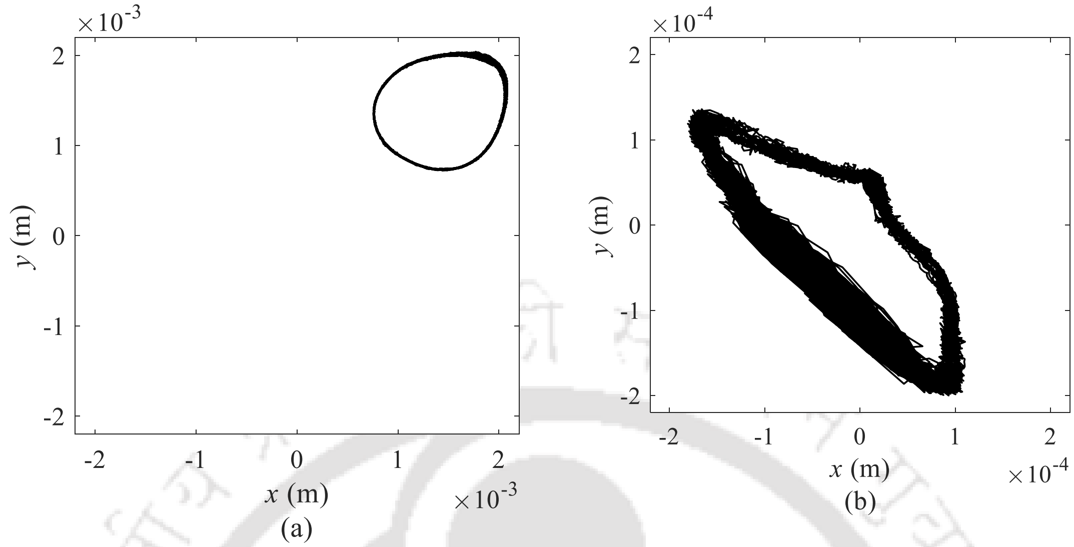

Figure 3.22 Orbit plot (x versus y) for higher spin speed at 22 Hz (a) with bow and sensor gap (b) without bow and without sensor gap

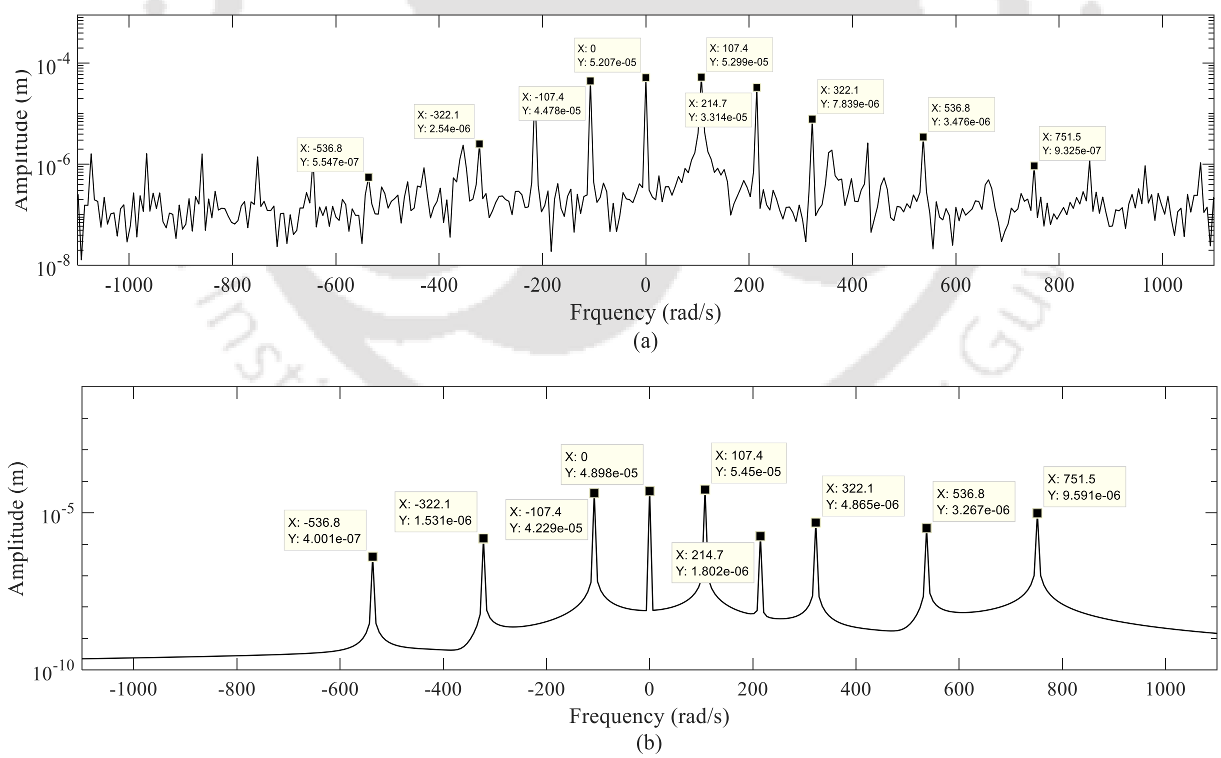

Figure 3.23 Full spectrum amplitude without bow and without sensor gap near at 17 Hz spin speed for 17 complete cycles (a) experimental (b) numerical model method

To investigate the same, full spectrum plots using experimental data, withbow and sensor gap, and without bow and sensor gap, for spin speeds of 17, 20 and 22 Hz are shown in Figures 3.13(a) through 3.15(a) and 3.23(a) through 3.25(a), respectively. On comparing, full spectrum plots for both cases, amplitudes of displacement are found to be higher at zeroth and first harmonic for measurement data with sensor gap and bow. In all these plots, trends of the forward and backward whirls are similar for different speeds considered. This is due to firstly similar manifestation of crack behavior in responses and secondly the choice of speed range at lower speeds to avoid propagation of crack at higher speeds.

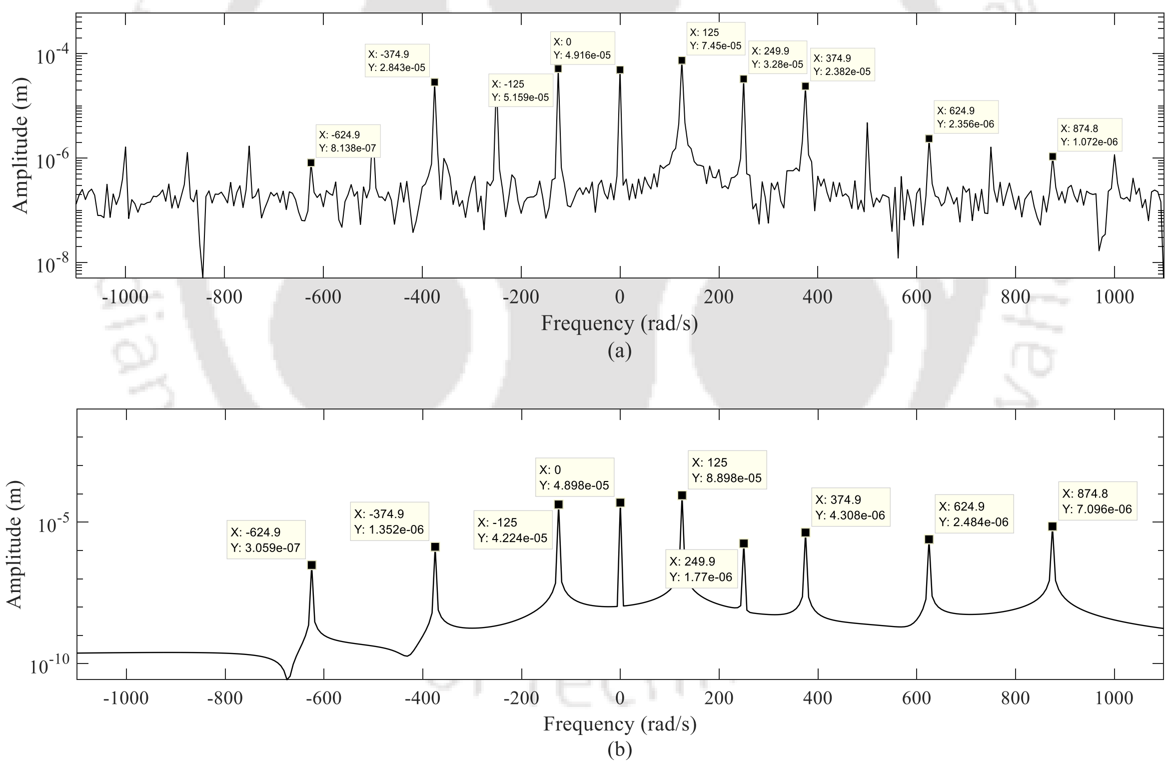

Figure 3.24 Full spectrum amplitude without bow and without sensor gap near at 20 Hz spin speed for 20 complete cycles (a) experimental (b) numerical model method

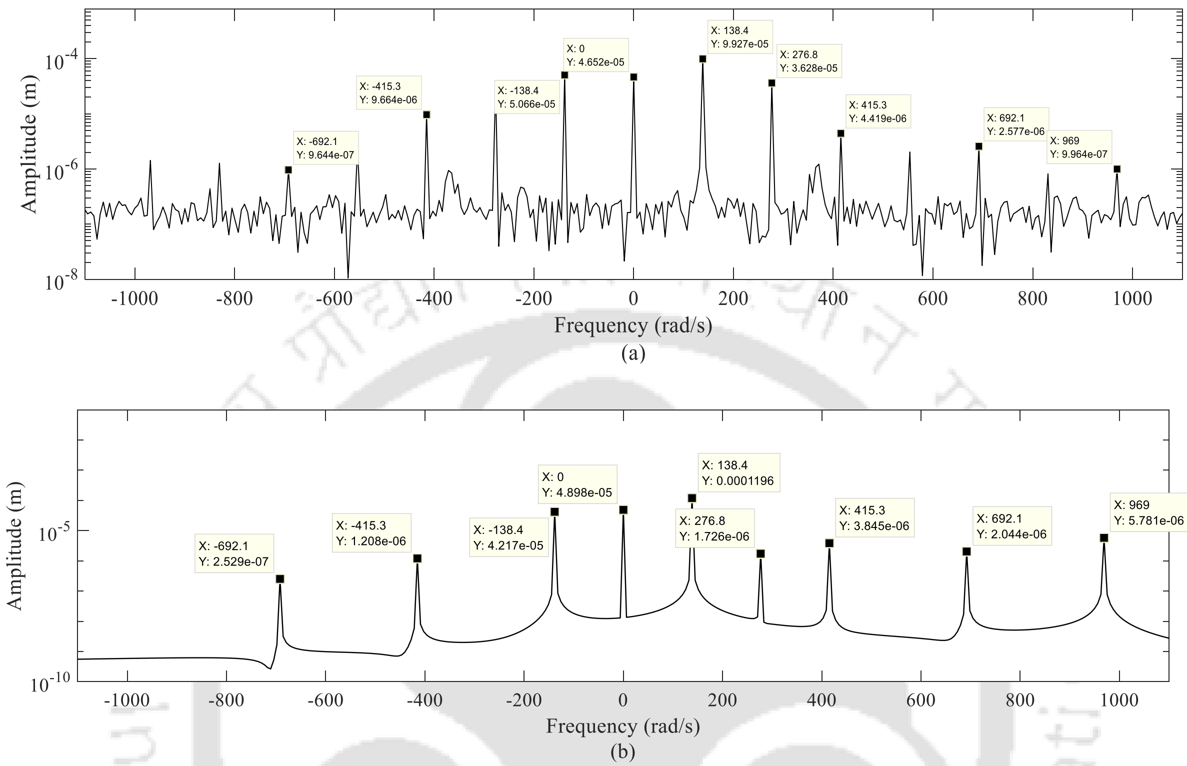

Figure 3.25 Full spectrum amplitude without bow and without sensor gap near at 22 Hz spin speed for 22 complete cycles (a) experimental (b) numerical model method

3.5 Identification Algorithm

Equations (2.30) and (2.31) are arranged in regression matrix form for identification of c_E, c_H, $e_{\mathrm{Re}}, e_{\mathrm{Im}}$ and $p_i \Delta k_\xi$ at different harmonic frequencies, which is written in following form

$$\mathbf{A}_2 \mathbf{x}_2 = \mathbf{b}_2 \tag{3.2}$$

With

$$
\mathbf{A}_2 = \begin{bmatrix}
0 & R_{0\,\mathrm{Im}}\omega & 0 & 0 & -u_{x0} & 0 & 0 & 0 & 0 & 0 & 0 & 0 & 0 \\
-R_{1\,\mathrm{Im}}\omega & 0 & -m\omega^2 & 0 & 0 & -u_{x0} & 0 & 0 & 0 & 0 & 0 & 0 & 0 \\
-2R_{2\,\mathrm{Im}}\omega & -R_{2\,\mathrm{Im}}\omega & 0 & 0 & 0 & 0 & -u_{x0} & 0 & 0 & 0 & 0 & 0 & 0 \\
-3R_{3\,\mathrm{Im}}\omega & -2R_{3\,\mathrm{Im}}\omega & 0 & 0 & 0 & 0 & 0 & -u_{x0} & 0 & 0 & 0 & 0 & 0 \\
-5R_{5\,\mathrm{Im}}\omega & -4R_{5\,\mathrm{Im}}\omega & 0 & 0 & 0 & 0 & 0 & 0 & -u_{x0} & 0 & 0 & 0 & 0 \\
-7R_{7\,\mathrm{Im}}\omega & -6R_{7\,\mathrm{Im}}\omega & 0 & 0 & 0 & 0 & 0 & 0 & 0 & -u_{x0} & 0 & 0 & 0 \\
R_{-1\,\mathrm{Im}}\omega & 2R_{-1\,\mathrm{Im}}\omega & 0 & 0 & 0 & 0 & 0 & 0 & 0 & 0 & -u_{x0} & 0 & 0 \\
3R_{-3\,\mathrm{Im}}\omega & 4R_{-3\,\mathrm{Im}}\omega & 0 & 0 & 0 & 0 & 0 & 0 & 0 & 0 & 0 & -u_{x0} & 0 \\
5R_{-5\,\mathrm{Im}}\omega & 6R_{-5\,\mathrm{Im}}\omega & 0 & 0 & 0 & 0 & 0 & 0 & 0 & 0 & 0 & 0 & -u_{x0} \\
0 & -\left(R_{0\,\mathrm{Re}} + u_{x0}\right)\omega & 0 & 0 & 0 & 0 & 0 & 0 & 0 & 0 & 0 & 0 & 0 \\
R_{1\,\mathrm{Re}}\omega & 0 & 0 & -m\omega^2 & 0 & 0 & 0 & 0 & 0 & 0 & 0 & 0 & 0 \\
2R_{2\,\mathrm{Re}}\omega & R_{2\,\mathrm{Re}}\omega & 0 & 0 & 0 & 0 & 0 & 0 & 0 & 0 & 0 & 0 & 0 \\
3R_{3\,\mathrm{Re}}\omega & 2R_{3\,\mathrm{Re}}\omega & 0 & 0 & 0 & 0 & 0 & 0 & 0 & 0 & 0 & 0 & 0 \\
5R_{5\,\mathrm{Re}}\omega & 4R_{5\,\mathrm{Re}}\omega & 0 & 0 & 0 & 0 & 0 & 0 & 0 & 0 & 0 & 0 & 0 \\
7R_{7\,\mathrm{Re}}\omega & 6R_{7\,\mathrm{Re}}\omega & 0 & 0 & 0 & 0 & 0 & 0 & 0 & 0 & 0 & 0 & 0 \\
-R_{-1\,\mathrm{Re}}\omega & -2R_{-1\,\mathrm{Re}}\omega & 0 & 0 & 0 & 0 & 0 & 0 & 0 & 0 & 0 & 0 & 0 \\
-3R_{-3\,\mathrm{Re}}\omega & -4R_{-3\,\mathrm{Re}}\omega & 0 & 0 & 0 & 0 & 0 & 0 & 0 & 0 & 0 & 0 & 0 \\
-5R_{-5\,\mathrm{Re}}\omega & -6R_{-5\,\mathrm{Re}}\omega & 0 & 0 & 0 & 0 & 0 & 0 & 0 & 0 & 0 & 0 & 0
\end{bmatrix}
$$

$$\mathbf{x}_2 = \begin{Bmatrix} c_E \\ c_H \\ e_{\mathrm{Re}} \\ e_{\mathrm{Im}} \\ \Delta k_\xi p_0 \\ \Delta k_\xi p_1 \\ \Delta k_\xi p_2 \\ \Delta k_\xi p_3 \\ \Delta k_\xi p_5 \\ \Delta k_\xi p_7 \\ \Delta k_\xi p_{-1} \\ \Delta k_\xi p_{-3} \\ \Delta k_\xi p_{-5} \end{Bmatrix} \text{ and } \mathbf{b}_2 = \begin{Bmatrix} (-k_0) R_{0\mathrm{Re}} \\ (m\omega^2 - k_0) R_{1\mathrm{Re}} \\ (4m\omega^2 - k_0) R_{2\mathrm{Re}} \\ (9m\omega^2 - k_0) R_{3\mathrm{Re}} \\ (25m\omega^2 - k_0) R_{5\mathrm{Re}} \\ (49m\omega^2 - k_0) R_{7\mathrm{Re}} \\ (m\omega^2 - k_0) R_{-1\mathrm{Re}} \\ (9m\omega^2 - k_0) R_{-3\mathrm{Re}} \\ (25m\omega^2 - k_0) R_{-5\mathrm{Re}} \\ (-k_0) R_{0\mathrm{Im}} \\ (m\omega^2 - k_0) R_{1\mathrm{Im}} \\ (4m\omega^2 - k_0) R_{2\mathrm{Im}} \\ (9m\omega^2 - k_0) R_{3\mathrm{Im}} \\ (25m\omega^2 - k_0) R_{5\mathrm{Im}} \\ (49m\omega^2 - k_0) R_{7\mathrm{Im}} \\ (m\omega^2 - k_0) R_{-1\mathrm{Im}} \\ (9m\omega^2 - k_0) R_{-3\mathrm{Im}} \\ (25m\omega^2 - k_0) R_{-5\mathrm{Im}} \end{Bmatrix}$$

Herein, $u_{x0} = mg / k_0$. For estimation of $\mathbf{x}_2$, Equation (3.2) is converted into a least-squares fit form, as

$$\mathbf{x}_2 = \left(\mathbf{A}_2^{\mathrm{T}} \mathbf{A}_2\right)^{-1} \mathbf{A}_2^{\mathrm{T}} \mathbf{b}_2 \tag{3.3}$$

Identification of $\mathbf{x}_2$ with combined effect of spin speeds $\omega_1, \omega_2, ..., \omega_n$ (with the assumption that parameters are speed independent) may be written as

$$\begin{bmatrix} \mathbf{A}_{2(\omega_1)} \\ \mathbf{A}_{2(\omega_2)} \\ \vdots \\ \mathbf{A}_{2(\omega_n)} \end{bmatrix} \mathbf{x}_2 = \begin{Bmatrix} \mathbf{b}_{2(\omega_1)} \\ \mathbf{b}_{2(\omega_2)} \\ \vdots \\ \mathbf{b}_{2(\omega_n)} \end{Bmatrix} \tag{3.4}$$

Estimation of parameters mentioned in vector $\mathbf{x}_2$ can be performed experimentally through above regression equation with the help of full spectrum responses.

3.6 Estimation of Rotor System Parameters

The estimated full spectrum amplitude and phase with phase compensation and after removing bow effect and sensor gap are used for identification of rotor fault parameters using Equations (3.3) and(3.4). Estimated parameters of cracked rotor system are shown in Table 3.9 for different combined spin speeds, i.e. 17-19 Hz, 20-22 Hz and 17-22 Hz. Present algorithm uses least-squares fit so with a single speed data due to lack of sufficient system information in the signal, estimates are deviating. But when more system information is given in the form of signals at multiple speeds then estimates are more accurate and stable. It is always preferred to give more information for better estimates of system parameters. From Table 3.9, estimation of rotor fault parameters such as disc eccentricity varies between 1.13×10^{-3} m to 1.31×10^{-3} m, whereas unbalance phase -161.99 deg. to -159.25 deg., internal damping varies between 42.36 Ns/m to 64.93 Ns/m, external damping varies between 781.42 Ns/m to 959.58 Ns/m, and additive crack stiffness coefficients corresponding to multiple harmonics are shown in Table 3.9. It is observed that internal damping parameter, c_H, varies between 42.36 Ns/m to 64.93 Ns/m for combined spin speed estimation cases, which has an increasing trend for higher speeds. Effect of internal stresses on cracked portion is low when the operating speed of the rotor is low and hence, internal damping value is lower for slow speed case as illustrated by (Smith and Birchak, 1968) also. It is expected that effect of shaft internal damping is insignificant due to a relatively moderate speed.

Table 3.9 Estimated experimental parameters

Parameters	17, 18 and 19 Hz combined speed	20, 21 and 22 Hz combined speed	17 to 22 Hz combined speed (All)
$c_E(10^2\ \mathrm{Nsm^{-1}})$	9.59	7.81	8.24
$c_H(\mathrm{Nsm^{-1}})$	42.36	64.93	55.16
$e\ (10^{-3}\ \mathrm{m})$	1.31	1.21	1.14
$\phi\ (10^2\ \mathrm{deg})$	-1.59	-1.62	-1.59
$\Delta k_\xi p_0(10^5\ \mathrm{Nm^{-1}})$	1.82	1.70	1.76
$\Delta k_\xi p_1(10^5\ \mathrm{Nm^{-1}})$	2.38	2.22	1.80
$\Delta k_\xi p_2(10^5\ \mathrm{Nm^{-1}})$	-1.58	-1.52	-1.52
$\Delta k_\xi p_3(10^4\ \mathrm{Nm^{-1}})$	-1.72	2.78	0.64
$\Delta k_\xi p_5(10^4\ \mathrm{Nm^{-1}})$	-2.46	-1.61	-1.95
$\Delta k_\xi p_7(10^3\ \mathrm{Nm^{-1}})$	-7.00	-6.40	-6.38
$\Delta k_\xi p_{-1}(10^5\ \mathrm{Nm^{-1}})$	-1.38	-1.37	-1.35
$\Delta k_\xi p_{-3}(10^4\ \mathrm{Nm^{-1}})$	-2.87	-2.03	-2.45
$\Delta k_\xi p_{-5}(10^3\ \mathrm{Nm^{-1}})$	3.36	3.00	3.06

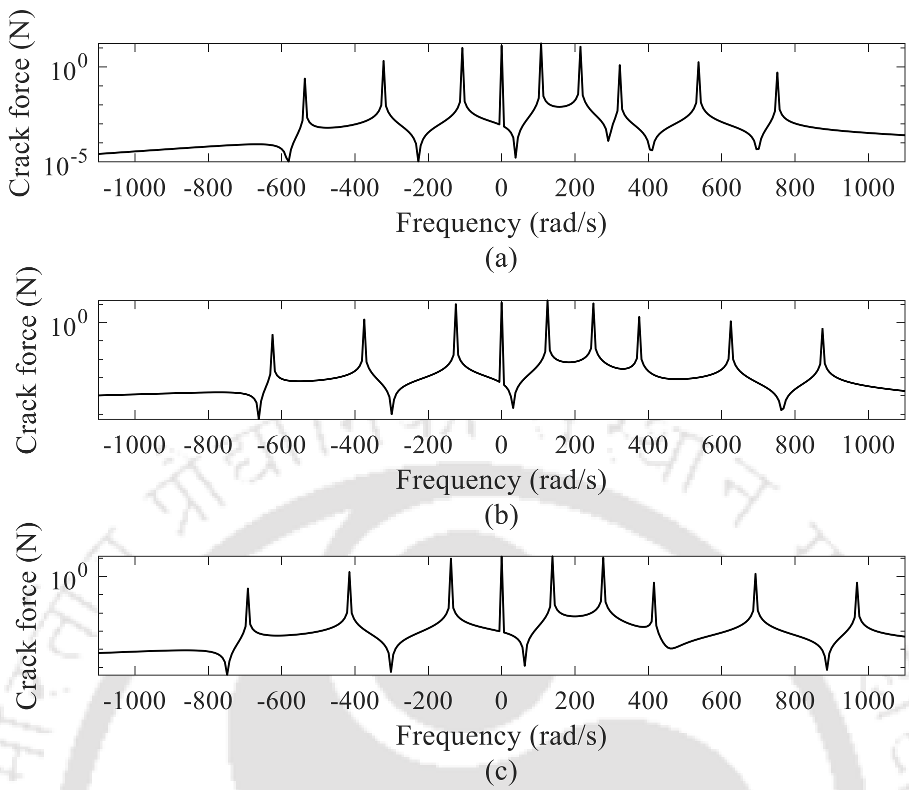

Figure3.26 Full spectrum amplitude of crack force at (a) 17 Hz spin speed (b) 20 Hz spin speed and (c) 22 Hz spin speed

Product of crack stiffness parameter and participation factor ($\Delta k_{\xi} p_i$) obtained (refer Table 3.9) is utilized to generate crack force based on Equation (2.19) and is shown in Figure 3.26. In Figure 3.26(a), full spectrum of crack force at 17 Hz is shown by utilizing the estimated $\Delta k_{\xi} p_i$ for combined speeds of 17, 18 and 19 Hz. Similarly, in Figures 3.26(b) and 3.26(c) full spectrum crack forces at 20 and 22 Hz, respectively, are shown by utilizing the estimated $\Delta k_{\xi} p_i$ for combined speeds mentioned in the second and third columns of Table 3.9. As seen from Figures 3.26(a-c), the crack force appears to varying in similar manner with change in rotor spin speeds.

3.7 Validation of Updated Model

The proposed algorithm for estimation of the internal and external damping, additive crack stiffness and unbalance is tested with actual experimental data from a rotor test rig designed and developed in the laboratory. Rotor system responses were measured at disc location (which was mounted at middle of shaft) for rotor speeds, such as 3 Hz (slow run) and 17 Hz through 22 Hz. Figures 3.13-3.15 are corresponding to measured raw signal without any filtering. However, Figures 3.23-3.26 are corresponding to measured signal with removal of bow effect and sensor gaps. Figures 3.23(a)-3.25(a) are experimentally measured signals after bow and sensor gaps removal according to Equation (3.1) without additional signal processing, i.e. noise and -2X harmonic response are now seen. But Figures 3.23(b)-3.25(b) are generated from numerical simulation based on parameters identified and mentioned in Table 3.9 from experimental responses and it is for validation. Herein, noise is absent and -2X harmonic response are not seen due model chosen for the switching crack function, It also applies to Figure 3.26 when switching crack force is shown. For validation purpose, system responses are generated through a numerical simulation (based on the SIMULINK model) using experimentally identified parameters for combined speeds as mentioned in Table 3.9. Full spectrum of system responses obtained for 17 Hz, 20 Hz and 22 Hz through numerical simulation are shown in Figures 3.23(b)-3.25(b). These are compared with those obtained from experimentation at respective speeds, as shown in Figures 3.23(a)-3.25(a). In Figure 3.23(b), larger amplitudes of full spectrum responses for 17 Hz speed are found to be 4.9×10^{-5} m at 0X, 5.5×10^{-5} m at 1X and 4.2×10^{-5}m at-1X. Whereas, in Figure 3.23(a), larger amplitudes are found to be 5.2×10^{-5} m at 0X, 5.3×10^{-5} m at 1X and 4.5×10^{-5}m at -1X. It shows that amplitudes of system responses are approximately same for both numerical simulation and experimental analysis. This is due to closeness of theoretical cracked rotor model with experimental rig as well as close fitting of experimental data with theoretical model during parameter estimation. Similarly, for spin speeds of 20 and 22 Hz, amplitudes of full spectrum are also similar as shown in Figures 3.24 and 3.25. In Figures 3.23(a) to 3.25(a) bow effect and sensor gaps were removed with slow roll data. This signal processing was done in frequency domain and leakage error was minimized by taking integer number of complete cycles of signals, and hence noise effect is minimum. In comparison to numerically simulated responses in Figures 3.23(b) through3.25(b), which is based on the use of experimentally estimated parameters in numerical model, amplitudes of system responses have similar pattern for both and are present at all harmonics. This shows closeness of updated numerical model with experimental test rig. This is due to a precise estimation of rotor system parameters during experimental identification process. This verifies the correctness of model based identification algorithm for estimation of the internal and external damping, additive crack stiffness, and unbalance.

For finding out location and depth of crack, fracture mechanics approach has already been used in refs.(Varney and Green, 2013, Karthikeyan et al., 2007; Karthikeyan and Tiwari 2010, and Singh and Tiwari, 2014). But the present work focuses on the crack characterization in terms of its additive stiffness and internal damping along with other system parameters. The system seems to be a simple model, but it covers a wide range of faults present in cracked rotor system. With 4-DOFs or the finite element modeling, more complex rotor-bearing system can be modelled more accurately, but present methodology would remain same for more accurate crack characterization.

3.8 Conclusions

The experimental investigation of internal damping is linked with detection of the additive crack presented in the present chapter. The change in the internal damping is an indicator of rubbing of crack indication. The crack develops internal damping inside the shaft surface that is reflect in the as rubbing of crack surfaces and show in the form of the internal damping. Additionally, obtained internal damping can be used to predict instable behaviour. To prevent such instable behavior the non-rotating damping to be provided by external dampers, for example squeeze-film damper, could be designed. The experimental identification of fault parameters, such as internal damping and external damping, unbalance and additive stiffness of a rotor bearing system is presented. The measured responses converted into full spectrum are used in the developed identification algorithm discussed in Chapter 2 for estimation of different fault parameters.

The following are the conclusions drawn from the present chapter

- The full spectrum amplitude and phase are compared using both regression and FFT based method found to be quite similar.
- The shaft residual bow and sensor gap present in the rotor system highly affects the amplitude of vibration and is removed using the first and zeroth harmonic of spin speed of the rotor for accurate estimation of the parameters. The orbit plots of measured responses with bow and sensor gap and after removal of bow and sensor gap are compared.
- The estimated fault parameters through the developed identification algorithm are used in the numerical simulation and find its viability in the full spectrum response.
- The behavior of crack force by the estimated additive stiffness and participation factors are studied.

Analysis of rotor system with an offset disc is discussed in the next chapter with the inclusion gyroscopic effects. The identification algorithm will be developed and tested its sensitivity through numerical simulation.

CHAPTER 4

Model-based identification of internal and external damping of a cracked rotor system with gyroscopic effects

Complexity of procedure for the estimation of internal damping in rotor system with an offset disc increases due to presence of gyroscopic effects. For thiscase, apart from translational DOFs, rotational DOFs also appear in EOMs. Difficulty comes in developing identification algorithm since now rotational DOFs also need to be measured along with translational DOFs, which is difficult to measure accurately. To overcome this difficulty dynamic condensation with some modification (Prasad and Tiwari, 2019) is applied to eliminate rotational DOFs from EOMs before developing identification methodology. Numerical testing of identification methodology is performed with noise in responses and bias error is system parameters.

4.1 Introduction

In the present work, a procedure for the estimation of internal damping in a cracked rotor system with an offset disc is described. The offset disc incorporates the rotary and translatory inertia, and hence gyroscopic effect of the disc is also considered. A rotor with crack during fatigue loading have rubbing action between two crack faces, which contributes to the internal damping. The estimation of internal damping can also be an indicator of the presence of a crack. The transverse crack is modelled based on the switching crack assumption, which gives multiple harmonics excitation to the rotor system. Moreover, due to the crack asymmetry, multiple harmonic excitations lead to the forward and backward whirls in rotor orbits. Based on equations of motion derived in the frequency domain (full spectrum), an estimation procedure is evolved based on only translational displacements to identify the internal and external damping, the additive crack stiffness and unbalance of the rotor system. Numerically the identification procedure is tested using noisy responses and bias errors in system parameters.

4.2 Cracked rotor system model

This section presents the derivation of EOMs of a cracked rotor with an offset disc. The rotor consists of a crack shaft incorporating internal damping due to crack and the gyroscopic effect owing to the offset disc. Moreover, it includes the external damping and unbalance. The generation of numerical responses and its analysis in full spectrum has been also been described.

This section presents the derivation of EOMs of a cracked rotor with an offset disc. The rotor consists of a crack shaft incorporating internal damping due to crack and the gyroscopic effect owing to the offset disc. Moreover, it includes the external damping and unbalance. The generation of numerical responses and its analysis in full spectrum has been also been described.

4.2.1 Configuration of rotor model and equations of motion

In this work, a simple rotor model configuration is considered with a transverse crack near the offset disc as shown in Figure 4.1. Support bearings at both ends are assumed to be transversely rigid, which allow rotation of the shaft. Point O is the origin on the bearing axis and near the disc, z is bearing axis and x is vertical axis in downward direction (along the direction of gravity). Let mg be the weight of the disc, φ_{y0} represent the initial (static) tilting of disc and u_{x0} is the static translational displacement of the disc. Rotating coordinate axes are ξ and η as in Chapter 2, and the crack front direction is considered along the ξ axis. Translational displacements of disc are shown in Figure 4.2 and is based on Figures 2.2 and 2.3 of Chapter 2. Similarly, ω be the shaft spin speed and t represents the time. Points C and G represent geometric centre and centre of gravity of disc, respectively. Let e be the radial eccentricity of the disc, which is the distance between points C and G, and ϕ is the phase angle between the unbalance force and the crack front direction (i.e., ξ axis direction). Forces due the internal damping (c_H), external damping (c_E) and gravity are shown in Figure 4.2.

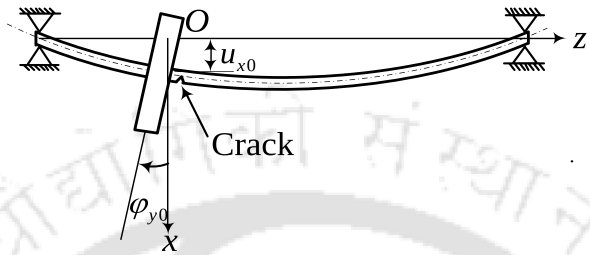

Figure4.1 A simple rotor with an offset disc in the presence of a transverse crack in static condition

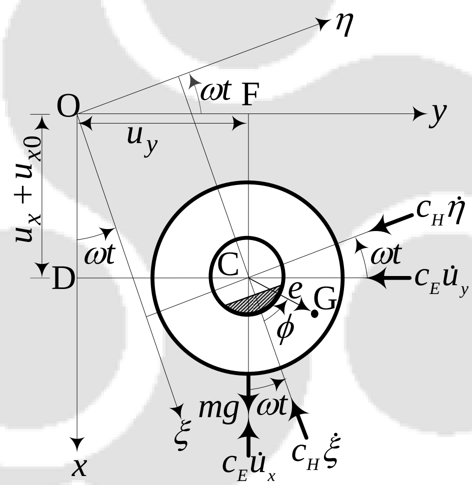

Figure 4.2 The rotor with unbalance, self-weight, internal and external damping forces and displacement (x=u_x+u_{x0} and y=u_y) with respect to the fixed and rotating frame of references

EOMs of the rotor with the cracked shaft and offset disc considering of gyroscopic effects, however, without internal damping is given as (Shravankumar, 2014)

$$\mathbf{M}\ddot{\mathbf{q}}(t) + \left(\mathbf{C}_E - \omega\mathbf{G}\right)\dot{\mathbf{q}}(t) + \left(\mathbf{K} - \Delta\mathbf{K}\left(\mathbf{u},\mathbf{t}\right)\right)\mathbf{q}(t) = \mathbf{f}_{st} + \mathbf{f}_{unb}(t) \qquad (4.1)$$

with,

$$\mathbf{M}=\begin{bmatrix} m & 0 & 0 & 0 \\ & m & 0 & 0 \\ & & I_d & 0 \\ \text{sym} & & & I_d \end{bmatrix};\ \mathbf{C}_E=\begin{bmatrix} c_{22} & 0 & c_{24} & 0 \\ 0 & c_{33} & 0 & c_{35} \\ c_{42} & 0 & c_{44} & 0 \\ 0 & c_{53} & 0 & c_{55} \end{bmatrix};\ \mathbf{K}=\begin{bmatrix} k_{22} & 0 & k_{24} & 0 \\ & k_{33} & 0 & k_{35} \\ & & k_{44} & 0 \\ \text{sym} & & & k_{55} \end{bmatrix};$$

$$\mathbf{G}=\begin{bmatrix} 0 & 0 & 0 & 0 \\ 0 & 0 & 0 & 0 \\ 0 & 0 & 0 & I_p \\ 0 & 0 & -I_p & 0 \end{bmatrix};\ \mathbf{f}_{unb}=\begin{Bmatrix} me\omega^2\cos(\omega t+\phi) \\ me\omega^2\sin(\omega t+\phi) \\ 0 \\ 0 \end{Bmatrix};\ \mathbf{f}_{st}=\begin{Bmatrix} mg \\ 0 \\ 0 \\ 0 \end{Bmatrix};\ \mathbf{q}=\begin{Bmatrix} x \\ y \\ \varphi_y \\ \varphi_x \end{Bmatrix} \text{ and } \mathbf{q}=\mathbf{q}_v+\mathbf{q}_0$$

Here $\mathbf{M}$, $\mathbf{C_E}$, $\mathbf{G}$, and $\mathbf{K}$ are the mass matrix, external damping matrix, gyroscopic matrix, and stiffness matrix, respectively. In addition, the matrix $\Delta\mathbf{K}_\xi$ is the flexibility matrix owing to the crack and details of it is discussed in the next section. Vectors $\mathbf{f}_{st}$ and $\mathbf{f}_{unb}$ are force vectors owing to the static deflection and the unbalance, respectively; $\mathbf{q}$ is the vector of displacement, and $\dot{\mathbf{q}}$ and $\ddot{\mathbf{q}}$ are the first and second time derivatives of $\mathbf{q}$. Also, m is the mass of disc, I_d is the diametral mass moment of inertia of the disc, I_p is the polar mass moment of inertia of the disc, c_{ij} and k_{ij} represent the external viscous damping and the shaft stiffness in the rotor system, respectively. Subscripts i and j can take values 2, 3, 4 or 5, where 2 and 3 represent shear force directions, and 4 and 5 represent moment directions (refer Figure 4.3). Whereas, 1 and 6 directions represent axial force and torque, respectively; and these effects have been ignored in the present study. Vector $\mathbf{q}_0$ contains the transverse translational and rotational displacements of the disc due to the gravity force, $\mathbf{q}_v$ contains the transverse translational and rotational displacements of the disc due to dynamic forces on the rotor.

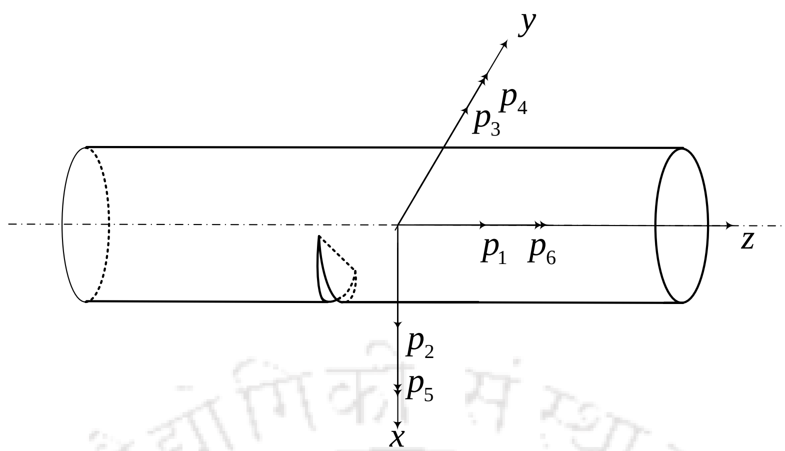

Figure 4.3 Various load directions across the transverse crack in a rotor element

4.2.2 Internal damping model

Internal damping comes on the shaft owing to rubbing of two faces of a crack, rubbing between disc and shaft, and due to hysteresis. Let the combined form of internal viscous damping factor is c_H. Forces due to these are shown in Figure 4.2 along with external viscous damping force. These forces in the stationary coordinate system can be written as

$$\mathbf{f}_{xd}(t) = c_H \dot{\xi} \cos(\omega t) - c_H \dot{\eta} \sin(\omega t) + c_E \dot{u}_x \tag{4.2}$$

and

$$\mathbf{f}_{yd}(t) = c_H \dot{\xi} \sin(\omega t) + c_H \dot{\eta} \cos(\omega t) + c_E \dot{u}_y \tag{4.3}$$

On combining damping forces in the complex form, we get

$$\mathbf{f}_d(t) = \mathbf{f}_{xd}(t) + \mathrm{j}\mathbf{f}_{yd}(t) \tag{4.4}$$

On using Equations (4.2) and (4.3) in Equation (4.4), we get

$$\mathbf{f}_{cd}(t) = c_H \dot{\zeta}\, \mathrm{e}^{\mathrm{j}\omega t} + c_E \dot{r} \tag{4.5}$$

Defining $\zeta = \xi + \mathrm{j}\,\eta$ as the complex displacement in a rotating coordinate system with $\mathrm{j}=\sqrt{-1}$, and $r = x + \mathrm{j}y$ as the complex displacement in the stationary coordinate system. This gives $\dot{\zeta}=\dot{\xi}+\mathrm{j}\dot{\eta}$ and $\dot{r}=\dot{x}+\mathrm{j}\dot{y}$ as the derivatives of complex displacements. The transformation from the stationary coordinate system to the rotating coordinate system is given as $\zeta = re^{-\mathrm{j}\omega t}$ with $\dot{\zeta}=\left(\dot{r}-\mathrm{j}\omega r\right)\mathrm{e}^{-\mathrm{j}\omega t}$. Hence, the damping force takes in the following form

$$\mathbf{f}_{cd}(t) = c_H\left(\dot{r}-\mathrm{j}\omega r\right)+c_E\dot{r} \tag{4.6}$$

Equation (4.6) in expanded form, it takes the following form

$$\mathbf{f}_{cd}(t)=\begin{bmatrix} c_E+c_H & 0 & 0 & 0 \\ 0 & c_E+c_H & 0 & 0 \\ 0 & 0 & 0 & 0 \\ 0 & 0 & 0 & 0 \end{bmatrix}\begin{Bmatrix} \dot{x} \\ \dot{y} \\ \dot{\varphi}_y \\ \dot{\varphi}_x \end{Bmatrix}+\omega\begin{bmatrix} 0 & c_H & 0 & 0 \\ -c_H & 0 & 0 & 0 \\ 0 & 0 & 0 & 0 \\ 0 & 0 & 0 & 0 \end{bmatrix}\begin{Bmatrix} x \\ y \\ \varphi_y \\ \varphi_x \end{Bmatrix} \tag{4.7}$$

Herein, it is assumed that $c_{22}= c_{33}= c_E$ and the value of c_{44}, c_{55}, c_{35}, c_{24}, c_{42}, and c_{53} are taken to be zero. On including the internal damping, the system of Equation (4.1) takes the following form

$$\mathbf{M}\ddot{\mathbf{q}}+\left(\mathbf{C}_E+\mathbf{C}_H - \omega\mathbf{G}\right)\dot{\mathbf{q}}+\left(\omega\mathbf{C}_{1H}+\mathbf{K}-\Delta\mathbf{K}\left(s,t\right)\right)\mathbf{q}=\mathbf{f}_{st}+\mathbf{f}_{unb}(t) \tag{4.8}$$

Where,

$$\mathbf{C}_E=\begin{bmatrix} c_E & 0 & 0 & 0 \\ 0 & c_E & 0 & 0 \\ 0 & 0 & 0 & 0 \\ 0 & 0 & 0 & 0 \end{bmatrix};\quad \mathbf{C}_H=\begin{bmatrix} c_H & 0 & 0 & 0 \\ 0 & c_H & 0 & 0 \\ 0 & 0 & 0 & 0 \\ 0 & 0 & 0 & 0 \end{bmatrix}\text{ and }\quad \mathbf{C}_{1H}=\begin{bmatrix} 0 & c_H & 0 & 0 \\ -c_H & 0 & 0 & 0 \\ 0 & 0 & 0 & 0 \\ 0 & 0 & 0 & 0 \end{bmatrix}$$

We have $\mathbf{q}(t)= \mathbf{q}_v(t)+ \mathbf{q}_0$, so that $\dot{\mathbf{q}}(t)= \dot{\mathbf{q}}_v(t)$ and $\ddot{\mathbf{q}}(t)= \ddot{\mathbf{q}}_v(t)$. Equation (4.8) takes the following form

$$\mathbf{M}\ddot{\mathbf{q}}_v + \left(\mathbf{C} + \mathbf{C}_H - \omega\mathbf{G}\right)\dot{\mathbf{q}}_v + \left(\omega\mathbf{C}_{1H} + \mathbf{K}\right)\mathbf{q}_v = \Delta\mathbf{K}\left(s,t\right)\left(\mathbf{q}_v + \mathbf{q}_0\right) - \omega\mathbf{C}_{1H}\mathbf{q}_0 + \mathbf{f}_{unb}(t) \tag{4.9}$$

with, $\mathbf{Kq}_0=\mathbf{f}_{st}$, for the static condition and detail of it is given as

$$\begin{bmatrix} k_{22} & 0 & k_{24} & 0 \\ & k_{33} & 0 & k_{35} \\ & & k_{44} & 0 \\ \text{sym} & & & k_{55} \end{bmatrix} \begin{Bmatrix} u_{x0} \\ u_{y0} \\ \varphi_{y0} \\ \varphi_{x0} \end{Bmatrix} = \begin{Bmatrix} mg \\ 0 \\ 0 \\ 0 \end{Bmatrix} \tag{4.10}$$

After expanding Equation (4.10), we get

$$\left.\begin{aligned} u_{x0} &= \frac{mgk_{44}}{k_{44}k_{22} - k_{24}^2} \\ u_{y0} &= 0 \\ \varphi_{y0} &= \frac{mgk_{24}}{k_{24}^2 - k_{44}k_{22}} \\ \varphi_{x0} &= 0 \end{aligned}\right\} \text{ and } \mathbf{q}(t) = \mathbf{q}_v(t) + \mathbf{q}_0 \text{ where, } \mathbf{q}_v(t) = \begin{Bmatrix} u_x(t) \\ u_y(t) \\ \varphi_y(t) \\ \varphi_x(t) \end{Bmatrix} \text{ and } \mathbf{q}_0 = \begin{Bmatrix} u_{x0} \\ 0 \\ \varphi_{y0} \\ 0 \end{Bmatrix} \tag{4.11}$$

Based on the weight dominance, in Equation (4.9), the terms $\mathbf{q}_v(t)$ in right-hand side can be ignored as compared to the static deflection, $\mathbf{q}_0$. It is because $\mathbf{q}_0$ is much larger than $\mathbf{q}_v(t)$ owing to the heavy weight of the rotor (Singh and Tiwari, 2016). Hence, the modified EOM is

$$\mathbf{M}\ddot{\mathbf{q}}_v + \left(\mathbf{C} + \mathbf{C}_H - \omega\mathbf{G}\right)\dot{\mathbf{q}}_v + \left(\omega\mathbf{C}_{1H} + \mathbf{K}\right)\mathbf{q}_v = \Delta\mathbf{K}\left(s,t\right)\mathbf{q}_0 - \omega\mathbf{C}_{1H}\mathbf{q}_0 + \mathbf{f}_{unb}(t) \tag{4.12}$$

4.2.3 Model of the Crack

The load (forces and moments) direction based on a transverse crack representation is shown in Figure 4.3. The additional flexibility matrix because of the crack, on the basis of the fracture mechanics approach, is generally used as a crack model (Dimarogonas, 1996; Singh and Tiwari, 2016). The time dependent additive crack has the following form

$$\Delta\mathbf{K}'_{rot}\left(t\right) = \sigma\left(t\right)\Delta\mathbf{K}'_{rot} \tag{4.13}$$

Where,

$$\mathbf{\Delta K}_{rot}^{'} = \begin{bmatrix} \Delta k_{22} & 0 & 0 & 0 \\ 0 & 0 & 0 & 0 \\ 0 & 0 & \Delta k_{44} & 0 \\ 0 & 0 & 0 & 0 \end{bmatrix}$$

Shaft stiffness in closed condition of the crack is $\mathbf{K}_{rot}^{'}$ (which is same as intact shaft stiffness) and for crack open condition the stiffness is $\mathbf{K}_{rot}^{'}$-$\mathbf{\Delta K}_{rot}^{'}$. Here, $\mathbf{\Delta K}_{rot}^{'}$is the additive crack stiffness, which comes into picture when the crack is in open condition. In rotating shaft, $\mathbf{\Delta K}_{rot}^{'}$ is not considered when crack is in closed condition and is subtracted only in its open condition. Thus, representing a switch on-off mode of the crack, which is a time-dependent phenomenon. To model this behavior, a switching crack model of an additive stiffness excitation function is chosen based on Fourier-series (Gasch, 2008). It considers a switching crack excitation function (SCEF) as $\sigma(t)$, which is used in Chapter 2 in Equation (2.5). The stiffness matrix of intact shaft, crack stiffness matrix and force vector are expressed in the stationary frame of reference, as

$$\mathbf{K}^{'} = \mathbf{T}^{T}\mathbf{K}_{rot}^{'}\mathbf{T}; \quad \mathbf{\Delta K}^{'}\left(t\right) = \mathbf{T}^{T}\Delta\mathbf{K}_{rot}^{'}\mathbf{T} \quad \text{and} \quad \mathbf{f}_{cr}(t) = \sigma\left(t\right)\mathbf{\Delta K}^{'}\left(t\right)\mathbf{q}_{0} \tag{4.14}$$

with,

$$\mathbf{T} = \begin{bmatrix} \cos\varphi_z & \sin\varphi_z & 0 & 0 \\ -\sin\varphi_z & \cos\varphi_z & 0 & 0 \\ 0 & 0 & \cos\varphi_z & \sin\varphi_z \\ 0 & 0 & -\sin\varphi_z & \cos\varphi_z \end{bmatrix}$$

Which can be written in expanded form, as

$$\mathbf{f}_{cr}(t) = \frac{1}{2}\sigma\left(t\right)\begin{Bmatrix} \Delta k_{22}\left(1+\cos 2\omega t\right)u_{x0} \\ \Delta k_{22}\sin\left(2\omega t\right)u_{x0} \\ \Delta k_{44}\left(1+\cos 2\omega t\right)\varphi_{y0} \\ \Delta k_{44}\sin\left(2\omega t\right)\varphi_{y0} \end{Bmatrix} \tag{4.15}$$

Noting Equations (4.12)and (4.15), the EOM takes the following form

$$\mathbf{M}\ddot{\mathbf{q}}_v + \left(\mathbf{C} + \mathbf{C}_H - \omega\mathbf{G}\right)\dot{\mathbf{q}}_v + \left(\omega\mathbf{C}_{1H} + \mathbf{K}\right)\mathbf{q}_v = \mathbf{f}_{cr}(t) - \omega\mathbf{C}_{1H}\mathbf{q}_0 + \mathbf{f}_{unb}(t) \tag{4.16}$$

Equation (4.16) in the complex form can be expressed, as

$$\bar{\mathbf{M}}\ddot{\mathbf{v}} + \left(\bar{\mathbf{C}} + \bar{\mathbf{C}}_H - \mathrm{j}\omega\bar{\mathbf{G}}\right)\dot{\mathbf{v}} + \left(\bar{\mathbf{K}} - \mathrm{j}\omega\bar{\mathbf{C}}_H\right)\mathbf{v} = \bar{\mathbf{f}}_{cr}(t) + \bar{\mathbf{f}}_{unb}(t) + \mathrm{j}\omega c_H \begin{Bmatrix} u_{x0} \\ 0 \end{Bmatrix} \tag{4.17}$$

with

$$r = u_x + \mathrm{j}u_y\,;\ \varphi = \varphi_y + \mathrm{j}\varphi_x\,; \qquad \left(-I_p\omega\dot{\varphi}_x\right) + \mathrm{j}\left(I_p\omega\dot{\varphi}_y\right) = \mathrm{j}I_p\omega\dot{\varphi}\,; \qquad \omega c_H u_y - \mathrm{j}\omega c_H u_x = -\mathrm{j}\omega c_H r\,;$$

$$u_{x0} + \mathrm{j}u_{y0} = r_0 \mathrm{e}^{\mathrm{j}\theta}\,;\ \bar{\mathbf{M}} = \begin{bmatrix} m & 0 \\ 0 & I_d \end{bmatrix};\ \bar{\mathbf{C}} = \begin{bmatrix} c_E & 0 \\ 0 & 0 \end{bmatrix};\ \bar{\mathbf{C}}_H = \begin{bmatrix} c_H & 0 \\ 0 & 0 \end{bmatrix};\ \bar{\mathbf{G}} = \begin{bmatrix} 0 & 0 \\ 0 & -I_p \end{bmatrix};\ \bar{\mathbf{K}} = \begin{bmatrix} k_{22} & k_{23} \\ k_{32} & k_{33} \end{bmatrix}$$

$$;\ \mathbf{v}(t) = \begin{Bmatrix} r(t) \\ \varphi(t) \end{Bmatrix};\ \bar{\mathbf{f}}_{cr}(t) = \frac{1}{2}\sigma(\mathrm{t}) \begin{Bmatrix} \Delta k_{22} u_{x0}\left(1+\mathrm{e}^{2\mathrm{j}\omega t}\right) \\ \Delta k_{44}\varphi_{y0}\left(1+\mathrm{e}^{2\mathrm{j}\omega t}\right) \end{Bmatrix} \text{ and } \bar{\mathbf{f}}_{unb}(t) = \begin{Bmatrix} me\omega^2 \mathrm{e}^{\mathrm{j}(\omega t+\phi)} \\ 0 \end{Bmatrix}$$

In crack force expression, following term is expressed in a series of multiple harmonics through Equation (2.5), as

$$\begin{aligned} \frac{1}{2}\sigma(t)\left(1+\mathrm{e}^{2\mathrm{j}\omega t}\right) &= 0.25 + 0.319\mathrm{e}^{\mathrm{j}\omega t} + 0.25\mathrm{e}^{2\mathrm{j}\omega t} + 0.106\mathrm{e}^{3\mathrm{j}\omega t} - 0.021\mathrm{e}^{5\mathrm{j}\omega t} \\ &\quad + 0.009\mathrm{e}^{7\mathrm{j}\omega t} + 0.106\mathrm{e}^{-\mathrm{j}\omega t} - 0.021\mathrm{e}^{-3\mathrm{j}\omega t} + 0.009\mathrm{e}^{-5\mathrm{j}\omega t} + \cdots \end{aligned} \tag{4.18}$$

Equation (4.18), in a notational form, is expressed as

$$\frac{1}{2}\sigma(t)\left(1+\mathrm{e}^{2j\omega t}\right) = \sum_{i=-n}^{i=n} p_i \mathrm{e}^{ji\omega t} \tag{4.19}$$

In Equation (4.19) , p_i denotes the coefficient of i^{th} term in harmonic function of the crack force excitation, also called as the *participation factor* of individual harmonics. Coefficients are small for higher order harmonics and they do not depend on crack depth, for whole range of $t_c/R<0.5$, where, t_c is the crack depth and R is the radius of the shaft. This is an assumption for hinge model of the crack (Gasch, 2008). Then, the crack force takes the following form

$$\bar{\mathbf{f}}_{cr}(t) = \begin{Bmatrix} \Delta k_{22} u_{x0} \\ \Delta k_{44} \varphi_{y0} \end{Bmatrix} \sum_{i=-n}^{i=n} p_i \mathrm{e}^{\mathrm{j}i\omega t} \tag{4.20}$$

Hence, the solution of Equation (4.17) will be of the following form

$$\mathbf{v}(t) = \sum_{i=-n}^{i=n} \bar{\mathbf{v}}_i \mathrm{e}^{\mathrm{j}i\omega t} \tag{4.21}$$

Hence, noting above equations, the EOM (i.e., Equation (4.17)) will be having following form in frequency domain

$$\left[-(i\omega)^2 \begin{bmatrix} m & 0 \\ 0 & I_d \end{bmatrix} + \mathrm{j}(i\omega) \left(\begin{bmatrix} c_E + c_H & 0 \\ 0 & 0 \end{bmatrix} + \mathrm{j}\omega \begin{bmatrix} 0 & 0 \\ 0 & I_p \end{bmatrix} \right) + \left(\begin{bmatrix} k_{22} & k_{23} \\ k_{32} & k_{33} \end{bmatrix} - \mathrm{j}\omega \begin{bmatrix} c_H & 0 \\ 0 & 0 \end{bmatrix} \right) \right] \bar{\mathbf{v}}_i = \mathbf{f}_i \tag{4.22}$$

with

$$\mathbf{f}_i = \begin{Bmatrix} \Delta k_{22} u_{x0} \\ \Delta k_{44} \varphi_{y0} \end{Bmatrix} \sum_{i=-n}^{i=n} p_i + \begin{Bmatrix} me\omega^2 \mathrm{e}^{\mathrm{j}\phi} \\ 0 \end{Bmatrix}_{i=1} + \mathrm{j}\omega c_H \begin{Bmatrix} u_{x0} \\ 0 \end{Bmatrix}_{i=0}$$

The force term $\mathbf{f}_i$ is represented in the following form

$$\left.\begin{aligned}
\mathbf{f}_0 &= \begin{Bmatrix} \Delta k_{22} u_{x0} \\ \Delta k_{44} \varphi_{y0} \end{Bmatrix} p_0 + \mathrm{j}\omega c_H \begin{Bmatrix} u_{x0} \\ 0 \end{Bmatrix} \quad \text{for } i=0 \\
\mathbf{f}_1 &= \begin{Bmatrix} \Delta k_{22} u_{x0} \\ \Delta k_{44} \varphi_{y0} \end{Bmatrix} p_1 + \begin{Bmatrix} me\omega^2 \mathrm{e}^{\mathrm{j}\phi} \\ 0 \end{Bmatrix} \quad \text{for } i=1 \\
\mathbf{f}_i &= \begin{Bmatrix} \Delta k_{22} u_{x0} \\ \Delta k_{44} \varphi_{y0} \end{Bmatrix} \sum_{i=-n}^{i=n} p_i \quad \text{for } i = 2,\ 3,\ 5,\ 7,\cdots\ -1,\ -3,\ -5,\ \cdots
\end{aligned}\right\} \tag{4.23}$$

Time domain responses of the system, $\mathbf{v}(t)$**,** is generated through integration of Equation (4.17). The forward and backward whirling of the rotor system, R_i, can be obtained through full spectrum of $\mathbf{v}(t)$.The full spectrum extraction from time domain signals and its application are presented in the next section.

4.3 Generation of Full Spectrum Responses

From Equation (4.21), the transverse displacement $\mathbf{v}(t)$ can be expanded based on Equation (2.22), as

$$\mathbf{v}(t) = R_0 + R_1 e^{j\omega t} + R_2 e^{2j\omega t} + R_3 e^{3j\omega t} + R_5 e^{5j\omega t} + \cdots + R_{-1} e^{-j\omega t} + R_{-3} e^{-3j\omega t} + R_{-5} e^{-5j\omega t} + \cdots \tag{4.24}$$

In above equation the aim is to obtain various terms, $R_0, R_1, R_{-1}, R_2, R_3, R_{-3}$,. It should be noted that these are complex quantities, and it gives amplitude and phase corresponding to various harmonics, ω, $-\omega$, 2ω, -3ω, …, which in graphical representation is called the full spectrum. Two procedures described in Chapter 2 to extract the full spectrum along with phase compensation has been utilized in the present work.

4.4 Identification of internal damping and other rotor parameters

In this section, an estimation procedure will be developed to estimate the rotor system parameters, like the internal damping, external damping, additive crack stiffness and unbalance, which are not possible to predict accurately by modeling. The developed procedure will use the system responses and some of the system parameters, like the mass of discs and stiffness of the shaft. The procedure will use the EOM Equation (4.22) to convert it to a regression form for estimation of the parameters. However, it contains the rotational DOFs, the measurement of such responses, in practice, is very difficult. To overcome this practical difficulty, the modified dynamic reduction scheme (Prasad and Tiwari, 2019) has been used in the identification procedure. This aspect was covered in Chapter 2.

4.4.1 Application of the Dynamic Reduction Scheme

With this scheme, rotational DOFs are eliminated. In Equation (4.22), the translational and rotational DOFs are considered as the master and slave DOFs, respectively. The master and slave are represented with subscripts *m* and *s*, respectively. The crack force in right side of Equation (4.22) due to rotational DOFs can be neglected in developing the transformation. The partitioned form of the equation takes the following form

$$\left(\begin{array}{l} -(i\omega)^2\begin{bmatrix}\mathbf{M}_{mm} & 0\\ 0 & \mathbf{M}_{ss}\end{bmatrix} + \mathrm{j}(i\omega)\left(\begin{bmatrix}\mathbf{C}_{mm} & \mathbf{C}_{ms}\\ \mathbf{C}_{sm} & \mathbf{C}_{ss}\end{bmatrix} - \mathrm{j}\omega\begin{bmatrix}0 & 0\\ 0 & \mathbf{G}_{ss}\end{bmatrix}\right) \\ +\left(\begin{bmatrix}\mathbf{K}_{mm} & \mathbf{K}_{ms}\\ \mathbf{K}_{sm} & \mathbf{K}_{ss}\end{bmatrix} - \mathrm{j}\omega\begin{bmatrix}\mathbf{C}_{\mathbf{H}_{mm}} & 0\\ 0 & 0\end{bmatrix}\right)\end{array}\right)\begin{Bmatrix}\mathbf{Q}_{mm}\\ \mathbf{Q}_{ss}\end{Bmatrix} = \begin{Bmatrix}\mathbf{f}_i\\ \mathbf{0}\end{Bmatrix} \tag{4.25}$$

where various matrices are given as

$$\left.\begin{array}{l} \begin{bmatrix}\mathbf{M}_{mm} & 0\\ 0 & \mathbf{M}_{ss}\end{bmatrix} = \begin{bmatrix}m & 0\\ 0 & I_d\end{bmatrix};\ \begin{bmatrix}\mathbf{C}_{mm} & \mathbf{C}_{ms}\\ \mathbf{C}_{sm} & \mathbf{C}_{ss}\end{bmatrix} = \begin{bmatrix}c_E & 0\\ 0 & 0\end{bmatrix};\ \begin{bmatrix}0 & 0\\ 0 & \mathbf{G}_{ss}\end{bmatrix} = \begin{bmatrix}0 & 0\\ 0 & -I_p\end{bmatrix}; \\ \begin{bmatrix}\mathbf{K}_{mm} & \mathbf{K}_{ms}\\ \mathbf{K}_{sm} & \mathbf{K}_{ss}\end{bmatrix} = \begin{bmatrix}k_{22} & k_{23}\\ k_{32} & k_{33}\end{bmatrix};\begin{bmatrix}\mathbf{C}_{H_{mm}} & 0\\ 0 & 0\end{bmatrix} = \begin{bmatrix}c_H & 0\\ 0 & 0\end{bmatrix};\ \begin{Bmatrix}\mathbf{Q}_{mm}\\ \mathbf{Q}_{ss}\end{Bmatrix} = \begin{Bmatrix}\mathbf{R}_i\\ \mathbf{\Phi}_i\end{Bmatrix} \text{ and} \\ \begin{Bmatrix}\mathbf{f}_i\\ \mathbf{0}\end{Bmatrix} = \begin{Bmatrix}\Delta k_{22}u_{x0}\sum\limits_{i=-n}^{i=n} p_i\\ 0\end{Bmatrix} + \begin{Bmatrix}me\omega^2\mathrm{e}^{\mathrm{j}\phi}\\ 0\end{Bmatrix}_{i=1} + \begin{Bmatrix}\omega c_H u_{x0}\mathrm{e}^{\mathrm{j}\frac{\pi}{2}}\\ 0\end{Bmatrix}_{i=0} \end{array}\right\} \tag{4.26}$$

The dynamic condensation transformation matrix, $\mathbf{T}^{\mathrm{D}}$, is obtained as (Prasad and Tiwari, 2019).

$$\mathbf{Q}_{mm} = \mathbf{I}\mathbf{Q}_{mm}\ ;\quad \begin{Bmatrix}\mathbf{Q}_{mm}\\ \mathbf{Q}_{ss}\end{Bmatrix} = \mathbf{T}^{\mathbf{D}}\mathbf{Q}_{mm} \tag{4.27}$$

with

$$\mathbf{T}^D = \begin{Bmatrix}I\\ L_i\end{Bmatrix} \text{where } L_i = \frac{-\mathbf{K}_{sm}}{\mathbf{K}_{ss} + i\omega^2\mathbf{G}_{ss} - (i\omega)^2\mathbf{M}_{ss}}$$

Herein ω is assumed to be the central frequency within the range of frequency of interest. Using this transformation and including of the crack force due to rotational DOFs in Equation(4.25), we get

$$\left(\mathbf{T}^{D}\right)^{T}\begin{bmatrix} -\left(i\omega\right)^{2}\begin{bmatrix} m & 0 \\ 0 & I_{d} \end{bmatrix} + i\mathrm{j}\omega\begin{bmatrix} c_{E} & 0 \\ 0 & 0 \end{bmatrix} + \\ \left(i-1\right)\mathrm{j}\omega\begin{bmatrix} c_{H} & 0 \\ 0 & 0 \end{bmatrix} + i\omega^{2}\begin{bmatrix} 0 & 0 \\ 0 & -I_{p} \end{bmatrix} + \begin{bmatrix} k_{22} & k_{23} \\ k_{32} & k_{33} \end{bmatrix} \end{bmatrix}\mathbf{T}^{D}\mathbf{Q}_{mm}$$
$$= \left(\mathbf{T}^{D}\right)^{T}\left(\begin{Bmatrix} \Delta k_{22}u_{x0} \\ \Delta k_{44}\varphi_{y0} \end{Bmatrix}\sum_{i=-n}^{i=n} p_{i} + \begin{Bmatrix} me\omega^{2}\mathrm{e}^{\mathrm{j}\phi} \\ 0 \end{Bmatrix}_{i=1} + \mathrm{j}\omega c_{H}\begin{Bmatrix} u_{x0} \\ 0 \end{Bmatrix}_{i=0}\right) \tag{4.28}$$

For typical i^{th} harmonic, $\mathbf{T}^{D}$ is given as

$$\mathbf{T}_{i}^{D} = \begin{bmatrix} 1 & 0 \\ 0 & 1 \\ t_{i}^{d} & 0 \\ 0 & t_{i}^{d} \end{bmatrix}, \text{ where } t_{i}^{d} = \frac{-k_{42}}{k_{44} - i\omega^{2}I_{p} - \left(i\omega\right)^{2} I_{d}} \tag{4.29}$$

At the time of development of dynamic condensation transformation, the external force including Δk_{44} corresponding to the slave degrees of freedom are considered to be zero, which is again added to the equation after the application of transformation matrix. In matrix form, the reduced EOM takes the following form

$$\left(-\left(i\omega\right)^{2}\mathbf{M}^{D} + i\mathrm{j}\omega\mathbf{C}^{D} + \left(i-1\right)\mathrm{j}\omega\mathbf{C}_{H}^{D} + i\omega^{2}\mathbf{G}^{D} + \mathbf{K}^{D}\right)\mathbf{Q}_{mm} = \mathbf{f}^{D} \tag{4.30}$$

where,

$$\left.\begin{aligned}
\mathbf{M}^D &= \left(\mathbf{T}^D\right)^T \begin{bmatrix} \mathbf{M}_{mm} & \mathbf{0} \\ \mathbf{0} & \mathbf{M}_{ss} \end{bmatrix} \mathbf{T}^D = \begin{bmatrix} m+\left(t_i^d\right)^2 I_d & 0 \\ 0 & m+\left(t_i^d\right)^2 I_d \end{bmatrix}; \\
\mathbf{C}^D &= \left(\mathbf{T}_i^D\right)^T \begin{bmatrix} \mathbf{C}_{mm} & \mathbf{C}_{ms} \\ \mathbf{C}_{sm} & \mathbf{C}_{ss} \end{bmatrix} \mathbf{T}_i^D = \begin{bmatrix} c_E & 0 \\ 0 & c_E \end{bmatrix}; \\
\mathbf{K}^D &= \left(\mathbf{T}_i^D\right)^T \begin{bmatrix} \mathbf{K}_{mm} & \mathbf{K}_{ms} \\ \mathbf{K}_{sm} & \mathbf{K}_{ss} \end{bmatrix} \mathbf{T}_i^D = \begin{bmatrix} k_{22}+2t_i^d k_{24}+\left(t_i^d\right)^2 k_{44} & 0 \\ 0 & k_{22}+2t_i^d k_{24}+\left(t_i^d\right)^2 k_{44} \end{bmatrix}
\end{aligned}\right\} \tag{4.31}$$

$$\left.\begin{aligned}
\mathbf{C}_H^D &= \left(\mathbf{T}_i^D\right)^T \begin{bmatrix} \mathbf{C}_{H_{mm}} & 0 \\ 0 & 0 \end{bmatrix} \mathbf{T}_\mathbf{i}^\mathbf{D} = \begin{bmatrix} \mathrm{c_H} & 0 \\ 0 & \mathrm{c_H} \end{bmatrix}; \\
\mathbf{G}^D &= \left(\mathbf{T}_i^D\right)^T \begin{bmatrix} \mathbf{0} & \mathbf{0} \\ \mathbf{0} & \mathbf{G}_{ss} \end{bmatrix} \mathbf{T}_\mathbf{i}^\mathbf{D} = \begin{bmatrix} -I_p\left(t_i^d\right)^2 & 0 \\ 0 & -I_p\left(t_i^d\right)^2 \end{bmatrix}; \\
\mathbf{f}^D &= \left(\mathbf{T}_i^D\right)^\mathbf{T} \begin{Bmatrix} \mathbf{f}_m \\ \mathbf{f}_s \end{Bmatrix} = \begin{Bmatrix} me\omega^2\cos(\phi) \\ me\omega^2\sin(\phi) \end{Bmatrix} + \begin{Bmatrix} \left(\Delta k_{22}u_{x0}+t_i^d\Delta k_{44}\varphi_{y0}\right)p_i \\ 0 \end{Bmatrix} - \omega \begin{Bmatrix} 0 \\ -c_H u_{x0} \end{Bmatrix}
\end{aligned}\right\} \tag{4.32}$$

On using Equations (4.31) through (4.32) into Equation (4.30) and on combining together in a complex form, it forms a single equation, as

$$\begin{aligned}
\left(-(i\omega)^2 m_i + \mathrm{i}\mathrm{j}\,\omega\left(c_E\right) + \left(i-1\right)\mathrm{j}\,\omega c_H - \mathrm{i}\omega^2 I_p\left(t_i^d\right)^2 + k_i\right) R_i &= me\omega^2 \mathrm{e}^{\mathrm{j}\phi} + \mathrm{j}\,\omega c_H u_{x0} \\
&\quad + \left(\Delta k_{22}u_{x0} + t_i^d \Delta k_{44}\varphi_{y0}\right) p_i
\end{aligned} \tag{4.33}$$

with $m_i = \left\{m+\left(t_i^d\right)^2 I_d\right\}$; $\quad k_i = \left\{k_{22}+2t_i^d k_{24}+\left(t_i^d\right)^2 k_{44}\right\}$ $\quad$ and $\quad R_i = R_{i_{\mathrm{Re}}} + \mathrm{j}R_{i_{\mathrm{Im}}}$

Real terms of above equation gives

$$\begin{aligned}
-i\omega\left(c_E\right)R_{i_{\mathrm{Im}}} - \left(i-1\right)\omega c_H R_{i_{\mathrm{Im}}} - m\omega^2 e_{\mathrm{Re}} - \left(\Delta k_{22}u_{x0} + t_i^d\Delta k_{44}\varphi_{y0}\right)p_i \\
= \left(\left(i\omega\right)^2 m_i + i\omega^2 I_p\left(t_i^d\right)^2 - k_i\right) R_{i_{Re}}
\end{aligned} \tag{4.34}$$

Similarly, imaginary terms gives

$$i\omega\left(c_E\right)R_{i_{Re}}+\left(\left(i-1\right)R_{i_{Re}}-u_{x0}\right)\omega c_H-m\omega^2 e_{\mathrm{Im}}=\left(\left(i\omega\right)^2 m_i+i\omega^2 I_p\left(t_i^d\right)^2-k_i\right)R_{i_{\mathrm{Im}}} \tag{4.35}$$

Further Equations (4.34) and (4.35) are rearranged in the matrix form for the identification of unknown parameters for various harmonics of the switching crack function as

$$\mathbf{Ax}=\mathbf{b} \tag{4.36}$$

with,

$$\mathbf{A}=\begin{bmatrix}
0 & \omega R_{0_{Im}} & 0 & 0 & -u_{x0}p_0 & -t_0^d\varphi_{y0}p_0\\
-\omega R_{1_{Im}} & 0 & -m\omega^2 & 0 & -u_{x0}p_1 & -t_1^d\varphi_{y0}p_1\\
-2\omega R_{2_{Im}} & -\omega R_{1_{Im}} & 0 & 0 & -u_{x0}p_2 & -t_2^d\varphi_{y0}p_2\\
-3\omega R_{3_{Im}} & -2\omega R_{3_{Im}} & 0 & 0 & -u_{x0}p_3 & -t_3^d\varphi_{y0}p_3\\
-5\omega R_{5_{Im}} & -4\omega R_{5_{Im}} & 0 & 0 & -u_{x0}p_5 & -t_5^d\varphi_{y0}p_5\\
-7\omega R_{7_{Im}} & -6\omega R_{7_{Im}} & 0 & 0 & -u_{x0}p_7 & -t_7^d\varphi_{y0}p_7\\
\omega R_{-1_{Im}} & 2\omega R_{-1_{Im}} & 0 & 0 & -u_{x0}p_{-1} & -t_{-1}^d\varphi_{y0}p_{-1}\\
3\omega R_{-3_{Im}} & 4\omega R_{-3_{Im}} & 0 & 0 & -u_{x0}p_{-3} & -t_{-3}^d\varphi_{y0}p_{-3}\\
5\omega R_{-5_{Im}} & 6\omega R_{-5_{Im}} & 0 & 0 & -u_{x0}p_{-5} & -t_{-5}^d\varphi_{y0}p_{-5}\\
0 & -\omega\left(R_{0_{\mathrm{Re}}}+u_{x0}\right) & 0 & 0 & 0 & 0\\
\omega R_{1_{\mathrm{Re}}} & 0 & 0 & -m\omega^2 & 0 & 0\\
2\omega R_{2_{\mathrm{Re}}} & \omega R_{2_{\mathrm{Re}}} & 0 & 0 & 0 & 0\\
3\omega R_{3_{\mathrm{Re}}} & 2\omega R_{3_{\mathrm{Re}}} & 0 & 0 & 0 & 0\\
5\omega R_{5_{\mathrm{Re}}} & 4\omega R_{5_{\mathrm{Re}}} & 0 & 0 & 0 & 0\\
7\omega R_{7_{\mathrm{Re}}} & 6\omega R_{7_{\mathrm{Re}}} & 0 & 0 & 0 & 0\\
-\omega R_{-1_{\mathrm{Re}}} & -2\omega R_{-1_{\mathrm{Re}}} & 0 & 0 & 0 & 0\\
-3\omega R_{-3_{\mathrm{Re}}} & -4\omega R_{-3_{\mathrm{Re}}} & 0 & 0 & 0 & 0\\
-5\omega R_{-5_{\mathrm{Re}}} & -6\omega R_{-5_{\mathrm{Re}}} & 0 & 0 & 0 & 0
\end{bmatrix}$$

$$
\mathbf{b} = \begin{Bmatrix}
-k_0 R_{0_{\mathrm{Re}}} \\
\left(\omega^2 m_1 + \omega^2 I_p \left(t_1^d\right)^2 - k_1\right) R_{1_{\mathrm{Re}}} \\
\left(4\omega^2 m_2 + 2\omega^2 I_p \left(t_2^d\right)^2 - k_2\right) R_{2_{\mathrm{Re}}} \\
\left(9\omega^2 m_3 + 3\omega^2 I_p \left(t_3^d\right)^2 - k_3\right) R_{3_{\mathrm{Re}}} \\
\left(25\omega^2 m_5 + 5\omega^2 I_p \left(t_5^d\right)^2 - k_5\right) R_{5_{\mathrm{Re}}} \\
\left(49\omega^2 m_7 + 7\omega^2 I_p \left(t_7^d\right)^2 - k_7\right) R_{7_{\mathrm{Re}}} \\
\left(\omega^2 m_{-1} - \omega^2 I_p \left(t_{-1}^d\right)^2 - k_{-1}\right) R_{-1_{\mathrm{Re}}} \\
\left(9\omega^2 m_{-3} - 3\omega^2 I_p \left(t_{-3}^d\right)^2 - k_{-3}\right) R_{-3_{\mathrm{Re}}} \\
\left(25\omega^2 m_{-5} - 5\omega^2 I_p \left(t_{-5}^d\right)^2 - k_{-5}\right) R_{-5_{\mathrm{Re}}} \\
-k_0 R_{0_{\mathrm{Im}}} \\
\left(\omega^2 m_1 + \omega^2 I_p \left(t_1^d\right)^2 - k_1\right) R_{1_{\mathrm{Im}}} \\
\left(4\omega^2 m_2 + 2\omega^2 I_p \left(t_2^d\right)^2 - k_2\right) R_{2_{\mathrm{Im}}} \\
\left(9\omega^2 m_3 + 3\omega^2 I_p \left(t_3^d\right)^2 - k_3\right) R_{3_{\mathrm{Im}}} \\
\left(25\omega^2 m_5 + 5\omega^2 I_p \left(t_5^d\right)^2 - k_5\right) R_{5_{\mathrm{Im}}} \\
\left(49\omega^2 m_7 + 7\omega^2 I_p \left(t_7^d\right)^2 - k_7\right) R_{7_{\mathrm{Im}}} \\
\left(\omega^2 m_{-1} - \omega^2 I_p \left(t_{-1}^d\right)^2 - k_{-1}\right) R_{-1_{\mathrm{Im}}} \\
\left(9\omega^2 m_{-3} - 3\omega^2 I_p \left(t_{-3}^d\right)^2 - k_{-3}\right) R_{-3_{\mathrm{Im}}} \\
\left(25\omega^2 m_{-5} - 5\omega^2 I_p \left(t_{-5}^d\right)^2 - k_{-5}\right) R_{-5_{\mathrm{Im}}}
\end{Bmatrix}
$$

and

$$
\mathbf{x} = \begin{Bmatrix} c_E & c_H & e_{\mathrm{Re}} & e_{\mathrm{Im}} & \Delta k_{22} & \Delta k_{44} \end{Bmatrix}^T
$$

In the identification, the unknown parameter vector **x** from Equation (4.36) takes the following form

$$\mathbf{x} = \left(\mathbf{A}^T\mathbf{A}\right)^{-1}\mathbf{A}^T\mathbf{b} \tag{4.37}$$

The identification of **x** is reliable while using information for multiple speeds of interest. On combining for different spin speeds, ω_1, ω_2, ...,ω_n, (with the assumption that parameters to be estimated are speed-independent) may be written as

$$\begin{bmatrix} \mathbf{A}(\omega_1) \\ \mathbf{A}(\omega_2) \\ \vdots \\ \mathbf{A}(\omega_n) \end{bmatrix} \mathbf{x} = \begin{Bmatrix} \mathbf{b}(\omega_1) \\ \mathbf{b}(\omega_2) \\ \vdots \\ \mathbf{b}(\omega_n) \end{Bmatrix} \tag{4.38}$$

Now the analysis and identification procedure developed in foregoing sections are now illustrated through numerical simulation in next section.

4.5 Numerical simulations

A numerical simulation has been done through the Simulink model in MATLAB™ environment to obtain time domain data from EOMs as in Equation (4.17). Simulink block for the proposed rotor system is shown in Figure 4.4. The simulation runs for 8 s duration. Responses have been considered for complete cycles (n) and incomplete cycles (in between (n-1) to n cycle) in time domain for same speed of the rotor.

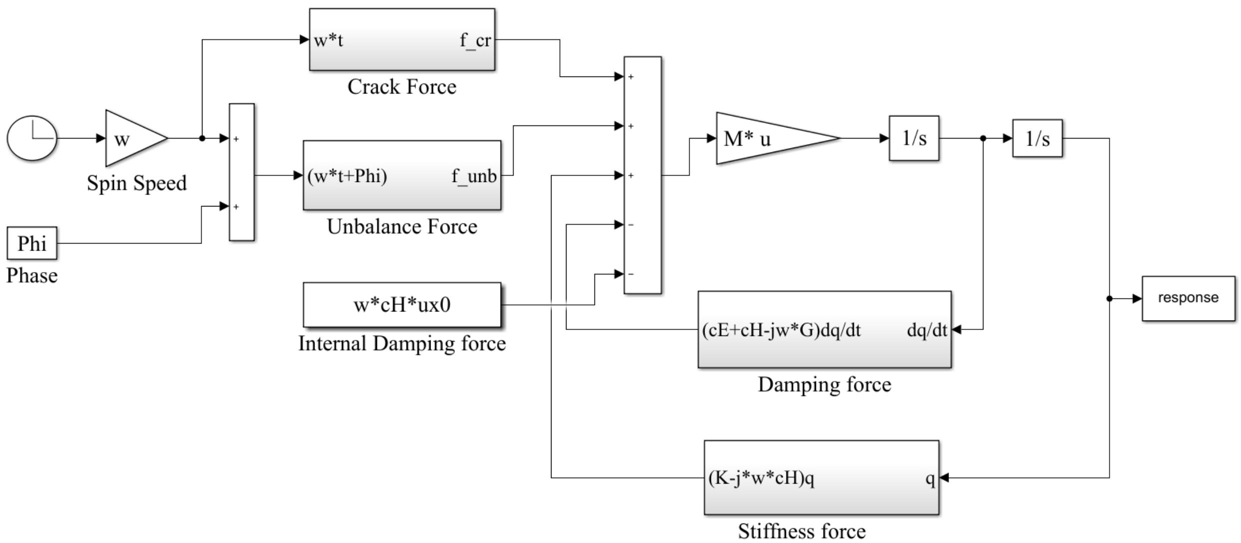

Figure 4.4 Simulink block of rotor system

4.5.1 Time domain and full spectrum response

For the numerical simulation, initially the rotor system parameters are assumed, which are summarized in Table 4.1. Numerically generated responses have been considered for *n*-complete cycles during 6 to 7 s duration. Initial 6 s response has been removed to avoid transients. Time domain signals have been generated for fixed value of ωt, in which, $\omega = 2\pi n$, where n is considered as an integer.

Time domain responses generated through Simulink block for 20 Hz are shown in Figure 4.5. The plot shows both the vertical and horizontal displacement responses, orbit plots, and vertical reference signal in Figures 4.5(a) through 4.5(d), respectively. Similarly, for 50 Hz spin speed, time domain responses are shown in Figures 4.6(a) through 4.6(d), which are the vertical and horizontal displacements, orbit plots, and vertical reference signal, respectively.

Table 4.1 Assumed initial parameter of rotor model for the numerical solution

Parameters		Value	Unit
Mass of disc	m	2	kg
Mass moment of inertia	I_p	0.0048	kg-m^2
	I_d	0.0024	kg-m^2
Intact shaft stiffness	k_{22}	5.779×10^{5}	N/m
	k_{24}	2.2016×10^{4}	N
	k_{44}	1.7613×10^{4}	Nm
Additive crack stiffness	Δk_{22}	1.7337×10^{5}	N/m
	Δk_{44}	1.7612×10^{3}	Nm
External damping	c_E	27	Ns/m
Internal damping	c_H	20	Ns/m
Shaft deflection	u_{x0}	3.57×10^{-5}	m
	φ_{y0}	-4.46×10^{-5}	rad
Disc eccentricity	e	3×10^{-5}	m
Phase of eccentricity	ϕ	30	deg
Length of shaft	l	0.36	m
	a	0.20	m
	b	0.16	m

Orbit plots show as the spin speed increases the unbalance force dominates and loopings due to multi-harmonics of crack forces are insignificant. The fundamental natural frequency (ω_{nf}) of the intact rotor system is 538 rad/s (85.63 Hz).

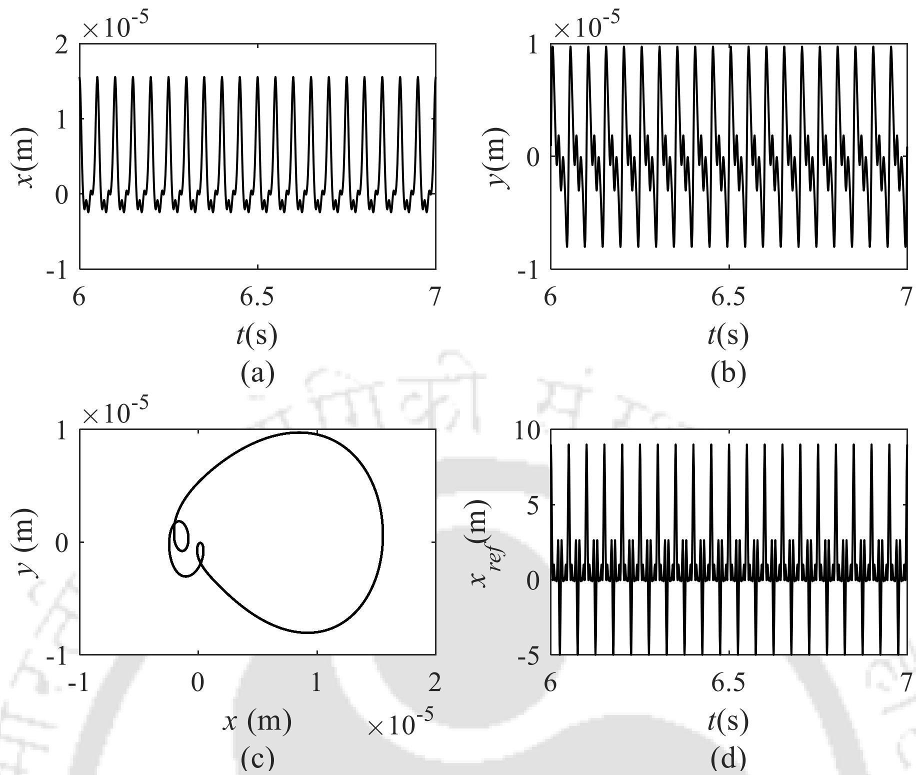

Figure 4.5 Time domain response generated at spin speed of 20 Hz: (a) vertical displacement, *x*, versus time, (b) horizontal displacement, *y*, versus time, (c) orbit plot (*x* versus *y*) and (d) vertical reference displacement, x_{ref}, versus time

Full spectrum responses of the proposed rotor system have been generated based on time domain responses. Responses of full spectrum show amplitude and phase, reference phase and with phase compensation for spin speed of 20 Hz and 50 Hz in Figure 4.7(a-b-c-d) and Figure 4.8(a-b-c-d), respectively. Figure 4.7(e-f-g-h) and Figure 4.8(e-f-g-h) are full spectrum response with 1% noise addition in time domain response for spin speed of 20 Hz and 50 Hz, respectively.

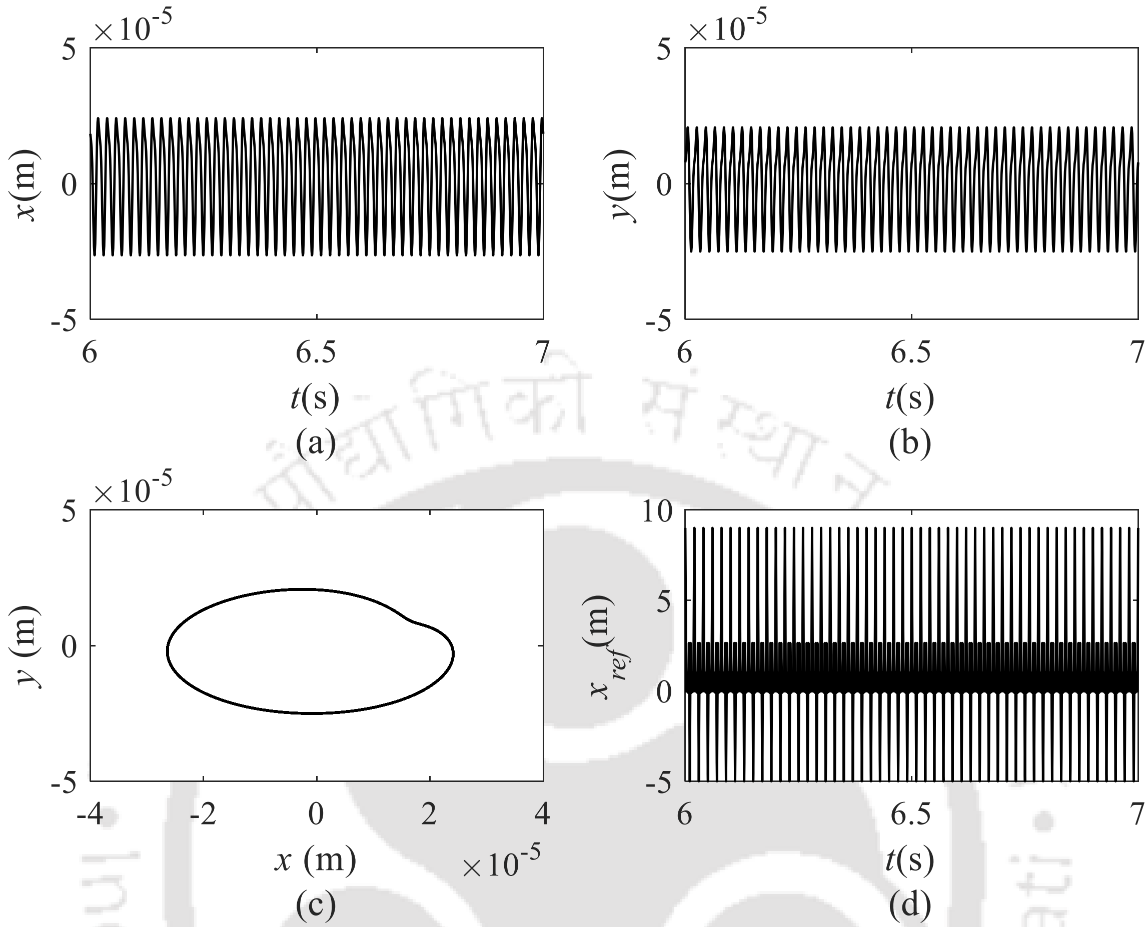

Figure 4.6 Time domain response generated at spin speed of 50 Hz: (a) vertical displacement, *x*, versus time, (b) horizontal displacement, *y*, versus time, (c) orbit plot (*x* versus *y*) and (d) vertical reference displacement, x_{ref}, versus time

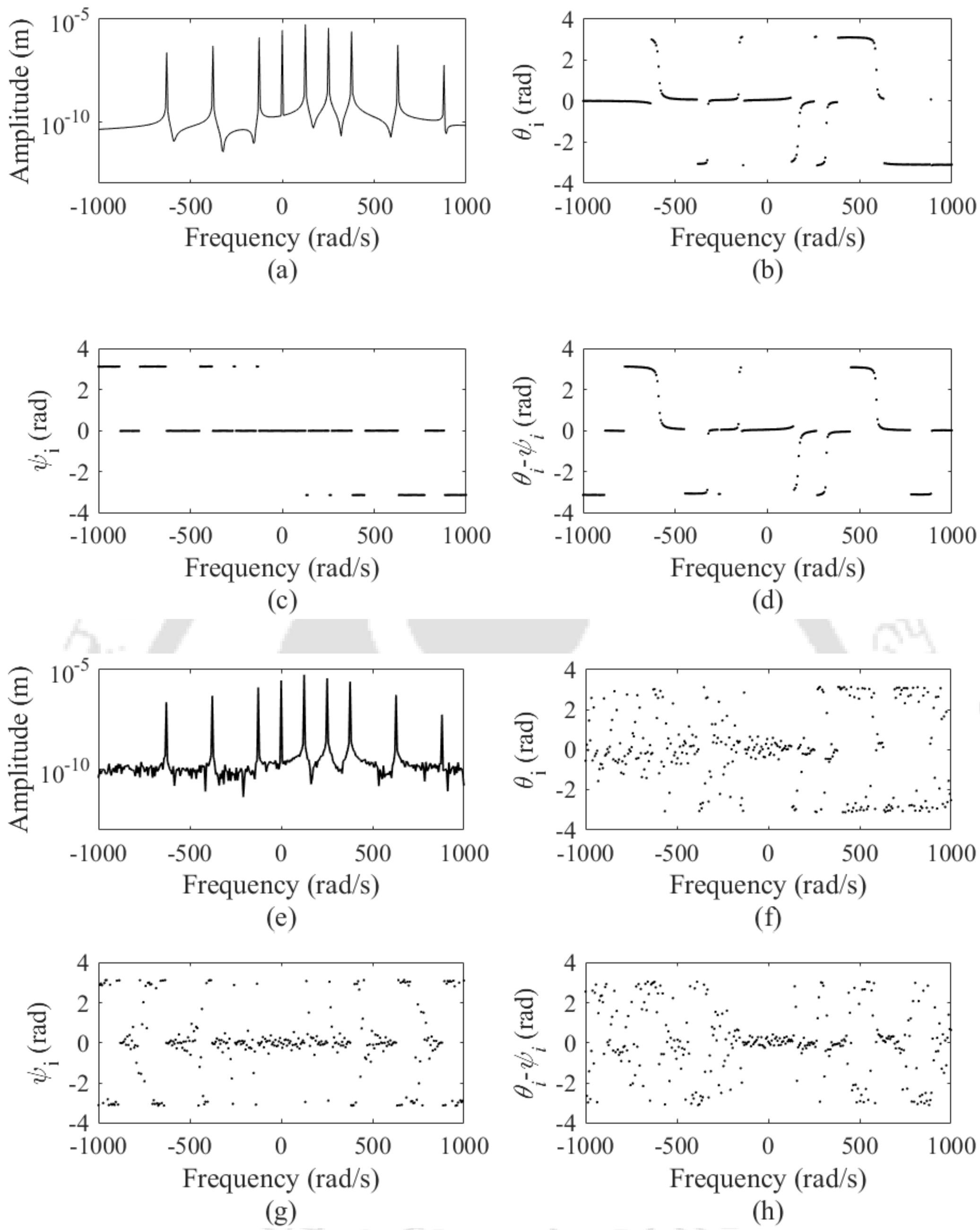

Figure 4.7 Full spectrum response at 20 Hz (a) amplitude and (b) phase without compensation, (c) phase of reference signal and (d) phase with compensation (e) amplitude with 1% noise and (f) phase without compensation with 1% noise, (g) phase of reference signal with 1% noise and (h) phase with compensation with 1% noise

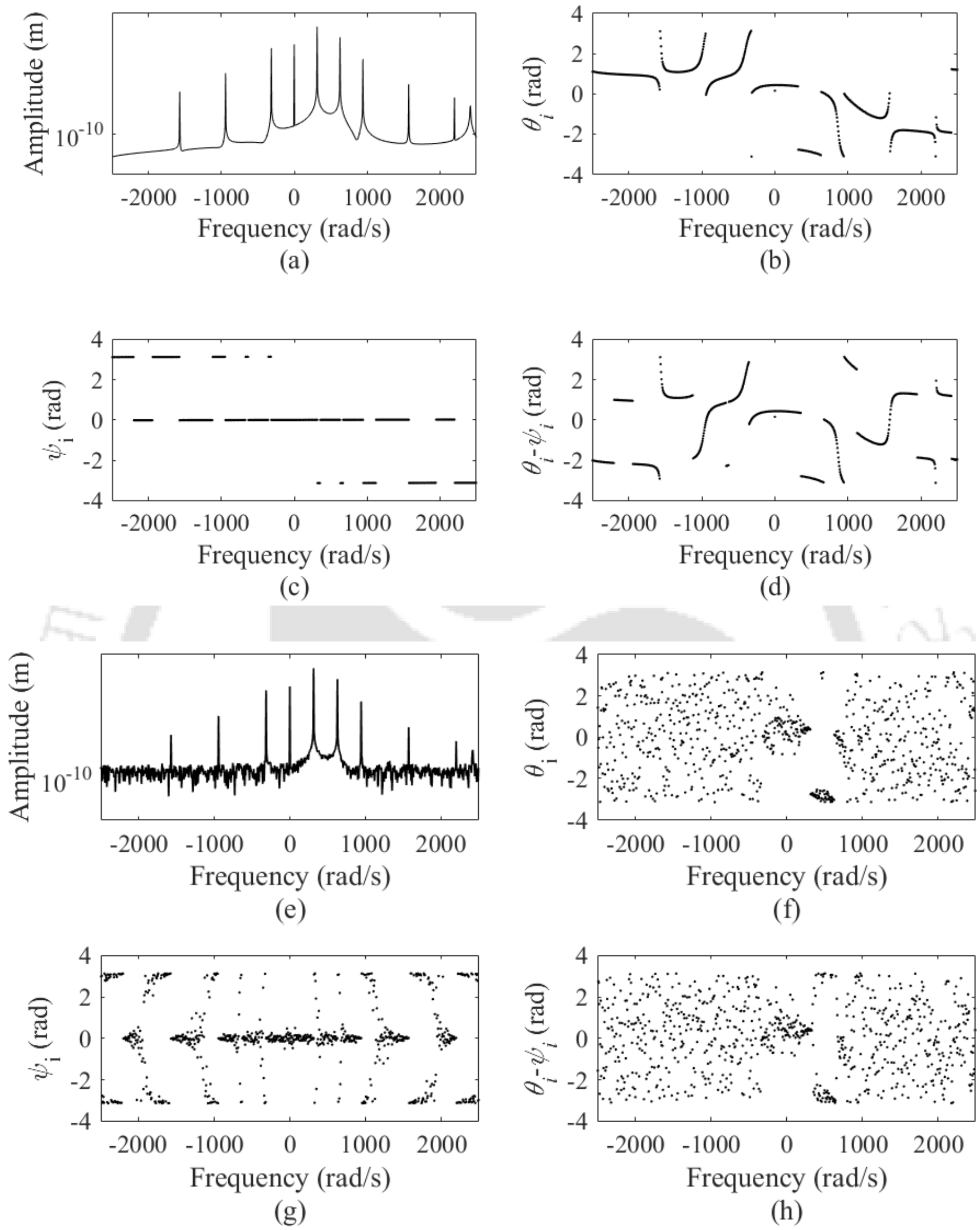

Figure 4.8 Full spectrum response at 50 Hz (a) amplitude and (b) phase without compensation, (c) phase of reference signal and (d) phase with compensation (e) amplitude with 1% noise and (f) phase without compensation with 1% noise, (g) phase of reference signal with 1% noise and (h) phase with compensation with 1% noise

The full spectrum amplitude for the complete and incomplete cycle of time domain signals using the regression based full spectrum and FFT based full spectrum are compared in Table 4.2 for a spin speed of 20 Hz and in Table 4.3 for a spin speed of 50 Hz. Amplitudes of the response for both forward and backward whirling conditions of the rotor are found to be similar for the complete cycle of signals with both the regression and FFT based full spectrums. However, amplitudes for incomplete cycle using above mentioned two methods have some differences. In fact, full spectrum amplitudes generated through the regression based FFT for complete and incomplete cycles of signals are found to be the same.

Table 4.2 Comparison of full spectrum amplitudes at different harmonics based on the complete and incomplete cycles of displacement signals at 20 Hz

	Complete cycle		Incomplete cycle	
Frequency	Regression based (10^{-6} m)	FFT based (10^{-6} m)	Regression based (10^{-6} m)	FFT based (10^{-6} m)
0	2.8563	2.8563	2.8563	2.8372
ω	5.5201	5.5201	5.5201	5.4937
2ω	3.7056	3.7056	3.7056	3.6788
3ω	2.5063	2.5063	2.5063	2.4855
5ω	0.5434	0.5434	0.5434	0.5339
7ω	0.0562	0.0562	0.0565	0.0448
-ω	1.2824	1.2824	1.2824	1.2711
-3ω	0.4943	0.4943	0.4943	0.4918
-5ω	0.2334	0.2334	0.2334	0.2283

However, the variation observed in amplitudes by the FFT based full spectrum for incomplete cycle case differs in only some decimal points with that of the complete cycle. The comparison of full spectrum phase for the spin speed of 20 Hz and 50 Hz for both complete and incomplete cycles of signals using the regression and FFT based method are provided in Table 4.4 and Table 4.5, respectively.

Table 4.3 Comparison of full spectrum amplitudes at different harmonics based on the complete and incomplete cycles of displacement signals at 50 Hz

	Complete cycle		Incomplete cycle	
Frequency	Regression based (10^{-6} m)	FFT based (10^{-6} m)	Regression based (10^{-6} m)	FFT based (10^{-6} m)
0	2.8804	2.8804	2.8804	2.8571
ω	21.9424	21.9424	21.9423	21.7519
2ω	6.4555	6.4555	6.4555	6.1765
3ω	0.5416	0.5416	0.5416	0.4988
5ω	0.0303	0.0303	0.0303	0.0243
7ω	0.0066	0.0066	0.0066	0.0032
-ω	1.8796	1.8796	1.8796	1.8547
-3ω	0.1074	0.1074	0.1074	0.0989
-5ω	0.0129	0.0129	0.0129	0.0089

Table 4.4 Comparison of full spectrum phases (θ_i) at different harmonics based on the complete and incomplete cycles of displacement signals at 20 Hz

	Complete cycle		Incomplete cycle	
Frequency	Regression based, (rad)	FFT based (rad)	Regression based (rad)	FFT based, (rad)
0	0.0616	0.0616	0.0616	0.0604
ω	0.1597	0.1597	0.5432	0.2557
2ω	-0.0219	-0.0219	0.7450	0.1696
3ω	-0.0572	-0.0572	1.0932	0.2298
5ω	0.1114	0.1114	2.0289	0.5827
7ω	-3.1028	-3.1028	-0.4184	-2.3554
-ω	0.0162	0.0162	-0.3673	-0.0827
-3ω	-3.0657	-3.0657	2.0670	2.9361
-5ω	3.0089	3.0089	1.0914	2.5459

Values of phase for complete cycles considering both methods are found to be similar and these are correct values. In case of incomplete cycles, these values of phase show appreciable variation with respect to correct values using both regression and FFT based methods. So in order to remove variation caused by leakage errors, complete cycles are collected with the help of a reference signal.

Table 4.5 Comparison of full spectrum phase angles (θ_i) at different harmonics based on the complete and incomplete cycles of displacement signals at 50 Hz

	Complete cycle		Incomplete cycle	
Frequency	Regression based (rad)	FFT based (rad)	Regression based (rad)	FFT based (rad)
0	0.1531	0.1531	0.1531	0.1499
ω	0.3694	0.3694	1.3281	0.6090
2ω	-3.0460	-3.0460	-1.1285	-2.5670
3ω	-3.1107	-3.1107	-0.2345	-2.3949
5ω	0.0150	0.0150	-1.4744	1.2181
7ω	-3.1265	-3.1265	-2.6982	-1.2401
-ω	0.0595	0.0595	-0.8992	-0.1839
-3ω	-0.0412	-0.0412	-2.9174	-0.7938
-5ω	3.1236	3.1236	-1.6702	2.1223

The reference signal full spectrum phase angle are also compared both with complete and incomplete cycles of signals, using methods mentioned above, in Table 4.6 and Table 4.7 for spin speed 20 and 50 Hz. respectively. Phase values of reference signal on considering complete cycles turn out to be zero ($\approx 10^{-14}$) using both methods, which confirms that there is no phase compensation required for complete cycles. In the case of incomplete cycles of signals, the phase angle shows appreciable deviations, which are found to be dissimilar by both methods.

Table 4.6 Comparison of full spectrum phases (ψ_i) at different harmonics by the regression and FFT based methods on the complete and incomplete cycles of reference signals at 20 Hz

Frequency	Complete cycle		Incomplete cycle	
	Regression based 10^{-14}(rad)	FFT based 10^{-14}(rad)	Regression based (rad)	FFT based (rad)
0	0.0011	0	0.0006	0
ω	-2.4634	-3.1921	0.3842	0.0960
2ω	-4.8942	-6.3477	0.7686	0.1918
3ω	-21.5703	-28.0384	1.1514	0.2879
5ω	1.9627	2.5495	1.9185	0.4798
7 ω	-31.3823	-40.7641	2.6866	0.6714
- ω	2.4303	3.1921	-0.3830	-0.0959
-3 ω	21.5779	28.03841	-1.1503	-0.2879
-5ω	-1.9625	-2.5495	-1.9175	-0.4798

To perform the phase compensation of displacement signals, a reference signal is required as shown in the phase compensation processing flow chart in Figure 2.5 (in Chapter 2).

The phase compensation for the incomplete cycle is done and phase values obtained are found to be similar to those obtained from the complete cycle using both methods as given in Table 4.8 and Table 4.9 for spin speed 20 and 50 Hz, respectively.

Table 4.7 Comparison of reference phases (ψ_i) at different harmonics by the regression and FFT based methods on the complete and incomplete cycles of reference signals at 50 Hz

Frequency	Complete cycle		Incomplete cycle	
	Regression based 10^{-14}(rad)	FFT based 10^{-14}(rad)	Regression based (rad)	FFT based (rad)
0	0.0026	0	0	0.0008
ω	0.9875	1.2793	0.2395	0.9595
2ω	1.9534	2.5394	0.4779	1.9190
3ω	-25.4703	-0.3311	0.7185	2.8769
5ω	33.3170	0.43312	1.1973	-1.4890
7 ω	92.3850	0.0120	1.6711	0.4285
- ω	-0.9654	-1.2793	-0.2395	-0.9580
-3 ω	25.4651	0.3311	-0.7185	-2.8758
-5ω	-33.3120	-0.4331	-1.1973	1.4894

From these tables, it is seen that the phase compensation is required if incomplete cycles are considered to avoid leakage errors. Similarly, for different spin speeds the amplitudes and phases are obtained, and are used in equation (4.38) for multiple or combined speeds to estimate system parameters as summarized in Table 4.10 for combined (20 to 50 Hz with increments 1 Hz) spin speed, respectively.

Table 4.8 Comparison of phase compensation (θ_i-ψ_i) at different harmonics by the regression and FFT based methods on the complete and incomplete cycles of displacement signals at 20 Hz

Frequency	Complete cycle		Incomplete cycle	
	Regression based (rad)	FFT based (rad)	Regression based (rad)	FFT based (rad)
0	0.0616	0.0616	0.0609	0.0604
ω	0.1597	0.1597	0.1590	0.1597
2ω	-0.0219	-0.0219	-0.0235	-0.0222
3ω	-0.0572	-0.0572	-0.0581	-0.0581
5ω	0.1114	0.1114	0.1104	0.1029
7 ω	-3.1028	-3.1028	-3.1050	-3.0268
- ω	0.0162	0.0162	0.0157	0.0133
-3 ω	-3.0657	-3.0657	3.2173	-3.0591
-5ω	3.0089	3.0089	3.0089	3.0258

The results obtained using complete cycles of signals are found to be accurate whereas for incomplete cycles with phase compensation a small variation is obtained between the assumed and identified parameters, except for the crack stiffness due to tilting, Δk_{44}. To check the robustness of the identification algorithm, different percentage of random white noise, i.e. 1%, 2%, or 5% are incorporated in time domain responses of the rotor system and results are shown in Figure 4.9 and Table 4.10.

Table 4.9 Comparison of phase compensation (θ_i-ψ_i) at different harmonics by the regression and FFT based methods on the complete and incomplete cycles of displacement signals at 50 Hz

Frequency	Complete cycle		Incomplete cycle	
	Regression based (rad)	FFT based (rad)	Regression based (rad)	FFT based (rad)
0	0.1531	0.1531	0.1523	0.1499
ω	0.3694	0.3694	0.3685	0.3695
2ω	-3.0460	-3.0460	-3.0476	-3.0449
3ω	-3.1107	-3.1107	-3.1115	-3.1134
5ω	0.0150	0.0150	0.0146	0.0207
7 ω	-3.1265	-3.1265	-3.1267	-2.9112
- ω	0.0595	0.0595	0.0588	0.0556
-3 ω	-0.0412	-0.0412	-0.0415	-0.0753
-5ω	3.1236	3.1236	3.1236	-2.9635

The identified parameters, excluding Δk_{44}, shows very small variation (< 0.15%) and (<0.7%) with consideration of the complete cycle and incomplete cycles with phase compensation, respectively, for the combined speed case. The parameter Δk_{44} shows moderate variation even for combined speeds, i.e. (<7%) and (<3%) for the complete cycle and incomplete cycles with phase compensation, respectively, as shown in Figure 4.9 and Table 4.10.

Table 4.10 Estimated parameters for combined speeds with noise addition

Input speed in Hz	Comparission		c_H (Nsm^{-1})	c_E (Nsm^{-1})	e (10^{-5} m)	ϕ (deg.)	Δk_{22} (10^5 N/m)	Δk_{44} (10^3 Nm/rad)
	Assumed value		20	27	3	30	1.7337	1.7613
	noise		Complete cycle					
Combined speed 20:50 Hz with increament of 1 Hz	A* and B*	add 0%	20.0000	27.0000	3.0000	30.0000	1.7338	1.7596
		variation	(0.000%)	(0.000%)	(0.000%)	(0.000%)	(0.006%)	(-0.009%)
		add 1%	20.0029	26.9987	3.0000	29.9999	1.7334	1.7835
		variation	(0.014%)	(-0.005%)	(0.000%)	(-0.000%)	(-0.017%)	(1.260%)
		add 2%	20.0058	26.9974	3.0001	29.9997	1.7330	1.8074
		variation	(0.029%)	(-0.009%)	(0.003%)	(-0.001%)	(-0.040%)	(2.617%)
		add 5%	20.0147	26.9937	3.0003	29.9994	1.7319	1.8792
		variation	(0.073%)	(0.023%)	(0.010%)	(-0.002%)	(-0.104%)	(6.694%)
			Incomplete cycle					
	A*	add 0%	19.7199	-22.3227	4.0062	77.03739	12.6407	-713.9713
	B*	add 0%	19.8639	27.0806	2.9993	29.9329	1.7341	1.7445
		variation	(-0.680%)	(0.298%)	(-0.023%)	(-0.223%)	(0.023%)	(-0.954%)
		add 1%	19.8643	27.0803	2.9994	29.9329	1.7339	1.7583
		variation	(-0.678%)	(0.297%)	(-0.020%)	(-0.223%)	(0.011%)	(-0.170%)
		add 2%	19.8646	27.0800	2.9994	29.9329	1.7336	1.7721
		variation	(-0.677%)	(0.296%)	(-0.020%)	(-0.223%)	(-0.006%)	(0.613%)
		add 5%	19.8655	27.0790	2.9996	29.9328	1.7330	1.8136
		variation	(-0.672%)	(0.292%)	(-0.013%)	(-0.224%)	(-0.040%)	(2.969%)

A*- without phase compensation, **B*-** with phase compensation

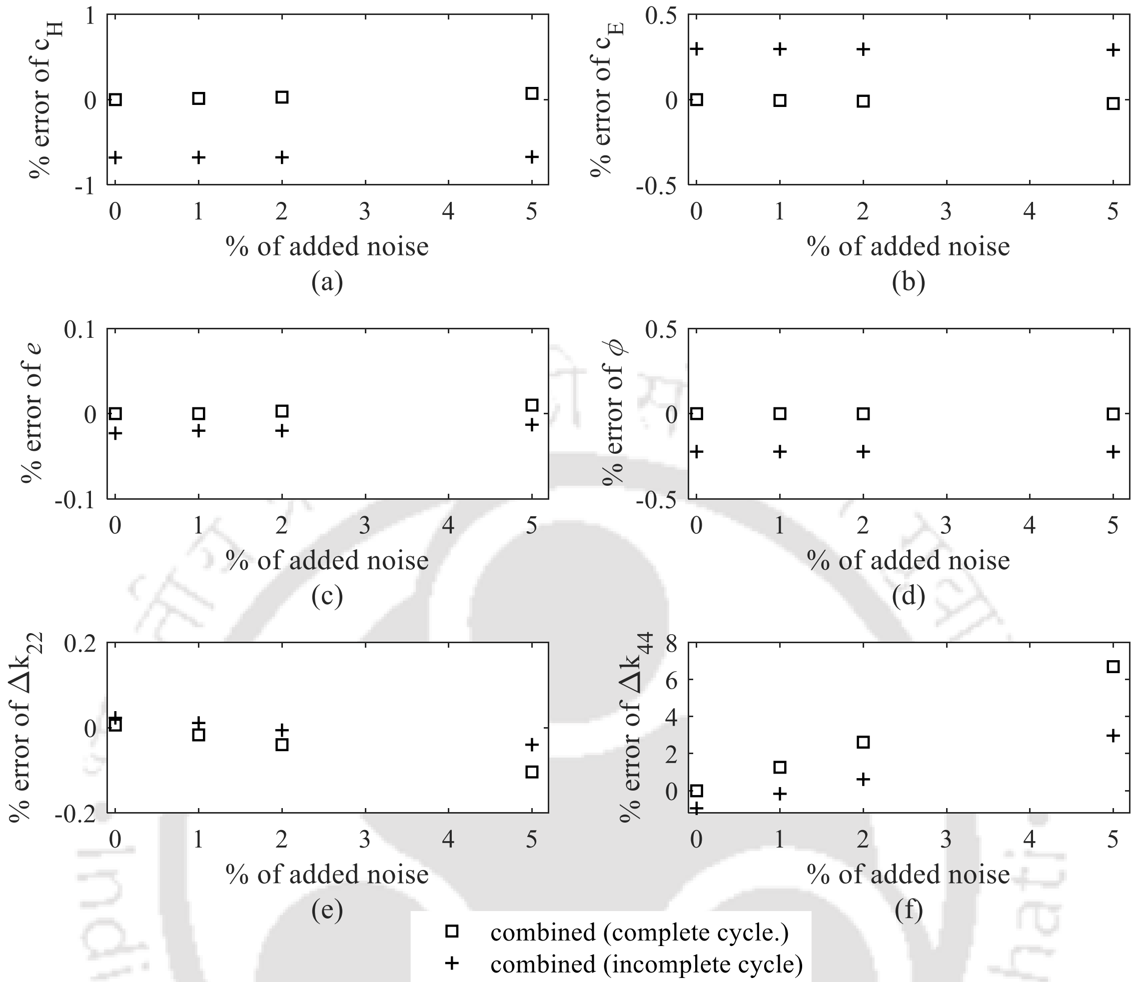

Figure 4.9 Percentage error of identification parameters versus percentage addition of noise for (a) internal damping (b) external damping (c) eccentricity (d) phase of unbalance (e) additive crack stiffness due to transverse force and (f) additive crack stiffness due to moment

In the proposed system apart from translational additive stiffness discussed in Chapter 2 the rotational additive stiffness is also considered in the identification. In this chapter Simulink block has been used to perform the numerical simulation.

4.6 Conclusions

This chapter presented an identification algorithm for fault parameters, such as internal damping and external damping, unbalance and additive stiffness in a rotor system with an offset disc. The generated time domain responses through Simulink model are converted into full spectrum and are used in the developed identification algorithm for estimation of different fault parameters. The following are the conclusions drawn from the present chapter:

- The estimation of translational as well as rotational additive stiffness is done to study its effect on the dynamic behavior of the cracked rotor system.
- In present work the dynamic condensation has been performed for the eliminating of rotational degree of freedom, which is difficult to measure experimentally.
- The developed identification algorithm is tested against random measurement noise in responses and found to be robust.
- All the parameters accept the rotational additive stiffness are quite similar with the assumed parameters.
- The rotational additive stiffness parameters is much deviating from the assumed one because in the dynamic condensation initially it is removed and again in the identification it is included for estimation.

The experimental analysis of the present work is discussed in next chapter. It consists of the estimation of model parameters, based on the observation of time domain responses from an experimental setup with a rotor having off-set disc.

CHAPTER 5

Experimental identification of internal and external damping in a cracked rotor system with gyroscopic effects

Identification methodology developed after elimination of rotational DOFs, using condensation schemein Chapter 4, is applied for the experimental estimation of internal and external damping. Measured transverse translational DOFs at offset disc location from the cracked rotor system are used for the estimation. A comparison is made of estimated parameters from the present chapter with the estimated parameters of Chapter 3.

5.1 Introduction

A model based experimental identification of internal damping in a cracked rotor with an offset disc has been presented. The model based identification is taken from Chapter 4 and it is experimentally investigated in the present chapter with necessary modications on signal processing part. Internal damping and other critical system parameters, like the external damping, additive crack stiffness, and disc unbalances have been estimated. For the purpose of experimentation, based on the artificial fatigue crack in a similar way as of Chapter 3, however the disc is placed at an axially offset position on to the shaft in the present case. The location of crack was near to the disc. The information of amplitude and phase at different frequencies have been extracted from measured displacement signals through full spectrum analysis with associated phase corrections. The identification algorithm uses experimental full spectrum amplitudes and phases to estimate fault parameters of a rotor system and it is validated numerically through mathematical model.

5.2 Experimental analysis and observation of responses

For an experimental study, a cracked rotor test rig with an offset disc was designed for application of the identification algorithm developed in Chapter 4 for the estimation of rotor system parameters. The parts of the test rig are summarized in Table 3.1 and a schematic of the experimental setup is illustrated in Figure 5.1. As per Figure 5.1, an experimental test rig was set up in Vibration and Acoustics Laboratory at IIT Guwahati as shown in Figure 5.2. Fault investigation was done with the help of a rotor test rig, which consists of a shaft containing a transverse fatigue crack. Other elements of the test rig were the ball bearings, disc, shaft, coupling, motor andvariable frequency drive (VFD).

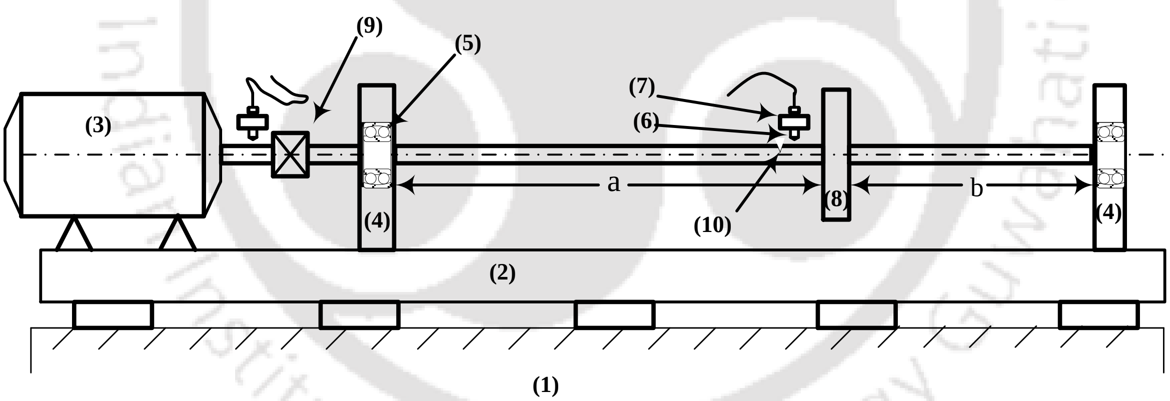

Figure5.1 Schematicofa cracked shaft with an offset disc in experimental setup

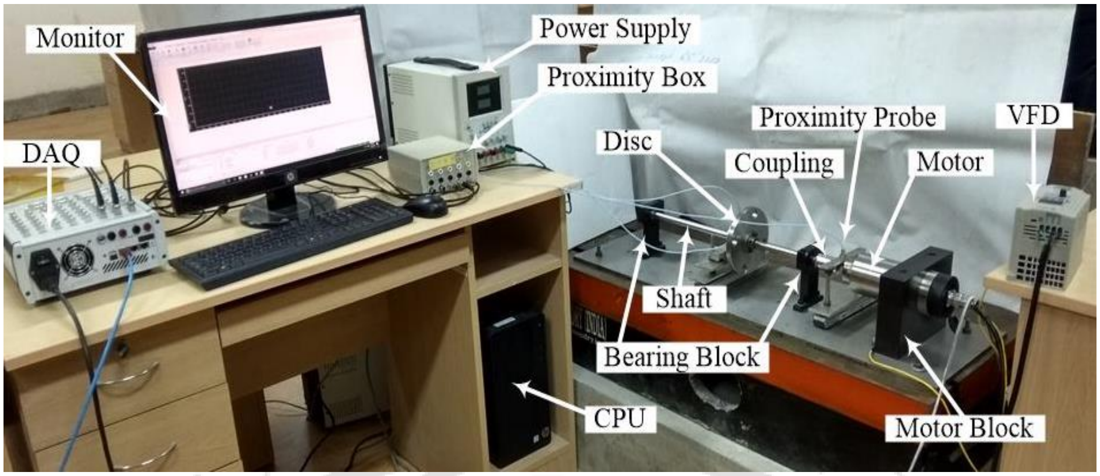

Figure 5.2 Arrangement of the crack shaft experimental setup with an offset disc

Two eddy-current proximity sensors are utilized for acquiring vibrational displacements of the cracked rotor system, which are located in two orthogonal transverse directions near the offset disc, as illustrated in Figure 5.2. The sensitivity of the proximity sensor is 7.478 V/mm. A third sensor is utilized for the phase reference and is placed at the slot of the rigid motor shaft, it ensured negligible transverse displacement of the motor shaft during its rotation. An impact test in the vertical direction of the cracked rotor system was done for different shaft orientations to obtainedthe highest and lowest natural frequencies corresponding to fully closed (healthy shaft) and fully open crack conditions.

Table 5.1 Rotor system parameters

Parameters	Symbol	Value	Unit
Mass of disc	m	1.87	kg
Mass moment of inertia	I_p	0.00489	kg-m^2
	I_d	0.00235	kg-m^2
Intact shaft stiffness	k_{22}	3.5056×10^5	N/m
	k_{24}	1.9671×10^4	N
	k_{44}	1.7048×10^4	Nm
Natural frequency	ω_{th}	67.9	Hz
	ω_{exp}	65.0	Hz
Shaft static deflection	u_{x0}	5.386×10^{-5}	m
Static tilting angle	φ_{y0}	-6.21×10^{-5}	rad
Length of shaft	l	0.46	m
	a	0.26	m
	b	0.20	m

The maximum natural frequency obtained is 65.0 Hz, when the crack was in horizontal position and direction of impact was in the vertical direction, as shown in Figure 5.3. For this case, the notch effect was minimum, which was made for the initiation of a fatigue crack. Minimum natural frequency was obtained when crack was in the downward direction and is 63.0 Hz. When the crack was in vertical direction, the natural frequency was 64.0 Hz. Using the influence coefficient method (Tiwari, 2017), also natural frequency was obtained for intact shaft based on geometry and material properties (refer Table 5.1) and a comparison is shown in Table 5.1.

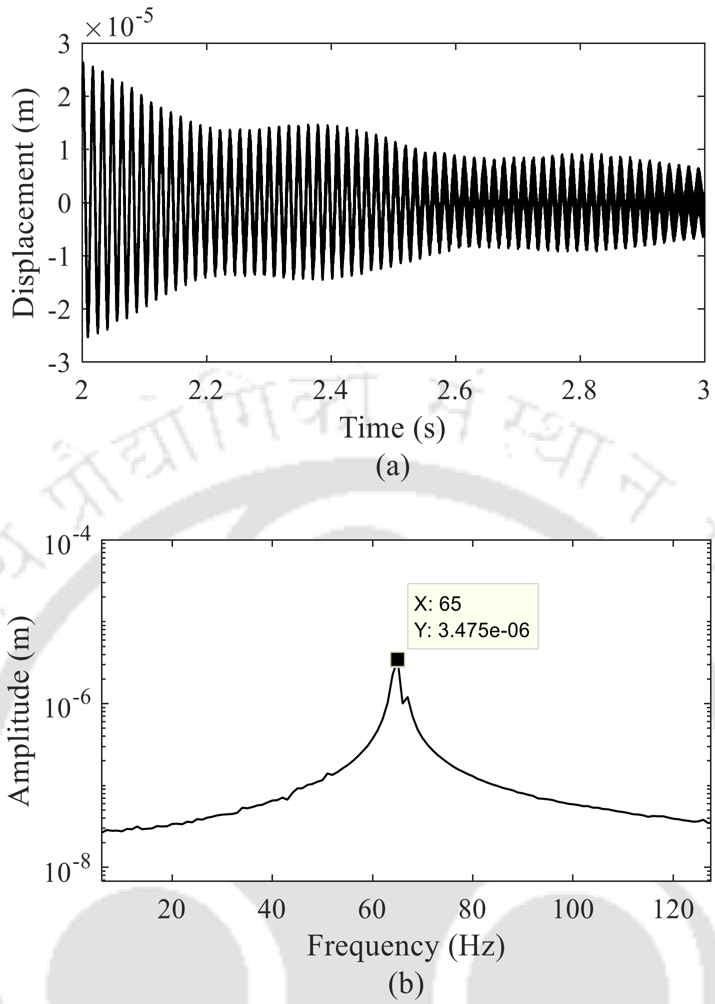

Figure 5.3 Free vibration response of shaft due to impulsive force with an orientation of crack is placed in the horizontal direction (a) time domain response and (b) frequency domain response

A VFD-M power source unit regulated the motor speed. Measurement was taken near 3 Hz of motor speed for the slow run condition (Maalouf, 2007; Shravankumar et al. 2015). The dSPACE DAQ system is utilized to store the measurement signal at a sampling frequency of 10,000 samples per second. A reference signal was utilized for acquiring displacement signals of shaft for complete multiple shaft rotational cycles, i.e., for $\omega t=2\pi n$, where n is the number of complete cycles. Using complete cycles of signals in identification as discussed in Chapter 4 has advantage over incomplete cycles, which has leakage error.

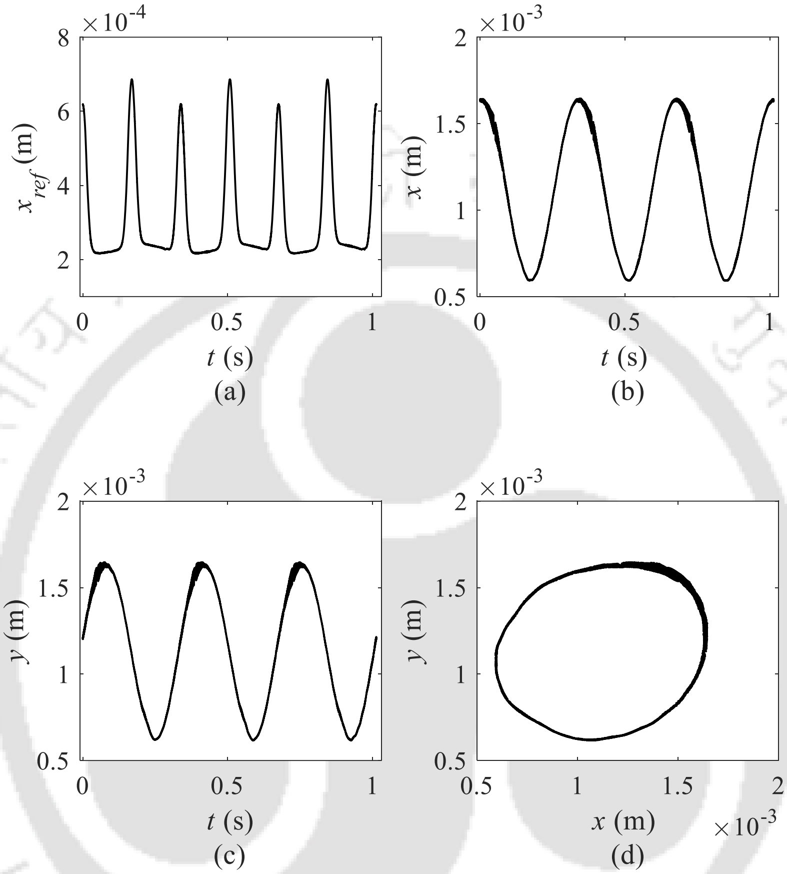

Figure 5.4 Time domain response for slow roll near at 3 Hz (a) vertical direction reference signal (x-direction) (b) vertical displacement (x-direction) (c) horizontal displacement (y-direction) and (d) orbit plot from the vertical and horizontal displacements

For the slow run condition, the acquisition of complete cycles of signals is illustrated in Figure 5.4. Figure 5.4(a) illustrates three complete cycles of the reference signal for 3 Hz motor speed from the vertical direction sensor. During the same time duration, displacement signals are acquired near the disc in both vertical (x-axis) and horizontal (y-axis) directions, and are illustrated in Figures 5.4(b) and 5.4 (c), respectively. Also, Figures 5.4(d) depicts the shaft displacement orbit plot and it is seen that the origin is not inside the plot, which shows the gap between the sensors and shaft in two orthogonal directions (*x* and *y*) at the slow run condition. Since at slow run condition the dynamic force is very low, hence Figures 5.4(d) shows only the bow and sensor gap. From Figures 5.4(b-d), it is to be noted that displacements have higher amplitudes due to bow of the shaft. Similarly, for the higher spin speeds of 15 and 20 Hz, complete cycle acquisition of signal is shown in Figures 5.5 and Figure 5.6, respectively.

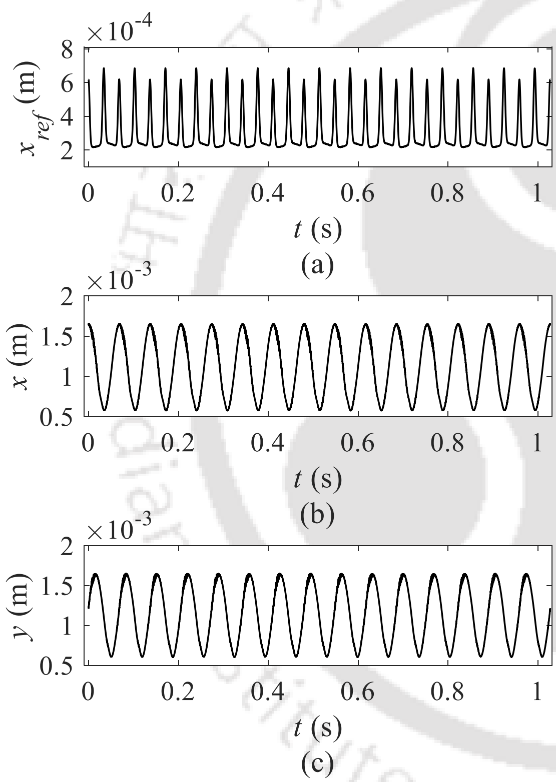

Figures 5.5 Time domain response at 15 Hz (a) vertical direction reference signal (x-direction) (b) vertical displacement and (c) horizontal displacement (*y*-direction)

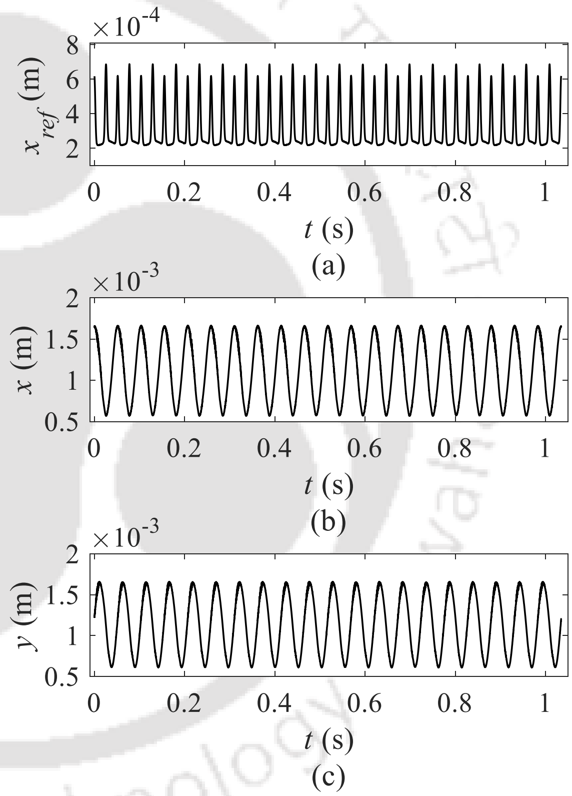

Figures 5.6 Time domain response at 20 Hz (a) vertical direction reference signal (x-direction) (b) vertical displacement and (c) horizontal displacement (*y*-direction)

Now the FFT-based full spectrum, which was earlier discussed in Chapter 4, is illustrated for acquired time domain responses from experimental setup for the slow roll and higher speeds. The responses in the vertical and horizontal directions at disc location along with the reference signal are transformed in full spectrum domain, which has a form of complex numbers.

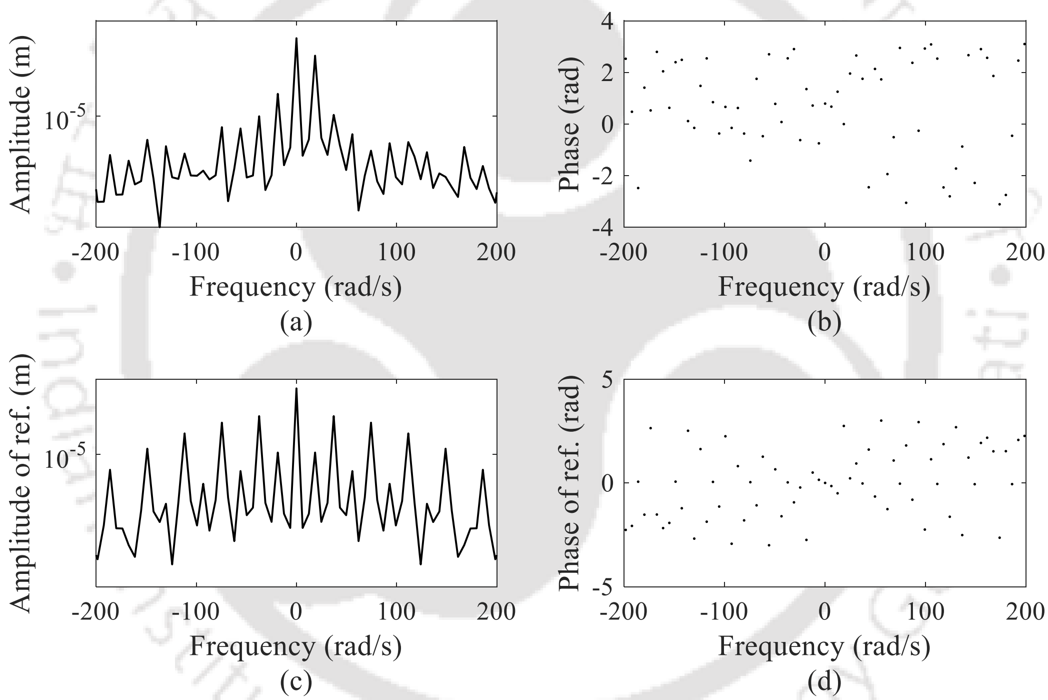

Figure 5.7 Full spectrum plots for the slow roll at 3 Hz (a) amplitude of shaft displacements (b) phase of shaft displacements (c) amplitude of reference signals and (d) phase of reference signals

These are illustrated in Figure 5.7(a-d) for 3 Hz for the slow roll condition and for higher spin speeds 15 and 20 Hz in 5.8(a-d) and Figure 5.9(a-d), respectively.

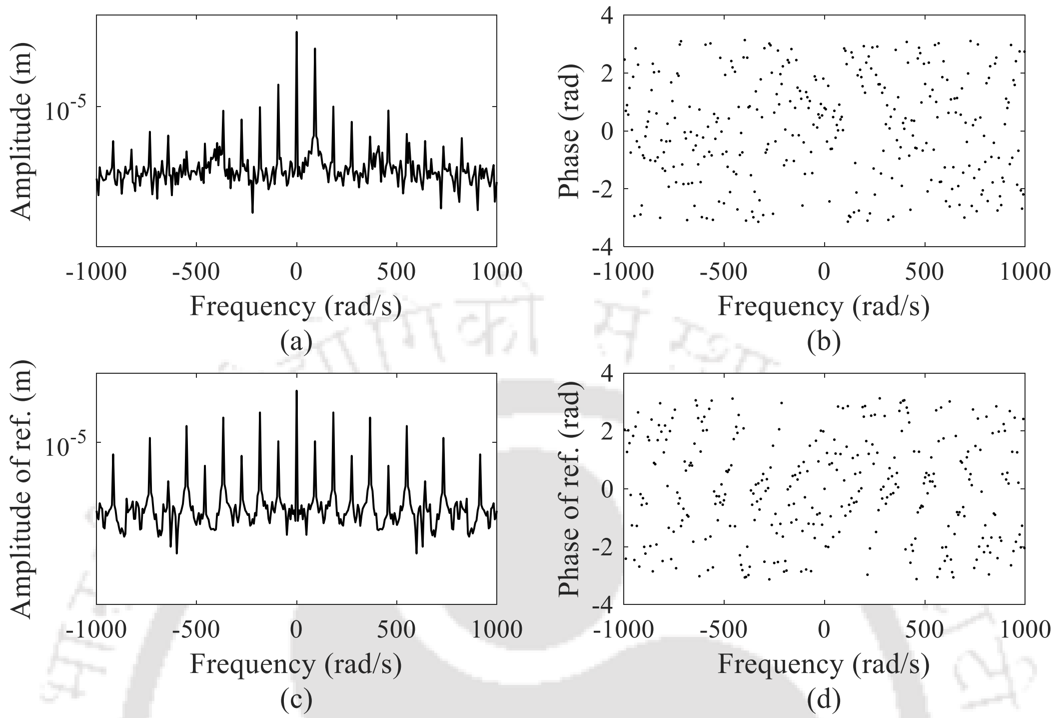

Figure 5.8 Full spectrum plots for the motor speed at 15 Hz (a) amplitude of shaft displacements (b) phase of shaft displacements (c) amplitude of reference signals and (d) phase of reference signals

Figure 5.7(a) through Figure 5.9(a) represent the full spectrum amplitudes with frequency, both in positive and negative directions of the motor speed corresponding to displacements near the disc. Similarly, Figure 5.7(b) through Figure 5.9(b) represent corresponding phase of the full spectrum. For the reference signal, Figure 5.7(c) through Figure 9(c) represent the amplitudes, and its phases are represented in Figure 5.7(d) through Figure 5.9 (d), respectively, for 3 Hz, 15Hz and 20 Hz of motor speed.

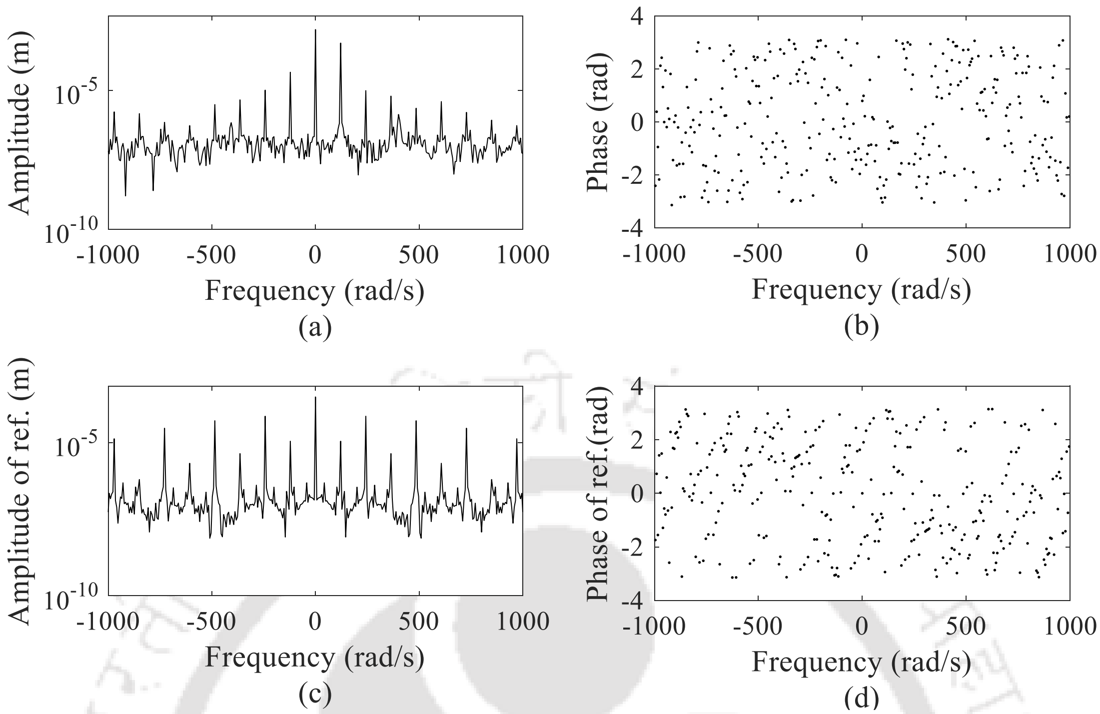

Figure 5.9 Full spectrum plots for the motor speed at 20 Hz (a) amplitude of shaft displacements (b) phase of shaft displacements (c) amplitude of reference signals and (d) phase of reference signals

Two full spectrum methods, i.e., regression-based and FFT-based, which is discussed in Chapter 3 are use here also. Amplitudes and phase angles of complex shaft displacements, and phase angles of the complex reference signal at different harmonics for the slow roll shaft speed (i.e., 3 Hz) are provided for both the first and second methods in Table 5.2. Similarly, displacement amplitudes and phase angles at different harmonics, for higher spin speeds of 15 Hz and 20 Hz are provided in Table 5.3 and Table 5.4, respectively. It can be inferred that the variations in amplitudes are found to be negligible by two independent methods, whereas, the variations in phase angles become negligible only after the phase compensation.

Table 5.2 Amplitudes, phase angles and reference phase angles at different harmonics of full spectrum for slow run rotor speed (3 Hz)

Frequency	Amplitudes		Phase angle		Reference phase angle	
	Regression (10^{-5} m)	FFT (10^{-5} m)	Regression (rad)	FFT (rad)	Regression (rad)	FFT (rad)
0	160.7689	160.7728	0.7931	0.7930	0	0
ω	51.3491	51.3489	-0.0022	-0.0013	2.7451	2.7457
2ω	1.0689	1.0698	1.7482	1.7547	-0.0281	-0.0262
$3\ \omega$	0.3017	0.3019	1.7213	1.7320	3.0001	3.0031
$5\ \omega$	0.1687	0.1675	-0.2610	-0.2588	2.9232	2.9303
$7\ \omega$	0.0928	0.0929	-1.7243	-1.7245	2.6542	2.6835
$-\ \omega$	4.2316	4.2322	1.3574	1.3559	-2.7451	-2.7457
$-3\ \omega$	0.4413	0.4397	2.7078	2.7046	-3.0002	-3.0031
$-5\ \omega$	0.0268	0.0278	-0.1526	-0.1491	-2.9234	-2.9303

The effect of shaft bow is nullified and it discussed in Section 3.4 of Chapter 3. To reduce the effect of bow, the complex displacement in full spectrum at slow roll of rotor speed (i.e., in vector form) for 1X harmonic is removed from the complex displacement in the full spectrum at higher rotor spin speed according to Equation (3.1).

Table 5.3 Amplitudes, phase angles and reference phase angles at different harmonics of full spectrum for the 15 Hz spin speed

Frequency	Amplitudes		Phase angle		Reference phase angle	
	Regression based (10^{-5} m)	FFT based (10^{-5} m)	Regression based (rad)	FFT based (rad)	Regression based (rad)	FFT based (rad)
0	160.5817	160.5776	0.7934	0.7934	0	0
ω	52.0386	52.0386	0.0232	0.0279	2.7832	2.7874
2ω	1.0143	1.0129	1.8362	1.8500	0.0095	0.0187
$3\ \omega$	0.3609	0.3612	1.5823	1.6021	3.1128	3.1264
$5\ \omega$	0.7777	0.7790	-0.6183	-0.5964	-3.1392	-3.1163
$7\ \omega$	0.09883	0.0992	-1.2613	-1.2368	-3.0935	-3.0612
$-\ \omega$	4.4956	4.4949	1.3481	1.3429	-2.7831	-2.7874
$-3\ \omega$	0.4244	0.4259	3.0287	3.0160	-3.1128	-3.1264
$-5\ \omega$	0.0832	0.0837	2.2522	2.2180	3.1392	3.1163

The corrected full spectrum amplitude and phase are utilized for the identification of rotor parameters, like the rotating damping, stationary damping, unbalance, and additive crack stiffness. The comparisons of responses with or without bow and sensor gap according to Equation (3.1) are discussed in the next section.

Table 5.4 Amplitudes, phase angles and reference phase angles at different harmonics of full spectrum for the 20 Hz spin speed

Frequency	Amplitudes		Phase angle		Reference phase angle	
	Regression (10^{-5} m)	FFT (10^{-5} m)	Regression (rad)	FFT (rad)	Regression (rad)	FFT (rad)
0	160.6459	160.6419	0.7933	0.7933	0	0
ω	52.2777	52.2767	0.0190	0.0251	2.7966	2.8024
2ω	0.9996	0.9982	1.7815	1.7984	-0.0053	0.0068
$3\ \omega$	0.6365	0.6375	1.3079	1.3296	-3.1343	-3.1163
$5\ \omega$	0.4044	0.4056	-0.5920	-0.5641	-3.1129	-3.0832
$7\ \omega$	0.0864	0.0871	-1.3129	-1.2764	-3.0795	-3.0409
$-\ \omega$	4.6157	4.6148	1.2915	1.2849	-2.7966	-2.8024
$-3\ \omega$	0.4653	0.4650	-1.5999	-1.6145	3.1344	3.1163
$-5\ \omega$	0.0546	0.0541	1.7239	1.6786	3.1131	3.0832

5.3 Response comparison analysis

Measured responses in the form of orbit plots, which are without bow and sensor gap for the rotor speed of 15 Hz and 20 Hz are illustrated in Figures 5.10(b) and 5.11(b), respectively. These are without the effect of bow and sensor gap from equilibrium position of the rotor shaft while using Equation (3.1). Displacements are reduced from order 10^{-3} m to 10^{-4} m and the bearing centre is outside the orbit in these figures, as compared with bow and sensor gap for the rotor speed of 15 Hz and 20 Hz presented in Figures 5.10(a) and 5.11(a) respectively. Since the crack was initiated by fatigue loading, hence the actual crack propagation is not known and so the orbit

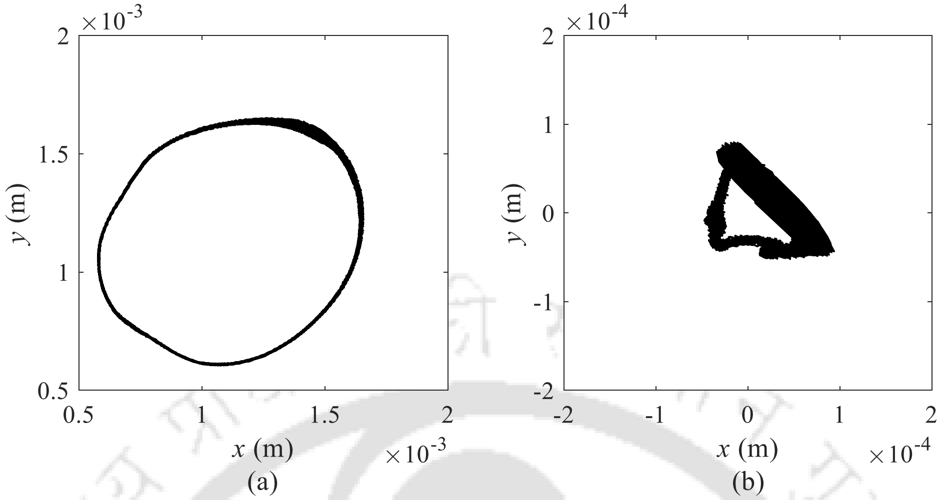

Figure. 5.10 Orbit plot (x vs. y) for higher spin speed at 15 Hz (a) with a bow from sensor position (b) without bow from the equilibrium position

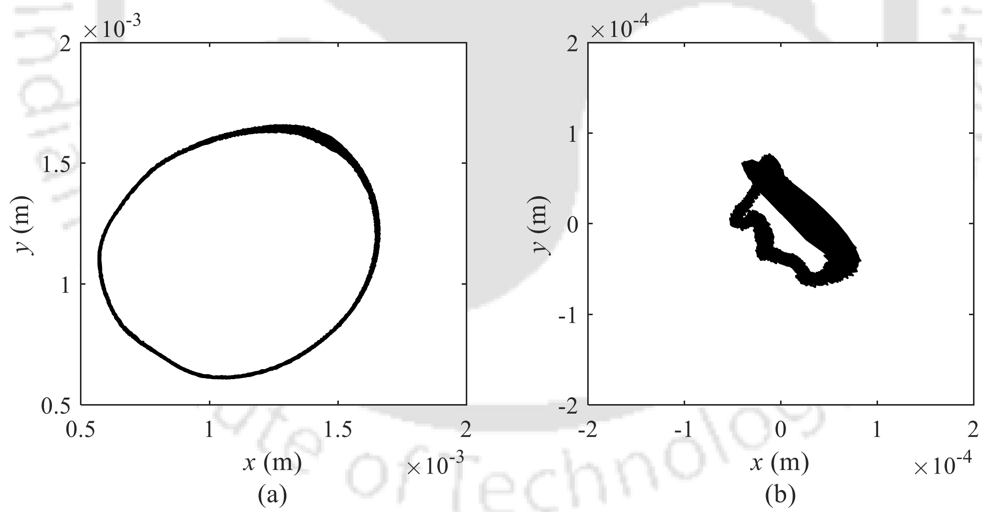

Figure. 5.11 Orbit plot (x vs. y) for higher spin speed at 20 Hz (a) with a bow from sensor position (b) without bow from the equilibrium position

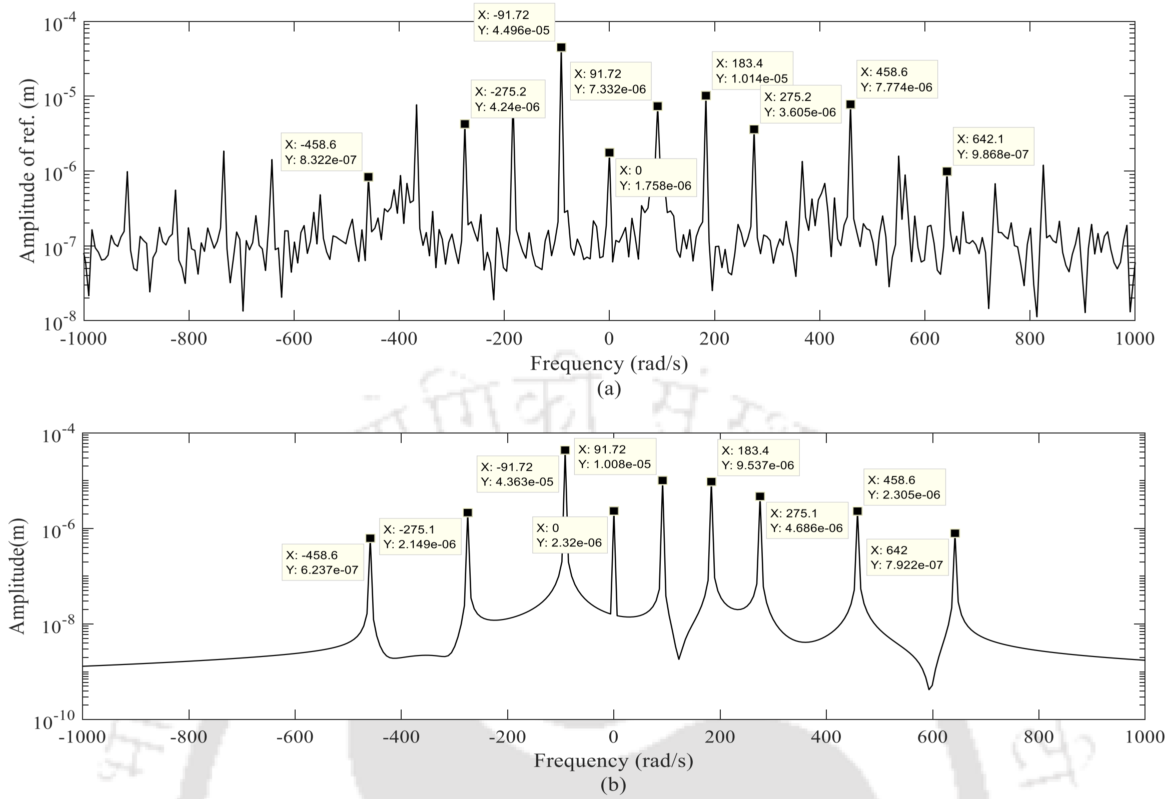

Figure 5.12 Full spectrum amplitude at the spin speed 15 Hz spin speed (a) without bow and without sensor gap experimental response (b) numerical response

is not correlating with hypothetical mathematical models in which symmetry prevails. Figures 5.12(a) and 5.13(a) shows the full spectrum amplitude without bow and without sensor gap at rotor spin speed of 15 Hz and 20 Hz for 15 and 20 complete cycles of data, respectively. It can be observed that full spectrum plot is not symmetric due to the nature of fatigue crack.

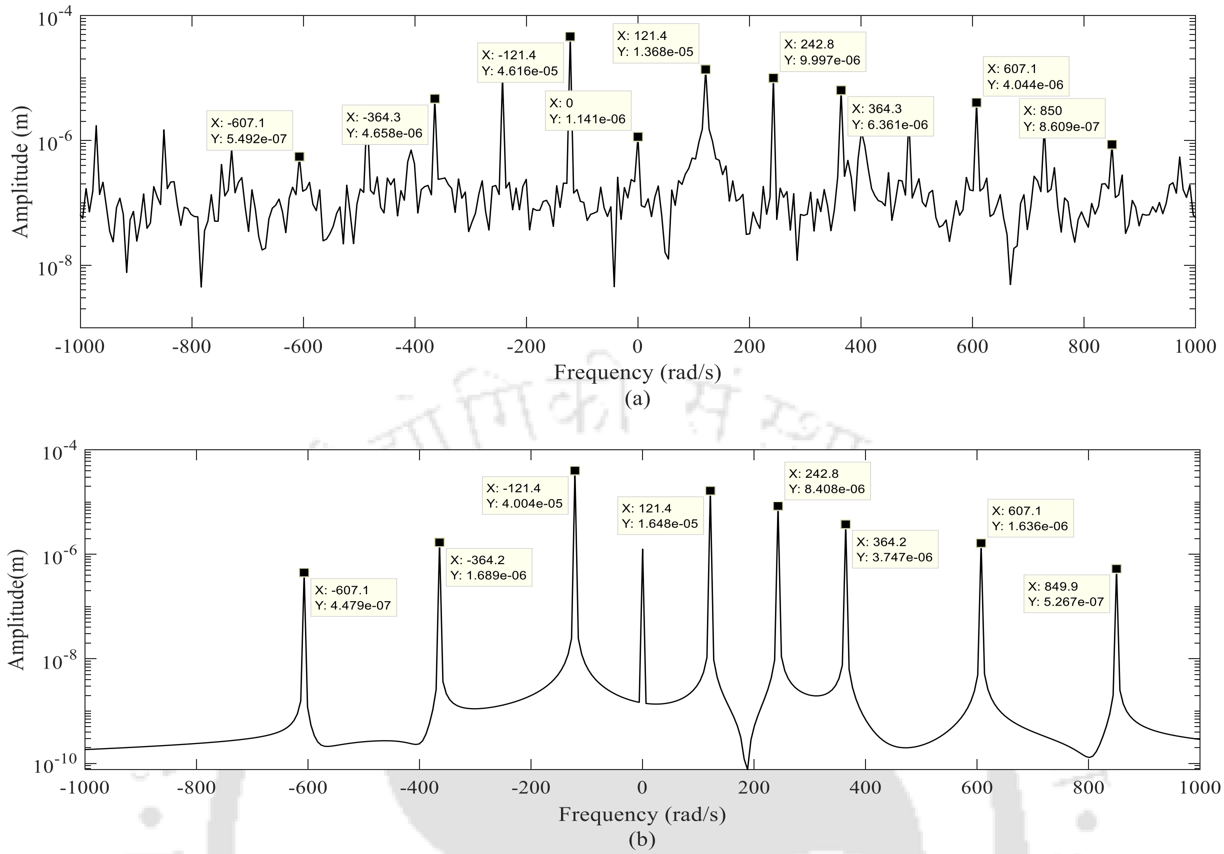

Figure 5.13 Full spectrum amplitude at the spin speed 20 Hz spin speed (a) without bow and without sensor gap experimental response (b) numerical response

5.4 Estimation of rotor system parameters

The amplitudes and phases of full spectrum displacement responses, after application of the phase compensation and the removal of bow and sensor gap through Equation (3.1) are utilized in identification of rotor parameters using the regression Equations (2.26) and (2.27). The rotational additive stiffness parameters are not appreciable in experimental case. Moreover, it was found in Chapter 4 that it deviates a lot from the assumed one because in the dynamic condensation initially it is removed and again considered in the identification during parameter estimation. Further Equations (4.37) and (4.38) have been modified without considering the rotational additive stiffness (Δk_{44}) to have better estimates from experimental result. Equations (4.37) and (4.38) are rearranged in a matrix form for identification of unknown parameters for various harmonics of the switching crack function as

$$\mathbf{Ax} = \mathbf{b} \tag{5.1}$$

with,

$$\mathbf{A} = \begin{bmatrix} 0 & \omega R_{0_{Im}} & 0 & 0 & -u_{x0} \\ -\omega R_{1_{Im}} & 0 & -m\omega^2 & 0 & -u_{x0} \\ -2\omega R_{2_{Im}} & -\omega R_{1_{Im}} & 0 & 0 & -u_{x0} \\ -3\omega R_{3_{Im}} & -2\omega R_{3_{Im}} & 0 & 0 & -u_{x0} \\ -5\omega R_{5_{Im}} & -4\omega R_{5_{Im}} & 0 & 0 & -u_{x0} \\ -7\omega R_{7_{Im}} & -6\omega R_{7_{Im}} & 0 & 0 & -u_{x0} \\ \omega R_{-1_{Im}} & 2\omega R_{-1_{Im}} & 0 & 0 & -u_{x0} \\ 3\omega R_{-3_{Im}} & 4\omega R_{-3_{Im}} & 0 & 0 & -u_{x0} \\ 5\omega R_{-5_{Im}} & 6\omega R_{-5_{Im}} & 0 & 0 & -u_{x0} \\ 0 & -\omega\left(R_{0_{Re}} + u_{x0}\right) & 0 & 0 & 0 \\ \omega R_{1_{Re}} & 0 & 0 & -m\omega^2 & 0 \\ 2\omega R_{2_{Re}} & \omega R_{2_{Re}} & 0 & 0 & 0 \\ 3\omega R_{3_{Re}} & 2\omega R_{3_{Re}} & 0 & 0 & 0 \\ 5\omega R_{5_{Re}} & 4\omega R_{5_{Re}} & 0 & 0 & 0 \\ 7\omega R_{7_{Re}} & 6\omega R_{7_{Re}} & 0 & 0 & 0 \\ -\omega R_{-1_{Re}} & -2\omega R_{-1_{Re}} & 0 & 0 & 0 \\ -3\omega R_{-3_{Re}} & -4\omega R_{-3_{Re}} & 0 & 0 & 0 \\ -5\omega R_{-5_{Re}} & -6\omega R_{-5_{Re}} & 0 & 0 & 0 \end{bmatrix}$$

$$
\mathbf{x}=\begin{Bmatrix} c_E \\ c_H \\ e_{\mathrm{Re}} \\ e_{\mathrm{Im}} \\ \Delta k_\xi p_0 \\ \Delta k_\xi p_1 \\ \Delta k_\xi p_2 \\ \Delta k_\xi p_3 \\ \Delta k_\xi p_5 \\ \Delta k_\xi p_7 \\ \Delta k_\xi p_{-1} \\ \Delta k_\xi p_{-3} \\ \Delta k_\xi p_{-5} \end{Bmatrix} \text{ and } \mathbf{b}=\begin{Bmatrix} -k_0 R_{0_{\mathrm{Re}}} \\ \left(\omega^2 m_1+\omega^2 I_p\left(t_1^d\right)^2-k_1\right)R_{1_{\mathrm{Re}}} \\ \left(4\omega^2 m_2+2\omega^2 I_p\left(t_2^d\right)^2-k_2\right)R_{2_{\mathrm{Re}}} \\ \left(9\omega^2 m_3+3\omega^2 I_p\left(t_3^d\right)^2-k_3\right)R_{3_{\mathrm{Re}}} \\ \left(25\omega^2 m_5+5\omega^2 I_p\left(t_5^d\right)^2-k_5\right)R_{5_{\mathrm{Re}}} \\ \left(49\omega^2 m_7+7\omega^2 I_p\left(t_7^d\right)^2-k_7\right)R_{7_{\mathrm{Re}}} \\ \left(\omega^2 m_{-1}-\omega^2 I_p\left(t_{-1}^d\right)^2-k_{-1}\right)R_{-1_{\mathrm{Re}}} \\ \left(9\omega^2 m_{-3}-3\omega^2 I_p\left(t_{-3}^d\right)^2-k_{-3}\right)R_{-3_{\mathrm{Re}}} \\ \left(25\omega^2 m_{-5}-5\omega^2 I_p\left(t_{-5}^d\right)^2-k_{-5}\right)R_{-5_{\mathrm{Re}}} \\ -k_0 R_{0_{\mathrm{Im}}} \\ \left(\omega^2 m_1+\omega^2 I_p\left(t_1^d\right)^2-k_1\right)R_{1_{\mathrm{Im}}} \\ \left(4\omega^2 m_2+2\omega^2 I_p\left(t_2^d\right)^2-k_2\right)R_{2_{\mathrm{Im}}} \\ \left(9\omega^2 m_3+3\omega^2 I_p\left(t_3^d\right)^2-k_3\right)R_{3_{\mathrm{Im}}} \\ \left(25\omega^2 m_5+5\omega^2 I_p\left(t_5^d\right)^2-k_5\right)R_{5_{\mathrm{Im}}} \\ \left(49\omega^2 m_7+7\omega^2 I_p\left(t_7^d\right)^2-k_7\right)R_{7_{\mathrm{Im}}} \\ \left(\omega^2 m_{-1}-\omega^2 I_p\left(t_{-1}^d\right)^2-k_{-1}\right)R_{-1_{\mathrm{Im}}} \\ \left(9\omega^2 m_{-3}-3\omega^2 I_p\left(t_{-3}^d\right)^2-k_{-3}\right)R_{-3_{\mathrm{Im}}} \\ \left(25\omega^2 m_{-5}-5\omega^2 I_p\left(t_{-5}^d\right)^2-k_{-5}\right)R_{-5_{\mathrm{Im}}} \end{Bmatrix}
$$

In identification, the unknown parameter vector **x,** Equation (4.36) takes the following form

$$
\mathbf{x}=\left(\mathbf{A}^T\mathbf{A}\right)^{-1}\mathbf{A}^T\mathbf{b} \tag{5.2}
$$

The identification of **x** is reliable while using information for multiple speeds of interest. On combining above equations for different spin speeds, ω_1, ω_2, ...,ω_n, (with the assumption that parameters to be estimated are speed-independent) may be written as

$$\begin{bmatrix} \mathbf{A}(\omega_1) \\ \mathbf{A}(\omega_2) \\ \vdots \\ \mathbf{A}(\omega_n) \end{bmatrix} \mathbf{x} = \begin{Bmatrix} \mathbf{b}(\omega_1) \\ \mathbf{b}(\omega_2) \\ \vdots \\ \mathbf{b}(\omega_n) \end{Bmatrix} \tag{5.3}$$

Equation (4.38)is utilized to estimate parameters of the cracked rotor system and are summarized in Table 5.5.

Table 5.5 Estimated rotor parameters from experimental data

Parameters	15, 16 and 17 Hz combined speeds	18, 19 and 20 Hz combined speeds	15 through 20Hz combined speeds
c_E(Nsm^{-1})	1291.9967	1775.0819	1377.2959
c_H(Nsm^{-1})	483.5822	311.0272	418.0876
e (10^{-4} m)	10.1009	8.3721	1.8464
ϕ (deg)	173.4	-179.3	176.2
$\Delta k_\xi p_0$	-11987.0984	-9913.9144	-9434.5097
$\Delta k_\xi p_1$	231606.6802	276027.9744	-8341.9619
$\Delta k_\xi p_2$	-65026.7530	-88689.1288	-70677.4922
$\Delta k_\xi p_3$	29917.1322	68000.1890	43761.9400
$\Delta k_\xi p_5$	-44649.7133	-31458.0987	-34736.0346
$\Delta k_\xi p_7$	-16868.7076	-23160.3580	-18251.1669
$\Delta k_\xi p_{-1}$	-285337.2953	-341353.1149	-304201.2771
$\Delta k_\xi p_{-3}$	11526.3482	38653.1516	23014.2936
$\Delta k_\xi p_{-5}$	-9579.1544	-12701.7005	-10344.1239

For different combined speeds, such as the first combined speeds for 15 Hz, 16 Hz, 17 Hz, the second combined speeds for 18 Hz, 19 Hz and 20 Hz and the final combined speeds for all 15 Hz through 20 Hz. It is observed from Table 5.5, that the obtained estimates of the product of crack stiffness parameter and participation factor ($\Delta k_{\xi} p_{i}$) are maintaining consistency (the estimated parameters for all combined speeds lie between estimates of parameters for lower speeds range and higher speed range) except for 1X harmonic. Since the bow and unbalance forces also lie at 1X harmonic. Even the bow effect was removed by slow roll rotor displacement, but still, it is affecting the estimates of the disc eccentricity and its phase. However, the consistency in estimates has been seen in the stationary damping and the rotating damping.

5.5 Validation through numerical simulations

In this section, a numerical simulation has been done through MATLAB^{TM} Simulink model based on test rig configuration and estimated parameters through experimental responses and data provided in Tables 5.1 and 5.5. Herein, the Simulink model developed based on EOMs illustrated in Equation (4.1), and it generates time domain responses for different rotor speeds. The Simulink block for the proposed rotor system is developed. The simulation runs for 8 s duration to obtain responses and is considered for complete cycles (n) of the rotor rotation. The sampling time is kept the same as that used in experimentally acquired data.

The generated numerical responses are used to generate the full spectrum amplitudes for 15 Hz and 20 Hz rotor speeds, and are shown in Figures 5.12(b) and 5.13(b), respectively. Tables 5.6 shows that the most of higher amplitudes are similar in the experimental and numerical full spectra, as well as lower amplitudes for 15 Hz and 20 Hz rotor speed. The similarity the full spectrum amplitudes from experimental data and numerical generated data validates the identification algorithm.

Table 5.6 Validation amplitudes at different harmonics of full spectrum in experimental and simulation

Frequency	15 Hz rotor spin speed Experimental (10^{-5} m)	Simulation (10^{-5} m)	20 Hz rotor spin speed Experimental (10^{-5} m)	Simulation (10^{-5} m)
0	0.1758	0.2320	0.1141	0.1254
ω	0.7332	1.008	1.3679	1.6481
2ω	1.0140	0.9537	0.9997	0.8408
3ω	0.3605	0.4686	0.6361	0.3747
5ω	0.7774	0.2305	0.4044	0.1636
7ω	0.0987	0.0792	0.0861	0.0527
$-\omega$	4.4959	4.3631	4.6157	4.0041
-3ω	0.4241	0.2149	0.4658	0.1689
-5ω	0.0832	0.0624	0.0549	0.0448

The identified multiple participation factor and crack stiffness product parameter ($\Delta k_{\xi} p_i$) are illustrated in Table 5.5. It is used to produce the crack force according to Equation (4.20) with transverse additive stiffness (Δk_{22}) without rotational additive stiffness (Δk_{44}) after dynamic condensation, i.e., on elimination of the slave part, as is given in Figure 5.14. In Figures 5.14 (a) and 5.14 (b), the full spectrum of the crack force for 15 Hz and 20 Hz rotor speed, respectively,are shown by using of the identified parameters, $\Delta k_{\xi} p_i$, for combined speeds (15 through 20 Hz).

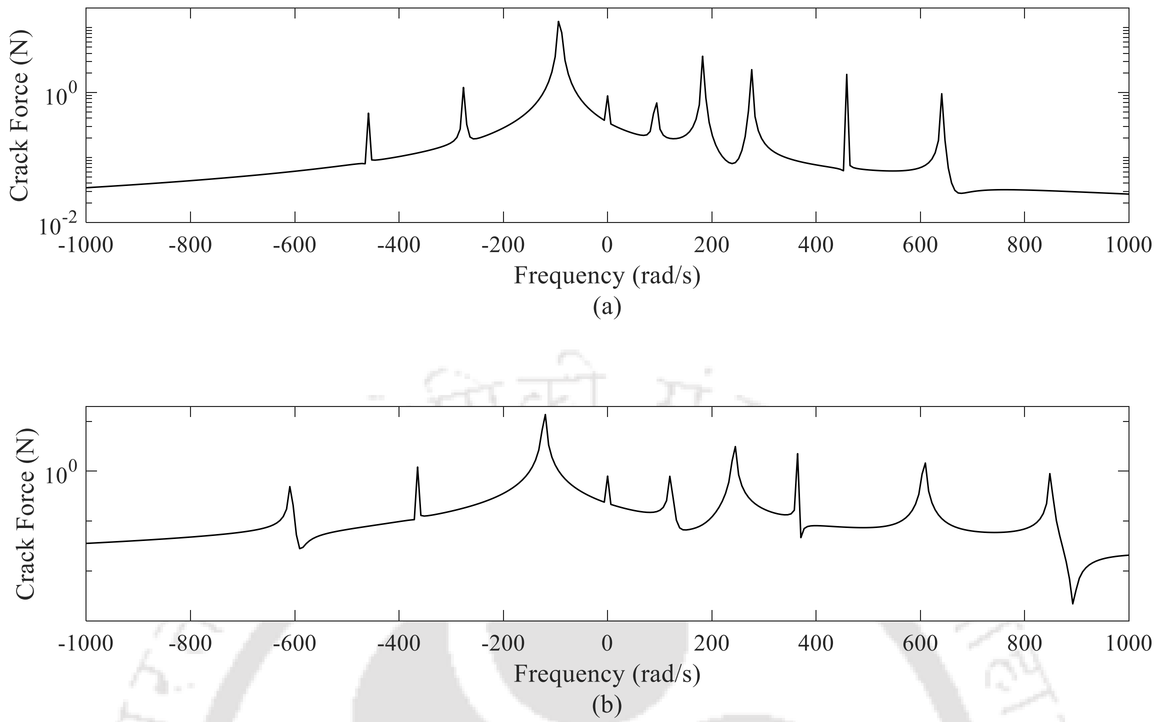

Figure 5.14 Crack force response at (a) 15 Hz spin speed (b) 20 Hz spin speed

5.6 Conclusions

This chapter contain the experimental identification of fault parameters of an offset discrotor system. The estimated fault parameters such as internal damping and external damping, unbalance and additive stiffness of a rotor bearing system is presented. The rotor containing fatigue crack on it is developed for laboratory test. The measured responses converted in to full spectrum and are used in the developed identification algorithm method is used which has been discussed in Chapter 4 for estimation of different fault parameters. The following are the conclusions drawn from the present chapter

- The full spectrum amplitude and phase are compared using both regression and FFT based method found to be quite similar.

- The shaft residual bow and sensor gap present in the rotor system highly affects the amplitude of vibration and are removed from the first harmonic and zeroth harmonic of the spin speed of the rotor for accurate estimation of the parameters. The orbit plots of measured responses with bow and sensor gap and after removal of bow sensor gap are compared.
- The estimated fault parameters through the developed identification algorithm are used in the numerical simulation and find its viability in the full spectrum response.
- The behavior responses due to crack force are presented for the different spin speeds by utilizing the estimated parameters that are present in multiplication form of additive stiffness and participation factors.

The FEM analysis of rotor system with flexible bearings and multiple discs is discussed in the next chapter. The identification algorithm will be developed and tested its sensitivity through numerical simulation.

CHAPTER 6

Finite element model based identification of internal and external damping of a cracked rotor-bearing system

The present chapter deals with development of an identification methodology for a more realistic flexible-shaft flexible-bearing rotor system with the help of finite element modelling technique. Herein, apart from the internal and external damping, unbalances in rotor, crack additive stiffness and bearing dynamic parameters are also estimated. Numerical testing of the identification methodology has been done on a two-disc cracked rotor supported on two flexible bearings.

6.1 Introduction

The proposedwork identifies both the internal and external damping in a cracked rotor-bearing system based on finite element model. Identifying distinctly these two types of damping is very important since their relative values contribute in generation of instability of the rotor systemabove its critical speed. Additionally, dynamic unbalances and additive crack stiffness have also been identified as discussed in Chapters 2-5. Development of the rotor crack is uncertain and imperceptible; it can propagate by fatigue loading and may lead to catastrophic failure. During whirling of rotor the faces of rotor crack rub due to opening and closure of the crack, and it contributes to the internal damping. The present work considers a model-based analysis and identification in a transverse cracked shaft with offset discs having gyroscopic effects. The transverse crack is modelled using a switching function, which gives multiple harmonics in the forward and backward modes of rotor responses. These responses are converted into full spectrum (amplitude and phase) to be used in the developed parameter identification procedure. Estimation of parameters are checked in the presence of measurement noise in the responses.

6.2 System rotor model

This section illustrates the configuration of the rotor model, and then the static and dynamic rotor analyses have been performed. The rotor consists of a cracked shaft model by incorporating the internal damping and considering of the gyroscopic effect owing to offset discs. Moreover, it includes the external damping and unbalances. Then generation of numerical responses have been described. In this work, a rotor model configuration is considered with a transverse crack and offset discs located on the shaft span as shown in Figure 6.1. The location of the crack is assumed to be known since already lot of research have been conducted on the detection and localization of crack (Karthikeyan and Tiwari, 2010). The torsional and axial vibration effects have been ignored. The stiffness of shaft affects due to the transverse crack and it provides local flexibility and gives multiple harmonics in vibration responses. In the figure O is the origin on the bearing centre line and at the left bearing, *z*-axis is along the bearing axis and *x*-axis is in the vertical downward direction (i.e. along the direction of gravity). Figure 6.2 (a) and (b) represents the typical displacements with sign convention of the disc in *y*-*z* plane and *x*-***z*,** plane respectively. Herein, u_{x0} and φ_{y0}represent thetransverse translational and rotational displacements of the shaft at the disc location due to self-weight (i.e., in the static condition), respectively.

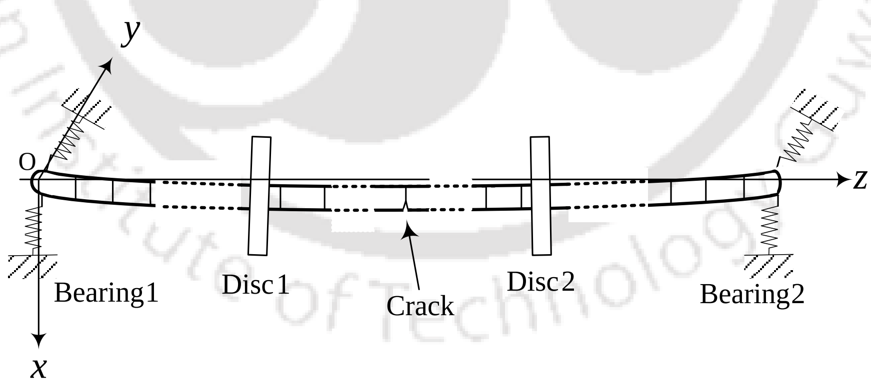

Figure 6.1A flexible rotor system in the presence of a transverse crack supported by flexible bearings

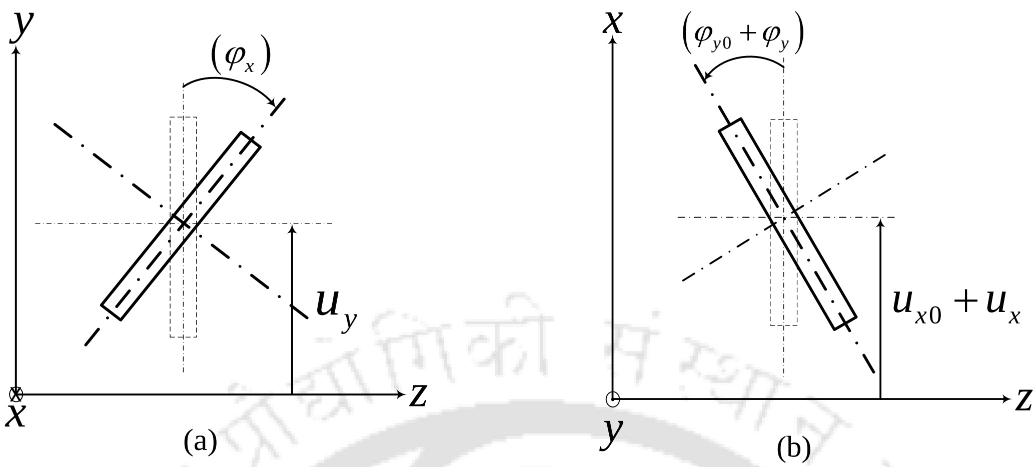

Figure 6.2 A typical disc displacement (a) in y-z plane (b) x-z plane.

Transverse translational and rotational displacement vectors at disc location are expressed as

$$\mathbf{u}(s,t)=\begin{Bmatrix} u_{x0}(s)+u_x(s,t) \\ u_y(s,t) \end{Bmatrix} \tag{6.1}$$

and

$$\boldsymbol{\varphi}(s,t)=\begin{Bmatrix} \varphi_{y0}(s)+\varphi_y(s,t) \\ \varphi_x(s,t) \end{Bmatrix} \tag{6.2}$$

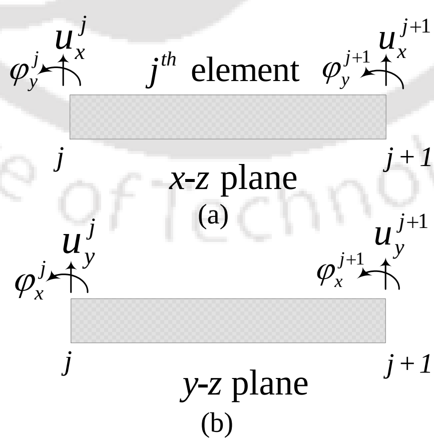

Figure 6.3 The j^{th} finite element with node numbers and field variables

Figure 6.3 represents an element with two nodes, j^{th} and $(j+1)^{th}$. For j^{th} node, $\mathbf{q}_{0j}$ represents the static displacement vector (or equilibrium position vector), which consists of transverse translational and rotational (slope) displacements due to the static load, and it is measured from the bearing centre-line of the rotor system. Whereas, $\mathbf{q}_{vj}$ is time dependent dynamic displacement vector, which consists of transverse translational and rotational displacements of j^{th} node of the element from the static equilibrium position of the rotor.

$$\mathbf{q}_j(t) = \mathbf{q}_{0j} + \mathbf{q}_{vj}(t) = \begin{Bmatrix} u_{x0j} \\ 0 \\ \varphi_{y0j} \\ 0 \end{Bmatrix} + \begin{Bmatrix} u_{xj}(t) \\ u_{yj}(t) \\ \varphi_{yj}(t) \\ \varphi_{xj}(t) \end{Bmatrix} \tag{6.3}$$

With complex quantities u_c and φ_c defined as $u_c = u_x + \mathrm{j}u_y$ and $\varphi_c = \varphi_y + \mathrm{j}\varphi_x$, the complex dynamic displacement vector is formed as

$$\mathbf{q}_{vj}^c(t) = \begin{Bmatrix} u_{xj}(t) + \mathrm{j}u_{yj}(t) \\ \varphi_{yj}(t) + \mathrm{j}\varphi_{xj}(t) \end{Bmatrix} \text{ and } \mathbf{q}_{0j}^c = \begin{Bmatrix} u_{0j} \\ \varphi_{0j} \end{Bmatrix} \tag{6.4}$$

6.3 Derivation of damping and crack forces

This section discusses the external and internal damping models along with the crack model. The viscous damping model is assumed for bearings, which is considered as the external damping. The internal damping considered due to rubbing between two faces of the crack, which is present in the rotor shaft as shown in Figure 6.1.

6.3.1 Damping force

Addition of external damping forces can be considered at relevant node points of shaft as per attachment of bearings and have fixed direction of application. The internal damping C_H has been considered mainly due to rubbing of rotating crack faces, the damping force due to this is present in the rotating frame of reference. Let ξ and η are rotating coordinate axes. The crack front direction is considered in the direction of ξ axis as shown in Figure 6.4. Transverse translational displacement of disc in rotating coordinates (ξ, η) are shown in Figure 6.4, where ω is the shaft spin speed and t is the time. Points C and G represent the geometric centre and centre of gravity of the disc, respectively. The eccentricity of disc is e_n, and its phase is ϕ_n, where n represent the disc number.

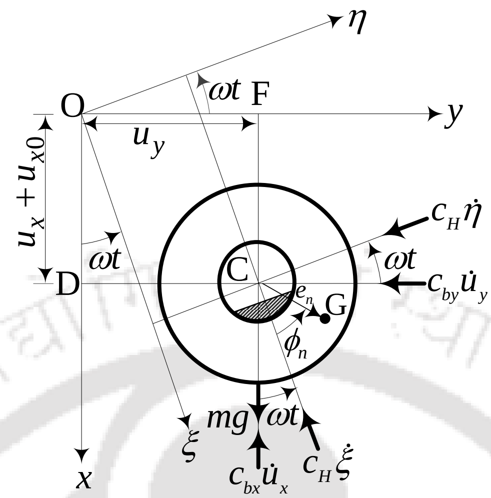

Figure 6.4 The disc motion owing to unbalance and damping force with respect to the fixed and rotating frame of references

Forces due to the internal damping (c_H) at crack in rotating coordinate system, and the external damping (c_{bx} and c_{by}) at bearings and the gravity in stationary coordinate system are shown in Figure 6.4. The internal damping comes, generally, on the shaft owing to various reasons, like the rubbing between of two faces of a crack, change in stress concentration at the crack during its opening and closure, and rubbing between disc and shaft, material hysteretic, etc. Hence, the combined form of rubbing and hysteresis is assumed to appear as the internal viscous damping factor $c_H$in the ξ and η rotating coordinate directions. These damping forces in stationary coordinate system can be written as

$$f_{xd} = c_H\dot{\xi}\cos\omega t - c_H\dot{\eta}\sin\omega t + c_{bx}\dot{u}_x \tag{6.5}$$

$$f_{yd} = c_H\dot{\xi}\sin\omega t + c_H\dot{\eta}\cos\omega t + c_{by}\dot{u}_y \tag{6.6}$$

Relations of responses between the rotating and stationary frame of references on considering of the static deflection are

$$\xi = (u_{x0} + u_x)\cos\omega t + u_y\sin\omega t;\quad \eta = -(u_{x0} + u_x)\sin\omega t + u_y\cos\omega t \tag{6.7}$$

With $\mathrm{j}=\sqrt{-1}$. Also, the complex displacement $u_c = u_x + \mathrm{j}u_y$ and the conjugate complex displacement $u_c^* = u_x - \mathrm{j}u_y$ and their derivatives are $\dot{u}_c = \dot{u}_x + \mathrm{j}\dot{u}_y$ and, $\dot{u}_c^* = \dot{u}_x - \mathrm{j}\dot{u}_y$. Hence, on combining damping forces in complex form, we get

$$f_{cd} = -\mathrm{j}u_{x0}\omega c_H + c_H\left(\dot{u}_c - \mathrm{j}\omega u_c\right) + \tfrac{1}{2}\left\{c_{bx}\left(\dot{u}_c + \dot{u}_c^*\right) + c_{by}\left(\dot{u}_c - \dot{u}_c^*\right)\right\} \tag{6.8}$$

Where the complex damping force is $f_{cd} = f_{xd} + \mathrm{j}f_{yd}$. The external damping force at bearing is f_{Ed} and the internal damping force owing to crack is f_{Hd}. In vector form, it takes the following form

$$\mathbf{f}_{Ed} = \frac{1}{2}\begin{Bmatrix} c_{bx}\left(\dot{u}_c + \dot{u}_c^*\right) + c_{by}\left(\dot{u}_c - \dot{u}_c^*\right) \\ 0 \end{Bmatrix} \text{ and } \mathbf{f}_{Hd} = \begin{Bmatrix} -\mathrm{j}u_{x0}\omega c_H + c_H\left(\dot{u}_c - \mathrm{j}\omega u_c\right) \\ 0 \end{Bmatrix} \tag{6.9}$$

In the presence of global stiffness $\mathbf{K}$, the overall static deflection due to discs attached on to the shaft is

$$\mathbf{q}_0^c = \mathbf{K}^{-1}\mathbf{f}_{\mathbf{st}} \tag{6.10}$$

with

$$[\mathbf{K}] = [\mathbf{K}]_{\mathbf{s}} + [\mathbf{K}]_{\mathbf{b}} \text{ and } \mathbf{f}_{st_n} = \begin{Bmatrix} m_n g \\ 0 \end{Bmatrix} \tag{6.11}$$

where$n$ indicate the disc number.

6.4 Crack force model

The direction of transverse loads (forces and moments) on a cracked shaft is shown in Figure 4.3 (Chapter 4). Variable p with subscripts 1, 2 and 3 represent forces respectively in z, x and y directions, and with subscripts 4, 5 and 6 represent moments respectively in z, x and y directions.

Shaft crack forces are modeled based on a switching crack assumption discussed in Chapter 4 and Equation (4.15) is given as

$$\mathbf{f}_{\mathbf{cr}}(t)=\frac{1}{2}\sigma(t)\begin{Bmatrix}\Delta k_{22}u_{x0}(1+\cos 2\omega t)\\ \Delta k_{22}u_{x0}\sin 2\omega t\\ \Delta k_{44}\varphi_{y0}(1+\cos 2\omega t)\\ \Delta k_{44}\varphi_{y0}\sin 2\omega t\end{Bmatrix} \tag{6.12}$$

The shaft crack model with additive stiffness excitation function is chosen based on Fourier series, which considers a switching crack excitation function (SCEF) as $\sigma(t)$. A detail description of the SCEF has already been discussed in Chapters 2 through 5 (e.g., section 2.2.2) and is given as,

$$\sigma(t)=\frac{1}{2}+\frac{2}{\pi}\cos(\omega t)-\frac{2}{3\pi}\cos 3(\omega t)+\frac{2}{5\pi}\cos(5\omega t)-\frac{2}{7\pi}\cos(7\omega t)+\cdots \tag{6.13}$$

As discussed in Chapters 2 through 5 (e.g., section 2.2.2) Equation (6.12) can be written, as

$$\tfrac{1}{2}\sigma(t)\left(1+e^{2\mathrm{j}\omega t}\right)=\left.\begin{matrix}0.25+0.319e^{\mathrm{j}\omega t}+0.25e^{2\mathrm{j}\omega t}+0.106e^{3\mathrm{j}\omega t}-0.021e^{5\mathrm{j}\omega t}\\ +0.009e^{7\mathrm{j}\omega t}+0.106e^{-\mathrm{j}\omega t}-0.021e^{-3\mathrm{j}\omega t}+0.009e^{-5\mathrm{j}\omega t}\end{matrix}\right\} \tag{6.14}$$

Equation (6.14), in a general form, is expressed as

$$\frac{1}{2}\sigma(\mathrm{t})\left(1+\mathrm{e}^{2\mathrm{j}\omega\mathrm{t}}\right)=\sum_{i=-\infty}^{i=\infty}p_i e^{\mathrm{j}i\omega t} \tag{6.15}$$

In Equation (6.15) , p_i denotes the coefficient of i^{th} term of the harmonic function of the crack force excitation, and is also called as the *participation factor* of individual harmonics. Finally, the crack force vector takes the following form

$$\bar{\mathbf{f}}_{\mathbf{cr}}=\begin{Bmatrix}\Delta k_{22}u_{x0}\\ \Delta k_{44}\varphi_{y0}\end{Bmatrix}\sum_{i=-\infty}^{i=\infty}p_i e^{\mathrm{j}i\omega t} \tag{6.16}$$

6.5 Unbalance and Gyroscopic effect

Discs on the shaft, having individual eccentricity and its phase produce unbalance forces and due to spinning and precession of offset discs the gyroscopic moments are experienced. The force and moment vectors in the complex form is given as

$$\mathbf{M}_{dn}\ddot{\mathbf{q}}_{dn}-\omega\mathbf{G}_{dn}\dot{\mathbf{q}}_{dn}=\mathbf{f}_{dn} \tag{6.17}$$

With

$$\mathbf{f}_{unb} = \begin{Bmatrix} m_n e_n \omega^2 \\ 0 \end{Bmatrix} \mathrm{e}^{\mathrm{j}(\omega t + \phi_n)}; \qquad \mathbf{M}_{dn} = \begin{bmatrix} m_n & 0 \\ 0 & I_{dn} \end{bmatrix} \qquad \text{and} \qquad \mathbf{G}_{dn} = \mathrm{j}\begin{bmatrix} 0 & 0 \\ 0 & -I_{pn} \end{bmatrix}$$

where the mass matrix of n^{th} disc is $\mathbf{M}_{dn}$ and the gyroscope matrix is $\mathbf{G}_{dn}$.

6.6 Bearing force model

The force owing to the flexible bearing can be considered in relations to the stiffness and damping in the transverse direction and are specified as

$$\mathbf{f}_{br} = \begin{Bmatrix} k_{bx} u_x \\ k_{by} u_y \\ 0 \\ 0 \end{Bmatrix} + \mathbf{f}_{Ed} \tag{6.18}$$

where, k_{bx} and k_{by} are the bearing stiffness along the direction of x and y respectively, and $\mathbf{f}_{Ed}$ is the external damping force vector due to bearing as illustrated in Section 6.3.1. Equation (6.18)is written in complex terms, as

$$\mathbf{f}_{br} = \begin{Bmatrix} \frac{1}{2}\left\{ k_{bx}\left(u_c + u_c^*\right) + k_{by}\left(u_c - u_c^*\right) \right\} \\ 0 \end{Bmatrix} + \mathbf{f}_{Ed} \tag{6.19}$$

These force vectors defined above are used in the finite element formulation of the rotor-bearing system.

6.7 Formulation of Global Equations of Motion

The rotor system considers a transverse crack, rigid discs, internal damping due to rubbing of crack faces and flexible bearings. Equations of motion of all sub-models are utilized to form global EOMs. The shaft is discretized into n finite elements with 4-DOFs (2 translational and 2 rotational displacements) at each node point as shown in Figure 6.3.

6.7.1 Shaft sub-model

The equation of motion for a shaft element is given as

$$\mathbf{M}_s^{(\mathbf{e})}\ddot{\mathbf{q}}_s^{(n\mathbf{e})} + \left(C^{(e)} - \omega G^{(e)}\right)\dot{\mathbf{q}}_s^{(n\mathbf{e})} + \mathbf{K}_s^{(e)}\mathbf{q}_s^{(n\mathbf{e})} = \mathbf{f}^{(ne)} \tag{6.20}$$

Where,

$$\mathbf{q}_s^{(n\mathbf{e})} = \begin{bmatrix} u_c^j & \varphi_c^j & u_c^{j+1} & \varphi_c^{j+1} \end{bmatrix} \tag{6.21}$$

Herein, $\mathbf{q}_s^{(n\mathbf{e})}$ represents the nodal displacement vector of an element, $\mathbf{f}^{(ne)}$represents the force vector, u_c and φ_c are the complex displacements at nodes of the nodal element. $\mathbf{M}^{(e)}$,$\mathbf{C}^{(e)}$, $\mathbf{G}^{(e)}$ and $\mathbf{K}_s^{(e)}$ represent the elemental mass, external damping, gyroscopic and stiffness matrices of the shaft, respectively (Tiwari, 2017; Goldman and Muszynska, 1999).

6.7.2 Crack force sub-model

The transverse crack force of switching behaviour is introduced at the particular node, as discussed in Section 6.4. The expression is given as

$$\mathbf{f}_{cr} = \left(\Delta k_{22}\mathbf{q}_{uc0} + \Delta k_{44}\mathbf{q}_{\varphi c0}\right)\sum_{i=-\infty}^{i=\infty} p_i e^{\mathrm{j}i\omega t} \tag{6.22}$$

with

$$\mathbf{q}_{uc0} = \begin{Bmatrix} u_{x0} + \mathrm{j}u_{y0} \\ 0 \end{Bmatrix} = \begin{Bmatrix} u_{x0} \\ 0 \end{Bmatrix} \text{and}\, \mathbf{q}_{\varphi c0} = \begin{Bmatrix} 0 \\ \varphi_{y0} + \mathrm{j}\varphi_{x0} \end{Bmatrix} = \begin{Bmatrix} 0 \\ \varphi_{y0} \end{Bmatrix}$$

Herein, vector $\mathbf{q}_{uc0}$ represents the complex static translational displacement vector and vector $\mathbf{q}_{\varphi c0}$represents the complex rotational displacement vector at the crack location. The equation is further modified as

$$\mathbf{f}_{cr}(t) = \left(\Delta k\mathbf{q}_{c0}\right)\sum_{i=-\infty}^{i=\infty} p_i e^{\mathrm{j}i\omega t} \tag{6.23}$$

with,

$$\Delta k\mathbf{q}_{c0} = \left(\Delta k_{22}\mathbf{q}_{uc0} + \Delta k_{44}\mathbf{q}_{\varphi c0}\right)$$

6.7.3 Disc sub-model

The disc is modelled as a rigid disc having mass and moment of inertia terms at the node of its location in the assumed configuration. The equation of motion for the rigid disc is expressed as

$$\mathbf{M}_d\ddot{\mathbf{q}}_d - \omega\mathbf{G}_d\dot{\mathbf{q}}_d = \mathbf{f}_d \tag{6.24}$$

Herein, vectors $\mathbf{q}_d$ and $\mathbf{f}_d$ are the disc displacement and force vectors respectively, at the disc location. Matrices $\mathbf{M}_d$ and $\mathbf{G}_d$ are disc mass and gyroscopic matrices, respectively; and are illustrated in Section 6.5.

6.7.4 Sub-model of support bearings

The mathematical model of the support bearing force is given as

$$\frac{1}{2}\left\{k_{bx}\left(\mathbf{u}_{cb} + \mathbf{u}_{cb}^{*}\right) + k_{by}\left(\mathbf{u}_{cb} - \mathbf{u}_{cb}^{*}\right)\right\} + \frac{1}{2}\left\{c_{bx}\left(\dot{\mathbf{u}}_{cb} + \dot{\mathbf{u}}_{cb}^{*}\right) + c_{by}\left(\dot{\mathbf{u}}_{cb} - \dot{\mathbf{u}}_{cb}^{*}\right)\right\} = \mathbf{f}_{br} \tag{6.25}$$

Where, the vectors, $\mathbf{u}_{cb}$, $\mathbf{u}_{cb}^{*}$, $\dot{\mathbf{u}}_{cb}$ and $\dot{\mathbf{u}}_{cb}^{*}$, contain the complex displacement, its conjugates and velocities, respectively, at the node location.

6.7.5 Internal damping sub-model

The internal damping force from Sections 6.3.1 is given as

$$-\mathrm{j}\omega c_H\mathbf{u}_{x0} + c_H\left(\dot{\mathbf{u}}_c - \mathrm{j}\omega\mathbf{u}_c\right) = \mathbf{f}_{Hd} \tag{6.26}$$

In the above expression, the vector $\mathbf{u}_{x0}$ is the static deflection in the vertical direction, the vectors $\mathbf{u}_c$ and $\dot{\mathbf{u}}_c$ contain complex displacement, and its velocity, respectively, at the node location of crack.

6.8 Assembled equations of motion of sub-models

The analysed elemental equations in the previous subsection in the form of sub-model for each individual forces, such as the shaft, crack, disc, gyroscopic effects, support bearing and the internal damping are combined together. The assembled equations of motion of the rotor with the application of boundary conditions is given as

$$\mathbf{M}_s\ddot{\mathbf{q}} + \left(\mathbf{C}_s - \omega\mathbf{G}_s\right)\dot{\mathbf{q}} + \mathbf{K}_s\mathbf{q} = \mathbf{f}_{unb} + \mathbf{f}_{cr} - \mathbf{f}_{br} - \mathbf{f}_{Hd} - \mathbf{f}_d \qquad (6.27)$$

In Equation (6.27), the right side force vector $\mathbf{f}_d$, is merge in left side and force vectors $\mathbf{f}_{unb}$, $\mathbf{f}_{cr}$, , $\mathbf{f}_{br}$ and $\mathbf{f}_{Hd}$are converted in the following form

$$\mathbf{M}\ddot{\mathbf{q}} + \left(\mathbf{C} - \omega\mathbf{G}\right)\dot{\mathbf{q}} + \mathbf{K}\mathbf{q} = \mathbf{f}_{unb} + \mathbf{f}_{cr} - \mathbf{f}_{br} - \mathbf{f}_{Hd} \qquad (6.28)$$

Herein, **M**, **C**, **G** and **K** are the global mass, damping, gyroscopic and stiffness matrices, respectively, and $\mathbf{f}_{unb}$, $\mathbf{f}_{cr}\mathbf{f}_{br}$ and $\mathbf{f}_{Hd}$ are the unbalance, crack, bearing and internal damping forces, respectively.

6.9 Responses in time and frequency domain

The unbalance force, crack force, bearing force and internal damping force are presented as per location of nodal points as $\mathbf{f}_{unbn}$ **=**$\mathbf{f}_{unbn} \circ \lambda_{unbn}$, $\mathbf{f}_{cr} = \mathbf{f}_{cr} \circ \lambda_{cr}$, $\mathbf{f}_{br} = \mathbf{f}_{brn} \circ \lambda_{brn}$ and $\mathbf{f}_{Hd} = \mathbf{f}_{Hd} \circ \lambda_{Hd}$, respectively, for the illustration in nodal displacement form. Herein, operator "∘" denotes the element wise multiplication andλ_{unbn}, λ_{cr}, λ_{brn} and λ_{Hd}, provides the location of the force vector$\mathbf{f}_{unbn}$, $\mathbf{f}_{cr}$, $\mathbf{f}_{brn}$ and $\mathbf{f}_{Hd}$ at right end of Equation (6.28). The unbalance force and bearing force are at more than one node, with λ_{unbn}, $\boldsymbol{\lambda}_{cr}$, $\boldsymbol{\lambda}_{brn}$ and $\boldsymbol{\lambda}_{Hd}$ are given as

$$\lambda_{unbn}=\begin{Bmatrix}\lambda_0 & \lambda_0\\ \vdots & \vdots\\ \lambda_0 & \lambda_0\\ \lambda_r & \vdots\\ \lambda_0 & \lambda_0\\ \vdots & \lambda_r\\ \lambda_0 & \lambda_0\\ \vdots & \vdots\\ \lambda_0 & \lambda_0\end{Bmatrix};\ \lambda_{brn}=\begin{Bmatrix}\lambda_r & \lambda_0\\ \lambda_0 & \vdots\\ \vdots & \lambda_0\\ \lambda_0 & \lambda_0\\ \lambda_0 & \lambda_0\\ \vdots & \vdots\\ \lambda_0 & \lambda_0\\ \vdots & \vdots\\ \lambda_0 & \lambda_r\end{Bmatrix};\lambda_{cr}=\begin{Bmatrix}\lambda_0 & \lambda_0\\ \vdots & \vdots\\ \lambda_0 & \lambda_0\\ \lambda_r & \lambda_\varphi\\ \lambda_0 & \lambda_0\\ \vdots & \vdots\\ \lambda_0 & \lambda_0\\ \vdots & \vdots\\ \lambda_0 & \lambda_0\end{Bmatrix}\text{ and }\lambda_{Hd}=\begin{Bmatrix}\lambda_0\\ \vdots\\ \lambda_0\\ \lambda_r\\ \lambda_0\\ \vdots\\ \lambda_0\\ \vdots\\ \lambda_0\end{Bmatrix} \tag{6.29}$$

Herein, $\lambda_0=\begin{Bmatrix}0\\0\end{Bmatrix}$; $\lambda_r=\begin{Bmatrix}1\\0\end{Bmatrix}$ and $\lambda_\varphi=\begin{Bmatrix}0\\1\end{Bmatrix}$ and 'n' indicates different row according to the node number where the disc/bearing is present on the shaft node. The combined form of Equations (6.28) and (6.29) is expressed in the following form

$$\mathbf{M}\ddot{\mathbf{q}}+\left(\mathbf{C}-\omega\mathbf{G}\right)\dot{\mathbf{q}}+\mathbf{K}\mathbf{q}=\sum_{n=d_1}^{d_2}\mathbf{f}_{unbn}\circ\lambda_{unbn}+\mathbf{f}_{cr}\circ\lambda_{cr}-\sum_{n=br_1}^{br_2}\mathbf{f}_{brn}\circ\lambda_{brn}-\mathbf{f}_{Hd}\circ\lambda_{Hd} \tag{6.30}$$

Equation (6.30)contains the translational and rotational DOFs, in which the rotational DOF measurement is very difficult from the experimental point of view. Therefore, dynamic condensation has been applied for elimination rotational DOFs, which is discussed in the next section.

6.10 Elimination of rotational DOFs based on dynamic condensation

The dynamic condensation technique has been utilized for elimination rotational DOFs, which is present due bending slope of shaft and tilting of disc. The precise measurement of rotational DOF responses in experimental case is a challenging work than in the transverse translational DOF responses. Estimation is expected to be more close to reality if the mathematical model chosen for fitting the experimental data is better representing the test rig and its associated phenomena. So by including higher effects (gyroscopic effects, rotational inertia, speed), the estimates are expected to be more accurate and reliable. To avoid this in Equation (6.30), the dynamic condensation has been applied and it gives transform EOMs, in which only transverse translational displacements are then present. Let the transverse translational displacement vector is $\mathbf{q}_m$ and the transverse rotational displacement vector is $\mathbf{q}_s$, which are referred as the master and slave DOFs, respectively. The moment corresponding to the crack rotational DOFs are ignored in the development of the transform matrix. On partitioning of matrices corresponding to the master and slave DOFs, Equation (6.30) takes the following form

$$\{\mathbf{q}_m\} = [I]\{\mathbf{q}_m\}; \quad \begin{Bmatrix} \mathbf{q}_m \\ \mathbf{q}_s \end{Bmatrix} = \mathbf{T}^D \{\mathbf{q}_m\} \tag{6.31}$$

The statement of the transformation matrix, $\mathbf{T}^D$, according to the dynamic condensation is obtained from Equation (6.31), as

$$\mathbf{T}^D = \begin{Bmatrix} \mathbf{I} \\ \mathbf{L}_i \end{Bmatrix} \tag{6.32}$$

with

$$\mathbf{L}_i = -\left(\mathbf{K}_{ss} - (i\omega)^2 \mathbf{M}_{ss}\right)^{-1} \left(\mathbf{K}_{sm} - (i\omega)^2 \mathbf{M}_{sm}\right)$$

where ω is considered as the central frequency within the range of frequency of interest. The illustration of matrices on the left side after the elimination of slave DOFs are given as

$$\mathbf{M}^d = \left(\mathbf{T}^d\right)^T \mathbf{M}\mathbf{T}^d; \;\; \mathbf{C}^d = \left(\mathbf{T}^d\right)^T \mathbf{C}\mathbf{T}^d; \;\; \mathbf{G}^d = \left(\mathbf{T}^d\right)^T \mathbf{G}\mathbf{T}^d; \;\; \mathbf{K}^d = \left(\mathbf{T}^d\right)^T \mathbf{K}\mathbf{T}^d \tag{6.33}$$

Vectors on the right side of Equation (6.30) are given as

$$\left.\begin{aligned} &\mathbf{f}^d_{unb} = \left(\mathbf{T}^d\right)^T \mathbf{f}_{unb}; \quad \mathbf{f}^d_{cr} = \left(\mathbf{T}^d\right)^T \mathbf{f}_{cr}; \quad \mathbf{f}^d_{br} = \left(\mathbf{T}^d\right)^T \mathbf{f}_{br}; \\ &\mathbf{f}^d_{Hd} = \left(\mathbf{T}^d\right)^T \mathbf{f}_{Hd} \quad \text{and} \quad \Delta k q_{c0} = \Delta k_{22} \mathbf{u}_{x0} \end{aligned}\right\} \tag{6.34}$$

The solution, according to the frequency of forcing term in Equation (6.30), is assumed in the following form

$$\mathbf{q}_m = \mathbf{q}(t) = \mathbf{R}_0 + \sum_{i=1}^{h} \mathbf{R}_i \mathrm{e}^{\mathrm{j}i\omega t} + \sum_{i=1}^{h} \mathbf{S}_i \mathrm{e}^{-\mathrm{j}i\omega t} \tag{6.35}$$

The conjugate of Equation (6.35), which is the complex time domain displacement vector, has the following form

$$\mathbf{q}_m^*(t) = \mathbf{R}_0^* + \sum_{i=1}^{h} \mathbf{R}_i^* \mathrm{e}^{-\mathrm{j}i\omega t} + \sum_{i=1}^{h} \mathbf{S}_i^* \mathrm{e}^{\mathrm{j}i\omega t} \tag{6.36}$$

Herein, i notifies the frequency of forcing harmonics (h is the number of harmonics), t is the time instant, ω is the spin speed of the rotor, $\mathbf{R}_0$ and $\mathbf{R}_0^*$ are displacement vector and its conjugate vector at zeroth harmonic. Similarly, two summation terms indicate for the backward and forward harmonics, respectively. Frequency domain complex displacements are$\mathbf{S}_i$ and $\mathbf{R}_i$, and their conjugates are$\mathbf{S}_i^*$ and$\mathbf{R}_i^*$, respectively.

In force vectors $\mathbf{f}_{unb}$, $\mathbf{f}_{cr}\mathbf{f}_{br}$ and $\mathbf{f}_{Hd}$ in Equation (6.30), and in Equations (6.31) through (6.36), the common terms $\mathrm{e}^{\mathrm{j}i\omega t}$ and $\mathrm{e}^{-\mathrm{j}i\omega t}$ are present in both sides and coefficients of which will be separated and to be utilized in development of identification equations to be discussed in the next section

6.11 Identification procedure

This section illustrates development of the identification procedure after applying boundary conditions on global finite element EOMs. Unknown fault parameters of n^{th} bearing, such as damping and stiffness coefficients are c_{bxn}, c_{byn}, $k_{bxn,}$ and k_{byn}. Similarly, n^{th} disc eccentricity e_n andits phase ϕ_n are at respective disc node. Also, the additive stiffness Δk_{22} and internal damping coefficient c_H are present at a node of the crack. These are considered as unknown value in development of the identification procedure. The arrangement of the λ_{unbn}, $\boldsymbol{\lambda}_{cr}$, $\boldsymbol{\lambda}_{brn}$ and $\boldsymbol{\lambda}_{Hd}$ are also reduced according to the master DOFs. According to node positions, equations of motion, which are in terms of master DOF form, are written as

For zeroth harmonic i =0, we have

$$\mathbf{K}^d R_0 = \left. \begin{array}{c} -\left\{ \frac{k_{bxn}}{2}\left(R_0 + R_0^*\right)_{bn} + \frac{k_{byn}}{2}\left(R_0 - R_0^*\right)_{bn} \right\} \circ \lambda_{bn} \\ \left\{ \mathrm{j}\omega c_H \left(R_0 + u_{x0}\right) + \left(\Delta k_{22} + L_0 \Delta k_{44}\right) u_{x0} p_0 \right\} \circ \lambda_{cr} \end{array} \right\} \tag{6.37}$$

For other harmonic $i \neq 0$

$$\begin{array}{c} \left[-\left(i\omega\right)^2 \mathbf{M}^d + \mathbf{K}^d\right]\left(R_i \mathrm{e}^{\mathrm{j}i\omega t} + S_i \mathrm{e}^{-\mathrm{j}i\omega t}\right) \\ + \mathrm{j}i\omega\left(\mathbf{C}^d - \omega \mathbf{G}^d\right)\left(R_i \mathrm{e}^{\mathrm{j}i\omega t} - S_i \mathrm{e}^{\text{-j}i\omega t}\right) \end{array} = \left. \begin{array}{c} -\frac{k_{bxn}}{2}\left\{\left(R_i + S_i^*\right)\mathrm{e}^{\mathrm{j}i\omega t} + \left(R_i^* + S_i\right)\mathrm{e}^{\text{-j}i\omega t}\right\}_{bn} \circ \lambda_{bn} \\ -\frac{k_{byn}}{2}\left\{\left(R_i - S_i^*\right)\mathrm{e}^{\mathrm{j}i\omega t} - \left(R_i^* - S_i\right)\mathrm{e}^{\text{-j}i\omega t}\right\}_{bn} \circ \lambda_{bn} \\ \text{-j}i\omega \frac{c_{bxn}}{2}\left\{\left(R_i + S_i^*\right)\mathrm{e}^{\mathrm{j}i\omega t} - \left(R_i^* + S_i\right)\mathrm{e}^{\text{-j}i\omega t}\right\}_{bn} \circ \lambda_{bn} \\ \text{-j}i\omega \frac{c_{byn}}{2}\left\{\left(R_i - S_i^*\right)\mathrm{e}^{\mathrm{j}i\omega t} + \left(R_i^* - S_i\right)\mathrm{e}^{\text{-j}i\omega t}\right\}_{bn} \circ \lambda_{bn} \\ + \left(\Delta k_{22} + L_i \Delta k_{44}\right) u_{x0}\left(p_i \mathrm{e}^{\mathrm{j}i\omega t} + p_{-i}\mathrm{e}^{\text{-j}i\omega t}\right) \circ \lambda_{cr} \\ -\mathrm{j}\omega c_H \left\{\left(i-1\right) R_i \mathrm{e}^{\mathrm{j}i\omega t} - \left(i+1\right) S_i \mathrm{e}^{\text{-j}i\omega t}\right\} \circ \lambda_{cr} \\ \mathrm{j}\omega u_{x0} c_H \circ \lambda_{cr} + m_n e_n \mathrm{e}^{\mathrm{j}(\omega t + \theta)} \circ \lambda_{unbn} \end{array} \right\} \tag{6.38}$$

The λ_{unbn}, $\boldsymbol{\lambda}_{cr}$, $\boldsymbol{\lambda}_{brn}$ and $\boldsymbol{\lambda}_{Hd}$ are also reduced according to the location of masters DOFs during the dynamic condensation. For the identification of previously mentioned parameters, the left side of Equation (6.38) takes the following form

$$\mathbf{D}_i = -\left(i\omega\right)^2 \mathbf{M}^d + \mathrm{j}i\omega\left(\mathbf{C}^d - \omega \mathbf{G}^d\right) + \mathbf{K}^d \;\text{ and }\; \mathbf{D}_i^* = -\left(i\omega\right)^2 \mathbf{M}^d - \mathrm{j}i\omega\left(\mathbf{C}^d - \omega \mathbf{G}^d\right) + \mathbf{K}^d \tag{6.39}$$

On separating coefficients of exponentials in Equations (6.37)and(6.38), and are arranged in a matrix form, as

$$\mathbf{Ax} = \mathbf{b} \tag{6.40}$$

with,

$$\mathbf{A}(\omega) = \begin{bmatrix} \mathrm{real}\left(\mathbf{A_1}\right) & \mathrm{real}\left(\mathbf{A}_2\right) & \mathbf{A}_4 & \mathbf{A}_0 & \mathbf{A}_5 & \mathbf{A}_0 & \mathbf{A}_3 \\ \mathrm{Imag}\left(\mathbf{A_1}\right) & \mathrm{Imag}\left(\mathbf{A}_2\right) & \mathbf{A}_0 & \mathbf{A}_4 & \mathbf{A}_0 & \mathbf{A}_5 & \mathbf{A}_0 \end{bmatrix} \text{ and } \mathbf{b}(\omega) = \begin{bmatrix} \mathrm{real}\left(\mathbf{b_1}\right) \\ \mathrm{Imag}\left(\mathbf{b_1}\right) \end{bmatrix}$$

$$
\mathbf{A}_1 = \begin{bmatrix}
0\circ\lambda_1 & 0\circ\lambda_1 & 0\circ\lambda_5 & 0\circ\lambda_5 \\
-0.5\mathrm{j}\omega\left(R_1+S_1^*\right)\circ\lambda_1 & -0.5\mathrm{j}\omega\left(R_1-S_1^*\right)\circ\lambda_1 & -0.5\mathrm{j}\omega\left(R_1+S_1^*\right)\circ\lambda_5 & -0.5\mathrm{j}\omega\left(R_1-S_1^*\right)\circ\lambda_5 \\
0.5\mathrm{j}\omega\left(R_1^*+S_1\right)\circ\lambda_1 & -0.5\mathrm{j}\omega\left(R_1^*-S_1\right)\circ\lambda_1 & 0.5\mathrm{j}\omega\left(R_1^*+S_1\right)\circ\lambda_5 & -0.5\mathrm{j}\omega\left(R_1^*-S_1\right)\circ\lambda_5 \\
-\mathrm{j}\omega\left(R_2+S_2^*\right)\circ\lambda_1 & -\mathrm{j}\omega\left(R_2-S_2^*\right)\circ\lambda_1 & -\mathrm{j}\omega\left(R_2+S_2^*\right)\circ\lambda_5 & -\mathrm{j}\omega\left(R_2-S_2^*\right)\circ\lambda_5 \\
\mathrm{j}\omega\left(R_2^*+S_2\right)\circ\lambda_1 & -\mathrm{j}\omega\left(R_2^*-S_2\right)\circ\lambda_1 & \mathrm{j}\omega\left(R_2^*+S_2\right)\circ\lambda_5 & -\mathrm{j}\omega\left(R_2^*-S_2\right)\circ\lambda_5 \\
-1.5\mathrm{j}\omega\left(R_3+S_3^*\right)\circ\lambda_1 & -1.5\mathrm{j}\omega\left(R_3-S_3^*\right)\circ\lambda_1 & -1.5\mathrm{j}\omega\left(R_3+S_3^*\right)\circ\lambda_5 & -1.5\mathrm{j}\omega\left(R_3-S_3^*\right)\circ\lambda_5 \\
1.5\mathrm{j}\omega\left(R_3^*+S_3\right)\circ\lambda_1 & -1.5\mathrm{j}\omega\left(R_3^*-S_3\right)\circ\lambda_1 & 1.5\mathrm{j}\omega\left(R_3^*+S_3\right)\circ\lambda_5 & -1.5\mathrm{j}\omega\left(R_3^*-S_3\right)\circ\lambda_5 \\
-2.5\mathrm{j}\omega\left(R_5+S_5^*\right)\circ\lambda_1 & -2.5\mathrm{j}\omega\left(R_5-S_5^*\right)\circ\lambda_1 & -2.5\mathrm{j}\omega\left(R_5+S_5^*\right)\circ\lambda_5 & -2.5\mathrm{j}\omega\left(R_5-S_5^*\right)\circ\lambda_5 \\
2.5\mathrm{j}\omega\left(R_5^*+S_5\right)\circ\lambda_1 & -2.5\mathrm{j}\omega\left(R_5^*-S_5\right)\circ\lambda_1 & 2.5\mathrm{j}\omega\left(R_5^*+S_5\right)\circ\lambda_5 & -2.5\mathrm{j}\omega\left(R_5^*-S_5\right)\circ\lambda_5 \\
-3.5\mathrm{j}\omega\left(R_7+S_7^*\right)\circ\lambda_1 & -3.5\mathrm{j}\omega\left(R_7-S_7^*\right)\circ\lambda_1 & -3.5\mathrm{j}\omega\left(R_7+S_7^*\right)\circ\lambda_5 & -3.5\mathrm{j}\omega\left(R_7-S_7^*\right)\circ\lambda_5 \\
3.5\mathrm{j}\omega\left(R_7^*+S_7\right)\circ\lambda_1 & -3.5\mathrm{j}\omega\left(R_7^*-S_7\right)\circ\lambda_1 & 3.5\mathrm{j}\omega\left(R_7^*+S_7\right)\circ\lambda_5 & -3.5\mathrm{j}\omega\left(R_7^*-S_7\right)\circ\lambda_5
\end{bmatrix}
$$

$$
\mathbf{A}_2 = \begin{bmatrix}
-\left(R_{0\mathrm{Re}}\right)\circ\lambda_1 & -\left(R_{0\mathrm{Im}}\right)\circ\lambda_1 & -\left(R_{0\mathrm{Re}}\right)\circ\lambda_5 & -\left(R_{0\mathrm{Im}}\right)\circ\lambda_5 & \mathrm{j}\omega\left(R_0+u_{x0}\right)\circ\lambda_3 \\
-0.5\left(R_1+S_1^*\right)\circ\lambda_1 & -0.5\left(R_1-S_1^*\right)\circ\lambda_1 & -0.5\left(R_1+S_1^*\right)\circ\lambda_5 & -0.5\left(R_1-S_1^*\right)\circ\lambda_5 & 0\circ\lambda_3 \\
-0.5\left(R_1^*+S_1\right)\circ\lambda_1 & 0.5\left(R_1^*-S_1\right)\circ\lambda_1 & -0.5\left(R_1^*+S_1\right)\circ\lambda_5 & 0.5\left(R_1^*-S_1\right)\circ\lambda_5 & 2\mathrm{j}\omega S_1\circ\lambda_3 \\
-0.5\left(R_2+S_2^*\right)\circ\lambda_1 & -0.5\left(R_2-S_2^*\right)\circ\lambda_1 & -0.5\left(R_2+S_2^*\right)\circ\lambda_5 & -0.5\left(R_2-S_2^*\right)\circ\lambda_5 & -\mathrm{j}\omega R_2\circ\lambda_3 \\
-0.5\left(R_2^*+S_2\right)\circ\lambda_1 & 0.5\left(R_2^*-S_2\right)\circ\lambda_1 & -0.5\left(R_2^*+S_2\right)\circ\lambda_5 & 0.5\left(R_2^*-S_2\right)\circ\lambda_5 & 3\mathrm{j}\omega S_2\circ\lambda_3 \\
-0.5\left(R_3+S_3^*\right)\circ\lambda_1 & -0.5\left(R_3-S_3^*\right)\circ\lambda_1 & -0.5\left(R_3+S_3^*\right)\circ\lambda_5 & -0.5\left(R_3-S_3^*\right)\circ\lambda_5 & -2\mathrm{j}\omega R_3\circ\lambda_3 \\
-0.5\left(R_3^*+S_3\right)\circ\lambda_1 & 0.5\left(R_3^*-S_3\right)\circ\lambda_1 & -0.5\left(R_3^*+S_3\right)\circ\lambda_5 & 0.5\left(R_3^*-S_3\right)\circ\lambda_5 & 4\mathrm{j}\omega S_3\circ\lambda_3 \\
-0.5\left(R_5+S_5^*\right)\circ\lambda_1 & -0.5\left(R_5-S_5^*\right)\circ\lambda_1 & -0.5\left(R_5+S_5^*\right)\circ\lambda_5 & -0.5\left(R_5-S_5^*\right)\circ\lambda_5 & -4\mathrm{j}\omega R_5\circ\lambda_3 \\
-0.5\left(R_5^*+S_5\right)\circ\lambda_1 & 0.5\left(R_5^*-S_5\right)\circ\lambda_1 & -0.5\left(R_5^*+S_5\right)\circ\lambda_5 & 0.5\left(R_5^*-S_5\right)\circ\lambda_5 & 6\mathrm{j}\omega S_5\circ\lambda_3 \\
-0.5\left(R_7+S_7^*\right)\circ\lambda_1 & -0.5\left(R_7-S_7^*\right)\circ\lambda_1 & -0.5\left(R_7+S_7^*\right)\circ\lambda_5 & -0.5\left(R_7-S_7^*\right)\circ\lambda_5 & -6\mathrm{j}\omega R_7\circ\lambda_3 \\
-0.5\left(R_7^*+S_7\right)\circ\lambda_1 & 0.5\left(R_7^*-S_7\right)\circ\lambda_1 & -0.5\left(R_7^*+S_7\right)\circ\lambda_5 & 0.5\left(R_7^*-S_7\right)\circ\lambda_5 & 8\mathrm{j}\omega S_7\circ\lambda_3
\end{bmatrix}
$$

$$\mathbf{A}_3 = \begin{bmatrix} u_{x0} p_0 \circ \lambda_3 \\ u_{x0} p_1 \circ \lambda_3 \\ u_{x0} p_{\_1} \circ \lambda_3 \\ u_{x0} p_2 \circ \lambda_3 \\ 0 \circ \lambda_3 \\ u_{x0} p_3 \circ \lambda_3 \\ u_{x0} p_{\_3} \circ \lambda_3 \\ u_{x0} p_5 \circ \lambda_3 \\ u_{x0} p_{\_5} \circ \lambda_3 \\ u_{x0} p_7 \circ \lambda_3 \\ 0 \circ \lambda_3 \end{bmatrix}; \mathbf{A}_4 = \begin{bmatrix} 0 \circ \lambda_2 \\ m_1 \omega^2 \circ \lambda_2 \\ 0 \circ \lambda_2 \\ 0 \circ \lambda_2 \\ 0 \circ \lambda_2 \\ 0 \circ \lambda_2 \\ 0 \circ \lambda_2 \\ 0 \circ \lambda_2 \\ 0 \circ \lambda_2 \\ 0 \circ \lambda_2 \\ 0 \circ \lambda_2 \end{bmatrix}; \; \mathbf{A}_5 = \begin{bmatrix} 0 \circ \lambda_4 \\ m_2 \omega^2 \circ \lambda_4 \\ 0 \circ \lambda_4 \\ 0 \circ \lambda_4 \\ 0 \circ \lambda_4 \\ 0 \circ \lambda_4 \\ 0 \circ \lambda_4 \\ 0 \circ \lambda_4 \\ 0 \circ \lambda_4 \\ 0 \circ \lambda_4 \\ 0 \circ \lambda_4 \end{bmatrix};$$

$$\mathbf{A}_0 = \begin{bmatrix} 0 \circ \lambda_4 \\ 0 \circ \lambda_4 \\ 0 \circ \lambda_4 \\ 0 \circ \lambda_4 \\ 0 \circ \lambda_4 \\ 0 \circ \lambda_4 \\ 0 \circ \lambda_4 \\ 0 \circ \lambda_4 \\ 0 \circ \lambda_4 \\ 0 \circ \lambda_4 \\ 0 \circ \lambda_4 \end{bmatrix}; \; b_1 = \begin{Bmatrix} D_0 R_0 \\ D_1 R_1 \\ D_1^* S_1 \\ D_2 R_2 \\ D_2^* S_2 \\ D_3 R_3 \\ D_3^* S_3 \\ D_5 R_5 \\ D_5^* S_5 \\ D_7 R_7 \\ D_7^* S_7 \end{Bmatrix} \text{ and } \mathbf{x} = \begin{Bmatrix} c_{bx1} \\ c_{by1} \\ c_{bx2} \\ c_{by2} \\ k_{bx1} \\ k_{by1} \\ k_{bx2} \\ k_{by2} \\ c_H \\ e_{1\mathrm{Re}} \\ e_{1\mathrm{Im}} \\ e_{2\mathrm{Re}} \\ e_{2\mathrm{Im}} \\ \Delta k_{22} \end{Bmatrix}$$

Here R_0 and R_0^* are because of zeroth harmonic. The unknown parameter vector is **x** in Equation (6.40) and other matrix/vector, such as **A** and **b,** are known with the help of full spectrum of Equation (6.39) and other rotor parameters.For the evaluation of **x**, Equation (6.40) is expressed in the following form

$$\mathbf{x} = \left(\mathbf{A}^T \mathbf{A}\right)^{-1} \mathbf{A}^T \mathbf{b}$$

The accuracy of identification vector **x** is expected to be better on considering multiple speeds, which will give different rotor displacements according to chosen speeds. Further, Equation (6.40) for combined spin speeds ω_1, ω_2, ...,ω_n, can be written as

$$\begin{bmatrix} \mathbf{A}(\omega_1) \\ \mathbf{A}(\omega_2) \\ \vdots \\ \mathbf{A}(\omega_n) \end{bmatrix} \mathbf{x} = \begin{Bmatrix} \mathbf{b}(\omega_1) \\ \mathbf{b}(\omega_2) \\ \vdots \\ \mathbf{b}(\omega_n) \end{Bmatrix} \tag{6.41}$$

The identification procedure of Equation (6.41) is utilized in the next section for illustration through a numerical simulation.

6.12 Numerical simulation

Numerical simulation of FEM rotor-bearing model has been done through Simulink module in MATLAB^{TM} environment and it is the similar as shown in Figure 4.4 of Chapter 4 to evaluate time domain responses with more complexity in it. It numerically solves the EOMs that is given by Equation (6.30). For the numerical simulation to be performed for rotor-bearing system the internal damping, bearing stiffness and damping parameters, mass and moment of inertia of discs, shaft stiffness and additive stiffness, and unbalances are assumed and are mentioned in Table 6.1. Bearing parameters, i.e. stiffness and damping are considered differently for both the bearings as well as along the *x*- and *y*- axes. A four-DOF per node rotor shaft system consists of four elements, having discs at nodes 2 and 4 with crack at node 3, is considered in the shaft of rotor. The shaft supported by end bearings are at node 1 and node 5. The Simulink model is run for ‘0’ to 4π s, in which for the identification, time-domain data are utilized for the duration of 2π to 4π s. Figures 6.5 to 6.6 show time-domain data only for duration of 7 to 8 s for clarity.

Table 6.1 Assumed rotor-bearing-crack parameters

Parameters	**Values**	**Parameters**	**Values**
ρ	7850 kg/m^3	E	2.1×10^{11} N/m^2
d	0.015 m	c_{bx1}	95 Ns/m
L	0.45 m	c_{by1}	90 Ns/m
m_1	0.7990 kg	c_{bx2}	86 Ns/m
m_2	0.7231 kg	c_{by2}	77 Ns/m
e_1	25 µm	c_H	10 Ns/m
e_2	30 µm	k_{bx1}	128592N/m
ϕ_1	15^0	k_{by1}	106788N/m
ϕ_2	45^0	k_{bx2}	127788 N/m
I_{d1}	6.8560×10^{-03} kgm^2	k_{by2}	115788 N/m
I_{d2}	5.6502×10^{-03} kgm^2	Δk_{22}	5000 N/m

6.13 The static, time domain and frequency domain responses

Initially, natural frequencies are estimated through eigenvalue problem by using the mass and stiffness matrices. The first critical speed is found to be 415.99 rad/s. The static deflection and slope at various nodes due to self-weight are shown in Figure 6.5. Time-domain responses of the rotor system at 100 rad/s for different node locations along x and y axes are shown in Figures 6.6 and 6.7, respectively. Similarly, the orbit plot is illustrated in Figure 6.8.

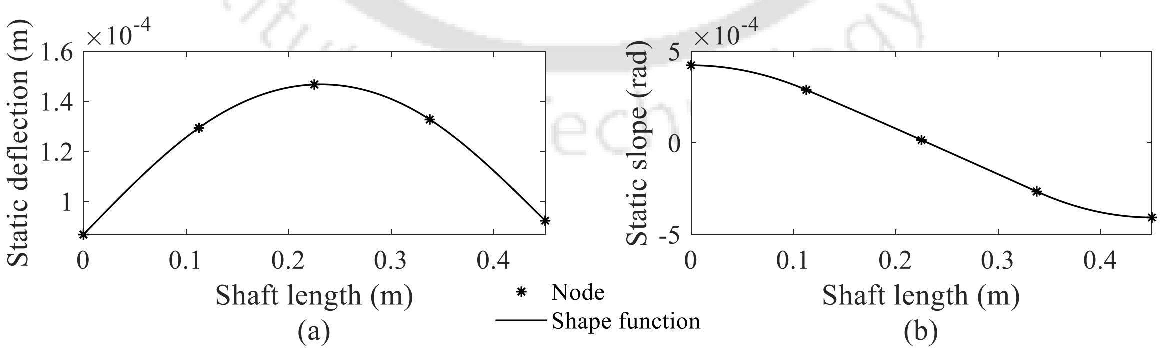

Figure 6.5 (a) Static deflection versus shaft length and (b) Slope versus shaft length

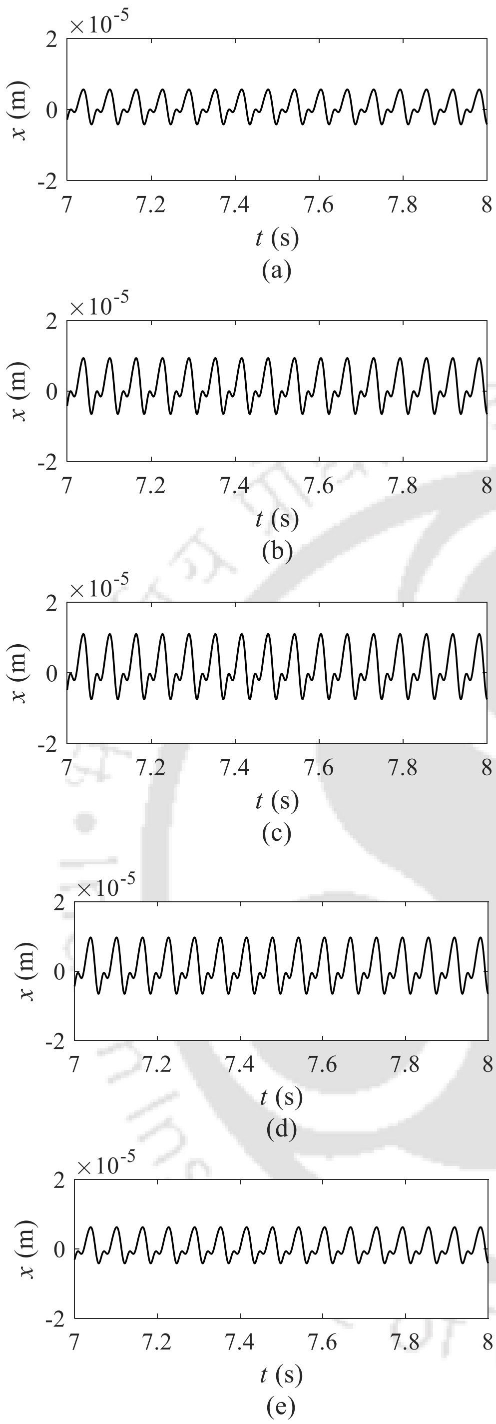

Figure 6.6 Time domain responses in vertical direction at 100 rad/s (a) at left bearing (b) node at disc1 (c) at crack (d) at disc2 (e) at right bearing

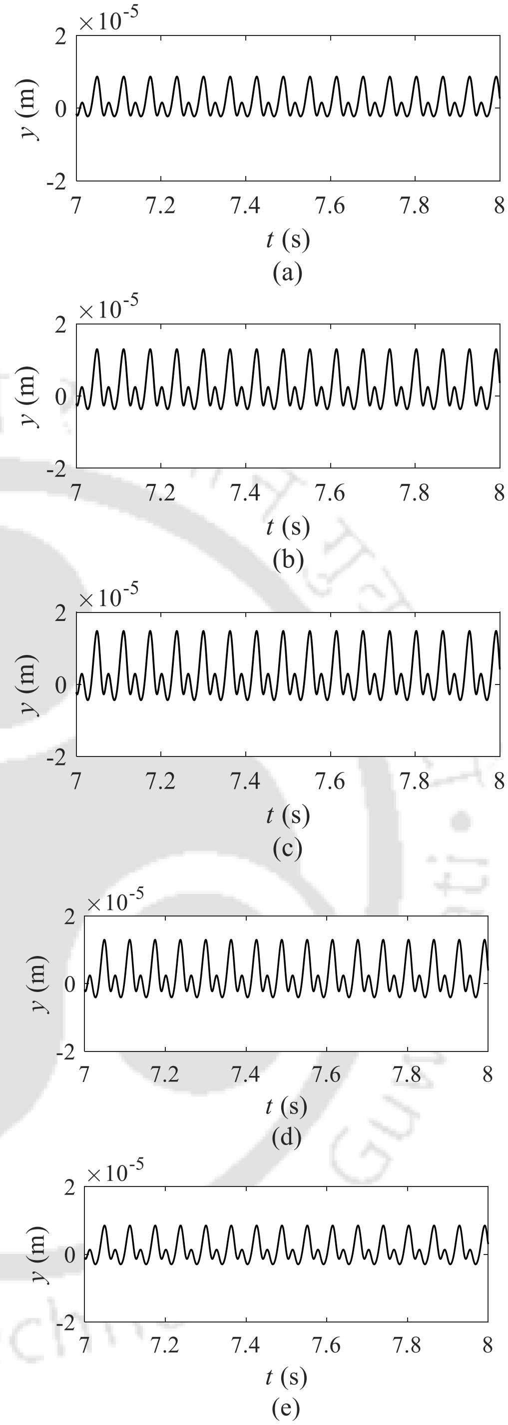

Figure6.7 Time domain responses in horizontal direction at 100 rad/s (a) at left bearing (b) at disc1 (c) at crack (d) at disc2 (e) at right bearing

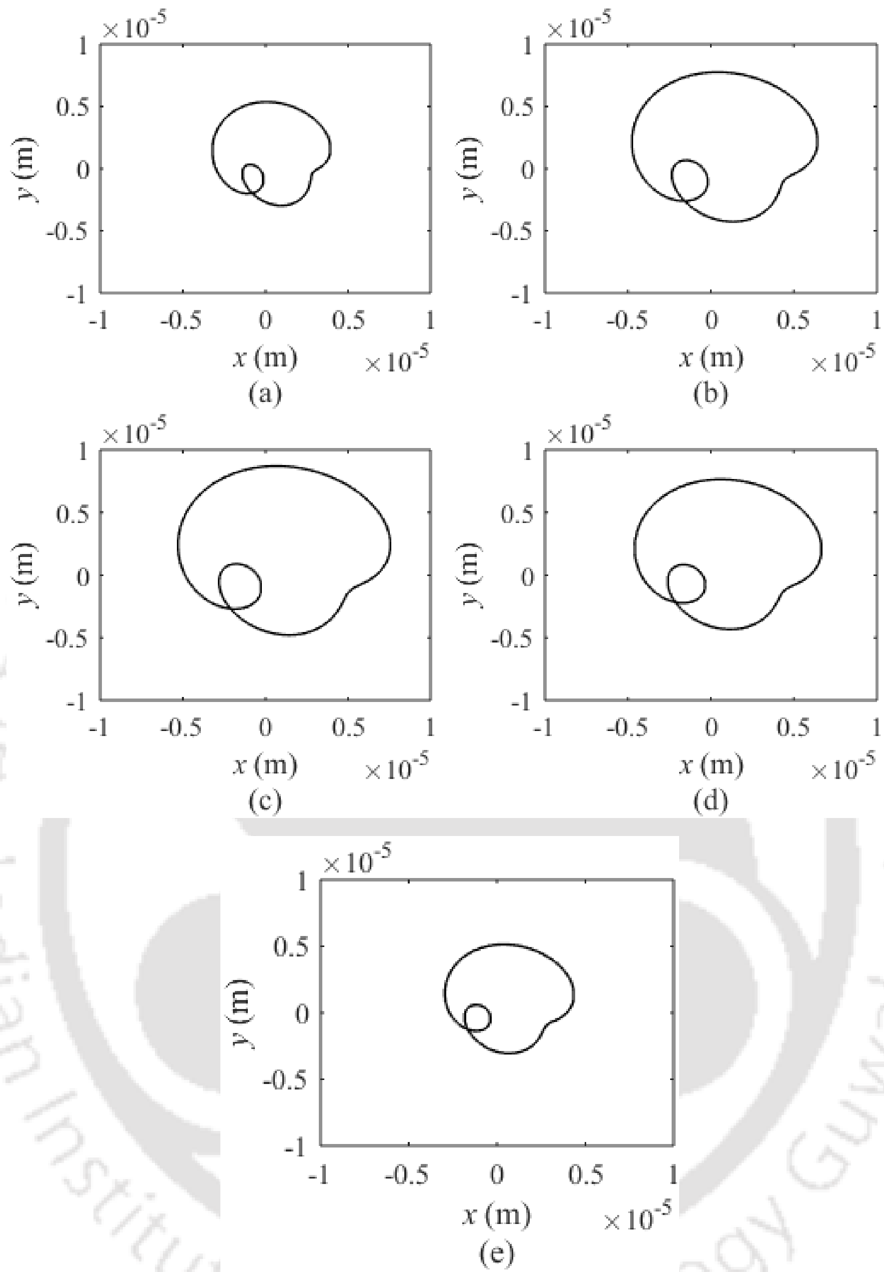

Figure 6.8 Orbit plots at 100 rad/s (a) at left bearing (b) at disc1 (c) at crack (d) at disc2 (e) at right bearing

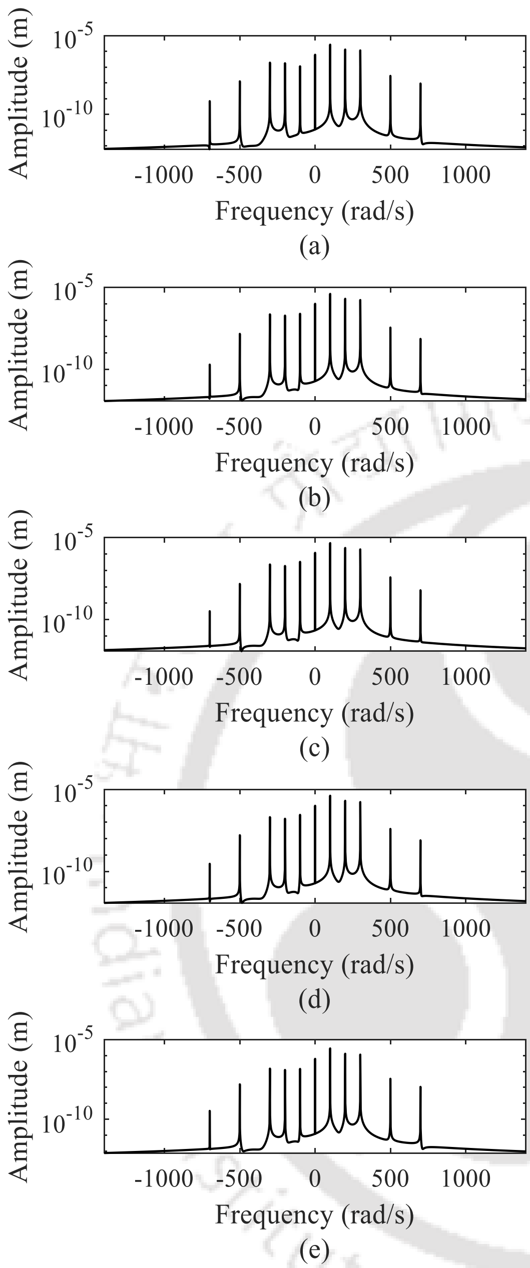

Figure 6.9 Full spectrum amplitude at 100 rad/s (a) at left bearing (b) at disc1 (c) at crack(d) node at disc2 (e) at right bearing

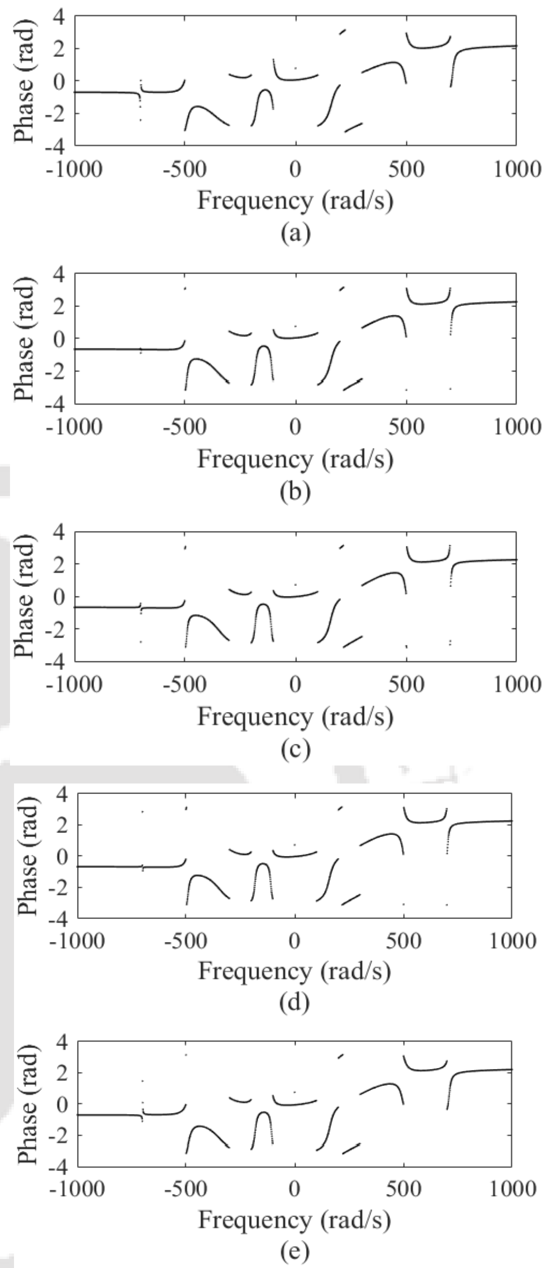

Figure 6.10 Full spectrum phase at 100 rad/s (a) at left bearing (b) at disc1 (c) at crack(d) at disc2 (e) at right bearing

Frequency domain responses are shown in Figure 6.9 for the amplitude and in Figure 6.10 for its phase angle. The comparison of full spectrum amplitude are illustrated in Tables 6.2 through 6.4 for displacements at nodes 1 through 3 and their phase are illustrated in Tables 6.5 through 6.7.

In these tables a comparison of the amplitude and phase angle of full spectrum with phase compensation are presented by two methods (2.2.4 and 2.2.5). The first is the regression-based method and the second is the FFT based method. It is found that similar results are obtained in the amplitude and for the compensated phase. Identification of rotor parameters are illustrated in the next section.

Table 6.2 Full spectrum amplitude at node 1

Frequency	Regression based	FFT based	Regression based	FFT based
	R_0 (10^{-6})		R_0^* (10^{-6})	
0	0.6205	0.6205	0.6205	0.6205
	R_i (10^{-6})		S_i^* (10^{-6})	
ω	2.7086	2.7086	0.1142	0.1142
2 ω	1.3324	1.3324	0.1793	0.1793
3 ω	1.1715	1.1715	0.1954	0.1954
5 ω	0.0281	0.0281	0.0127	0.0127
7 ω	0.0092	0.0092	0.0007	0.0007
	S_i (10^{-6})		R_i^* (10^{-6})	
- ω	0.1142	0.1142	2.7086	2.7086
-2 ω	0.1793	0.1793	1.3324	1.3324
-3 ω	0.1954	0.1954	1.1715	1.1715
-5 ω	0.0127	0.0127	0.0281	0.0281
-7 ω	0.0007	0.0007	0.0092	0.0092

Table 6.3 Full spectrum amplitude at node 2

Frequency	Regression based	FFT based	Regression based	FFT based
	R_0 (10^{-6})		R_0^* (10^{-6})	
0	1.0053	1.0053	1.0053	1.0053
	R_i (10^{-6})		S_i^* (10^{-6})	
ω	4.059	4.059	0.2458	0.2458
2 ω	2.040	2.040	0.1907	0.1907
3 ω	1.7069	1.7069	0.2273	0.2273
5 ω	0.0352	0.0352	0.0145	0.0145
7 ω	0.0071	0.0071	0.0002	0.0002
	S_i (10^{-6})		R_i^* (10^{-6})	
- ω	0.2458	0.2458	4.059	4.059
-2 ω	0.1907	0.1907	2.040	2.040
-3 ω	0.2273	0.2273	1.7069	1.7069
-5 ω	0.0145	0.0145	0.0352	0.0352
-7 ω	0.0002	0.0002	0.0071	0.0071

Table 6.4 Full spectrum amplitude at node 3

Frequency	Regression based	FFT based	Regression based	FFT based
	R_0 (10^{-6})		R_0^* (10^{-6})	
0	1.1797	1.1797	1.1797	1.1797
	R_i (10^{-6})		S_i^* (10^{-6})	
ω	4.6278	4.6278	0.3319	0.3319
2 ω	2.3362	2.3362	1.8609	1.8609
3 ω	1.9099	1.9099	0.2297	0.2297
5 ω	0.0375	0.0375	0.0149	0.0149
7 ω	0.0061	0.0061	0.0003	0.0003
	S_i (10^{-6})		R_i^* (10^{-6})	
- ω	0.3319	0.3319	4.6278	4.6278
-2 ω	1.8609	1.8609	2.3362	2.3362
-3 ω	0.2297	0.2297	1.9099	1.9099
-5 ω	0.0149	0.0149	0.0375	0.0375
-7 ω	0.0003	0.0003	0.0061	0.0061

Table 6.5 Full spectrum phase angle at node 1

Frequency	Regression based	FFT based	Regression based	FFT based
	Phase of R_0		Phase of R_0^*	
0	0.4575	0.4575	-0.4575	-0.4575
	Phase of R_i		Phase of S_i^*	
ω	0.3566	0.3566	-1.1918	-1.1918
2 ω	-0.2872	-0.2872	2.6376	2.6377
3 ω	-2.5580	-2.5580	-0.1763	-0.1763
5 ω	-0.1361	-0.1362	3.0819	3.0819
7 ω	2.7364	2.7366	0.0211	0.0203
	Phase of S_i		Phase of R_i^*	
- ω	1.1918	1.1918	-0.3566	-0.3566
-2 ω	-2.6376	-2.6377	0.2872	0.2872
-3 ω	0.1762	0.1762	2.5580	2.5580
-5 ω	-3.0819	-3.0819	0.1361	0.1362
-7 ω	-0.0211	-0.0202	-2.7364	-2.7366

Table 6.6 Full spectrum phase angle at node 2

Frequency	Regression based	FFT based	Regression based	FFT based
	Phase of R_0		Phase of R_0^*	
0	0.4258	0.4258	-0.4258	-0.4258
	Phase of R_i		Phase of S_i^*	
ω	0.3212	0.3212	-0.4110	-0.4110
2 ω	-0.2175	-0.2175	2.6406	2.6406
3 ω	-2.4390	-2.4390	-0.2350	-0.2350
5 ω	0.1032	0.1031	-3.0017	-3.0016
7 ω	-3.0692	-3.0687	0.9738	0.9778
	Phase of S_i		Phase of R_i^*	
- ω	0.4110	0.4110	-0.3212	-0.3212
-2 ω	-2.6406	-2.6406	0.2175	0.2175
-3 ω	0.2350	0.2350	2.4390	2.4390
-5 ω	3.0017	3.0016	-0.1032	-0.1031
-7 ω	-0.9738	-0.9778	3.0692	3.0687

Table 6.7 Full spectrum phase angle at node 3

Frequency	Regression based	FFT based	Regression based	FFT based
	Phase of R_0		Phase of R_0^*	
0	0.4157	0.4157	-0.4157	-0.4157
	Phase of R_i		Phase of S_i^*	
ω	0.2892	0.2892	-0.2670	-0.2670
2 ω	-0.1965	-0.1965	2.6487	2.6487
3 ω	-2.3990	-2.3990	-0.2537	-0.2537
5 ω	0.1975	0.1973	-2.9129	-2.9128
7 ω	-2.7412	-2.7405	2.6986	2.7050
	Phase of S_i		Phase of R_i^*	
- ω	0.2670	0.2670	-0.2892	-0.2892
-2 ω	-2.6487	-2.6487	0.1965	0.1965
-3 ω	0.2537	0.2537	2.3990	2.3990
-5 ω	2.9129	2.9128	-0.1975	-0.1972
-7 ω	-2.6986	-2.7050	2.7412	2.7405

6.14 Result and discussions

The present section shows the identification results. These are illustrated in Table 6.8 for a single spin speed of 100 rad/s and in Table 6.9 for combined spin speeds from 50 rad/s to 100 rad/s with increment of 1 rad/s. The estimated parameters are quite similar to assumed parameters even with various noise levels. Variation of identification parameters are shown with and without combined spin speeds along with addition of noise 0%, 1%, 2% or 5%. Hence, the percent variation in the internal damping (c_H) is from the -2.39 to -0.49; in external damping, c_{bx1} from 2.48 to 14.35, in c_{by1} from 9.99 to 15.74, in c_{bx2} from -1.94 to 3.58 and in c_{by2} from 10.59 to 12.28. The percent variation in the external damping, k_{bx1} is from -4.44 to -4.16, in k_{by1} from 8.95 to 10.04, in k_{bx2} from -1.95 to -1.83 and in k_{by2} from 5.80 to 7.11. The percent variation in the eccentricity e_1 is from -4.89 to -3.50 and in e_2 is from -4.56 to -3.71 and their phases have percent variation, in ϕ_1 from 2.67 to 3.70 and in ϕ_2 from -0.50 to 0.13; and last one the percent variation in the additive stiffness, Δk_{22} is from -5.07 to -1.87. The identification shows the overall parameters percentage variation is from the -5.07 to 15.74, which can be considered acceptable for high level of noise considered in the present study. According to Tables 6.8 and 6.9, it can be seen more percentage variation of parameters are related to the end bearings, which can be due to different bearing properties exist in the both axis (x and y direction).

Table 6.8 Estimated parameters for a single speed with noise addition

Parameters Comparision						
	Symbol	Assumed value	Noise addition			
			0%	1%	2%	5%
Input single speed 100 rad/s	c_H(Nsm^{-1})	10	9.8550	9.8742	9.8935	9.9512
	% variation		(-1.45)	(-1.26)	(-1.06)	(-0.49)
	c_{bx1}(Nsm^{-1})	95	108.5397	108.5586	108.5776	108.6345
	% variation		(14.25)	(14.27)	(14.29)	(14.35)
	c_{by1}(Nsm^{-1})	90	100.5429	100.2339	99.9248	98.9978
	% variation		(11.71)	(11.37)	(11.03)	(9.99)
	c_{bx2}(Nsm^{-1})	86	89.0806	88.9949	88.9092	88.6521
	% variation		(3.58)	(3.48)	(3.38)	(3.08)
	c_{by2}(Nsm^{-1})	77	85.1601	85.2924	85.4248	85.8217
	% variation		(10.59)	(10.76)	(10.94)	(11.45)
	k_{bx1}(Nm^{-1}) 10^5	1.28592	1.2324	1.2316	1.2309	1.2287
	% variation		(-4.16)	(-4.22)	(-4.27)	(-4.44)
	k_{by1}(Nm^{-1})10^5	1.06788	1.1671	1.1663	1.1656	1.1635
	% variation		(9.29)	(9.21)	(9.14)	(8.95)
	k_{bx2}(Nm^{-1})10^5	1.27788	1.2545	1.2545	1.2545	1.2545
	% variation		(-1.83)	(-1.83)	(-1.83)	(-1.83)
	k_{by2}(Nm^{-1})10^5	1.15788	1.2391	1.2393	1.2395	1.2402
	% variation		(7.01)	(7.03)	(7.04)	(7.11)
	e_1 (m) 10^{-5}	2.5	2.3978	2.3937	2.3897	2.3776
	% variation		(-4.09)	(-4.25)	(-4.41)	(-4.89)
	e_2 (m) 10^{-5}	3	2.8722	2.8704	2.8686	2.8632
	% variation		(-4.26)	(-4.32)	(-4.38)	(-4.56)
	ϕ_1(degree)	45	46.3068	46.3777	46.4488	46.6636
	% variation		(2.90)	(3.06)	(3.22)	(3.70)
	ϕ_2(degree)	15	14.9254	14.9283	14.9312	14.9400
	% variation		(-0.50)	(-0.48)	(-0.46)	(-0.40)
	Δk_{22}(Nm^{-1}) 10^3	5	4.8759	4.8821	4.8882	4.9065
	% variation		(-2.48)	(-2.36)	(-2.24)	(-1.87)

Table6.9 Parameters for combined speeds with noise addition

	Parameters Comparision					
	Symbol	Assumed value	Noise addition			
			0%	1%	2%	5%
Input combined speed 50:100 rad/s with increament of 1 rad/s	c_H(Nsm^{-1})	10	9.7611	9.7612	9.7613	9.7616
	% variation		(-2.39)	(-2.39)	(-2.39)	(-2.38)
	c_{bx1}(Nsm^{-1})	95	97.3694	97.3683	97.3672	97.3639
	% variation		(2.49)	(2.49)	(2.49)	(2.48)
	c_{by1}(Nsm^{-1})	90	104.0811	104.0986	104.1161	104.1686
	% variation		(15.64)	(15.66)	(15.68)	(15.74)
	c_{bx2}(Nsm^{-1})	86	84.3330	84.3449	84.3568	84.3925
	% variation		(-1.94)	(-1.92)	(-1.91)	(-1.87)
	c_{by2}(Nsm^{-1})	77	86.3350	86.3594	86.3837	86.4569
	% variation		(12.12)	(12.15)	(12.19)	(12.28)
	k_{bx1}(Nm^{-1}) 10^5	1.28592	1.2311	1.2311	1.2312	1.2312
	% variation		(-4.26)	(-4.26)	(-4.25)	(-4.25)
	k_{by1}(Nm^{-1})10^5	1.06788	1.1751	1.1751	1.1751	1.1750
	% variation		(10.04)	(10.04)	(10.04)	(10.03)
	k_{bx2}(Nm^{-1})10^5	1.27788	1.2530	1.2531	1.2531	1.2531
	% variation		(-1.95)	(-1.94)	(-1.94)	(-1.94)
	k_{by2}(Nm^{-1})10^5	1.15788	1.2251	1.2252	1.2252	1.2252
	% variation		(5.80)	(5.81)	(5.81)	(5.81)
	e_1 (m) 10^{-5}	2.5	2.4125	2.4124	2.4124	2.4121
	% variation		(-3.50)	(-3.50)	(-3.50)	(-3.52)
	e_2 (m) 10^{-5}	3	2.8881	2.8882	2.8883	2.8885
	% variation		(-3.73)	(-3.73)	(-3.72)	(-3.71)
	ϕ_1(degree)	45	46.21	46.21	46.21	46.20
	% variation		(2.70)	(2.70)	(2.69)	(2.67)
	ϕ_2(degree)	15	15.02	15.01	15.01	14.99
	% variation		(0.13)	(0.07)	(0.07)	(-0.07)
	Δk_{22}(Nm^{-1}) 10^3	5	4.7484	4.7481	4.7476	4.7464
	% variation		(-5.03)	(-5.04)	(-5.05)	(-5.07)

6.15 Conclusions

This chapter illustrated an identification algorithm for fault parameters, such as internal damping in the shaft, stiffness and external damping of flexible bearings, unbalances of the discs and additive stiffness of the cracked shaft consisting of offset discs. The generated time domain responses through Simulink model converting into full spectrum are used in the developed identification algorithm for estimation of different fault parameters. The following are the main contribution and conclusions drawn from the present chapter

- In present work, flexible bearing properties are considered different in horizontal and vertical direction both for stiffness and external damping.
- Analysis of work is based on finite element method by discretizing rotor model into elements consisting of two nodes per element.
- Each node has four DOFs, two translational and two rotational.
- The dynamic condensation technique has been applied for eliminating rotational degrees of freedom.
- The developed identification algorithm is tested against random noise and found to be robust.
- The trends of estimated parameters has been discussed and it has been found that reasonable good agreement of different properties even of both flexible bearings in both axes (i.e., x and y directions) are found.

The overall contribution, conclusions and future works for the present study are discussed in next chapter.

CHAPTER 7

Conclusions and Future Scopes from the Present Work

This chapter provides an overall conclusions and contributions of the present research work. Future direction derived from the limitations of the present work is also presented.

7.1 Conclusions

- The identification of internal damping due to a combination of rubbing of crack surfaces and hysteretic in a rotor system having a single transverse crack, has been performed in the present work. In addition to internal damping, estimation of other considered system parameters, i.e. the viscous external damping, eccentricity, and loss of stiffness has been considered in the mathematical modelling. EOMs are developed for a 2-DOF, 4-DOF and MDOF (Multi DOF, i.e. FEM) rotor system model.
- For estimation of the internal damping along with the other system parameters, an identification algorithm is developed based on the regression matrix method from developed EOMs. The estimation of other considered system parameters, i.e. the viscous damping, eccentricity, and loss of stiffness have also been performed.
- Responses are generated through closed-form expressions and numerical integration for 2-DOF and 4-DOF models. For the Multi-DOF model, the only latter approach is followed. Then these responses are transformed into full-spectrum through regression-based and FFT based methods.
- In FFT based method, the phase ambiguity is found and for the phase compensation, a multi-frequency reference signal is used. Also, it is illustrated that the time instance of picking of

signal and capturing a complete cycle of the signal with the help of a reference signal aids a lot to avoid the phase and leakage errors.

- A comparison is made with two full spectrum generation methods for the identification of various system parameters and is found to be excellent with phase compensation technique.
- The dynamic condensation has been done in 4-DOF models and the Multi-DOF model to eliminate the rotational degrees-of-freedom displacement for the identification of the system parameters.
- In FEM based method, the stiffness and damping coefficients of bearings are assumed to be different in the horizontal and vertical directions, and successfully estimated them using developed identification algorithm.
- The noise in numerically generated responses of 1%, 2% and 5% has been added, sequentially, to test the identification algorithm robustness and it is found to be performing well against noise at both single and various ranges of multiple rotor speeds. The estimated parameters are similar to the assumed parameters with the variation in noises, which shows the effectiveness and robustness of the developed algorithm.
- An experimental study on the laboratory test rig containing a fatigue crack is also done to identify the parameters of the rotor system with both 2-DOF and 4-DOF rotor models. The parameters are successfully obtained in the desirable range as found in the real system. The parameters estimated from the developed test rig are found to be different in 4-DOF analysis than the 2-DOF. The variation of fault parameters as compared to 2-DOF analysis is due to the gyroscopic effect of the offset disc in the 4-DOF.
- Bow effect has been removed in the experimental identification to avoid error in the estimation of parameters as it affects the amplitude of 1x harmonic in the signal. The estimated fault

parameters of the test rig are numerically tested to find its viability in the full spectrum response.

7.2 Main Contribution of the research work

The present work adds to the internal damping in the crack model of rotor system and contribution of the present work in the following counts

- The internal damping due to the rubbing of crack faces has been envisioned first time in the literature.
- The reference signal with multiple harmonics is implemented in the numerical and experimental test responses of the rotor system for correction of the phase ambiguity that arises in the full spectrum.
- The phase correction algorithm is tested numerically and its effectiveness is compared in the results with and without phase compensation in the identification algorithm.
- The transverse fatigue crack developed in shaft experimentally, and it was tested with the assumption of switching behaviour function base on Fourier series.
- The experimental identification parameters are validated with numerical simulation response in full spectrum amplitudes.
- The developed algorithm based on FFT analysed responses in the finite element modelling of the rotor system has been numerically tested in the estimation of different stiffness and damping properties of both bearings along both the transverse directions.
- Developed the equation for removing of bow effect to improve accuracy of identification in the experimental analysis of the system parameters.

- The present work has application to rotor shafts, such as in turbine, compressor, and flywheel in industrial machines or vehicles. Planning of maintenance through such study can be useful for detecting the crack growth through internal damping study.

7.3 Limitation of the present work

- The identification algorithm is developed for simple cracked rotor models with two translational and two rotational co-ordinates. The rotational DOF is eliminated based on the dynamic condensation utilization in the system equation in motion. As a result of this, the identification of rotational additive stiffness is not accurate in experimental work. Hence, it is neglected to obtain other system parameters accurately.
- The developed identification algorithms considered a switching crack. This model of crack is applicable for the initial stages of a rotor fatigue crack. The developed identification algorithm can be effectively used for early crack detection in the rotor system. However, the crack system can be modelled differently, i.e. of gradual breathing nature, which is common in most cases.
- The identification algorithms are model-based and the mathematical models developed to use a single crack parameter for the identification of crack. Only the additive stiffness due to crack is considered. The crack axial location and size parameters are not considered, so these parameters cannot be directly obtained from the identification algorithms.
- All the identification algorithms require measurements in two orthogonal directions. In reality, the measurement locations on the shaft may not be accessible because of other mountings over the shaft.

- Weight dominance is considered in the present work, which may not be present in different rotor systems.
- The non-linearity present in the system due to various faults, such as the crack, fluid-film bearing, are not considered.
- The modelling parameters required in the identification needs to be considered accurately.

7.4 Future scope of work

- The different crack models can be considered such as breathing crack, open crack, multiple cracks.
- Instead of removal of bow effect by the signal processing, it’s modelling and parameter estimation can be done mathematically.
- With a flexible-bearing test rig, the application of the identification algorithm with FEM could be checked experimentally.
- The mathematical model does not include parameters for crack quantification and location. The algorithms can also be extended for the estimation of crack size and location.
- The mathematical model can be extended with misalignment or bearing faults along with the existing faults of crack, internal and external damping, unbalance and shaft bow.

References

- Adams, M. L. (2009). Rotating Machinery Vibration: From Analysis to Troubleshooting. CRC Press, *Boca Raton, FL, USA.*
- Adams, R. D. Cawley, P., Pye, C. J. and Stone, B. J. (1978). A vibration technique for non-destructively assessing the integrity of structures. *Journal of Mechanical Engineering Science*, 20(2), 93-100.
- Ahmed, F., Abdelhamid, H., Brahim, B. and Ahmed, S. (2019). Study of the effect of an open transverse crack on the vibratory behavior of rotors using the h-p version of the finite element method. *Journal of Solid Mechanics*, 11(1), 181-200.
- Allen, J. W. and Bohanick, J. S. (1991). Cracked shaft diagnosis and detection on reactor recirculation pumps at grand gulf nuclear station. *International Nuclear Information System*, 23(4), 23011936.
- Al-Shudeifat, M. A. (2013). On the finite element modeling of the asymmetric cracked rotor. *Journal of sound and vibration*, 332(11), 2795-2807.
- AL-Shudeifat, M. A., Al Hosani, H., Saeed, A. S. and Balawi, S. (2019). Effect of unbalance force vector orientation on the whirl response of cracked rotors. *ASME Journal of Vibration and Acoustics*, 141(2).
- Ayoubi, M. and Isermann, R. (1997). Neuro-fuzzy systems for diagnosis. *Fuzzy sets and Systems*, 89(3), 289-307.

- Bachschmid N, Pennacchi P and Tanzi E (2010). In: Cracked Rotors A Survey on Static and Dynamic Behaviour Including Modelling and Diagnosis. *Springer, Berlin – Heidelberg*.
- Bachschmid, N., Pennacchi, P. and Tanzi, E. (2008). Some remarks on breathing mechanism, on non-linear effects and on slant and helicoidal cracks. *Mechanical Systems and Signal Processing*; 22 (4), 879–904.
- Bachschmid, N., Pennacchi, P., Tanzi, E. and Audebert, S. (2004). Transverse crack modeling and validation in rotor systems including thermal effects. *International Journal of Rotating Machinery*, 10(4), 253-263.
- Basseville, M. (2001). On fault detectability and isolability. *European Journal of Control*, 7(6), 625-637.
- Bently, D. and Muszynska, A. (1986a). Early detection of shaft cracks on fluid-handling machines. *In Proceedings of ASME International Symposium on Fluid Machinery Trouble Shooting*, (7) 53-58.
- Bently, D. E. and Muszynska, A. (1985). Rotor internal friction instability. *Conference Paper.Organization Bently Rotor Dynamics Research Corp., NASA*,337-348.
- Bently, D. E. and Muszynska, A. (1986b) Detection of Rotor Cracks, Texas AandM University 15th Turbomachinery Symposium and Short Courses. *Corpus Christi, Texas*, 129–139.
- Besselink, B., Tabak, U., Lutowska, A., van de Wouw, N., Nijmeijer, H., Rixen, D.J., Hochstenbach, M.E. and Schilders, W.H.A. (2013). A comparison of model reduction techniques from structural dynamics, numerical mathematics and systems and control. *Journal of Sound and Vibration*, (332), 4403–4422.

- Bucciarelli, L. L. (1982). On the instability of rotating shafts due to internal damping, *ASME*, 49(2), 425-428.
- Cai, Z. (2011). Vibration Diagnostics of Elastic Shafts with a Transverse Crack,*Thesis, Faculty of Computing, Health and Science, Edith Cowan University*. Australia.
- Capecchi, D. and Vestroni, F. (1999). Monitoring of structural systems by using frequency data. *Earthquake Engineering & Structural Dynamics*, 28(5), 447-461.
- Chandra, N. H. and Sekhar, A. S. (2016). Nonlinear damping identification in rotors using wavelet transform. *Mechanism and Machine Theory*, 100, 170-183.
- Chen, L. W. and Ku, D. M. (1991). Analysis of whirl speeds of rotor-bearing systems with internal damping by C0 finite elements. *Finite Elements in Analysis and Design*, 9(2), 169-176.
- Childs, D. W. and Jordan, L. T. (1997). Clearance effects on spiral vibrations due to rubbing. *In Proceedings of the 1997 ASME Design Engineering Conferences, DETC* (97) 1-9.October, Sacramento, California.
- Chondros T. G., Dimarogonas A. D. and Yao J. (1998). A continuous cracked beam vibration theory. *Journal of Sound and Vibration*, 215(1), 17–34.
- Chouksey, M., Dutt, J. K. and Modak, S. V. (2012). Modal analysis of rotor-shaft system under the influence of rotor-shaft material damping and fluid film forces. *Mechanism and Machine Theory*, (48), 81-93.
- Chouksey, M., Modak, S. V. and Dutt, J. K. (2010). Influence of rotor-shaft material damping on modal and directional frequency response characteristics. *Proceedings of ISMA*, 1543-1557.20-22 September,Leuven.

- Christides S. and Barr A. D. S. (1984). One dimensional theory of cracked Bernoulli-Euler Beams. *International Journal of Mechanical Science*, 26(11), 639-648.
- Darpe, A. K. (2007). Coupled vibrations of a rotor with slant crack. *Journal of Sound and Vibration*, 305(1-2), 172-193.
- Darpe, A. K., Gupta, K. and Chawla, A. (2003). Experimental investigations of the response of a cracked rotor to periodic axial excitation. *Journal of Sound and Vibration*, 260, 265-286.
- Darpe, A. K., Gupta, K. and Chawla, A. (2004). Coupled bending, longitudinal and torsional vibrations of a cracked rotor. *Journal of Sound and Vibration*, 269(1-2), 33-60.
- Dharmaraju, N., Tiwari, R. and Talukdar, S. (2004). Identification of an open crack model in a beam based on force-response measurements, *Computers and Structures*, 82 (2-3), 167-179.
- Dharmaraju, N., Tiwari, R. and Talukdar, S. (2005). Development of a novel hybrid reduction scheme for identification of an open crack model in a beam. *Mechanical Systems and Signal Processing*, 19(3), 633-657.
- Dimarogonas, A. D. (1996). Vibration of cracked structures: a state of the art review. *Engineering Fracture Mechanics*, 55(5), 831-857.
- Dimarogonas, A. D. and Papodopoulos, C. A. (1983). Vibration of cracked shafts in bending. *Journal of Sound and Vibration,* 91(4), 583-593.
- Dimarogonas, A. D., and Papadopoulos, C. A. (1983). Vibration of cracked shafts in bending. *Journal of Sound and Vibration*, 91(4), 583-593.
- Dimentberg, F. M. (1961). Flexural Vibration of Rotating Shafts.*Butterworths, London.*

- Dimentberg, M. F. (2005). Vibration of a rotating shaft with randomly varying internal damping. *Journal of Sound and Vibration*, 285(3), 759-765.
- Doebling, S. W., Farrar, C. R., Prime, M. B. and Shevitz, D. W. (1996). Damage identification and health monitoring of structural and mechanical systems from changes in their vibration characteristics: a literature review (No. LA-13070-MS). *Los Alamos National Lab*., *New Mexico, USA.*
- Edwards, S., Lees, A. W. and Friswell, M. I. (1998). Fault diagnosis of rotating machinery. *Shock and Vibration Digest*, 30(1), 4-13.
- Ehrich, F. F. (1964). Shaft whirl induced by rotor internal damping, *Journal of Applied Mechanics, ASME*, 31(2), 279-282.
- Eisemann, R. C. (1998). Machinery malfunction diagnosis and correction: Vibration analysis and troubleshooting for process industries.*U.S. Department of Energy Office of Scientific and Technical Information, United States.*
- El Arem, S. and Maitournam, H. (2008). A cracked beam finite element for rotating shaft dynamics and stability analysis. *Journal of Mechanics of Materials and Structures*, 3 (5), 893-910.
- Fischer, J. and Strackeljan, J. (2006). Stability analysis of high speed lab centrifuges considering internal damping in rotor-shaft joints. *TechnischeMechanik*, 26(2), 131-147.
- Forrai, L. (2000). Instability due to internal damping of symmetrical rotor-bearing systems. *Journal of Computational and Applied Mathematics*, 1(2), 137-147.
- Forsthoffer, W. E. (2011). Forsthoffer's Best Practice Handbook for Rotating Machinery. *Elsevier*.*Butterworth-Heinemann*,Oxford, United Kingdom.

- Friswell, M. I. (2007). Damage identification using inverse methods. *Philosophical Transactions of the Royal Society A: Mathematical, Physical and Engineering Sciences*, 365(1851), 393-410.
- Friswell, M. I. and Penny, J. E. T. (2002). Crack modeling for structural health monitoring. *Structural Health Monitoring*, 1(2), 139-148.
- Friswell, M. I., Penny, J. E., Garvey, S. D. and Lees, A. W., (2010). Dynamics of Rotating Machines: *Cambridge University Press. USA.*
- Friswell, M.I., Garvey, S.D. and Penny, J.E.T. (1995). Model reduction using dynamic and iterative IRS techniques. *Journal of Sound and Vibration*, 186, 311–323.
- Friswell, M.I., Garvey, S.D. and Penny, J.E.T. (1998). The convergence of the iterated IRS method. *Journal of Sound and Vibration*, 211, 123–132.
- Gasch, R. (1993). A survey of the dynamic behaviour of a simple rotating shaft with a transverse crack. *Journal of Sound and Vibration*, 160, 313-332.
- Gasch, R. (2008). Dynamic behaviour of the Laval rotor with a transverse crack. *Mechanical Systems and Signal Processing*, 22(4), 790-804.
- Gasch, R. and Liao, M. (1996).Process for the Early Detection of a Crack in a Rotating Shaft. *U.S. Patent No. 5,533,400. Washington, DC: U.S. Patent and Trademark Office*.
- Genta, G. (2004). On a persistent misunderstanding of the role of hysteretic damping in rotordynamics. *ASME,Journal of Vibration and Acoustics*, 126(3), 459-461.
- Genta, G. (2007). Dynamics of rotating systems. *Springer Science and Business Media*, *Politecnico di Torino, Italy*.
- Goldman, P. and Muszynska, A. (1999). Application of full spectrum to rotating machinery diagnostics. *Orbit*, 20(1), 17-21.

- Gordis, J. H. (1992). An analysis of the improved reduced system (IRS) model reduction procedure. *In 10th International Modal Analysis Conference* (1), 471-479.
- Göttlich, E. H. (1988). A method for overall condition monitoring by controlling the efficiency and vibration level of rotating machinery. *In Proceedings of the Institution of Mechanical Engineers-Vibrations in Rotating Machinery*, 445-447.13-15 September 1988, Heriot-Watt University, Edinburgh.
- Gounaris, G. and Dimarogonas, A. (1988). A finite element of a cracked prismatic beam for structural analysis. *Computers and Structures*, 28 (3), 309-313.
- Green, I. and Casey, C. (2005). Crack detection in a rotor dynamic system by vibration monitoring—part I: *analysis. J. Eng. Gas Turbines Power*, 127(2), 425-436.
- Gudmundson, P. (1983). The dynamic behaviour of slender structures with cross-sectional cracks, *Journal of the Mechanics and Physics of Solids*, 31 (4), 329-345.
- Gunter Jr, E. J. (1967). The influence of internal friction on the stability of high speed rotors. *ASME,Journal of Manufacturing Science and Engineering*,89(4), 683-688.
- Gunter Jr, E. J. and Trumpler, P. R. (1969). The influence of internal friction on the stability of high speed rotors with anisotropic supports.*ASME,Journal of Manufacturing Science and Engineering*, 91(4), 1105-1113.
- Guyan, R.J. (1965) Reduction of stiffness and mass matrices. *AIAA Journal*, 3(2), 380-380.
- Hasan, W. M. (1995). Crack detection from the variation of the eigenfrequencies of a beam on elastic foundation. *Engineering Fracture Mechanics*, 52(3), 409-421.
- Henshell, R. D. and Ong, J. H. (1974). Automatic masters for eigenvalue economization. *Earthquake Engineering and Structural Dynamics*, 3(4), 375-383.

- Hill, J. W. and Baines, N. C. (1988). Application of an expert system to rotating machinery health monitoring. *In Proceedings of the Institution of Mechanical Engineers-Vibrations in Rotating Machinery*, 449-454. 13-15 September 1988, Heriot-Watt University, Edinburgh.
- Hossain, M. (2018). Crack Breathing Mechanism in a Cracked Shaft Subject to Nontrivial Mass Unbalance. *Doctoral Dissertation, Western Sydney University, Australia*.
- Irons, B. (1965). Structural eigenvalue problems-elimination of unwanted variables. *AIAA Journal*, 3(5), pp.961-962.
- Irwin, G. R. (1957). Analysis of stress and strains near the end of a crack traversing a plate. *ASME, Applied Mechanics*,24,109-114
- Isermann, R. (1994). Integration of fault detection and diagnosis methods. *IFAC Proceedings Volumes*, 27(5), 575-590.
- Isermann, R. and Balle, P. (1997). Trends in the application of model-based fault detection and diagnosis of technical processes. *Control Engineering Practice*, 5(5), 709-719.
- Iwatsubo, T. (1976). Error analysis of vibration of rotor/bearing system. *In Proceedings of the Institution of Mechanical Engineers* (190), 87-92.
- Jeong, J., Baek, S. and Cho, M. (2012). Dynamic condensation in a damped system through rational selection of primary degrees of freedom. *Journal of Sound and Vibration*, 331(7), 1655-1668.
- Jha, A. K. and Dasgupta, S. S. (2019). Attenuation of Sommerfeld effect in an internally damped eccentric shaft-disk system via active magnetic bearings. *Meccanica*, 54(1-2), 311-320.

- Jun, O. S., Eun, H. J., Earmme, Y. Y. and Lee, C. W. (1992). Modelling and vibration analysis of a simple rotor with a breathing crack. *Journal of Sound and Vibration*, 155(2), 273-290.
- Karthikeyan, M. and Tiwari, R. (2010). Detection, localization, and sizing of a structural flaw in a beam based on forced response measurements-An experimental investigation. *Mechanism and Machine Theory*, 45(4), 584-600.
- Karthikeyan, M., Tiwari, R. and Talukdar, S. (2007). Development of a technique to locate and quantify a crack in a beam based on modal parameters, *ASME, Journal of Vibration and Acoustics*, 129(3), 390-395.
- Khorrami, H. (2016). Vibration Analysis of a Shaft-Disc System for On-line Crack Detection. *Doctoral dissertation, Concordia University*. Canada.
- Khorrami, H., Rakheja, S. and Sedaghati, R. (2017). Vibration behaviour of a two-crack shaft in a rotor disc-bearing system. *Mechanism and Machine Theory*, (113), 67-84.
- Kirmser, P. G. (1944). The effects of discontinuities on the natural frequency of beams. *Proceedings of American Society of Testing and Materials*, (44), 897-904
- Ku, D. M. (1998). Finite element analysis of whirl speeds for rotor-bearing systems with internal damping. *Mechanical Systems and Signal Processing*, 12(5), 599-610.
- Kurnik, W., (1994). Stability and bifurcation analysis of a nonlinear transversally loaded rotating shaft. *Nonlinear Dynamics*, 5(1), 39-52.
- Lazzeri L., Cecconi S., Faravelli M., Scala, M. and Tolle, E. (1992) Second Harmonic Vibration Monitoring of a Cracked Shaft in a Turbo-Generator. *Proceedings of the American Power Conference,Chicago, Illinois*, 54(2), 1337–1342.

- Lee, C. W. and Joh, C. Y. (1994). Development of the use of directional frequency response functions for the diagnosis of anisotropy and asymmetry in rotating machinery: theory. *Mechanical Systems and Signal Processing*, 8(6), 665-678.
- Lee, Y. S. and Chung, M. J. (2001) A study on crack detection using eigenfrequency test data, *Computers and Structures*, (77), 327-342.
- Lees, A. W. (2016). Vibration Problems in Machines: Diagnosis and Resolution. *CRC Press,Boca Raton, FL, USA.*
- Lemahieu, W., Loccufier, M., Vervisch, B. and De Baets, P. (2012). Instability due to internal damping of rotating shafts. *In Sustainable Construction and Design,Laboratory Soete, Ghent University,Belgium* 3(2), 123-127.
- Leung, A. Y. T. (1978). An accurate method of dynamic condensation in structural analysis. *International Journal for Numerical Methods in Engineering*, 12(11), 1705-1715.
- Liang, R. Y., Hu, J. and Choy, F. (1992). Quantitative NDE technique for assessing damages in beam structures. *Journal of Engineering Mechanics*, 118(7), 1468-1487.
- Liao, M. and Gasch, R. (1992). Crack detection in rotating shafts-an experimental study. *In Institution of Mechanical Engineers Conference Publications, Medical Engineering Publications Ltd*. (6) 289-289.
- Lin, Y. and Chu, F. (2010). The dynamic behavior of a rotor system with a slant crack on the shaft. *Mechanical Systems and Signal Processing*, 24(2), 522-545.
- Liu, C. and Jiang, D. (2017). Dynamics of slant cracked rotor for a steam turbine generator system. *ASME, Journal of Engineering for Gas Turbines and Power*, 139(6).

- Lund, J. W. (1990). Destabilisation of Rotors from Friction in Internal Joints. *In Vibration and Wear in High Speed Rotating Machinery,Springer, Dordrecht,*174,617-629.
- Maalouf, M. G. (2007). Slow speed vibration signal analysis: if you can't do it slow, you can't do it fast. *In ASME Turbo Expo,Power for Land, Sea, and Airduring May 14–17, 2007, Montreal, Canada, American Society of Mechanical Engineers Digital Collection,* 5,559-567.
- Mayes, I. W. and Davies, W. G. R. (1976). The vibrational behaviour of a rotating shaft system containing a transverse crack.*Conference Proceedings Vibrations in Rotating Machinery, Institution of Mechanical Engineering, London*, 53-65.
- Mayes, I. W. and Davies, W. G. R. (1984). Analysis of the response of a multi-rotor-bearing system containing a transverse crack in a rotor. *ASME, Journal of Vibration and Acoustics*, 106(1), 139-145.
- Melanson, J. and Zu, J. W. (1998). Free vibration and stability analysis of internally damped rotating shafts with general boundary conditions. *ASME, Journal of Vibration and Acoustics*,120(3), 776-783
- Mevel, L., Hermans, L. and Van der Auweraer, H. (1999). Application of a subspace-based fault detection method to industrial structures. *Mechanical Systems and Signal Processing*, 13(6), 823-838.
- Miller, K. S. (1981). On the inverse of the sum of matrices. *Mathematics Magazine*, 54(2), 67-72.
- Montagnier, O. and Hochard, C. (2007). Dynamic instability of supercritical driveshafts mounted on dissipative supports-effects of viscous and hysteretic internal damping. *Journal of Sound and Vibration*, 305(3), 378-400.

- Muszynska, A. (1992). Vibrational diagnostics of rotating machinery malfunctions. *VKI Vibration Rotor Dynamics, Provided by the SAO/NASA Astrophysics Data System.*
- Muszynska, A. (1995). Vibrational diagnostics of rotating machinery malfunctions. *International Journal of Rotating Machinery*, 1(3-4), 237-266.
- Nelson, H. and Nataraj, C. (1986). The dynamics of a rotor system with a cracked shaft. *Journal of Vibration, Acoustics, Stress, and Reliability in Design*, 108(2), 189-196.
- Nelson, H. D. (1980). A finite rotating shaft element using Timoshenko beam theory. *ASME,Journal of Mechanical Design,*102(4), 793-803.
- Nelson, H. D. and McVaugh, J. M. (1976). The dynamics of rotor-bearing systems using finite elements.*Journal of Engineering for Industry*, 98, (2) 593-600.
- Niu, Q. and Yang, S. X. (2018). Study on Fatigue Degradation Behavior of a Cracked Rotor Subjected to Lateral Vibration. *Shock and Vibration, Hindawi*. 1-21 (Volume 2018, Article ID 3239523)
- O'callahan J.C. (1989). A procedure for an improved reduced system (IRS) model. *Proceedings of Seventh International Modal Analysis Conference*, Las Vegas, 17–21.
- Osinski, Z. (Ed.). (2018). Damping of Vibrations. *CRC Press*. *Boca Raton, FL, USA.*
- Pandey A. K., Biswas M. and Samman M. M. (1991). Damage detection from changes in curvature mode shapes. *Journal of Sound and Vibration*, 145(2), 321-332.
- Papadopoulos, C. A. (2008). The strain energy release approach for modeling cracks in rotors: A state of the art review. *Mechanical Systems and Signal Processing*, 22(4), 763-789.
- Paz, M. (1984). Dynamic condensation. *AIAA journal*, 22(5), 724-727.

- Peng, H. and He, Q. (2019). The effects of the crack location on the whirl motion of a breathing cracked rotor with rotational damping. *Mechanical Systems and Signal Processing*, 123, 626-647.
- Pennacchi, P., Bachschmid, N. and Vania, A. (2006). A model-based identification method of transverse cracks in rotating shafts suitable for industrial machines. *Mechanical Systems and Signal Processing*, 20(8), 2112-2147.
- Plaut, R. H., Andruet, R. H. and Suherman, S. (1994). Behavior of a cracked rotating shaft during passage through a critical speed. *Journal of Sound and Vibration*, 173(5), 577-589.
- Prasad, S. R. and Sekhar, A. S. (2018). Life estimation of shafts using vibration based fatigue analysis. *Journal of Mechanical Science and Technology*, 32(9), 4071-4078.
- Prasad, S. R. and Sekhar, A. S. (2019). Diagnostics of Fatigue Crack in the Shaft Using Spectral Kurtosis. *In Turbo Expo: Power for Land, Sea, and Air.June 17–21, Phoenix, Arizona, USA. American Society of Mechanical Engineers (Vol. 58684, p. V07AT31A004.*
- Prasad, V. and Tiwari, R. (2019). Identification of speed-Dependent active magnetic bearing parameters and rotor balancing in high-speed rotor Systems. *Journal of Dynamic Systems, Measurement, and Control*, 141(4).
- Randall, R. B. (2011). Vibration-based Condition Monitoring: Industrial, Aerospace and Automotive Applications. *John Wiley and Sons*. *Hoboken, New Jersey, United States*.
- Rao, J. S. (1996). Rotor dynamics. *New Age International Limited Publishers, New Delhi, India*
- Ren, Y. S., Shi, Y. Y. and Zhang, Y. H. (2017). Effects of internal damping on dynamic stability of a rotating composite shaft J. *Journal of Vibration and Shock*, 36(23), 181-186.

- Rice, J.R. (1968). A Path Independent Integral and the Approximate Analysis of Strain Concentration by Notches and Cracks. *Journal of Applied Mechanics*, (35), 379-386.
- Rytter, A. (1993). Vibrational based inspection of civil engineering structures. *Doctoral dissertation, Dept. of Building Technology and Structural Engineering, Aalborg University.Denmark.*
- Saavedra, P. N. and Cuitino, L. A. (2002). Vibration analysis of rotor for crack identification. *Journal of Vibration and Control*, 8(1), 51-67.
- Sabnavis, G., Kirk, R. G., Kasarda, M. and Quinn, D. (2004). Cracked shaft detection and diagnostics: a literature review. *The Shock and Vibration Digest*, 36(4), 287-296.
- Sanderson A. F. P. (1992). The vibration behavior of a large steam tur- bine generator during crack propagation through the generator rotor. *International Conference on Vibrations in Rotating Machinery, 7-10 September, University of Bath, UK*, (432/102), 6, 263–273.
- Sarmah, N. and Tiwari, R. (2019a). Dynamic analysis and identification of multiple fault parameters in a cracked rotor system equipped with active magnetic bearings: a physical model based approach. *Inverse Problems in Science and Engineering*, Dec 14, 1-32.
- Sarmah, N. and Tiwari, R. (2019b). Experimental investigation of active control of cracked rotor-bearing system equipped with magnetic bearing. *In Gas Turbine India Conference,American Society of Mechanical Engineers.* (83525), V001T05A016. December 5–6, Chennai, Tamil Nadu, India.
- Sarmah, N. and Tiwari, R. (2020). Analysis and identification of the additive and multiplicative fault parameters in a cracked-bowed-unbalanced rotor system integrated with an auxiliary active magnetic bearing. *Mechanism and Machine Theory*, 146, 103744.

- Sekhar A. S. (1999). Vibration characteristics of a cracked rotor with two open cracks. *Journal of Sound and Vibration*, 223(4), 497–512.
- Sekhar A. S. (2004a). Crack identification in a rotor system: a model-based approach. *Journal of Sound and Vibration*, 270, 887-902.
- Sekhar A. S. (2004b). Model-based identification of two cracks in a rotor system. *Mechanical Systems and Signal Processing*, 18 (4), 977-983.
- Sekhar A. S. (2004c). Detection and monitoring of crack in a coast-down rotor supported on fluid film bearings. *Tribology International*, 37(3), 279-287.
- Sekhar A. S. and Prabhu B. S. (1994). Vibration and stress fluctuation in cracked shafts. *Journal of Sound and Vibration*, 169(5), 655–667.
- Sekhar A. S. and Prasad P. B. (1997). Dynamic analysis of a rotor system considering a slant crack in the shaft. *Journal of Sound and Vibration*, 208(3), 457–474.
- Shaw, J. and Shaw, S. W. (1991). Non-linear resonance of an unbalanced rotating shaft with internal damping. *Journal of Sound and Vibration*, 147(3), 435-451.
- Shaw, J. and Shaw, S., (1989). Instabilities and bifurcations in a rotating shaft. *Journal of Sound and Vibration*, 132(2): 227-244.
- Shravankumar, C. and Tiwari, R. (2013). Identification of stiffness and periodic excitation forces of a transverse switching crack in a Laval rotor. *Fatigue and Fracture of Engineering Materials and Structures*, 36(3), 254-269.
- Shravankumar, C. and Tiwari, R. (2019). Experimental identification of cracked rotor system parameters from the forward and backward whirl responses. *Archive of Mechanical Engineering*, 329-353.

- Shravankumar, C., (2014). Crack Identification in Rotors with Full-Spectrum. *Doctoral dissertation, Indian Institutes of Technology Guwahati, India.*
- Shravankumar, C., Tiwari, R. and Mahibalan, A., (2015). Experimental identification of rotor crack forces. *In Proceedings of the 9th IFToMM International Conference on Rotor Dynamics, Springer, Cham*, 361-371.
- Singh, S. and Tiwari, R. (2017). Model-based fatigue crack identification in rotors integrated with active magnetic bearings. *Journal of Vibration and Control*, 23(6), 980-1000.
- Singh, S. and Tiwari, R., (2016). Model-based switching-crack identification in a Jeffcott rotor with an offset disk integrated with an active magnetic bearing. *ASME,Journal of Dynamic Systems, Measurement, and Control*, 138(3),031006.
- Singh, S. and Tiwari, R., (2018). Model based identification of crack and bearing dynamic parameters in flexible rotor systems supported with an auxiliary active magnetic bearing. *Mechanism and Machine Theory*, 122: 292-307.
- Singh, S. K. and Tiwari, R. (2014). Detection and localisation of multiple cracks in a shaft system: An experimental investigation. *Measurement*, 53, 182-193.
- Singh, S. K. and Tiwari, R., (2010). Identification of a multi-crack in a shaft system using transverse frequency response functions. *Mechanism and Machine Theory*, 45(12): 1813-1827.
- Singh, V. P. and Srinivas, J. (2018). Crack effect on rotors using mode-i failure model with transfer matrix approach. *In Proceedings of Fatigue, Durability and Fracture Mechanics,Springer, Singapore.* 153-165.

- Sinha, J. K. (2007). Higher order spectra for crack and misalignment identification in the shaft of a rotating machine. *Structural Health Monitoring*, 6(4), 325-334.
- Sinha, J. K. (2014). Vibration Analysis, Instruments, and Signal Processing. *CRC press, Boca Raton, FL, USA.*
- Sino, R., Chatelet, E., Montagnier, O. and Jacquet-Richardet, G. (2007, January). Dynamic instability analysis of internally damped rotors. *In ASME Turbo Expo 2007*: *Power for Land, Sea, and Air,American Society of Mechanical Engineers Digital Collection,* 727-736.May 14–17, Montreal, Canada.
- Smalley, A. J., Baldwin, R. M., Mauney, D. A. and Millwater, H. R. (1996). Towards risk based criteria for rotor vibration. *In IMECHE conference transactions. Mechanical Engineering Publications*, (6), 517-528.
- Smith, D. M. (1980). Recognition of the causes of rotor vibration in turbomachinery.*Vibrations in Rotating Machinery-International Conference-2, Cambridge; London: Mechanical engineering publications; DA.*, 1-4 September.
- Smith, G. W. and Birchak, J. R. (1968). Effect of internal stress distribution on magnetomechanical damping. *Journal of Applied Physics*, 39(5), 2311-2316.
- Smyth, P. A., Varney, P. A. and Green, I. (2016). A fractional calculus model of viscoelastic stator supports coupled with elastic rotor–stator rub. *Journal of Tribology*, 138(4).
- Stewart, R. M. (1976). Vibration analysis as an aid to the detection and diagnosis of faults in rotating machinery. *In Proceedings of the Institution of Mechanical Engineers-Vibrations in Rotating Machinery*, 223-229.

- Suarez L.E. (1992). Dynamic condensation method for structural eigenvalue analysis. *AIAA Journal*, 30, 1046–1054.
- Tada, H. (1985). The Stress Analysis of Cracks Handbook, *Paris Productions.Inc., St. Louis.*
- Taylor, J. I. (1995). Back to the basics of the rotating machinery vibration analysis. *Sound and Vibration*, 29(2), 12-16.
- Thomas, D. L. (1984). Vibration monitoring strategy for large turbogenerators. *In Proceedings of the Institution of Mechanical Engineers, Vibrations in Rotating Machinery*, 91-99. 11-13 September, University of York, Heslington, U. K.
- Thomson, W. (2018). Theory of Vibration with Applications. *CRC Press. Boca Raton, FL, USA.*
- Thomson, WJ (1943). Vibration of slender bars with discontinuities in stiffness",*Journal of Applied Mechanics*, 17, 203-207
- Tiwari, R. (2005). Conditioning of regression matrices for simultaneous estimation of the residual unbalance and bearing dynamic parameters. *Mechanical Systems and Signal Processing*, 19(5), 1082-1095.
- Tiwari, R. (2017). Rotor Systems: Analysis and Identification. *CRC Press.Boca Raton, FL, USA.*
- Tondl, A. (1965). Some Problems of Rotor Dynamics *Chapman and Hall, Ltd., London, U K.*
- Varney, P. and Green, I. (2012). Crack detection in a rotor dynamic system by vibration monitoring-Part II: extended analysis and experimental results. *ASME, Journal of Engineering for Gas Turbines and Power,* 134(11), 112501.

- Varney, P. and Green, I. (2013). Rotordynamic crack diagnosis: distinguishing crack depth and location.*ASME, Journal of Engineering for Gas Turbines and Power*, 135(11),112101.
- Varney, P. and Green, I. (2015). Nonlinear phenomena, bifurcations, and routes to chaos in an asymmetrically supported rotor–stator contact system. *Journal of Sound and Vibration*, (336) 207-226.
- Varney, P. and Green, I. (2016). Rotordynamic analysis of rotor–stator rub using rough surface contact. *ASME,Journal of Vibration and Acoustics*, 138(2), 021015.
- Varney, P. and Green, I. (2016). Rough surface contact of curved conformal surfaces: an application to rotor-stator rub.*ASME,Journal of Tribology*, 138(4),041401.
- Varney, P. and Green, I. (2017). Comparing the Floquet stability of open and breathing fatigue cracks in an overhung rotordynamic system. *Journal of Sound and Vibration*, (408), 314-330.
- Varney, P. and Green, I. (2017). Impact phenomena in a noncontacting mechanical face seal. *Journal of Tribology, ASME*, 139(2), 022201.
- Vatta, F. and Vigliani, A. (2008). Internal damping in rotating shafts. *Mechanism and Machine Theory*, 43(11), 1376-1384.
- Vervisch, B. (2016). Experimental analysis of rotating damping in high speed machinery. *Doctoral Dissertation, Ghent University, Belgium*
- Vervisch, B., Derammelaere, S., Stockman, K. and Loccufier, M. (2014). Frequency response functions and modal parameters of a rotating system exhibiting rotating damping. *In International Conference on Noise and Vibration Engineering (ISMA),* 2837-2849.15-17 September, Leuven, Belgium.

- Vervisch, B., Derammelaere, S., Stockman, K., De Baets, P. and Loccufier, M. (2016). On the experimental prediction of the stability threshold speed caused by rotating damping. *Journal of Sound and Vibration*, (375), 63-75.
- Walton, J., Artiles, A., Lund, J., Dill, J. and Zorzi, E. (1990). Internal rotor friction instability.*Mechanical Technology, Inc*., *NASA.*February 01, ID 19900012079.
- Wang, S., Bi, C., Li, J. and Zheng, C. (2019). Parametric instability of anisotropic rotor-bearing systems with a transverse crack. *Journal of Sound and Vibration*, 443, 253-269.
- Wauer J. (1990) Modelling and formulation of equations of motion for cracked rotating shafts. *International Journal of Solids and Structures*, 26, 901-914.
- Wells, A. A. (1973). Fracture control: past, present and future. *Experimental Mechanics*, 13(10), 401-410.
- Werner, F. (1993). The Ratio of 2X to 1X Vibration–A Shaft Crack Detection Myth. *Orbit*, 14(3), 11.
- Woodley, B. J. (1978). Failure prediction by condition monitoring (part 1). *International Journal of Materials in Engineering Applications*, 1(1), 19-26.
- Xia Y. and Lin R. M. (2004). A New iterative order reduction (IOR) method for eigensolutions of large structures. *International Journal for Numerical Methods in Engineering*, 59, 153–172.
- Zhao X., Patel T. H. and Zuo M. J. (2012). Multivariate EMD and full spectrum based condition monitoring for rotating machinery. *Mechanical Systems and Signal Processing* 27, 712-728.
- Zhengjia, H., Yudi, S. and Liangsheng, Q. (1990). Rub failure signature analysis for large rotating machinery. *Mechanical Systems and Signal Processing*, 4(5), 417-424.

- Zhou T., Sun, Z. Xu, J. and Han, W. (2005). Experimental analysis of cracked rotor. *Journal of Dynamic systems, Measurement and Control*, 127, 313-320.
- Zorzi, E. S. and Nelson, H. D. (1977). Finite element simulation of rotor-bearing systems with internal damping. *ASME, Journal of Engineering for Gas Turbines and Power*, 99(1), 71-76.

Publications from the Present Work

Journals:

1. Roy, D. K., and Tiwari, R. (2019). Development of identification procedure for the internal and external damping in a cracked rotor system undergoing forward and backward whirls. *Archive of Mechanical Engineering*, 66(2), 229-255.
2. Roy, D. K., and Tiwari, R. (2019). Experimental identification of rotating and stationary damping in a cracked rotor system with an offset disc. *Archive of Mechanical Engineering*, 66(4), 447-474.

3. Roy, D. K., and Tiwari, R. (2020). Estimation of the internal and external damping from the forward and backward spectrum of a rotor with a fatigue crack. *Propulsion and Power Research*, 9(1), 62-74.
4. Roy, D. K., and Tiwari, R. (2020). Experimental identification of internal and external damping in a rotor system with a fatigue-crack using full spectrum, Experimental Techniques, 1-20, Online available (DOI: https://doi.org/10.1007/s40799-020-00368-7).

5. Roy, D. K., and Tiwari, R. (2020). Finite element model based identification of the internal and external damping in a rotor-bearing system having switching crack (Communicated)

Conferences:

1. Roy, D. K., and Tiwari, R. (2017). A full spectrum analysis of a Jeffcott rotor with switching crack in the presence of internal and external damping. *ICOVP, 13th International Conference on Vibration Problems, During 29th November - 2nd December, Indian Institute of Technology Guwahati, India.*

2. Roy, D. K., and Tiwari, R. (2019, December). Finite Element Model Based Full Spectrum Response Analysis of a Cracked Rotor With Internal and External Damping. *In Gas Turbine India Conference (Vol. 83525, p. V001T05A017) during 5th to 6th December. American Society of Mechanical Engineers. Indian Institute of Technology Madras, India.*